January 2021

Flexure And Punching Shear Behavior Of Uhpc Elements Post-Tensioned With Unbonded Tendons

Mehmet Dogu
Wayne State University

FLEXURE AND PUNCHING SHEAR BEHAVIOR OF UHPC ELEMENTS POST-TENSIONED WITH UNBONDED TENDONS

by

MEHMET DOGU

DISSERTATION

Submitted to the Graduate School

of Wayne State University,

Detroit, Michigan

in partial fulfillment of the requirements

for degree of

DOCTOR OF PHILOSOPHY

2021

MAJOR: Civil and Environmental

Engineering (Structural Engineering)

Approved By:

_____

Advisor Date

_____

_____

_____

_____

DEDICATION

This dissertation is dedicated to my family and sweetheart Yasemin.

ACKNOWLEDGEMENTS

I would like to thank my supervisor Dr. Menkulasi for giving me the opportunity to work on my dissertation. He has been instrumental in acquiring technical knowledge on post-tensioned concrete and Ultra-High-Performance concrete (UHPC).

Special thanks also go to Dr. Eamon for serving in my committee, for his thought provoking comments during my proposal defense. I would like to thank Dr. Gruber for serving in my committee and for his feedback on my proposal. Also, I would like to thank Dr. Wollmann for serving in my committee and for her feedback on my proposal defense.

Special thanks go to Mr. Richard Barber for partial funding in 2018 summer semester under Richard Barber interdisciplinary program.

I would like to express my gratitude to Dr Erhan Karaesmen for helping me on my graduate level education path. Dr Karaesmen played key role in my life, which is career path.

I would like to express my special thanks to my roommate Furkan Cakmak on motivation and technical topics. I cannot miss mentioning my friends Mehmet Kolcu, Suleyman Yildirim, Salih Rakici and Tunc Kulaksiz for their psychological support on graduate level education.

Words would not be adequate to express my gratitude towards my family. My mother Bahriye, my father Zafer Sahin, my grandmother Medine and my sisters Medine and Melek have made my entire life a source of happiness. This dissertation is dedicated to my family and sweetheart Yasemin…

TABLE OF CONTENTS

1. Chapter 1: Introduction 1

2. Chapter 2: Literature Review 4

2.1 Flexural capacity of beams post-tensioned with internal unbonded tendons 4

2.2 Moment-curvature relationship of post-tensioned beams 8

2.3 Punching shear capacity of slabs 12

3. Chapter 3 : A Flexural Design Methodology for UHPC Beams Post-tensioned with Unbonded Tendons 16

3.1 INTRODUCTION 16

3.2 INVESTIGATED POST-TENSIONED UHPC BEAMS WITH UNBONDED TENDONS 18

3.3 FINITE ELEMENT ANALYSES 21

3.3.1 Modeling Protocol 21

3.3.1.1 *Simulation of Unbonded Post-tensioning* 23

3.3.2 Validation 31

3.4 RESULTS AND DISCUSSION 34

3.4.1 Failure Mode 34

3.4.2 Sensitivity Analysis 41

3.4.3 Flexural Design Methodology 54

3.4.4 Comparison of Predicted and Computed Results 64

3.4.5 Evaluation of the Proposed Methodology for Various Classes of UHPC Materials 68

3.5 SUMMARY AND CONCLUSIONS 70

3.6 RECOMMENDATIONS FOR FUTURE WORK 71

4. Chapter 4 : Moment-Curvature-Deformation Response of UHPC Beams Post-tensioned with Internal Unbonded Tendons: Analysis and Algorithm 73

4.1 Introduction 73

4.2 Definition of Cross-sectional and Member Level Ductility 78

4.3 Procedure for Computing Moment Curvature and Load Displacement Relationship 80

4.3.1 Before Cracking 85

4.3.2 After Cracking 90

4.3.3 Discussion of the Proposed Procedure 99

4.4 Validation of Proposed Procedure 100

4.5 Parametric Analysis , Failure Mode and Ductility 102

4.5.1 Effect of ε_{tu} on complete flexural behavior 106

4.5.2 Effect of f_{cr} on complete flexural behavior 112

4.5.3 Effect of ρ_{ps} on complete flexural behavior 113

4.5.4 Effect of $\rho_{stension}$ on complete flexural behavior 115

4.5.5 Effect of loading configuration and tendon profile on complete flexural behavior .. 116

4.5.6 Effect of constitutive model for UHPC on complete flexural behavior 118

4.5.7 Effect of no mild steel on subroutine 119

4.6 Summary and Conclusions 120

5. Punching Shear Strength of Post-tensioned UHPC Plates 123

5.1 INTRODUCTION 123

5.2 RESEARCH SIGNIFICANCE 124

5.3 CREATION OF SPECIMEN DATABASE 125

5.3.1 Distinction of Punching and Flexural Failures in the Numerical Model 127

5.3.2 Validation of Numerical Modeling Protocol 131

5.4 PROPOSED PREDICTION METHODOLOGY 133

5.4.1 Load-Rotation Relationship 133

5.5 Moment Curvature 138

5.6 Failure Criteria 139

5.7 Distinction of Punching Shear and Flexural Failures in the Proposed Method 143

5.8 COMPARISON OF COMPUTED AND PREDICTED CAPACITIES 144

5.8.1 Parametric Analyses 144

5.8.2 Comparison of Computed and Predicted Plate Punching Shear Capacities 149

5.9 SUMMARY AND CONCLUSIONS 150

6. Chapter 6: Summary, Conclusions, and Recommendations 152

6.1 Summary 152

6.2 Conclusions 152

6.2.1 Flexural Strength of PT UHPC Beams 153

6.2.2 Moment Curvature Deformation Response of PT UHPC Beams 154

6.2.3 Punching Shear Strength of PT UHPC Plates 155

6.3 Recommendation for Future Work 157

APPENDIX A **159**

APPENDIX B **165**

REFERENCES **170**

ABSTRACT **180**

AUTOBIOGRAPHICAL STATEMENT **181**

LIST OF FIGURES

Fig. 3.1 Characteristics of investigated UHPC beams post-tensioned with unbonded strands ... 19

Fig. 3.2 Distribution of the number of specimens for several parameters ... 20

Fig. 3.3 a) Modelling approach for simulating the behavior of unbonded post-tensioning tendons, b) finite element mesh for concrete, c) finite element mesh for sheathing, tendon, and mild steel ... 24
Fig. 3.4 Assumed uniaxial stress-strain relationship for: a) UHPC, b) normal strength concrete, c) prestressing steel, d) mild steel ... 30
Fig. 3.5 Validation of adopted modeling protocol: a) ability of CDP model to capture the behavior of UHPC members prestressed with bonded strands, b), c), d), e), f), g), h) and i) ability of adopted modeling protocol to capture the behavior of normal strength concrete beam ... 33
Fig. 3.6 a) Flexural behavior of post-tensioned UHPC beams: a) rectangular beams, b) T-beams ... 36
Fig. 3.7 Stress diagrams at various stages for a fiber tension controlled rectangular specimen ... 38

Fig. 3.8 Illustration of fiber tension-controlled and concrete compression-controlled failures in: a) simply supported post-tensioned UHPC beams with a rectangular cross-section, b) continuous post-tensioned UHPC beams with a T cross-section ... 41
Fig. 3.9 a) Influence of loading configuration on Δf_{ps}, b) Proposed relationship between loading configuration and function f included in Eq. 3.10 ... 49
Fig. 3.10 Effect of d_p on the change in strand stress at the ultimate limit state ... 50

Fig. 3.11. Collapse mechanisms and total number of hinges for patterned loading (adapted after Harajli 2011) ... 52
Fig. 3.12. Influence of the number of hinges on the change in strand stress at the ultimate limit state ... 53
Fig. 3.13 Failure mechanism in UHPC beams post-tensioned with unbonded tendons: a) concrete compression-controlled members, and b) fiber tension-controlled members ... 55
Fig. 3.14 Proposed methodology for the flexural design of UHPC beams post-tensioned with unbonded tendons: a) Concrete compression-controlled failure, b) Fiber tension-controlled failure ... 62
Fig. 3.15. Comparison of computed and predicted a) change in strand stress at ultimate limit state, b) strand stress at ultimate limit state, and c) nominal moment capacity of the member ... 67
Fig. 4.1 Qualitative illustration of moment-curvature-deformation response for a typical UHPC beam post-tensioned with internal unbonded tendons ... 78
Fig. 4.2 Typical post-tensioned UHPC beam detail considered in moment-curvature and load-deformation response analysis ... 80
Fig. 4.3 Deformed a) uncracked and b) cracked configuration for a simply supported UHPC beam post-tensioned with internal unbonded tendons ... 81
Fig. 4.4 Stress-strain relationship for: a) UHPC in compression (left) and tension (right), b) prestressing steel, and c) mild steel ... 83

Fig. 4.5 Validation of: a) bilinear model, and b) trilinear model for the tensile domain of UHPC 84
Fig. 4.6 Flowchart used to obtain moment-curvature-deformation response in an uncracked UHPC beam post-tensioned with internal unbonded tendons 86
Fig. 4.7 Flowchart used to obtain moment-curvature-deformation response in a cracked UHPC beam post-tensioned with internal unbonded tendons 91
Fig. 4.8 Sensitivity analyses for the number of sections considered for half of the span in a typical UHPC beam post-tensioned with internal unbonded tendons 99
Fig. 4.9 Validation of proposed approach to compute moment-curvature-deformation response of UHPC beams post-tensioned with internal unbonded tendons: a) straight tendons, b) draped tendons 102
Fig. 4.10 Influence of various parameters on the moment-curvature relationship of UHPC beams post-tensioned with internal unbonded tendons: a) ε_{tu}, b) f_{cr}, c) A_{ps}, d) $A_{stension}$, e) loading configuration on straight tendon profile, f) loading configuration on draped tendon profile..... 103
Fig. 4.11 Influence of various parameters on the load-deformation relationship of UHPC beams post-tensioned with internal unbonded tendons: a) ε_{tu}, b) f_{cr}, c) A_{ps}, d) $A_{stension}$, e) loading configuration on straight tendon profile, f) loading configuration on draped tendon profile..... 104
Fig. 4.12 Influence of various constitutive models for UHPC on the moment-curvature and load-deformation relationship: a) influence of the compressive domain, and b) tensile domain 105
Fig. 4.13 Influence of various parameters on flexural capacity: a) ε_{tu}, b) f_{cr}, c) ρ_{ps}, d) $\rho_{stension}$, e) tendon profile 107
Fig. 4.14 Influence of the increase in ε_{tu} on strain, stress, and force diagrams for a typical UHPC beam post-tensioned with internal unbonded tendons 108
Fig. 4.15 Variation in the tension force provided by each component as a function of: a) ε_{tu}, b) f_{cr}, c) ρ_{ps}, and d) ρ_s. 109
Fig. 4.16 Influence of various parameters on cross-section and member level ductility: a) ε_{tu}, b) f_{cr}, c) ρ_{ps}, d) $\rho_{stension}$, e) tendon profile 110
Fig. 4.17 Influence of various parameters on L/Δ_u: a) ε_{tu}, b) f_{cr}, c) ρ_{ps}, d) $\rho_{stension}$, e) tendon profile 111
Fig. 4.18 Validation of unreinforced UHPC beam 120

Fig. 5.1 Proposed framework for predicting punching shear capacity of PT UHPC plates 123

Fig. 5.2 Modelling approach for simulating the behavior of PT UHPC plates under concentrated loads 126
Fig. 5.3 a) PT UHPC plates subject to punching (a1) and flexural (a2) failures; b) variation of maximum principal tensile strain in punching (b1) and flexure (b2) critical plates; c) load-deflection relationship in punching (c1) and flexure (c2) critical plates. 128
Fig. 5.4 Validation of numerical modeling protocol - comparison of computed and measured plate load-deflection relationship for: a) PT NSC plates; b) unreinforced UHPC plates 132
Fig. 5.5 a) Simplified plate kinematics at punching shear failure, b) internal and external forces acting on a typical plate pie strip. 135
Fig. 5.6 Proposed moment-curvature relationship for PT UHPC elements used in the derivation of plate load-rotation relationship 136
Fig. 5.7 Comparison of computed and predicted: a) plate load-rotation relationship; b) mid-plate moment-curvature relationship (per unit width of plate) 137

Fig. 5.8 Validation of proposed failure criterion and impact of adjusting plate rotation to account for prestressing force..... 142
Fig. 5.9 Influence of various parameters on PT UHPC plate punching shear strength..... 144

Fig. 5.10 Comparison of computed and predicted PT UHPC plate punching shear strength 150

LIST OF TABLES

Table 3.1 Characteristics of investigated UHPC beams post-tensioned with unbonded strands 18

Table 3.2. Adopted Concrete Damage Plasticity parameters for NSC and UHPC 27

Table 3.3. Effect of f'_c on Δfps 43

Table 3.4. Effect of A_{ps} on Δfps and on failure mode 44

Table 3.5. Effect of A_s on Δf_{ps} 45

Table 3.6. Effect of f_{cr} on Δf_{ps} 45

Table 3.7. Effect of ε_{tu} on Δf_{ps} 46

Table 3.8. Effect of continuity on Δf_{ps} 47

Table 3.9. Effect of loading configuration on Δf_{ps} 48

Table 3.10. Effect of dp on Δfps 50

Table 3.11. Effect of number of hinges on Δfps 52

Table 3.12. Effect of μ on Δfps 54

Table 3.13. Comparison of predicted and computed Δf_{ps}, f_{ps}, M_n 66

Table 4.1 Gauss-Legendre Coefficients (Hornbeck 1975) 85

Table 4.2. Beam properties used in parametric analysis (See Fig. 4.2 for illustration) 105

Table 4.3. Influence of ε_{tu} on flexural capacity and ductility 106

Table 4.4. Influence of cracking stress f_{cr} on flexural capacity and ductility 113

Table 4.5. Influence of ρ_{ps} on flexural capacity and ductility 114

Table 4.6. Influence of $\rho_{stension}$ on flexural capacity and ductility 116

Table 4.7. Influence of tendon configuration on flexural capacity and ductility 117

Table 5.1 Characteristics of investigated PT UHPC plates 126

Table 5.2 Influence of several parameters on PT UHPC plate punching shear capacity 129

LIST OF TERMS

A_g : gross area of section

A_p: horizontally projected area of punching shear failure surface

A_{ps}: prestressing tendon area

A'_s : total area of compression mild steel

A_s: total area of tension mild steel

b: width of section

b_c: cross section dimension of square column

b_o: control perimeter set d/2 from column

b_w: width of section

C : total force carried by UHPC in section

c: neutral axis depth measured from the topmost compression fiber

d : effective depth of longitudinal reinforcement

d_f : fiber diameter

d_g : maximum diameter of aggregate

$d_{g,0}$: reference aggregate size (16mm)[0.63 in.]

$dL_{cracked}$: distance between evaluated sections for member level compatibility

d_p : distance from centroid of tendons to uppermost compression fiber

d_{ps} : distance from centroid of tendons to uppermost compression fiber

d'_s : distance between centroid of compression mild steel to uppermost compression fiber

d_s: distance between centroid of tension mild steel to uppermost compression fiber

E_c : modulus of elasticity of UHPC

E_{ps}: modulus of elasticity of prestressing tendon

E'_s : modulus of elasticity of compression mild steel

E_s: modulus of elasticity of tension mild steel

EI_0: uncracked bending stiffness

EI_1: bending stiffness between cracking and yielding

EI_2: bending stiffness between yielding and ultimate

e : eccentricity of prestressing tendon

e_{tendon} : eccentricity of prestressing tendon

f : term for loading configuration

f_c' : compressive strength of UHPC

f_y' : yield stress of compression mild steel

f_y: yield stress of tension mild steel

f_{cr} : cracking stress of UHPC

$f_{jacking}$: jacking prestress

f_{pe} : effective prestress

f_{ps} : total strand stress

f_{pu} : strand ultimate stress

f_{py} : strand yield stress

F_{tendon} : total force in prestressing tendon

h: total section height

I_g: gross moment of inertia

K_f: global orientation factor

k_b: bond coefficient

l_{crit}: critical fiber length

l_f: fiber length

$L_{elastic}$ *($L_{uncracked}$):* length of elastic/uncracked portion of the member in the half the span

L : total length of member

$L_{cracked}$: length of cracked portion of the loaded member

L_p: plastic hinge length

m_p : unitary bending moment due to prestressing

m_r : unit radial moment

m_t : unit tangential moment

$M_{applied}$: externally applied moment

$M_{cracking}$: external moment that is causing first cracking

$M_{midspan}$: external moment at midspan

M_n (M_p) : nominal moment capacity of the beam

n: number of sections considered in cracked region

n : unit normal force from prestressing

N_{actual} : existing number of hinges depending on loading configuration

N_p : total number of hinges

N_{total} : total possible number of hinges when all spans loaded

r : radius

r_c : radius of circular column

r_{cr} : radius of uncracked region

r_m : location of unitary bending moment due to prestressing

r_s : radius of slab

r_o : radius of critical shear crack

r_y : radius of yielded region

r_q : radius of load introduction at perimeter

S_{bottom}: bottom sectional modulus

S_{top} : top sectional modulus

T_C : total force carried by fibers in UHPC in section

T_{PS} : total force carried by prestressing tendon in section

T_S' : total force carried by compression mild steel reinforcement in section

T_S : total force carried by tension mild steel reinforcement in section

V_P : vertical component of prestressing force in tendon

V_R : punching shear strength

$V_{R,c}$: concrete contribution to punching shear strength

$V_{R,f}$: fiber contribution to punching shear strength

w : critical shear crack opening

y_{bottom} : distance from neutral axis to bottom most fiber

y_{top} : distance from neutral axis to topmost fiber

α_f : fiber aspect ratio

α_I : engagement parameter

ξ : distance of a point with respect to soffit of slab

$\varepsilon_{bottom,c}$: strain in bottom most fiber of UHPC

ε_c : compressive strain of UHPC in uppermost most fiber

ε_{cr} : cracking strain of UHPC

ε_{cu} : ultimate compressive strain of UHPC

ε_{tu} : maximum usable tensile strain of UHPC

$\varepsilon_{top,c}$: strain in topmost fiber of UHPC

ε_{pe}: initial effective strain in prestressing tendon

ε_{ps_total} (ε_{ps}): total strain in prestressing tendon

ε_t : tensile strain of UHPC in bottom most fiber

θ_p : total plastic rotation

φ : curvature

φ_r : curvature in radial direction

φ_t : curvature in tangential direction

φ_u : ultimate curvature

δ : elongation of tendon at collapse mechanism

Δ: deflection

Δf_{ps}: change in strand stress

$\Delta f_{ps,assumed}$: assumed change in strand stress

$\Delta f_{ps,calculated}$: calculated change in strand stress

$\Delta\varepsilon_{ps\_decompression}$: strain increase in tendon due to decompression

$\Delta\varepsilon_{concrete\_elastic}$: elastic change in concrete strain at centroid of tendons

$\Delta\varepsilon_{concrete\_cracked}$: change in concrete strain at centroid of tendons

$\Delta\varepsilon_{ps\_elastic}$: elastic change in strain in prestressing tendon

$\Delta\varepsilon_{ps}$: change in strain in prestressing tendon

$\Delta L_{elastic}$: length increase in prestressing tendon in the uncracked part of the member

$\Delta L_{decompression}$: length increase in prestressing tendon due to decompression

$\Delta L_{cracked}$: length increase in prestressing tendon in the cracked part of the member

$\Delta_{midspan}$: midspan displacement

Δ_u : midspan displacement

$\Delta\theta$: angle of slab piece

λ : ratio of existing hinge number to total possible hinge number

μ : friction coefficient

ρ_f: fiber reinforcement ratio (in volume)

σ_{fu}: tensile strength of fiber

σ_n: average stress due to in-plane forces

σ_{tf}: fiber bridging stress

σ_{top}: stress in topmost fiber of UHPC

σ_{bottom}: stress in bottommost fiber of UHPC

$\sigma_{cracking}$ (f_{cr}): cracking stress of UHPC

τ_b : bond strength

χ_{TS1} : decrease in curvature due to tension stiffening between cracking and yielding

χ_{TS2} : decrease in curvature due to tension stiffening between yielding and ultimate

Ψ : slab rotation outside column region

Ψ' : reduced rotation of slab

1. Chapter 1: Introduction

Careful thinking about likely future realities is what civil engineers do every day when planning, designing, and implementing their projects (ASCE 2020). American Society of Civil Engineer's Future World Vision Project examines a variety of plausible future outcomes in our built world, but at a scale much larger than civil engineers typically consider. This glimpse into an array of possible future world scenarios is intended to help civil engineers and the broader infrastructure industry, make decisions today that will lead to better outcomes tomorrow (ASCE 2020). A total of four possible future world scenarios were developed and for each scenario, an in-depth analysis was performed to understand the implications to the infrastructure industry over future timeframes (10, 25, and 50 years from today) (ASCE 2020). Scenario No. 2 is called Progressive Megacities and one of its characteristics is mass urbanization. There is an opportunity in this scenario for structural engineers to make a contribution by designing super slender structures that maximize the available rentable or usable space. This can be achieved by maximizing the number of floors that can be supported for a given structural footprint. This challenge cannot be met with traditional materials, the limitations of which are well known by the engineering community. ASCE's Future World Vision Project alludes to the use of stronger materials among other things. While the development and utilization of stronger construction materials have been a focus of research for quite some time, there are some unique combinations of stronger and traditional materials that have yet to be explored.

The purpose of this dissertation is to understand the mechanics of structural elements constructed with ultra-high-performance concrete (UHPC) and post-tensioned with unbonded prestressing strands so that this information can be used in the creation of super slender structures that meet the challenge stated above. Potential applications for such elements include super thin

and super slender floors in building structures, which help reduce the dead load at every level and result in significant reduction in overall building mass. This reduction in gravitational loads results in lower load demand on columns, walls, and foundations. This provides an opportunity to accommodate more floors for a given column or wall footprint. Additionally, the reduction in building mass results in lower seismic load demand on the lateral load resisting system making possible the utilization of low volume lateral load resisting systems.

The focus of this dissertation is understanding the mechanics of horizontal structural members such as beams, and flat plates constructed with UHPC and post-tensioned with unbonded tendons. This study deals primarily with two structural actions: flexure in beams and punching shear in flat plates. The understanding of one-way flexural behavior of PT UHPC elements can inform the design of two-way flat plates, since the design of these floor systems is typically simplified by considering equivalent frames in each orthogonal direction. The part of the study that focuses on flexure is divided into two chapters, namely Chapter 3 and Chapter 4, whereas Chapter 5 is concerned with the development of a methodology to predict the punching capacity of post-tensioned UHPC flat plates.

Chapter 3 deals with the development of a methodology to determine the flexural strength of UHPC beams post-tensioned with unbonded tendons. A methodology for predicting strand stress at the ultimate limit state is proposed and a characterization of the flexural failure mode is conducted. The methodology for predicting strand stress at the ultimate limit state is based on a collapse mechanism approach and relies on the use of an empirically obtained formulation for the plastic hinge length.

Chapter 4 is concerned with the development of an algorithm, which can be used to characterize the full moment curvature and load deformation response of UHPC beams post-

tensioned with unbonded tendons. The methodology used to develop this algorithm is free of any empiricism other than the one used in the assumed material constitutive relationships.

Chapter 5 is concerned with understanding the behavior of post-tensioned UHPC flat plates subject to concentrated loads. A failure criterion for predicting punching shear capacity of these plates is proposed. The failure criterion is a function of plate rotation, cross-sectional geometry, material properties including contribution of fibers, as well as post-tensioning force magnitude, and simultaneously supplies the punching load and rotation capacity of the plate thus providing insight about plate ductility. The punching capacity is determined by superimposing the failure criteria and a load-rotation relationship obtained from a moment curvature analysis of the plate in bending. The intersection of these two curves provides the punching and rotation capacity of the post-tensioned UHPC flat plate. Given that such plates are likely to provide significant ductility, a criterion for distinguishing between punching and flexural failures is developed for the numerical models as well as for the proposed prediction methodology.

The dissertation is presented in a manuscript format in the sense that Chapters 3, 4, and 5 are written as stand-alone chapters. The author believes that the presented work is pioneering effort since the behavior of PT UHPC elements appears to be unexamined in the scientific literature. Chapter 2 provides a literature review on topics that deal with the flexure and punching shear behavior of normal strength concrete (NSC) or fiber reinforced concrete (FRC) elements. Although the behavior of PT UHPC elements is believed to be different from that NSC or FRC elements a brief discussion of relevant topics is presented in Chapter 2 has well as in Chapters 3-5 in their introduction sections. Conclusions and recommendations are presented in Chapter 6.

2. Chapter 2: Literature Review

As noted in the introduction chapter, the flexural and punching shear behavior of PT UHPC elements appears to be unexamined and provided the motivation to conduct this study. This chapter provides a brief summary of previous relevant studies as many of them provided the framework for developing prediction methodologies for the flexural and punching shear behavior of PT UHPC elements.

2.1 Flexural capacity of beams post-tensioned with internal unbonded tendons

The lack of bond between concrete and post-tensioned tendons creates an analytical problem in terms of developing a methodology for predicting the flexural strength of concrete beams post-tensioned with unbonded tendons because tendon stress at ultimate strength is system dependent rather than section dependent. The literature on strand stress increase of unbonded tendons in post-tensioned beams constructed with NSC contains many prediction methodologies with some based on phenomenological principles and others simply on statistics (AASHTO 2017, Roberts-Wollmann et al. 2005, MacGregor et al. 1989, BSI 2001, DIN 1980, SIA 1979, Tam and Pannel 1976, Harajli 2011, Naaman and Alkhairi 1991, He and Liu 2010, ACI 2014, Six et al. 2019, Kim and Kang 2019, Peng and Xue 2019, Maguire et al. 2017, Maguire et al. 2016). A detailed discussion of these methodologies is provided in Peng and Xue (2019). The following is a summary of various approaches for calculating the strand stress at the ultimate limit state, f_{ps}, or the change in strand stress at the ultimate limit state, Δf_{ps}.

The formulation presented in AASHTO LRFD Specifications (2020) for the calculation of strand stress at the ultimate limit state, provides a term that accounts for PT NSC beam continuity through the consideration of the number of potential plastic hinges. Loaded and unloaded spans

are distinguished using the total plastic hinge number. Type of loading is not included in the formulation. The inclusion of neutral axis depth in the ultimate tendon stress equation accounts for the influence of nonprestressed reinforcement. The equation in AASHTO LRFD Specifications (2020) for predicting the change in strand stress was derived considering a collapse mechanism approach based on the work conducted by Roberts-Wollman et al. (2005) and MacGregor (1989). The ratio of plastic hinge length to neutral axis depth is taken as a constant value of 10.5 for simplification, and is based on recommendations by Tam and Pannell (1976). Rotation at support hinges is taken equal to half of that at mid-span.

The formulation presented in the British code (BSI 2001) for the calculation of strand stress is similar to that presented in AASHTO LRFD Specifications (2020), except that the ratio of plastic hinge length to neutral axis depth is taken equal to 10. The ratio of total tendon length to effective tendon depth, total tendon area, ultimate tendon stress, compressive strength of concrete, width of section, and effective tendon depth, are all parameters that are included in the calculation of strand stress increase at flexural failure.

The approach presented in DIN (1980) and SIA (1979) for the calculation of strand stress at the ultimate limit state includes a calculation of rotation at plastic hinge location by utilizing deflection estimates for different span to depth ratios.

Harajli (2011) introduced a loading parameter for calculating Δf_{ps}, where the loading parameter is a function of the number of positive and negative plastic hinges and a loading pattern coefficient. Neutral axis depth, effective depth of tendon, modulus of elasticity of tendon and ultimate compressive strain of concrete are the parameters included in the Δf_{ps} equation. Point load, two-point load, and distributed loading can be distinguished by a loading pattern coefficient.

Naaman and Alkhairi (1991) developed an approach for calculating f_{ps} that includes a bond reduction coefficient. Unbonded tendons, typically, have almost constant stress along the length of the member. Therefore, there is typically no stress concentration like the one exhibited by bonded tendons. The introduction of a reduction coefficient allows the treatment of unbonded tendons similar to that of bonded tendons and provides great analytical convenience. Depending on the configuration of the tendon (draped, straight, or harped) and loading type (point load, two-point load, or distributed load), different bond reduction formulations were proposed for different stages of loading. For design at the ultimate limit state, a quadratic equation needs to be solved for the determination of the neutral axis depth and ultimate tendon stress. Member span to depth ratio is accounted for in a gradual manner unlike the stepwise approach used in ACI 318-19 (2019).

He and Liu (2010) proposed an approach for calculating f_{ps} that accounts for second order effects, tendon configuration, and loading type. A deflection reduction coefficient was introduced as a function of loading type.

ACI 318-19 (2019) offers two different ultimate tendon stress equations as a function of member span to depth ratio and accounts for the amount of prestressed reinforcement. The method presented in ACI 318-19 (2019) for the calculation of f_{ps} does not account for various loading configurations, continuity, or the presence of nonprestressed reinforcement, and is applicable for concretes with compressive strength up to 10 ksi.

Six et al. (2019) conducted experiments on four three span continuous PT beams. The equation presented by Maguire et al. (2017) for the increase in tendon stress was found to be the most accurate. Nonprestressed reinforcement was reported to be an important parameter in terms of ductility and moment redistribution. Also, tendon stress increase was found to have marginal effect on the flexural strength of the beam.

Kim and Kang (2019) conducted seven experiments on two-span continuous beams where the variables of interest were effective tendon depth, prestressing magnitude and tendon strength. The use of strands with f_{pu} = 350 ksi was investigated. The change in strand stress at the ultimate limit state was determined to be similar to that measured for strands with f_{pu} = 270 ksi.

Peng and Xue (2019) proposed a simplified methodology for tendon stress increase where member level compatibility between tendon and beam was used. A large number of experimental results were compared with the proposed methodology with a mean value of measured over predicted change in strand stress equal to 1.13 and a standard deviation of 31%.

Maguire et al. (2017) created an experimental database for simple and continuous beams to conduct a comparison of different methodologies for calculating the change in strand stress. A large scatter between predictions and experimental results was reported. Different plastic hinge length formulations for internally unbonded and externally unbonded tendons were proposed based on regression analysis.

Maguire et al. (2016) conducted experiments on four post-tensioned two-span continuous slabs with unbonded tendons. A large scatter between various prediction methodologies and measured strains [stresses] was found. The method proposed by Naaman and Alkhairi (1991) was found to be the most accurate.

All these methodologies are based on the assumption that concrete offers no strength in tension after cracking, which is not valid for UHPC for which the nonlinear domain in tension is an important part in the design of an UHPC structure. The behavior of precast pretensioned UHPC components reinforced with bonded strands was investigated by Chen and Graybeal (2012) for bridge I-girders. However, the interaction between UHPC and strands in this case is simpler

because strain compatibility between concrete and steel can be assumed, and a sectional analysis can be performed.

2.2 Moment-curvature relationship of post-tensioned beams

The determination of the complete flexural response of a PT member is related to the determination of unbonded strand stress at various stages of loading. Various approaches have been used to determine this stress and consequently the complete flexural response for normal strength concrete (NSC) members. Some (Balaguru 1981, Naaman and Alkhairi 1991, Harajli and Kanj 1992, Pannell 1969, Tam and Pannell 1976, Au and Du 2004, Harajli 2006, Harajli 1990, Lee et al. 1999, Harajli et al. 2002, van Weerdhuizen and Bartlett 2020, Au et al. 2005, Vega and Dotreppe 1988) include the determination of strand stress at discrete points and limited ranges such as ultimate limit state and service, respectively, whereas others (Alkhairi and Naaman 1993, Knight et al. 2014, Ariyawardena and Ghali 2002, Ozkul et al. 2008, Vu et al. 2010, Kim et al. 2012) provide guidance for how to obtain the complete flexural response.

Balaguru (1981) proposed a methodology to predict strand stress at service and ultimate level loads for NSC beams post-tensioned with unbonded tendons. Change in strand strain at service was empirically expressed as a function of span-eccentricity and eccentricity-maximum deflection ratio. To obtain the change in strand stress at the ultimate limit state, a maximum deflection at ultimate is assumed based on what would be acceptable for this stage, and the attainability of this deflection is checked using the rotation capacity of the beam.

Naaman and Alkhairi (1991) proposed a simplified methodology to predict the stress in unbonded tendons in NSC beams under service and ultimate loading conditions by employing empirically obtained bond reduction coefficients, which facilitate the use of solutions based on strain compatibility while accounting for the lack of bond. This approach is attractive from a design

perspective, since it addresses critical loading stages for a member, such as behavior at service and at ultimate limit state. The concept of using a coefficient to account for the relative slip between concrete and tendons was also used by Harajli and Khanj (1992).

Naaman and Alkhairi 1991, Pannell 1969, Tam and Pannell 1976, Au and Du 2004, Harajli 2006, Harajli 1990, Lee et al. 1999, Harajli et al. 2002 developed empirical formulations for calculating an equivalent plastic hinge length, which is attractive not only for calculating strand strain at the ultimate limit state, ε_{ps}, but also nominal flexural capacity, M_n.

Van Weerdhuizen and Bartlett (2020) discussed methods to calculate deflection at incipient failure, Δ_u, which was presented as a warning of failure metric. Deflection at incipient failure depends on the ductility of sections and plastic hinge length, where plastic hinge length is dependent on loading type and boundary conditions. Redundancies in structures were reported to reduce deflection at incipient failure. Deflections were normalized in terms of a warning factor as function of span length, nonprestressed reinforcement ratio and effective beam depth.

Au et al. (2005) extended Pannell's (1969) approach to investigate cracked PT NSC beam behavior under service loads. Au et al. (2005) compared stress predictions under service loads with available test data. Equivalent plastic hinge length to neutral axis depth ratio was reported to be a constant value. Using this constant value, a cubic function was proposed to predict tendon stress increase. Third point loading was determined to produce a tendon stress increase that was quite similar to that caused by distributed loading. The span to depth ratio had a very minor effect on increase in tendon stress at service level loads.

Vega and Dotreppe (1988) investigated the moment-curvature response of NSC beams prestressed with unbonded tendons at service and ultimate level loads using linear elastic beam flexure theory and an assumption for the plastic hinge length, respectively.

These studies dealt primarily with understanding the behavior of NSC beams post-tensioned with unbonded tendons under service and ultimate level loads. While these two stages of loading are of great importance to practicing engineers from the perspective of being able to calculate deflections at service and flexural capacities at the ultimate limit state, they provide limited insight about cross-section and member level ductility, the calculation of which is better informed by the availability of the full moment-curvature-deformation response. Additionally, as performance-based design transitions from being an exception to becoming a norm in structural design, approaches that provide the means to obtain the full response of the structural members under loading will be needed.

Alkhairi and Naaman (1993) and Knight et al. (2014) used mechanics-based approaches to address analytically the complete range of behavior of NSC beams post-tensioned with unbonded tendons thus addressing this need for NSC members. Alkhairi and Naaman (1993) used force and moment equilibrium in various locations of a member. Member level deformation compatibility was assumed between the length of the concrete beam and the length of the tendon. Numerical integration was conducted to correlate the curvature diagram along the length of the member to tendon stress increase and computation of deflection. The proposed prediction methodology is applicable to internally bonded and unbonded tendons and externally unbonded tendons. The approach presented by Alkhairi and Naaman (1993) presented the basis for the formulation of the procedure to obtain the moment-curvature-deformation response of PT UHPC beams presented in Chapter 4.

Ariyawardena and Ghali (2002) developed a computer model to predict the complete response of PT NSC members with internal or external tendons. In this method of analysis, the PT element is modeled as an assemblage of plane frame members connected at nodes. Tension

stiffening effects, material nonlinear behavior of concrete and reinforcement can be accounted in the proposed computer model. Slippage at deviation points of external tendons and change of eccentricity of external tendons were also considered in the proposed analysis procedure.

Ozkul et al. (2008) proposed a methodology, which considers the beam and tendon as a trussed beam system that allows for the use of equilibrium and compatibility equations as well as the law of conservation of energy to predict behavior at various load levels. Compressive strength of concrete and nonprestressed reinforcement area were found to not influence the increase in tendon stress. The proposed method allows the analysis of bonded and unbonded tendons. The number of cracks and plastic hinge length were found to be affected by the amount of nonprestressed reinforcement.

Vu et al. (2010) proposed a model that allows the calculation of the structural response of PT NSC beams including deflections under service loading, before and after cracking, as well as at the ultimate limit state. The model uses a non-linear beam macro finite element, which is characterized mainly by its homogenous average moment of inertia (Vu et al. 2010). Monotonic and cycled load effects were considered in methodology. Tension stiffening effect was considered while calculating average inertia. Also, effect of corrosion on bond between mild steel and concrete can be accounted for using the proposed macro finite element model.

Kim and Lee (2012) developed an algorithm for predicting the load deformation response of continuous PT NSC members including the ability to capture moment redistribution. Proposed methodology was compared with test results of continuous beams with internal and external tendons, different tendon configurations and section shapes. Effect of loading type was captured through moment diagram and curvature values along beam sections evaluated.

While the need to predict the complete flexural response of PT NSC members has been met, there is currently no efficient tool to predict the complete response of PT UHPC members whose behavior is significantly different from that of their NSC counterparts. For example, the studies mentioned above are based on the assumption that concrete is a material that resists primarily compression forces after cracking and flexural capacity is achieved when concrete ultimately crushes in compression. These assumptions do not reflect the behavior of UHPC as a material, which has unique compressive and tensile domains and do not represent the flexural failure mode of PT UHPC members as will be demonstrated in Chapter 3 and 4. As a result, the tensile domain of UHPC plays an important role in dictating the failure mode of such members. Nonlinear finite element analysis can be used to obtain the complete flexural response of PT UHPC beams, however, the creation and analysis of reliable models even for simple beams requires considerable time.

2.3 Punching shear capacity of slabs

The behavior of reinforced and post-tensioned concrete flat plates constructed with normal strength concrete (NSC) and fiber reinforced concrete (FRC) under concentrated loads has been investigated by Muttoni (2008), Clement et al. (2012; 2014), Maya et al. (2012); Neto et al. (2014); and Gouveia et al. (2017). Similarly, the behavior of unreinforced UHPC plates has been investigated by Harris (2004), Harris and Roberts-Wollmann (2005), and Joh et al. (2008).

Kinnunen and Nylander (1960) conducted experimental work on circular slabs without transverse reinforcement by varying the flexural reinforcement ratio. A truncated slab section was considered to establish force and moment equilibrium. The main failure mode was found to be tangential cracks at the slab to column connection. Similar work was conducted by Hallgreen (1996) and Broms (2006).

Muttoni (2008) developed a methodology to predict the punching shear capacity of NSC slabs based on critical shear crack theory and using a similar approach with that was used by Kinnunen and Nylander (1960), Hallgreen (1996) and Broms (2006). The proposed method is based on critical slab rotation and crack width at punching shear failure. The methodology is based on the concept that the larger the crack width the smaller the force transferred through the critical shear crack region. Crack width is related to slab rotation and effective slab depth. The load rotation relationship for the slab was derived using a quadrilinear moment curvature relationship for a typical plate strip. An empirical failure criterion which is a function of critical perimeter, effective depth of slab, compressive strength of concrete, slab rotation, reference aggregate size and maximum size of aggregate was proposed. The intersection of the curve representing the empirical failure criterion and the one representing the load rotation relationship provides the punching shear strength of the slab. Radial and tangential moments in a typical pie strip were equated to moments created by external loads. The shape of the slab was assumed to be conical outside of the column region and spherical inside of the column region. Slab rotation was calculated based on the conical slab shape assumption and was used to calculate curvature and corresponding moments at a given section. The proposed method was compared to experimental data resulting in an average value of measured over predicted punching shear strength of 1.02 and a coefficient of variation of 8%.

Maya et al. (2012) extended the critical shear crack theory to fiber reinforced concrete where the contribution of fibers was accounted for by a separate term. The variable engagement model (VEM) proposed by Voo et al. (2010) was utilized to calculate the fiber term. To quantify the contribution of fibers the average fiber bridging stress along the crack region was assumed for

simplicity. Crack width was assumed to be correlated with slab rotation and effective depth. Fiber pullout was assumed to occur prior to fiber rupture while calculating the contribution of fibers to punching shear strength. Large number of test data were compared. The proposed method was compared to experimental data resulting in an average value of measured over predicted punching shear strength of 1.08 and a coefficient of variation of 9%.

Gouveia et al. (2017) conducted 5 experiments on steel fiber reinforced concrete slabs subject to concentrated loads. Parameters of interest included fiber percentage by volume and non-prestressed reinforcement ratio. Experimentally obtained load-rotation relationships were compared with predicted ones and good agreement was observed. The average ratio of measured over predicted capacities was 1.12 and the COV was 3%.

Clement et al. (2014) investigated the behavior of prestressed concrete slabs constructed with NSC under concentrated loads. A total of 15 specimens were tested for punching shear including different amounts of prestressing force and eccentricity, compressive strength and nonprestressed reinforcement. An expression for calculating a reduced rotation due to the effect of prestressing was developed. Measured punching shear capacities were compared to predicted ones and featured an average ratio of measured over predicted capacity of 1.10 and a COV of 8%.

The prediction methodologies presented in this section provided the framework for developing the prediction methodology presented in Chapter 5. The procedure presented in Chapter 4 for obtaining the moment curvature relationship of a PT UHPC beam or plate strip, together with results from FEA were used to develop a simplified method to obtain this relationship. The simplified method was then used in the proposed prediction methodology for punching shear.

Harris (2004) and Harris and Roberts-Wollmann (2005) conducted a series of punching shear tests on unreinforced UHPC plates. Different plate boundary conditions were investigated. Some plate specimens failed in flexure rather than punching shear. Measured flexural capacities were lower than predicted capacities based on the yield line method. One possible explanation for this discrepancy may be the lack of uniformity in fiber distribution in each orthogonal direction. It was concluded that the casting method has a strong influence on orientation of steel fibers, which also affects flexural strength in each orthogonal direction. Fibers tend to align in the direction of the flow of material and also formwork. A formulation for predicting punching shear capacity of unreinforced UHPC plates was proposed.

Joh et al. (2008) conducted punching shear tests on unreinforced UHPC plates and compared measured capacities with predicted capacities using different prediction methods. It was concluded that the ratio of predicted over measured punching shear strength when the ACI 318-05 formulation for NSC plates was used was 0.73 based on three tests. Average measured over predicted punching shear ratios when the formulations by Graddy et al. (2002) and Harris and Roberts-Wollmann (2005) were considered were 1.06 and 0.71, respectively. It was concluded that the formulation provided by Graddy et al. (2002) with an assumed failure angle of 38^{o} resulted in good predictions for the considered boundary conditions.

The studies summarized in this chapter addressed either the flexure or punching shear behavior of PT NSC or FRC elements. Additionally, studies that addressed the punching shear behavior of unreinforced UHPC plates were presented. The behavior of PT UHPC elements appeared unexamined during the course of this study and provided the motivation to conduct this work.

3. Chapter 3: A Flexural Design Methodology for UHPC Beams Post-tensioned with Unbonded Tendons

3.1 INTRODUCTION

Post-tensioned flexural members have the ability to maximize the available usable space by offering long spans and slender structures. This is achieved by combining the high compressive strength of concrete and the high tensile strength of post-tensioned tendons to create a system in which the layout of tendons is configured such that it can most efficiently counterbalance external effects. Research on unbonded post-tensioned beams has been mainly focused on understanding the behavior of normal strength concrete (NSC) beams post-tensioned with unbonded tendons at service and ultimate limit states. To the author's knowledge, the behavior of post-tensioned beams constructed with ultra-high-performance concrete (UHPC) and unbonded tendons has not been investigated before and provided the motivation for this study. The combination of these two materials provides an opportunity for creating slender structures that further maximize the available usable space by capitalizing on the nonlinear domain of UHPC in tension.

The lack of bond between concrete and post-tensioned tendons creates an analytical problem in terms of developing a methodology for predicting the flexural strength of concrete beams post-tensioned with unbonded tendons because tendon stress at ultimate strength is system dependent rather than section dependent. The literature on strand stress increase of unbonded tendons in post-tensioned beams constructed with NSC contains many prediction methodologies with some based on phenomenological principles and others simply on statistics (AASHTO 2017, Roberts-Wollmann et al. 2005, MacGregor et al. 1989, BSI 2001, DIN 1980, SIA 1979, Tam and Pannel 1976, Harajli 2011, Naaman and Alkhairi 1991, He and Liu 2010, ACI 2014, Six et al. 2019, Kim and Kang 2019, Peng and Xue 2019, Maguire et al. 2017, Maguire et al. 2016). A detailed discussion of these methodologies is provided in Peng and Xue (2019). All these methodologies

are based on the assumption that concrete offers no strength in tension after cracking, which is not valid for UHPC for which the nonlinear domain in tension is an important part in the design of an UHPC structure. The behavior of precast pretensioned UHPC components reinforced with bonded strands was investigated by Chen and Graybeal (2012) for bridge I-girders. However, the interaction between UHPC and strands in this case is simpler because strain compatibility between concrete and steel can be assumed, and a sectional analysis can be performed.

The goal of the research presented in this paper is to provide a framework for predicting the flexural behavior of UHPC beams post-tensioned with unbonded tendons. A mechanics based phenomenological model is presented to predict flexural capacity, and a set of equations is proposed to predict the change in strand stress at the ultimate limit state, Δf_{ps}. The flexural design methodology is presented in terms of the failure mode observed when the considered specimens reach their ultimate load carrying capacity. The failure mode is characterized as either a fiber tension-controlled failure, or a concrete compression-controlled failure. Nonlinear numerical simulations based on validated submodels are used to investigate the behavior of 221 post-tensioned UHPC beams from the onset of loading to failure. A sensitivity analysis is conducted to understand the influence of concrete compressive strength, area of tendons, effective depth of tendons, continuity, loading configuration, loading pattern, friction coefficient, area of mild steel, maximum usable UHPC tensile strain and cracking stress on the strand stress at ultimate strength. The considered beams feature rectangular as well as T cross-sections in simply supported as well as continuous configurations.

The proposed flexural design methodology is general and provides numerous advantages: 1) it accounts for simply supported and continuous members featuring various loading configurations and loading patterns, 2) it accounts for rectangular and T-section behavior, 3) it captures the

influence of key parameters such as beam cross-sectional dimensions, effective depth of tendons and span over effective depth ratio, area of tendons and mild steel, and different classes of UHPC exhibiting various compressive and tensile strengths and containing various percentages of fibers.

3.2 INVESTIGATED POST-TENSIONED UHPC BEAMS WITH UNBONDED TENDONS

To develop a generalized flexural design methodology, including a set of equations for predicting the change in strand stress at the ultimate limit state in UHPC beams post-tensioned with unbonded strands, beams with a wide range of characteristics were considered (Table 3.1 and Fig. 3.1).

Table 3.1 Characteristics of investigated UHPC beams post-tensioned with unbonded strands

	Cross-section	Depth (mm)	Span (mm)	f_c' (MPa)	A_{ps} (mm^2)	Cont.	d_p (mm)	A_s (mm^2)	ε_{tu}	f_{cr} (MPa)	Loading pattern
Range of variation	R,T	305-610	4267-17069	152-207	197-1138	S, C	152 – 559	63-568	0.005-0.015	2.75-9.65	One point, two point, distributed

R = rectangular, T = T-beam, S = simple span, C = Two-span continuous

The investigated beams feature rectangular and T cross-sections with the purpose of studying the behavior of beams with various failure modes in terms of the magnitude of top and bottom strains at failure. Simply supported as well as two-span continuous configurations were considered given that unbonded strand stress is system dependent rather than section dependent. The depth of beams varies from 305 mm to 610 mm and beam span varies from 4267 mm to 17069 mm. Concrete compressive strength varies from 152 MPa to 207 MPa in 14 MPa increments to study the behavior of various classes of UHPC. The area of unbonded tendons varies from 198 mm^2 (2-13 mm diameter strands) to 1138 mm^2 (6-18 mm diameter strands) to study the behavior of lightly and heavily post-tensioned beams. The area of mild steel varies from 63 mm^2 to 568

mm^2 to study its influence on the change in strand stress at the ultimate limit state, Δf_{ps}. The effective depth, d_p, varies from 152 mm to 559 mm to study the behavior of beams with various tendon drape configurations and its influence on Δf_{ps}. All cases feature draped tendon configurations. For simply supported beams tendon eccentricities at the exterior support vary from 0 mm to 51 mm and at mid-span from 51 mm to 255 mm.

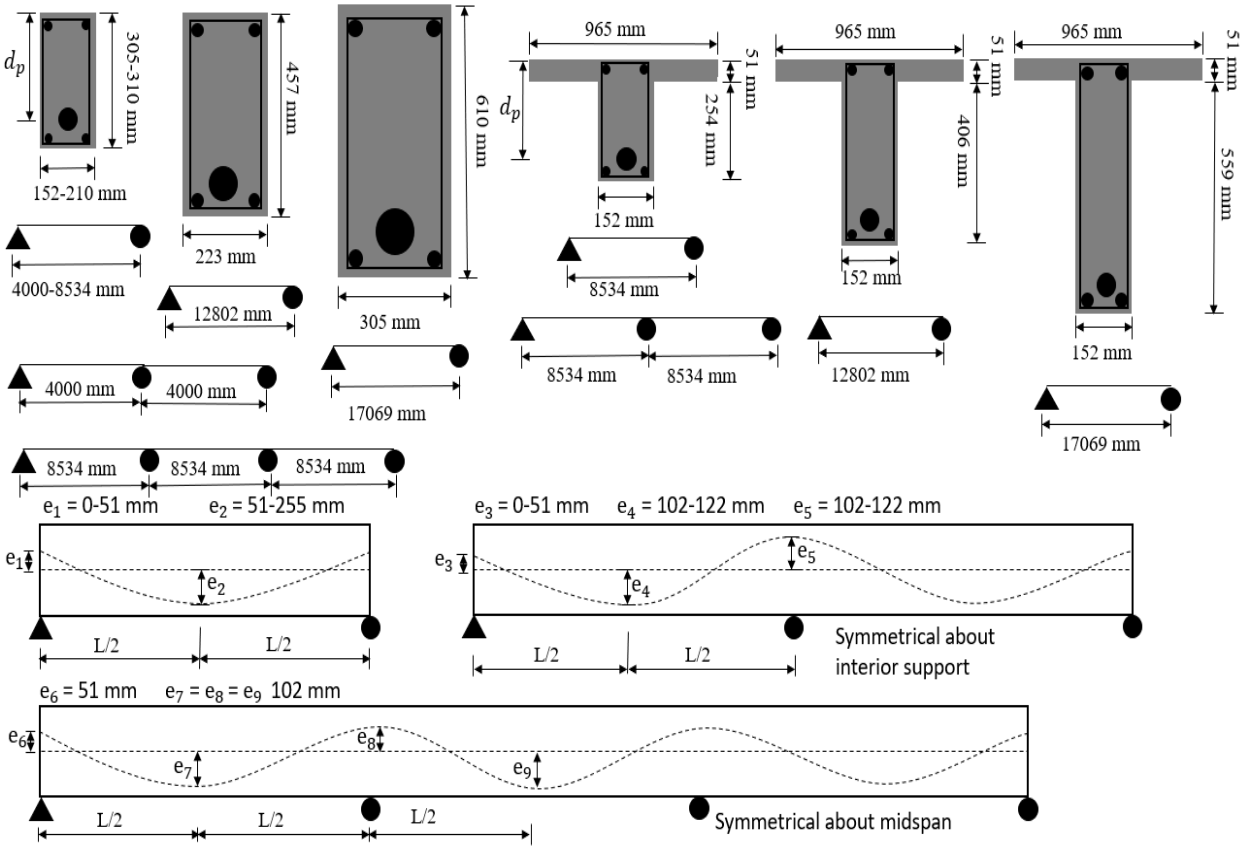

Fig. 3.1 Characteristics of investigated UHPC beams post-tensioned with unbonded strands

For two-span and three-span continuous specimens tendon eccentricity at the exterior support varies from 0 mm to 51 mm, at mid-span from 102 mm to 122 mm, and at the interior support from 102 mm to 122 mm (Fig. 3.1). The maximum usable tensile strain for UHPC varies from 0.005 to 0.015 to study the behavior of various classes of UHPC featuring various

percentages of fibers and their influence on Δf_{ps}. A similar exercise was conducted for the cracking stress of UHPC, which is typically expressed as a function of compressive strength.

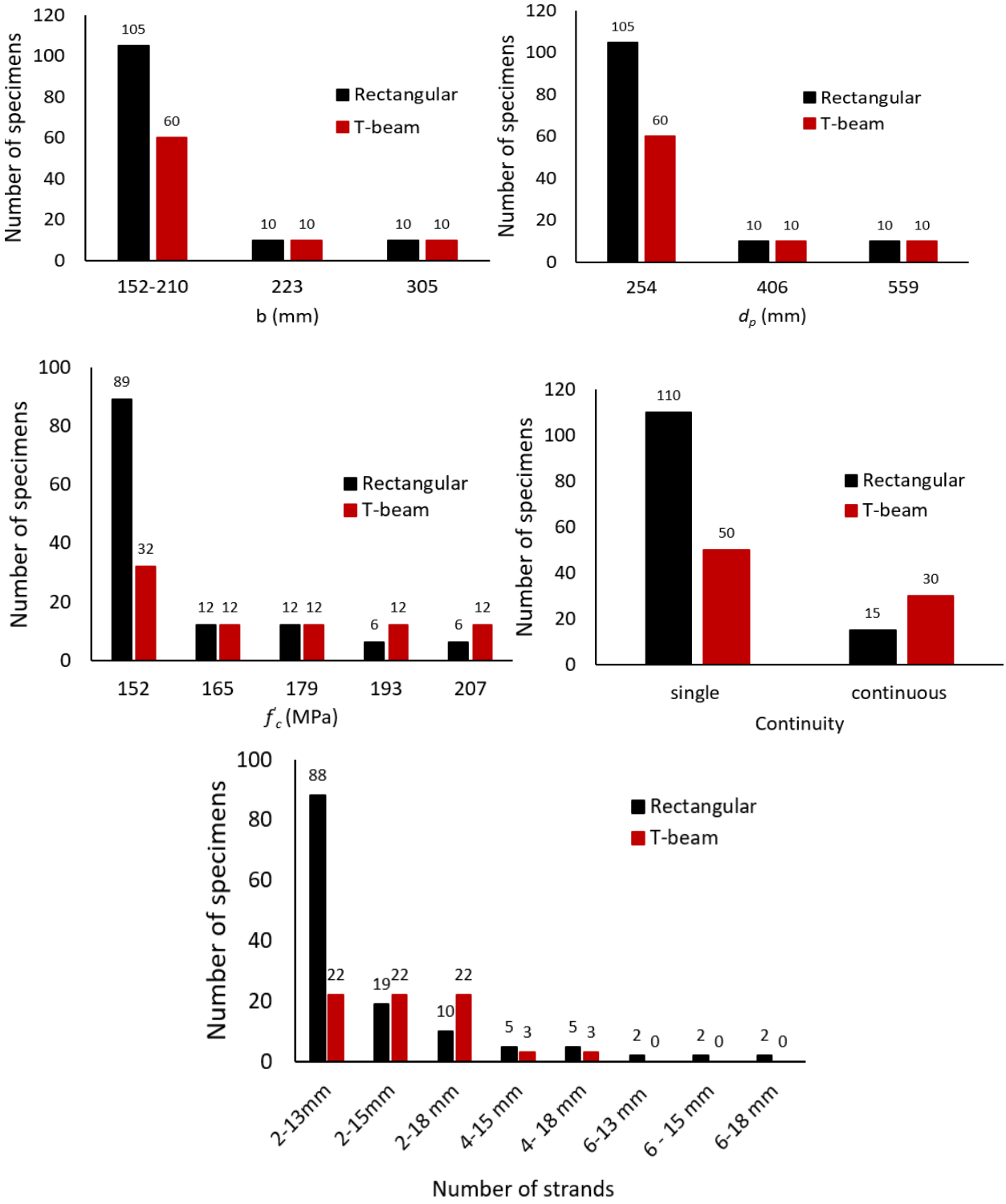

Fig. 3.2 Distribution of the number of specimens for several parameters

The cracking stress varies from 2.75 MPa to 9.65 MPa and is intended to represent a variety of classes of UHPC including cracking strengths that are lower and higher than those that would be expected for a given compressive strength. Three loading patterns were considered to study their influence on Δf_{ps} and they consist of: 1) one-point loading, 2) two-point loading, and 3) distributed loading. Effective prestress, f_{pe}, varies from 1241 MPa to 1310 MPa. Table 3.1 summarizes the range of parameters investigated and Fig. 3.1 illustrates the dimensions of the cross-sections considered. Additionally, Fig. 3.2 shows the distribution of the number of specimens for various parameters. Some of the beam cross-sections and dimensions were based on previous experimental work on normal strength concrete post-tensioned beams. Material properties for UHPC as well as key parameters were varied to create a large enough database (221 specimens) to allow the derivation of a generalized flexural design methodology and the development of a set of equations for predicting strand stress at the ultimate limit state. It should be noted that the database includes a variety of beam cross-sections including beams with longer and deeper sections than those used in previous experimental work for normal strength concrete beams. All specimens were loaded monotonically to failure and the evolution of the applied load, most extreme concrete compressive and tensile stress, and unbonded tendon stress were monitored using high fidelity finite element analyses.

3.3 FINITE ELEMENT ANALYSES

3.3.1 Modeling Protocol

A numerical study was undertaken with the purpose of characterizing the behavior of UHPC beams post-tensioned with unbonded tendons, developing a framework for flexural design, and informing future experimental work. The numerical simulations were conducted using the

commercially available finite element analyses software Abaqus Dassault. The numerical models consider material nonlinearities as well as the interaction between unbonded tendons and the surrounding concrete. Because experimental data on UHPC beams post-tensioned with unbonded tendons does not exist, the adopted modeling protocol was validated by considering two submodels. The first deals with the ability of the modeling protocol to capture the nonlinear behavior of reinforced and prestressed UHPC elements with bonded bars or strands and the second deals with its ability to properly capture the behavior of normal strength concrete beams post-tensioned with unbonded tendons. The second is of utmost importance because the adopted modeling protocol needs to capture with good accuracy the change in strand stress, Δf_{ps}, after the beams are post-tensioned and loaded to failure so that a reliable approach can be developed to predict strand stress at ultimate, f_{ps}, and consequently the nominal moment capacity, M_n, of UHPC beams post-tensioned with unbonded tendons. As such, a total of 27 numerical models of tested post-tensioned beams constructed with normal strength concrete were created with the purpose of demonstrating that the adopted modeling protocol can capture with good accuracy the change in strand stress after the beams are post-tensioned and loaded to failure. The validation of both submodels is discussed later in this paper in detail in the validation section.

An explicit dynamic analyses approach was used to conduct all numerical simulations to facilitate convergence due to the nonlinear material response, complex contact definitions, and relative component deformations during the analyses. Simulations were conducted using either a displacement control or load controlled approach and in all cases the displacement or load was applied in a long enough period of time to simulate quasi-static loading and avoid dynamic effects. Specimens that were subject to a single concentrated load at mid-span, or two point loads symmetrical about mid-span were loaded in a displacement-controlled mode whereas those that

featured uniformly distributed loading were loaded in a load-controlled mode. A displacement-controlled approach is preferred in cases that feature concentrated loads because it helps with numerical convergence compared to a load-controlled approach in which the beam may experience sudden displacements especially when it is close to failure. When the beams are subject to a uniformly distributed load, a displacement-controlled approach is not appropriate because the load is uniformly distributed and there is no location along the span of the beam at which a displacement history could be provided without interfering with the natural deformation of the beam as a result of the uniformly distributed load. To account for some of the numerical challenges mentioned above, the number of time steps at which data was collected when a load-controlled approach was used was increased so that the peak load as well as the descending branch of the load displacement curve were properly captured. The relationship between the internal energy and kinetic energy during each time step was monitored to ensure a quasi-static behavior.

3.3.1.1 *Simulation of Unbonded Post-tensioning*

The simulation of unbonded post-tensioning was based on the robust contact penalty approach developed by Huang et al. (2010).Fig. 3.3 shows the three main components used in the simulation, which are the concrete beam, the sheathing around the tendons, and the unbonded tendons. The concrete beam and the sheathing around the tendon were modeled using first order 8-node 3D continuum elements with reduced integration and hourglass control (C3D8R) (Fig. 3.3b and Fig. 3.3c). The tendons, mild longitudinal steel and stirrups were modeled using first order 2-node 3D truss elements (T3D2). A perfect bond between stirrups, longitudinal mild steel, sheathing and the surrounding concrete is assumed, and this is enforced through the use of an embedded region constraint in which the host is the concrete beam. The layout of the sheathing followed the layout of the tendons. The interaction between the tendons and the surrounding sheathing was

specified using a hard contact definition in the normal direction to prevent penetration of tendon into the sheathing/concrete and a friction contact definition in the tangential direction. A surface-to-surface contact was introduced between the tendon and the inside surface of the sheathing. A friction coefficient of 0.05 was used between the tendon and sheathing. This number is the lower bound of what the PTI Manual (2006) suggests as coefficient of friction. This was done to simulate maximum slip and consequently to obtain minimum (conservative) estimates of tendon stress increase at the ultimate limit state.

There is no interaction defined between the tendon and the concrete beam. As a result, the sheathing acts as a spatial constraint for the tendon and also as a medium for relating the behavior of the tendon to that of the concrete beam. A low modulus of elasticity (E = 200 MPa) was specified for the sheathing material to reduce its contribution to the overall stiffness of the post-tensioned beams.

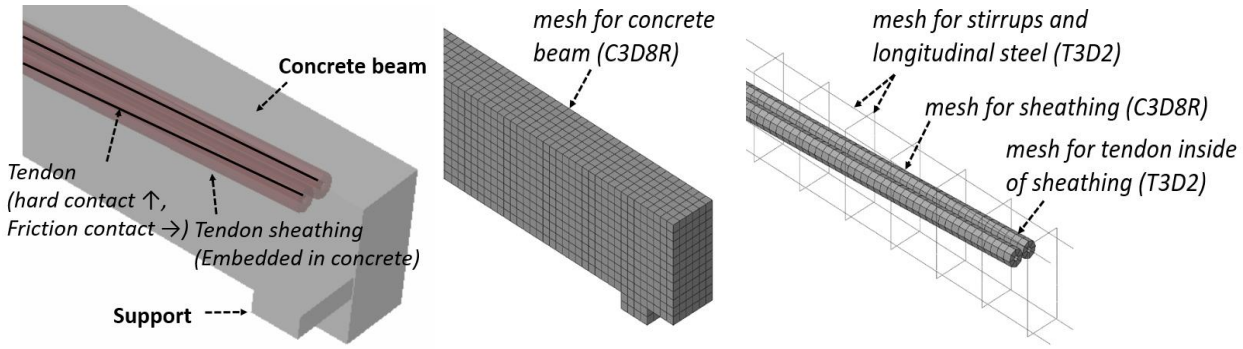

a) b) c)

Fig. 3.3 a) Modelling approach for simulating the behavior of unbonded post-tensioning tendons, b) finite element mesh for concrete, c) finite element mesh for sheathing, tendon, and mild steel

3.3.1.2 *Anchorage Zone Modeling*

A multipoint constraint (MPC) between the end of the tendon and a concrete area equal to the footprint of the anchorage device was used to simulate the behavior at the anchorage zones. The footprint of the anchorage device for each tendon was assumed to be centered on the tendon. The control point was set as the node at the end of the tendon element and the slaves nodes were

selected as the nodes of the solid elements in the concrete beam in the region equal to that of the anchorage. A MPC allows the imposition of constraints between different degrees of freedom of the model and consists of several types. In this case a beam type MPC was adopted because this type of constraint provides a rigid beam between the control and slave nodes, which constraint the displacement and rotation of the slave node to that of the control node, thus enforcing deformation compatibility between the end of the tendon and the anchorage zone.

3.3.1.3 *Simulation of Prestressing Force*

The prestressing force was simulated by iteratively cooling the tendon using a temperature type predefined field to achieve a target prestress of $f_{jacking} = 0.7f_{pu}$, which is the recommended value for the jacking stress in post-tensioned beams based on ACI 318 (2014) section 20.3.2.5. Also, Eq. 3.1 was used to determine the required temperature change, ΔT, to achieve the level of target prestress specified above. The modulus of elasticity for the tendon, E_{ps}, was taken equal to 196,500 MPa and the coefficient of thermal expansion, c, was taken equal to unity. Therefore, the required ΔT to create a jacking stress equal to $0.7f_{pu}$ was determined by dividing the jacking stress with the modulus of elasticity for the prestressing strands. Post-tensioning was created as a separate analysis step applied over an appropriate amount of time to minimize dynamic effects and simulate quasi-static loading. Beam self-weight was applied in the same analysis step. As described in the section that discusses the simulation of the unbonded post-tensioning, the numerical modeling protocol considers losses incurred due to elastic shortening and friction, therefore the effective prestress is automatically computed.

$$f_{jacking} = E_{ps}\, c\, \Delta T \qquad \text{Eq. 3.1}$$

3.3.1.4 *Concrete material model*

UHPC material nonlinearity was captured using Concrete Damage Plasticity (CDP) theory using the parameters shown in Table 3.2. The CDP model used in Abaqus is based on the models proposed by Lubliner et al. (1989) and Lee and Fenves (1998) and consists of the following main ingredients: strain rate decomposition, stress-strain relations, hardening variables, yield function, and flow rule. An additive strain rate decomposition is assumed and stress-strain relations are governed by scalar damaged elasticity. Damaged states in tension and compression are characterized independently by two hardening variables, which are referred to as equivalent plastic strains in tension and compression, respectively (Abaqus Dassault). Microcracking and crushing in the concrete are represented by increasing values of the hardening variables. These variables control the evolution of the yield surface and the degradation of the elastic stiffness (Abaqus Dassault). The damage parameters defined in the CDP model are intended to capture the elastic stiffness degradation during unloading and subsequent loading such as in cyclic loading conditions (Abaqus Dassault, Huang et al. 2010, PTI 2006, ACI 2019, Lubliner et al. 1989, Lee and Fenves 1998, Esmaeeli 2015). Because all specimens investigated as part of this research are loaded monotonically to failure the damage variables were set equal to zero when calculating plastic strains since the specimens were neither unloaded nor were they subject to cyclic loading.

The yield condition is based on the yield function proposed by Lubliner et al. (1989) and incorporates the modifications proposed by Lee and Fenves (1998) to account for different evolutions of strength under direct tension and compression. The CDP model assumes nonassociated potential flow and the flow potential is the Drucker-Prager hyperbolic function (Abaqus Dassault). In Table 3.2 the dilation angle represents concrete's internal friction angle. The value of eccentricity is related to the ratio between the tensile strength and compressive strength

of concrete. The ratio of initial equibiaxial compressive yield stress to the initial uniaxial compressive yield stress is f_{bo}/f_{co}. *K* is the ratio of the second stress invariant on the tensile meridian to that on the compressive meridian at initial yield for any given value of the pressure invariant such that the maximum principal stress is negative. Baghi et al. (2017) gives a detailed explanation for the adoption of each plasticity parameter for simulations that involve UHPC. CDP theory assumes isotropic damage elasticity combined with isotropic compressive and tensile plasticity to represent the inelastic behavior of concrete. Formation of tensile microcracks is represented macroscopically with a softening stress-strain relationship and fracture is assumed to be distributed over a certain volume. Additional information on CDP model can be found in references (Abaqus Dassault, Lubliner et al. 1989, Lee and Fenves 1998).

Table 3.2. Adopted Concrete Damage Plasticity parameters for NSC and UHPC

Parameter	NSC	UHPC
Dilation angle	31°	45°
K	0.67	0.67
Viscosity parameter	0	0
Eccentricity	0.1	0.1
f_{bo}/f_{co}	1.16	1.77

The adopted stress-strain curves for UHPC in compression and tension are shown in Fig. 3.4a. The stress-strain curve in compression that was used in the majority of simulations and which is labeled as the default curve was based on Graybeal's (2007) recommendations. While it is generally accepted that the stress-strain behavior of UHPC is primarily linear with some softening taking place as the compressive strength is reached, there is currently no consensus regarding the numerical relationship between stress and strain especially after the attainment of the compressive strength. This lack of consensus can be partially attributed to the inherent variability that exists between different classes of UHPC and partially to the difficulties inherent in the process of experimentally capturing these behaviors (Graybeal 2007). For example, one key parameter is the

specification of the maximum usable compressive strain, which for normal strength concrete has served as the anchor point in the strain diagram at the ultimate limit state. The variability in the amount of fibers and the variety of classes of UHPC have led to different recommendations provided in various codes many of which require material testing in compression and tension to characterize the behavior of the material used. To account for this variability, the numerical relationship recommended by Graybeal (2007) for the ascending branch was complemented by three different descending branches to understand their influence on the behavior of UHPC beams post-tensioned with unbonded tendons. In Graybeal's (2007) recommendations the relationship between compressive stress, f_c, and compressive strain, ε_c, is expressed by Eq. 3.2, and is a function of the modulus of elasticity, E, and a coefficient α, which can be calculated using Eq. 3.3. In Eq. 3.3, α is a function of two constants a and b, the modulus of elasticity, E, the compressive strain, ε_c, and specified compressive strength, f'_c. Eq. 3.4 is used to express the modulus of elasticity, E, as a function of the specified compressive strength, f'_c. The stress-strain curve for UHPC in compression was generally developed up until the point when the compressive stress, f_c, reached the specified compressive strength, f'_c. Therefore, for the majority of the cases, the ultimate compressive strain, ε_{cu}, was assumed to be equal to the compressive strain, ε_c, that corresponds with the specified compressive strength, f'_c. The region in the stress-strain curve beyond the point of specified compressive strength is characterized by a steep descending branch up until a negligible compressive stress to capture the peak load and to avoid convergence problems during the nonlinear analyses. Such an idealization of the descending branch for the stress-strain curve was conducted since obtaining accurate and consistent experimental stress-strain data for the full range of compressive behavior is a difficult task, especially after the strain that corresponds with the compressive strength is reached. This is due to the fact that the collection of strain data for the

range of compressive behavior that corresponds with the attainment of compressive strength and beyond is very much dependent on the experimental loading and strain measurements techniques employed (Graybeal 2007). However, the influence of various shapes of descending branches for the stress-strain curve was investigated to determine the impact that it may have on the flexural behavior of UHPC beams post-tensioned with unbonded tendons. The shape of all considered stress-strain curves in compression is illustrated in Fig. 3.4a.

The tensile stress-strain relationship for UHPC was assumed to be bilinear with the cracking stress, f_{cr}, determined by Eq. 3.5 (Russel and Graybeal 2013) and the ultimate tensile strain was limited to 0.01 for the majority of simulations. The maximum usable tensile strain of 0.01 for UHPC was based on the study conducted by Haber et al. (2018) who characterized the behavior of various classes of UHPC. This maximum usable tensile strain was varied by +/- 50% as part of a sensitivity analysis to study the influence that this parameter can have on strand stress at ultimate strength by considering other UHPC classes that may have enhanced or reduced tensile ductility compared to those studied by Haber et al. (2018). Similar to compressive stress-strain behavior the region in the stress-strain curve beyond the points of assumed ultimate tensile strain is characterized by a steep descending branch up until a negligible tensile stress to capture the peak load and to avoid convergence problems during the nonlinear analyses. While the bilinear stress-strain relationship for UHPC in tension was used in the majority of simulations, the influence of various shapes of tensile stress-strain behavior was investigated as part of a sensitivity analysis to determine its impact on the flexural behavior of UHPC beams post-tensioned with unbonded tendons. The shape of all considered stress-strain curves in tension is illustrated in Fig. 3.4a. The influence of key parameters in the stress-strain curve for UHPC on the strand stress at the ultimate

limit state as well as on the flexural strength of the beams is presented later in this paper under the sensitivity analysis section.

$$f_c' = \varepsilon_c E_c (1 - \alpha) \qquad \text{Eq. 3.2}$$

$$\alpha = a e^{\frac{\varepsilon_c E_c}{b f_c'}} - a \quad , a = 0.011, b = 0.44 \qquad \text{Eq. 3.3}$$

$$E_c = 3840\sqrt{f_c'} \quad where\ f_c'\ in\ MPa \qquad \text{Eq. 3.4}$$

$$f_{cr} = 0.56\sqrt{f_c'} \quad where\ f_c'\ in\ MPa \qquad \text{Eq. 3.5}$$

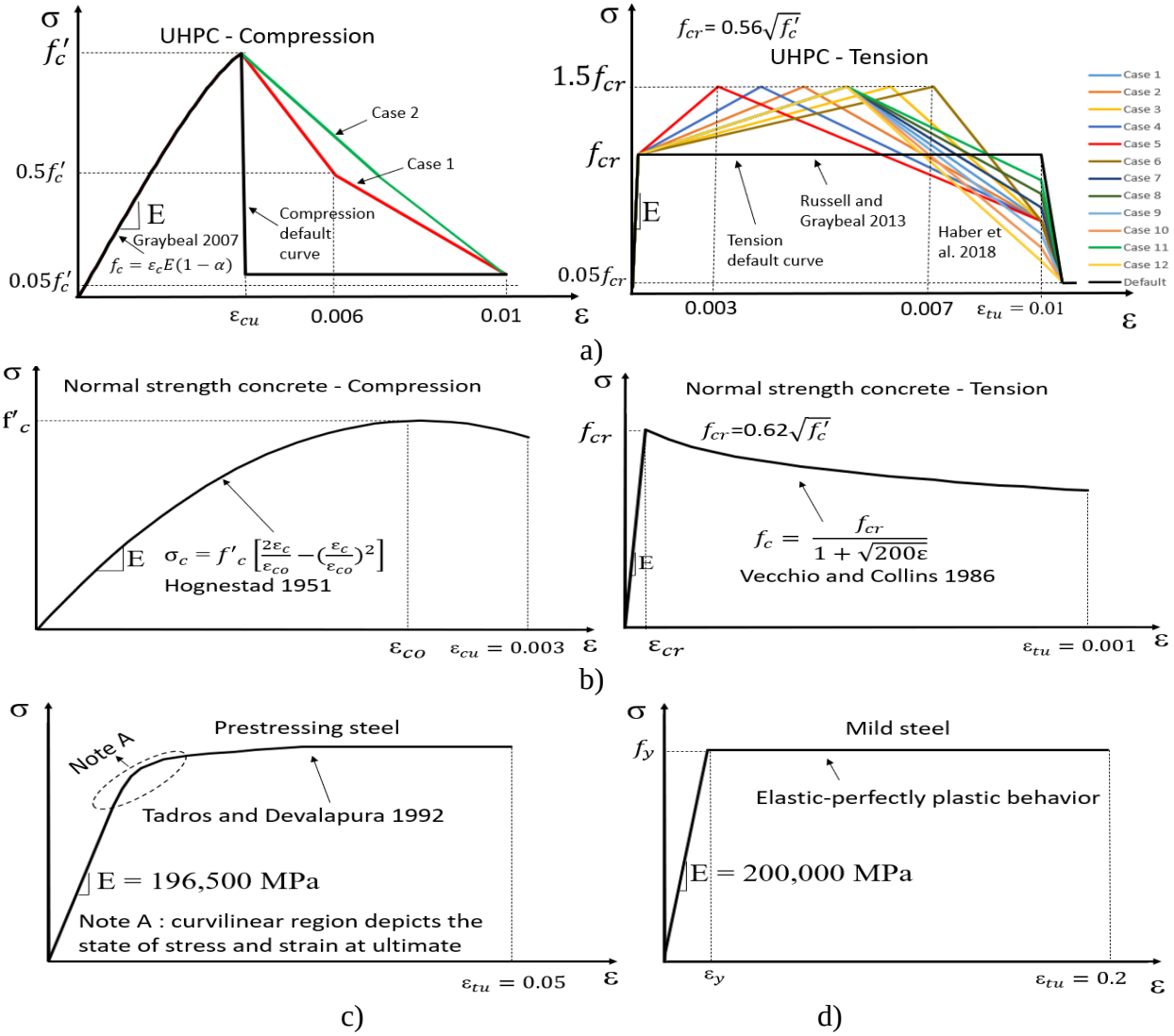

Fig. 3.4 Assumed uniaxial stress-strain relationship for: a) UHPC, b) normal strength concrete, c) prestressing steel, d) mild steel

Fig. 3.4b shows the stress-strain curves for normal strength concrete (NSC) in compression and tension, which were used to validate the ability of the adopted modeling protocol to capture the behavior of NSC post-tensioned beams for which experimental data exists. The relationship between NSC stress and strain were based on Hognestad (1951) and Vecchio and Collins (1986) equations for the compressive and tensile domains, respectively.

3.3.1.5 *Prestressing Steel and Mild Steel Material Model*

The uniaxial stress-strain relationship for the post-tensioning tendons was defined based on Eq. 3.6 (Devalapura and Tadros 1992) and that of mild steel was assumed to be elastic perfectly plastic (Fig. 3.4c and 3.4d). These stress-strain relationships were entered into *Abaqus* and material nonlinearity was simulated with classical metal plasticity theory, including the assumption of a *Von Mises* yield surface. Young's modulus, *E*, was set at 200,000 MPa for mild steel, and 196,500 MPa for prestressing steel. Poisson's ratio, *v*, was set to 0.3. Mild steel was modeled as an embedded element in the concrete beam to simulate bonded behavior.

$$f_{ps} = \varepsilon_{ps} * 6.895 * \left[A + \frac{B}{\left\{1 + \left(C\varepsilon_{ps}\right)^{D}\right\}^{1/D}} \right] \leq f_{pu} \qquad \text{Eq. 3.6}$$

where A = 887, B = 27613 , C= 112.4 , D = 7.36 for 1861.65 MPa tendon $f_{py}/f_{pu} = 0.9$

3.3.2 Validation

Because experimental data on UHPC beams post-tensioned with unbonded tendons do not exist, the adopted modeling protocol was validated by considering two submodels. The first deals with the ability of the modeling protocol to capture the nonlinear behavior of reinforced and prestressed UHPC elements with bonded bars or strands and the second deals its ability to properly

capture the behavior of normal strength concrete beams post-tensioned with unbonded tendons. The second is of particular importance because one of the objectives of this research is to develop a set of equations for predicting the change in strand stress at the ultimate limit state, Δf_{ps}, in UHPC beams post-tensioned with unbonded tendons. As such, the adopted modeling protocol needs to capture with good accuracy the change in strand stress after the beams are post-tensioned and loaded to failure.

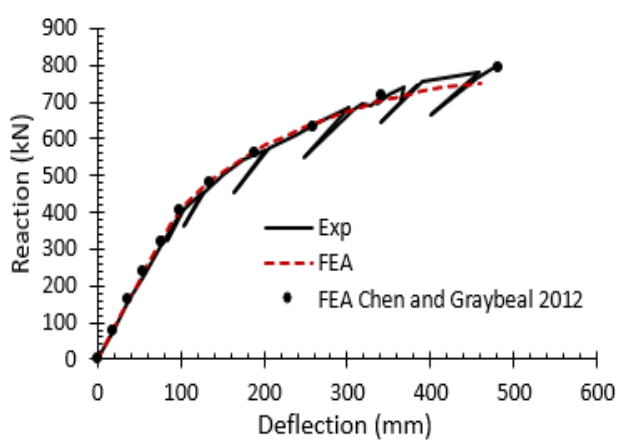

a)

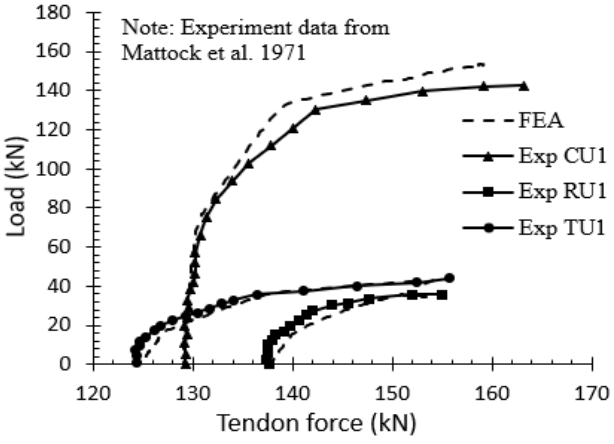

b)

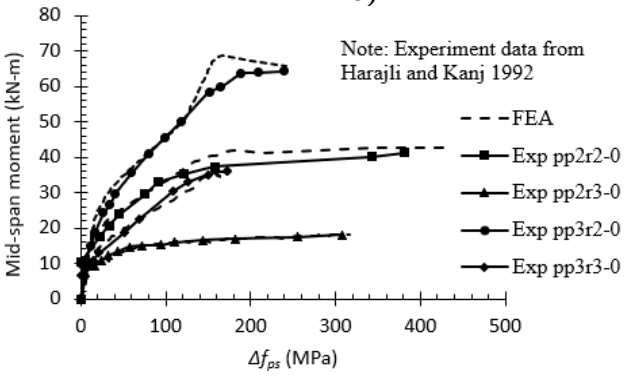

c)

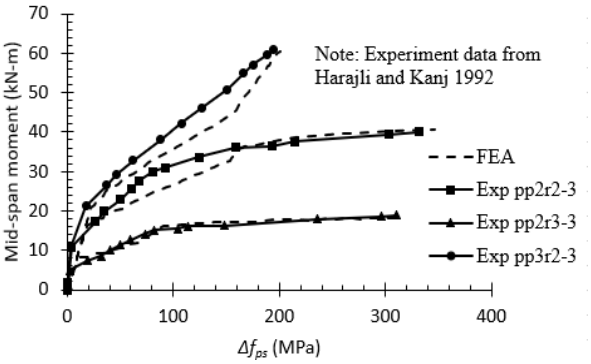

d)

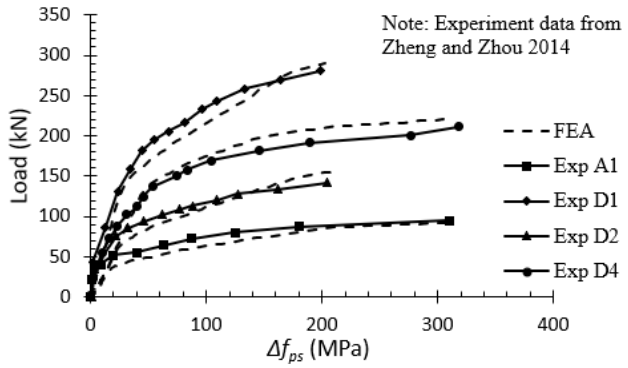

e)

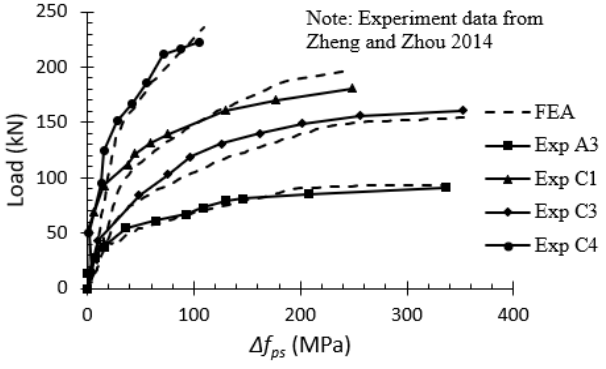

f)

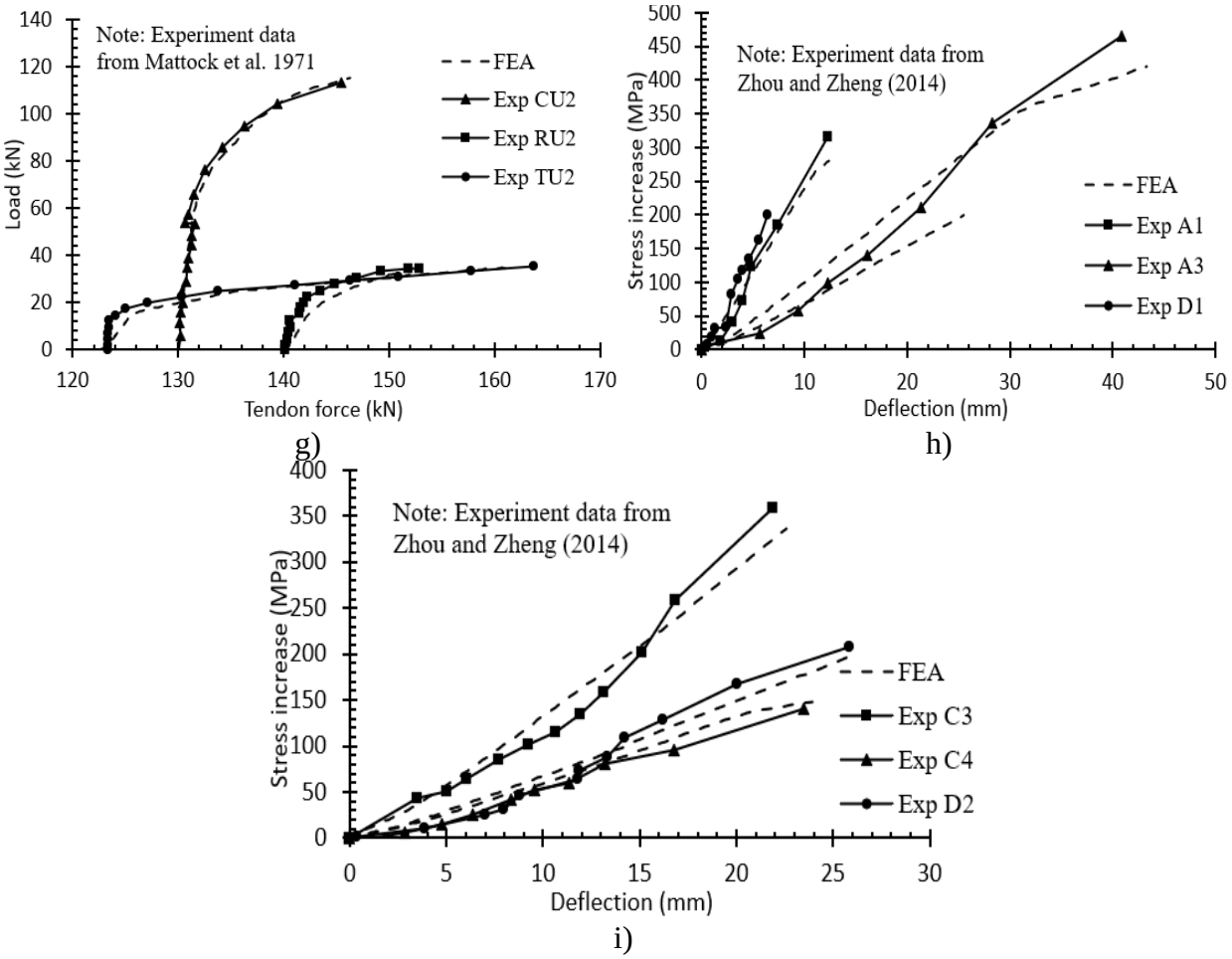

Fig. 3.5 Validation of adopted modeling protocol: a) ability of CDP model to capture the behavior of UHPC members prestressed with bonded strands, b), c), d), e), f), g), h) and i) ability of adopted modeling protocol to capture the behavior of normal strength concrete beam

Although UHPC exhibits significantly different mechanical properties from normal strength concrete, especially in the tensile domain, the ability of existing constitutive models with adjustable material parameters such as CDP theory to capture the behavior of reinforced and prestressed UHPC elements with bonded bars or strands has been proven by many researchers (Chen and Graybeal 2012, Baghi et al. 2017, Chen and Graybeal 2012, Solhmirzaei and Kodur 2017, Mahmud et al. 2013, Meng and Khayat 2016). For brevity, only some of the results of the study conducted by Chen and Graybeal (2012) are shown in Fig. 3.5a to illustrate the ability of the CDP model to successfully capture the behavior of UHPC beams prestressed with bonded strands. Since there are small differences between the CDP model parameters used by Chen and Graybeal

(2012) and those adopted in this study, the beams tested by Chen and Graybeal (2012) were monotonically loaded to failure using the modeling protocol used in this study. The results in Fig. 3.5a suggest that the adopted modeling protocol is able to capture with good accuracy the behavior of UHPC beams prestressed with bonded tendons.

A total of 27 numerical models of tested post-tensioned beams constructed with normal strength concrete were created with the purpose of simulating the change in strand stress as these beams were loaded to failure. Experimental data on the tested beams were obtained from studies conducted by Mattock et al. (1971), Harajli and Kanj (1992), and Zheng and Zhou (2014). For brevity, Fig. 3.5b, 3.5c, 3.5d, 3.5e, 3.5f, 3.5g, 3.5h and 3.5i are provided to illustrate the ability of the adopted modeling protocol to capture the variation in tendon force and tendons stress for 18 of these beams. The similarity between experimental and numerical curves suggests that the adopted modeling protocol can predict with good accuracy not only the global behavior of UHPC beams post-tensioned with unbonded tendons but also the variation in tendon stress as these beams are loaded to failure.

Using deductive reasoning in the absence of experimental data on UHPC beams post-tensioned with unbonded tendons, it is concluded that since the modeling protocol is able to capture with good accuracy the behavior of UHPC beams prestressed with bonded tendons as well as the behavior of NSC beams with unbonded tendons, it should be able to capture with good accuracy the behavior of UHPC beam post-tensioned with unbonded tendons.

3.4 RESULTS AND DISCUSSION

3.4.1 Failure Mode

The behavior of simply supported and two-span continuous rectangular beams when the

peak load was achieved was typically characterized by the attainment of the ultimate usable tensile strain, ε_{tu}, in the most extreme tensile fiber, while the maximum compressive strain in the most extreme compression fiber was below the ultimate usable compressive strain. This suggests that, in general, the failure mode of rectangular UHPC beams post-tensioned with unbonded tendons is a fiber tension-controlled failure, which is defined as a failure in which the fibers rupture before concrete crushes. This is illustrated in Fig. 3.6a which shows that the peak load is achieved at the point when the entire nonlinear domain of UHPC in tension is exhausted while the maximum compressive stress is well below the specified compressive strength. This is an indication that the potential of UHPC in terms of its compressive strength is not fully mobilized. For example, Fig. 3.6a3 shows that the stress in the most extreme tension fiber is initially compressive due to prestressing and gradually switches to a tensile stress as the beam is loaded to failure. The stress in this fiber then reaches the cracking stress, remains constant, and finally drops to a negligible value for the case in which elastic perfectly plastic tensile region of UHPC assumed. This means that the stress in the most extreme fiber in tension precisely follows the specified stress-strain curve for UHPC in tension (Fig. 3.4a). The peak load is achieved when the entire tensile domain is exhausted (i.e. strain in most extreme tension fiber is equal to maximum usable tensile strain).

Similarly, Fig. 3.5a2 illustrates that the stress in the most extreme compression fiber is initially tensile due to prestressing and then gradually switches to a compressive stress as the beam is loaded to failure. When the peak load is achieved, the stress in the most extreme fiber in compression is well below the specified compressive strength of UHPC, f'_c.

As the total load drops as shown in Fig. 3.6a1, the stress in the most extreme fiber in compression continues to increase to make up for the shrinking of the UHPC tension block, but such an increase is not sufficient to increase the load carrying capacity of the beam.

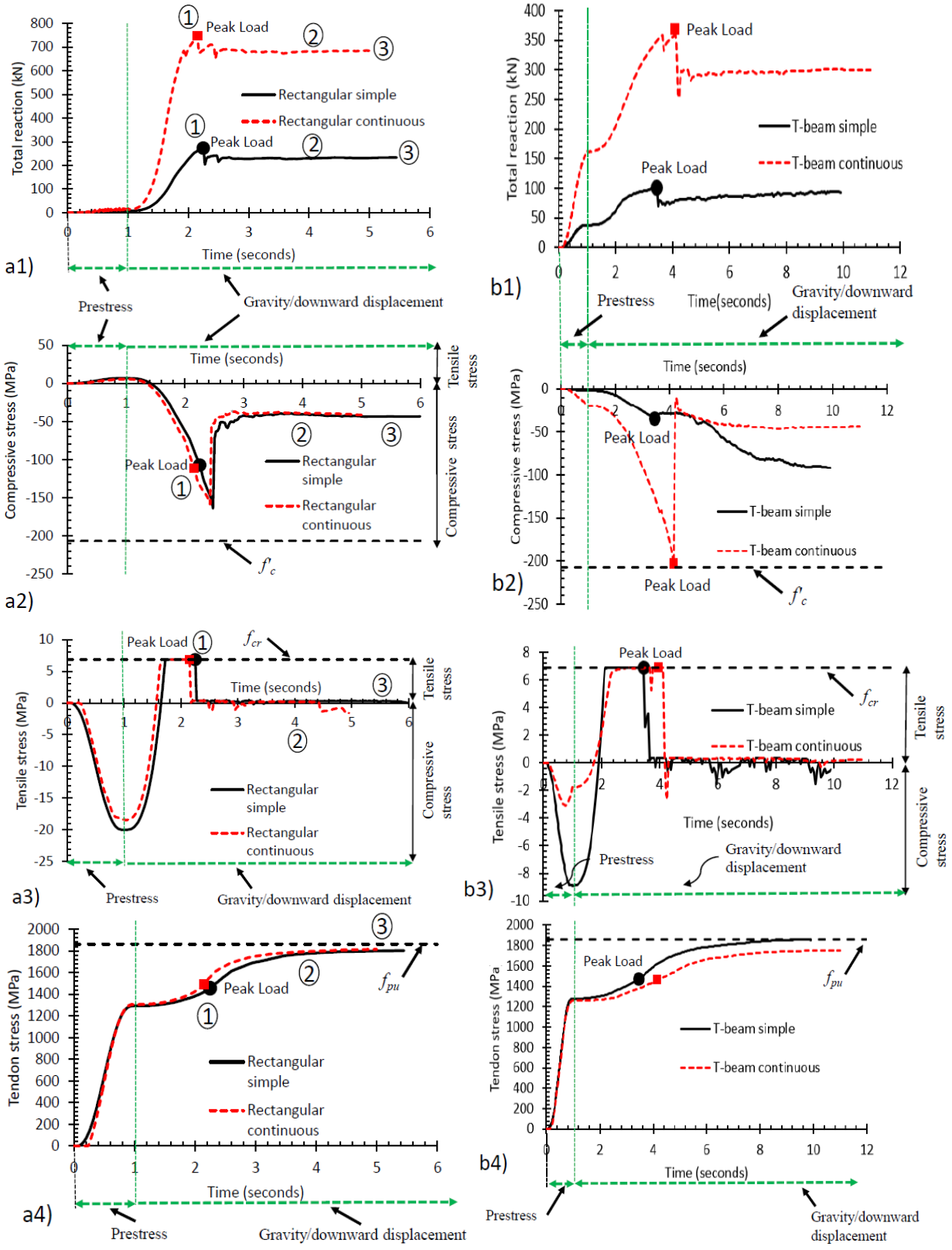

Fig. 3.6 a) Flexural behavior of post-tensioned UHPC beams: a) rectangular beams, b) T-beams

Tendon stress continues to increase up as shown in Fig. 3.5a4 until the last time step as the beam continues to deflect and reaches values that are near the specified ultimate tensile stress, f_{pu} (Fig. 3.6a4). The strand stress at ultimate, f_{ps}, was recorded at the point when the beam reaches its maximum load carrying capacity (Fig. 3.6a1 Peak Load - Stage 1).

Fig. 3.7 shows the strain and stress diagrams for a rectangular beam for the three stages denoted as 1, 2, and 3 in Fig. 3.6a. The stress diagram that corresponds with the attainment of the peak load is the one in which the entire nonlinear domain of UHPC in tension is utilized and the strain in the most extreme fiber in tension is equal to the maximum usable tensile strain, ε_{tu}. After stage 1, the beam continues to carry load because the stress in the strand is less than the ultimate stress, f_{pu}, mild steel still offers the same tensile force, and the maximum concrete compressive stress is smaller than the specified compressive strength, f'_c. However, the combination of the tendon force and the force provided by mild steel in tension cannot compensate for the lost tension force that results due the reduction of the UHPC tension block (stages 2 and 3) since this force is significant. As a result, the total tension and compression forces in the section start to drop. Additionally, for the tendon stress to increase markedly beyond the value computed in stage 1, the strain in the tendon must increase considerably. Since the tendon is unbonded, this would result in very large beam deflection since a similar strain must be maintained throughout the length of the tendon, which may render the structure unusable after an ultimate load event. In any case, even if such large deflections at the ultimate limit state are considered acceptable considering that the main concern at that stage is life safety, the total load and consequently the moment capacity that the beam can provide in stages 2 and 3 is less than that computed for stage 1. Tendon stress at peak load, f_{ps}, was recorded to be between 1379-1724 MPa and is therefore in the vicinity of the

curvilinear portion in the stress-strain curve, which is past the linear portion, but before the region where the modulus is significantly reduced (Fig. 3.6a4 and 3.4c).

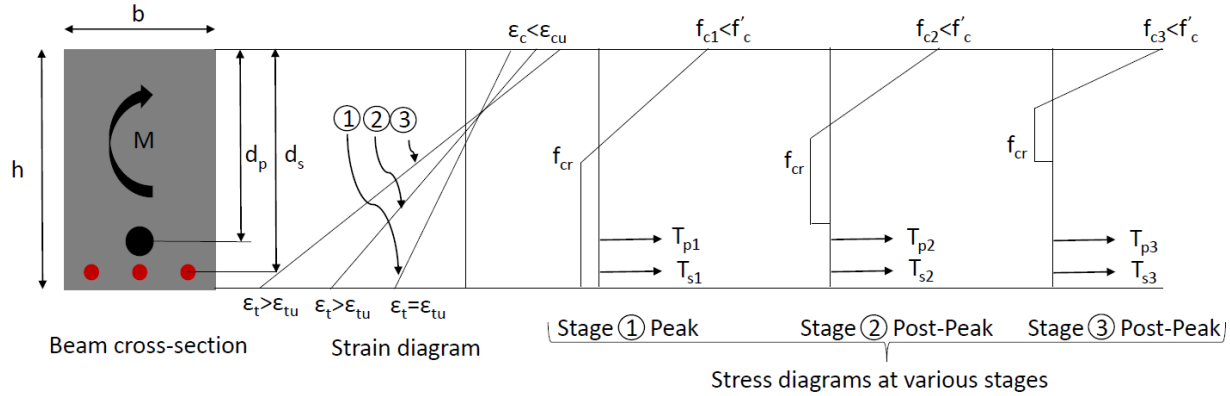

Fig. 3.7 Stress diagrams at various stages for a fiber tension controlled rectangular specimen

As will be shown later, heavily post-tensioned rectangular beams are an exception, and when the tendon area exceeds a certain number, the failure mode switches from a fiber tension-controlled failure to a concrete compression-controlled failure. It should be noted that a compression-controlled failure in this case is characterized as one in which the ultimate compressive strain, ε_{cu}, in the most extreme compressive fiber is reached before the ultimate tensile strain, ε_{tu}, in the most extreme tensile fiber is attained (i.e. concrete crushes before fibers rupture). Tendon stress is still in the vicinity of the curvilinear portion in the stress-strain curve.

Two-span continuous rectangular beam behavior was characterized by two sequential peaks in the total reaction versus time diagram, which correspond with the formation of two plastic hinges at mid-span(between supports) and at intermediate support(at the top of middle support), respectively. Tendon stress at ultimate strength, f_{ps}, was recorded when the applied load reached its maximum value and is similar to that computed for simply supported specimens (Fig. 3.6a4). The failure mode for such beams is identical with that observed in simply supported configurations and is characterized as a fiber tension controlled failure, because, as can be seen from Fig. 3.6a, the attainment of the peak load corresponds with the point where the entire nonlinear domain of

UHPC in tension is exhausted while the maximum compressive stress is well below the specified compressive strength.

The behavior of simply supported beams with a T cross-section was similar to that of rectangular beams (Fig. 3.6b1) except that the maximum compressive stress in the most extreme compressive fiber was much lower than that observed in rectangular beams and also much lower than the specified concrete compressive strength, f'_c, due to the greater compressive width offered by the top flange. This is illustrated in Fig. 3.6b2 and suggests that the compressive strength of UHPC in the top flange is not well mobilized. The failure mode of simply supported T-beams is the same with that observed in rectangular beams and is characterized as a fiber tension-controlled failure (Fig. 3.6b3).

The behavior of two-span continuous T-beams was different from that of continuous rectangular beams in the sense that the failure mode switched from a fiber tensioned controlled failure to a concrete compression-controlled failure at the intermediate support (Figs. 3.6b2/3.6b3). Although the ultimate compressive strain, ε_{cu}, and the corresponding specified compressive strength, f'_c, at the intermediate support at the bottom most fiber was reached before the tensile strain in the top most fiber reached its ultimate value, ε_{tu}, the magnitude of the tensile strain in the uppermost tensile fiber at the intermediate support was very close to ε_{tu}. This is illustrated in Fig. 3.6b3, which shows that the tensile stress in the most extreme tension fiber is near the point where it drops to a negligible value, which corresponds with the attainment of the ultimate tensile strain, ε_{tu}, in the stress-strain curve shown in Fig. 3.4a. This suggests that although the failure mode of two-span continuous T-beams is characterized as a concrete compression-controlled failure, it is very close to being classified as a balanced failure, in which the compressive and tensile strain in the most extreme fibers in concrete reach their ultimate values simultaneously. In this case, both

the compressive strength and tensile strength of UHPC are fully mobilized. The reason why the failure mode in a two-span continuous member with a T cross-section switched to a concrete compression-controlled failure is due to the narrow compression block at the bottom of the web and the much wider tension block, which consists of the top flange and a portion of the web in addition to the tension force provided by the tendons. The strand stress at ultimate, f_{ps}, in simply supported and continuous T-beams was similar, this was recorded at the point when the beams reached their ultimate load carrying capacity and is illustrated in Fig. 3.6b4.

Fig. 3.8 illustrates the two different failure modes using principal strain contours for a simply supported rectangular beam (Fig. 3.8a) and a two-span continuous T-beam subject to two-point loading symmetrical about mid-span (Fig. 3.8b). In fiber tension-controlled specimens gray regions indicate areas in which the principal strain exceeds the assumed maximum usable tensile strain for UHPC, $\varepsilon_{tu} = 0.01$, and in compression-controlled specimens black regions indicate areas in which the principal strain exceeds the assumed maximum usable compressive strain, $\varepsilon_{cu} = 0.0038$. Fig. 3.8a shows a fiber tension-controlled failure on the left and a concrete compression-controlled failure on the right. The stress contours shown represent the time step when the peak load is achieved. To induce a concrete compression-controlled failure in the rectangular beam, tendon area was increased significantly. In both cases shown in Fig. 3.8a the plastic hinge is located either slightly offset from mid-span or under the concentrated load due to the boundary conditions of the beam in which one is pin and other end is roller support. Fig. 3.8b shows the formation of the first plastic hinge at mid-span due to fiber rupture and that of the second hinge at the intermediate support due to concrete crushing for a two-span continuous T-beam. The formation of the first and second plastic hinges occur at different time steps. As stated earlier, the failure mode for the two-span continuous T-beams was characterized as a concrete compression-

controlled failure because the attainment of the peak load corresponded with the formation of the second plastic hinge, which occurred due to concrete crushing.

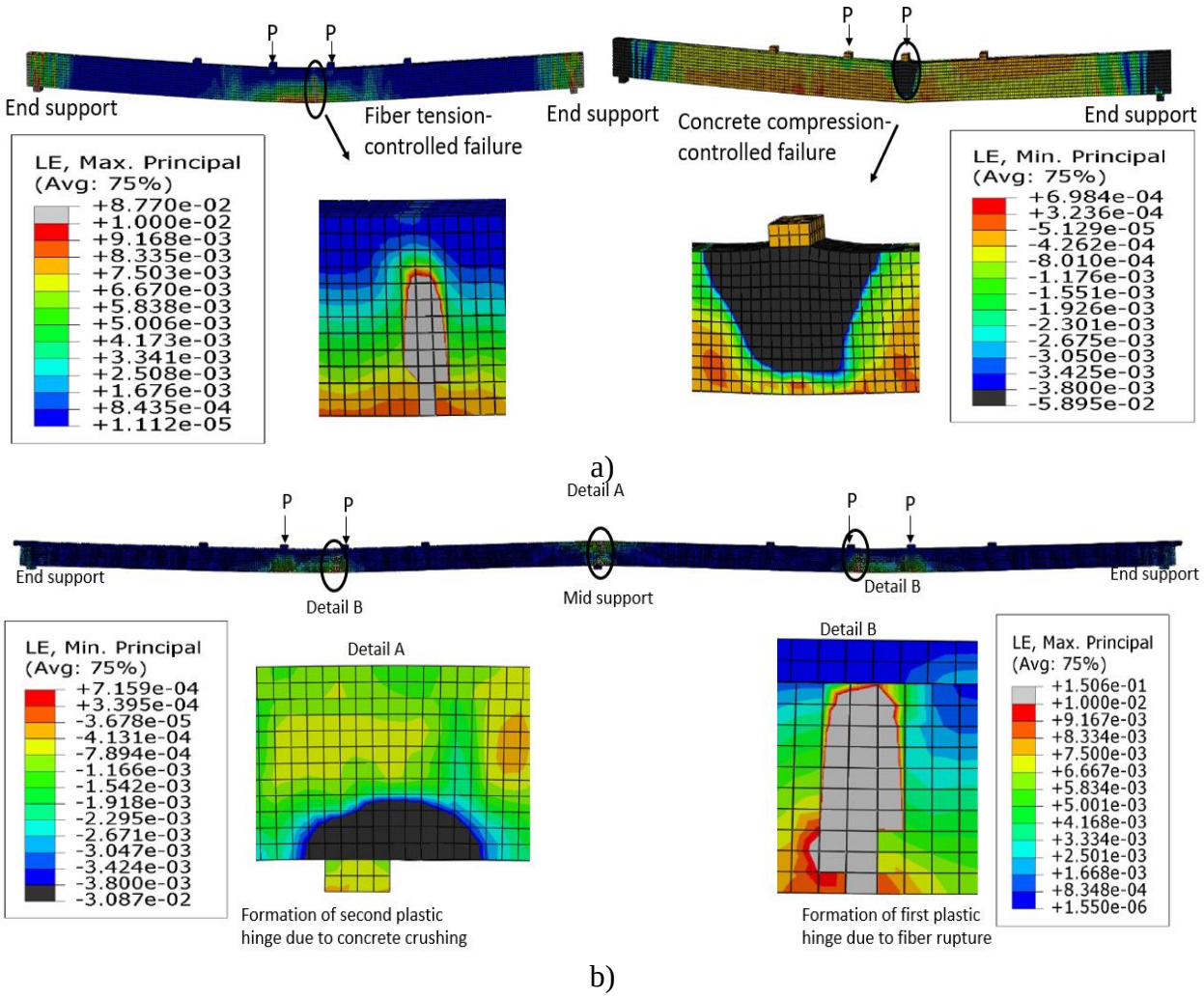

Fig. 3.8 Illustration of fiber tension-controlled and concrete compression-controlled failures in: a) simply supported post-tensioned UHPC beams with a rectangular cross-section, b) continuous post-tensioned UHPC beams with a T cross-section

3.4.2 Sensitivity Analysis

The influence of various parameters on the change in strand stress at the ultimate limit state, Δf_{ps}, was investigated so that a generalized flexural design methodology as well as a set of equations for predicting strand stress at the ultimate limit state, f_{ps}, could be developed. It should be noted that when evaluating prediction equations for f_{ps} for unbonded tendons, it would be

prudent to assess the increment of stress beyond effective prestress, that is, $\Delta f_{ps}=f_{ps}-f_{pe}$, because the reference stress for all equations is the same, that is, f_{pe}. Since Δf_{ps} is relatively small compared to f_{pe} one can be misled by the accuracy of a given equation simply by checking the accuracy of its predicted value of f_{ps} (Naaman 2012).

The investigated parameters include: 1) specified concrete compressive strength, f'_c, 2) area of tendons, A_{ps}, 3) area of mild steel reinforcement, A_s, 4) UHPC cracking stress, f_{cr}, 5) UHPC maximum usable tensile strain, ε_{tu}, 6) effective depth of tendons, d_p, and span over effective depth ratio, L/d_p, 7) continuity, 8) loading configuration, 9) loading pattern, and 10) friction coefficient. The effect of the first five parameters on the strand stress at ultimate strength can be captured by using equilibrium equations at a cross-sectional level, while the effect of the last five parameters can only be captured at a system level. The influence of each of these parameters on the change in strand stress at ultimate, Δf_{ps}, is discussed below.

3.4.2.1 *Effect of f'_c, on Δf_{ps}*

The effect of the specified UHPC compressive strength, f'_c, on the change in strand stress at ultimate, Δf_{ps}, was studied by incrementally increasing f'_c from 152 MPa to 207 MPa in 14 MPa increments in compression controlled two-span continuous specimens (Table 3.3). To induce a concrete compression-controlled failure at the bottom of the web at the intermediate support, specimens with a T cross-section were chosen due to the substantial tension area that they provide at that location. It was generally difficult to induce a compression-controlled failure in rectangular specimens unless the tendon area and the number of tendon layers were increased beyond what may be considered practical. The T-beams considered had an overall depth of 305 mm and each span was 8530 mm. The width of the flange was 965 mm and the thickness of the flange was 51 mm. Additional information about this set of specimens can be found in Table 3.3.

Table 3.3. Effect of f'_c on Δf_{ps}

Specimen ID	Specimen description[a]	Depth (mm)	Span length (mm)	Span config.	f'_c (MPa)	f_{pe} (MPa)	f_{ps} (MPa)	Δf_{ps} (MPa)
BF-1	152MPa254dp218CU1	305	8534	Cont.	152	1248	1462	207
BF-2	165MPa254dp218CU1	305	8534	Cont.	165	1255	1462	207
BF-3	179MPa254dp218CU1	305	8534	Cont.	179	1255	1469	214
BF-4	193MPa254dp218CU1	305	8534	Cont.	193	1255	1462	207
BF-5	207MPa254dp218CU1	305	8534	Cont.	207	1255	1462	207

[a]152MPa = f'c, 254dp = effective depth of tendon at mid-span in mm, 218 = 2-18 mm diameter strands, CU1= two-span continuous T-beam

As shown in Table 3.3, the change in f'_c had no marked effect on the strand stress at ultimate strength, f_{ps}, as well as on the change in strand stress after the beams were post-tensioned and loaded to failure, Δf_{ps}. The strand stress at ultimate strength, f_{ps}, varied from 1462 MPa to 1469 MPa and the change in strand stress, Δf_{ps}, varied from 193 MPa to 207 MPa. The insensitivity of the tendon stress to the increase in UHPC compressive strength is due to the fact that the increase in the compression force was counterbalanced by an increase in the tension force offered by UHPC. The increase in the tension force provided by UHPC was due to the fact that the sustained tensile strength after cracking was assumed to be a function of f'_c (Eq. 3.5) and also due to an upward shift of the neutral axis (decrease in neutral axis depth). As a result, it was decided to let the equilibrium equations determine the net effect of the variation in f'_c on the flexural capacity of UHPC beams post-tensioned with unbonded tendons, rather than include it as a variable in the proposed equation for the strand stress at ultimate.

3.4.2.2 *Effect of A_{ps} on Δf_{ps} and Failure Mode*

The influence of tendon area on the change in the strand stress at ultimate, Δf_{ps}, as well as on the failure mode of the beam specimens was investigated by increasing the area of the tendons in the 305 mm deep and 152 mm wide rectangular beams from 2-13 mm diameter strands to 4-18 mm diameter strands. The results are shown in Table 3.4. The failure mode switches from a fiber tension-controlled failure to a concrete compression-controlled failure when the tendon's area

transitions from 2-15 mm diameter strands to 4-15 mm diameter strands. Additionally, the strand stress at ultimate, f_{ps}, as well as the change in strand stress, Δf_{ps}, decreases as the tendon area increases; f_{ps} varied from 1462 MPa to 1407 MPa, and Δf_{ps} varied from 172 MPa to 124 MPa. This is intuitive and logical because the larger the area of the strands the lower the strand stress required to counterbalance a given compression force. For this reason, it was once again determined to let the equilibrium equations determine the net effect of the variation in A_{ps} on the flexural capacity of UHPC beams post-tensioned with unbonded tendons, rather than include it as a variable in the proposed equation for the strand stress at ultimate, f_{ps}.

Table 3.4. Effect of A_{ps} on Δf_{ps} and on failure mode

Specimen ID	Specimen description[a]	Depth (mm)	Span length (mm)	A_{ps} (mm^2)	f_{pe} (MPa)	f_{ps} (MPa)	Δf_{ps} (MPa)	Failure Mode
BP-1	152MPa229dp213RU1	305	8534	197	1289	1462	172	Tens.
BP-2	152MPa229dp215RU1	305	8534	280	1276	1441	165	Tens.
BP-3	152MPa229dp415RU1	305	8534	560	1289	1434	145	Comp.
BP-4	152MPa229dp418RU1	305	8534	759	1282	1407	124	Comp.

[a]152MPa = f'_c, 229dp = effective depth of tendon at mid-span in mm, 213 = 2-13 mm diameter strands, RU1 = Rectangular simple span beam

3.4.2.3 *Effect of A_s on Δf_{ps}*

To understand the influence of the mild steel area, A_s, on Δf_{ps}, the area of mild steel was increased until the tension force provided by mild steel equaled the tension force provided by the tendons. All investigated beams had a certain amount of mild steel with the minimum area being equal to 63 mm^2 and the maximum area equal to 568 mm^2. The influence of the variation of mild steel area did not have a pronounced effect on the change in strand stress at ultimate, Δf_{ps} (Table 3.5); Δf_{ps} varied from 334 MPa to 341 MPa. As a result, the area of mild steel was not considered as a key parameter to be explicitly included in the formulation of the equations for the determination of Δf_{ps}. The equations of equilibrium can capture its influence during the calculation of the depth to the neutral axis and flexural capacity.

Table 3.5. Effect of A_s on Δf_{ps}

Specimen ID	Specimen description[a]	Depth (mm)	Span length (mm)	A_s (mm^2)	f_{pe} (MPa)	f_{ps} (MPa)	Δf_{ps} (MPa)	Failure Mode
BS-1	152MPa213bs2-2RU1	305	8534	63	1281	1622	341	Tens.
BS-2	152MPa213bs2-3RU1	305	8534	142	1281	1620	339	Tens.
BS-3	152MPa213bs2-4RU1	305	8534	258	1281	1615	334	Tens.
BS-4	152MPa213bs2-5RU1	305	8534	400	1281	1618	337	Tens.
BS-5	152MPa213bs2-6RU1	305	8534	568	1281	1619	338	Tens.

[a]152MPa = f'c, All beams have effective depth of 254 mm and have 0.01 maximum usable strain, 213 = 2-13 mm diameter strands,bs2-2 = 2 #2 bottom mild steel , RU1 = Rectangular simple span beam

3.4.2.4 *Effect of f_{cr} on Δf_{ps}*

The stress-strain curve for UHPC in tension was generally idealized as elastic perfectly plastic, with the cracking stress, f_{cr}, being equal to the post-cracking stress (Fig. 3.4a). Additionally, the cracking stress, f_{cr}, was expressed as a function of the specified compressive strength of UHPC, f'_c (Eq. 3.5). Realizing that determining the cracking stress in such a manner is an approximation, the influence of the magnitude of the cracking stress on the change in strand stress was investigated by varying the cracking stress from 2.75 MPa to 9.65 MPa. All specimens considered for this investigation were fiber tension-controlled specimens.

Table 3.6. Effect of f_{cr} on Δf_{ps}

Specimen ID	Specimen description[a]	Depth (mm)	Span length (mm)	σ_{tu} (MPa)	f_{pe} (MPa)	f_{ps} (MPa)	Δf_{ps} (MPa)	Failure Mode
BTP-1	152MPa213sut2.75RU1	305	8534	2.75	1281	1576	295	Tens.
BTP-2	152MPa213sut4.15RU1	305	8534	4.15	1281	1620	339	Tens.
BTP-3	152MPa213sut5.52RU1	305	8534	5.52	1281	1623	342	Tens.
BTP-4	152MPa213sut6.89RU1	305	8534	6.89	1281	1620	339	Tens.
BTP-5	152MPa213sut8.24RU1	305	8534	8.24	1281	1614	333	Tens.
BTP-6	152MPa213sut9.65RU1	305	8534	9.65	1281	1617	336	Tens.

[a]152MPa = f'c, All beams have effective depth of 254 mm and have 0.01 maximum usable strain, 213 = 2-13 mm diameter strands,sut2.75 = maximum tensile stress of 2.75 MPa , RU1 = Rectangular simple span beam

Table 3.6 shows that the influence of the variation of the magnitude of the cracking stress on the change in strand stress was minimal. The change in strand stress varied from 295 MPa to 342 MPa. As a result, a change of 351% in the magnitude of the UHPC cracking stress resulted only in a 16% variation in the change in strand stress at ultimate strength. Therefore, it was decided

to let the equations of equilibrium capture the influence of the magnitude of the cracking stress of UHPC on the strand stress at ultimate and moment capacity of the member

3.4.2.5 *Effect of ε_{tu} on Δf_{ps}*

One of the advantages of UHPC is that it offers significant ductility in the tensile domain due to the presence of fibers. This tensile ductility, expressed as the ratio between the ultimate tensile strain, ε_{tu}, and cracking strain, ε_{cr}, depends primarily on the amount of fibers included in the mix as well as the class of UHPC materials used. As a result, it is paramount to study the influence that the assumed maximum usable tensile strain, ε_{tu}, has on the change in strand stress at ultimate, Δf_{ps}. To accomplish this, the ultimate tensile strain, ε_{tu}, was varied from 0.005 to 0.015. All the specimens included in this investigation were fiber tension-controlled specimens. Table 3.7 shows that the assumed value for the ultimate tensile strain has a strong effect on the change in strand stress at ultimate, which varied from 204 MPa to 408 MPa. As a result, it was decided to explicitly include the direct proportionality of ε_{tu} to Δf_{ps} in the formulation for predicting Δf_{ps}.

Table 3.7. Effect of ε_{tu} on Δf_{ps}

Specimen ID	Specimen description[a]	Depth (mm)	Span length (mm)	ε_{tu}	f_{pe} (MPa)	f_{ps} (MPa)	Δf_{ps} (MPa)	Failure Mode
BTU-1	152MPa213etu0.005RU1	305	8534	0.005	1281	1485	204	Tens.
BTU-2	152MPa213etu0.007RU1	305	8534	0.007	1281	1535	254	Tens.
BTU-3	152MPa213etu0.009RU1	305	8534	0.009	1281	1592	311	Tens.
BTU-4	152MPa213etu0.01RU1	305	8534	0.01	1281	1620	339	Tens.
BTU-5	152MPa213etu0.012RU1	305	8534	0.012	1281	1657	376	Tens.
BTU-6	152MPa213etu0.015RU1	305	8534	0.015	1281	1689	408	Tens.

[a]152MPa = f`c, All beams have effective depth of 254 mm at mid-span, 213 = 2-13 mm diameter strands, etu0.005 = maximum usable tensile strain of 0.005, RU1 = Rectangular simple span beam

3.4.2.6 *Effect of Continuity on Δf_{ps} and Failure Mode*

Because strand stress at the ultimate limit state in concrete beams post-tensioned with unbonded strands is system dependent rather than section dependent, the effect of continuity on the change in strand stress, Δf_{ps}, was investigated for the beams with a rectangular cross-section.

The characteristics of the beams included in this investigation are shown in Table 3.8. The loading configuration for both single span and continuous specimens featured two-point loading symmetrical about mid-span similar to that shown in Fig. 3.8.

Table 3.8. Effect of continuity on Δf_{ps}

Specimen ID	Specimen description[a]	Depth (mm)	Span (mm)	Continuity	A_{ps} (mm^2)	f_{pe} (MPa)	f_{ps} (MPa)	Δf_{ps} (MPa)	Failure Mode
BC-1	152MPa215A1	310	4000	Single	280	1303	1462	159	Tens.
BC-2	152MPa215A1	310	4000	Cont.	280	1324	1503	179	Tens.
BC-3	152MPa315A1	310	4000	Single	420	1282	1455	172	Comp.
BC-4	152MPa315A1	310	4000	Cont.	420	1303	1482	179	Comp.
BC-5	152MPa415A1	310	4000	Single	560	1289	1469	179	Comp.
BC-6	152MPa415A1	310	4000	Cont.	560	1262	1462	200	Comp.
BC-7	152MPa218A1	310	4000	Single	379	1297	1455	159	Tens.
BC-8	152MPa218A1	310	4000	Cont.	379	1310	1489	179	Tens.
BC-9	152MPa318A1	310	4000	Single	569	1269	1455	186	Comp.
BC-10	152MPa318A1	310	4000	Cont.	569	1282	1476	193	Comp.
BC-11	152MPa418A1	310	4000	Single	759	1269	1448	179	Comp.
BC-12	152MPa418A1	310	4000	Cont.	759	1269	1476	207	Comp.

[a]152 MPa = f'_c, 215 = 2-15 mm diameter strands, A1: Rectangular beam

Both spans in the continuous specimens were loaded simultaneously until failure. The effect of loading configuration and patterned loading is discussed in the subsequent sections. As can be seen, the introduction of continuity generally resulted in an increase in the change in strand stress after the beams were post-tensioned and loaded to failure. However, this increase was minimal and varied from 7 MPa to 28 MPa. Also, the variation in strand stress at ultimate was no more than 2-3%. In addition, the influence of such a small increase in strand stress at ultimate due to continuity becomes even more negligible when the tension force provided by the UHPC block and that provided by any mild steel present are considered. As a result, it was decided not to explicitly include a variable or a coefficient that accounts for continuity in the equations for predicting strand stress at ultimate strength. The small increase in strand stress due to continuity can serve as reserve capacity when predicting the flexural strength of continuous UHPC beams post-tensioned with unbonded strands.

3.4.2.7 *Effect of Loading Configuration on Δf_{ps}*

To determine the effect of loading configuration on the change in strand stress after the UHPC beams were post-tensioned and loaded to failure, three different loading conditions were investigated: 1) one-point loading, 2) two-point loading, and 3) distributed loading. The distance between the two point loads, *d*, was incrementally increased until that distance became equal to *L/3* where *L* is the span of the beam. The results are summarized in Table 3.9 and are illustrated in Fig. 3.9a. The two-point loading configurations represent the scenarios in which the distance between the concentrated loads, *d*, was equal to *0.1L* and *0.33L*. Changes in strand stress, Δf_{ps}, vary from 159 MPa to 338 MPa. As a result, loading pattern plays an important role in determining strand stress at ultimate flexural strength. It was determined that when the distance between the two-point loads became equal to *L/3*, there was not a significant difference in the change in strand stress between that case and what was obtained for a uniform load (Fig. 3.9a). Because the loading pattern had a strong effect on the change in strand stress at ultimate, this parameter was directly included in the formulation of equations for determining the change in strand stress at ultimate, Δf_{ps}, by using a function, *f*, (Fig. 3.9b) the development of which is discussed later in the section titled plastic hinge length and patterned loading.

Table 3.9. Effect of loading configuration on Δf_{ps}

Specimen ID	Specimen description[a]	Depth (mm)	Span (mm)	Δf_{ps} (MPa)			
				One-point	Two-point		Distributed
					d/L^b=0.1	d/L^b=0.33	
BL-1	152MPa254dp213RU1	305	8534	159	207	331	324
BL-2	152MPa254dp213RU2	305	8534	165	221	331	331
BL-3	165MPa254dp213RU1	305	8534	159	207	331	331
BL-4	165MPa254dp213RU2	305	8534	165	214	331	338
BL-5	179MPa254dp213RU1	305	8534	159	207	331	324
BL-6	179MPa254dp213RU2	305	8534	165	200	317	310

[a]152MPa = compressive strength, RU1 and RU2 = Rectangular simple span beam, 254dp = effective depth of tendon in mm at mid-span, 213 = 2-13 mm diameter strands, [b]*d*=distance between the concentrated loads, *L*=span length.

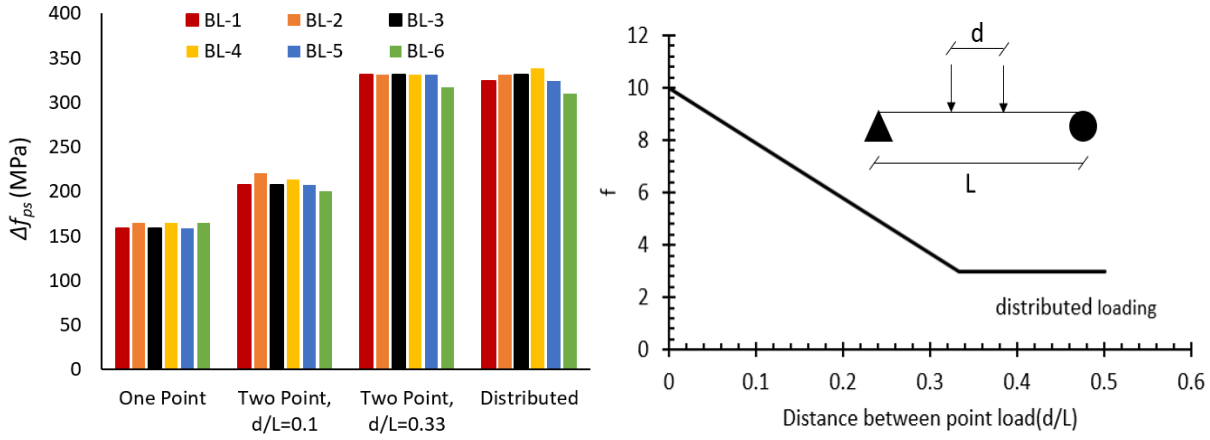

Fig. 3.9 a) Influence of loading configuration on Δf_{ps}, b) Proposed relationship between loading configuration and function f included in Eq. 3.10

3.4.2.8 *Effect of d_p and L/d_p on Δf_{ps}*

The influence of the effective depth, d_p, and L/d_p ratio was investigated to continue capturing the system effect on the change in strand stress at ultimate in UHPC beams. This was accomplished by varying d_p from 216 mm to 267 mm in simply supported rectangular beams with an overall depth of 305 mm and a span of 8534 mm. Concrete compressive strength and area of tendons were kept constant at 152 MPa and 2-13 mm diameter strands, respectively. L/d_p was also varied from 16 to 56. The results are shown in Table 3.10 and Fig. 3.10. There is a direct relationship between the effective depth and change in strand stress. As the effective depth decreases the change in strand stress also decreases. Conversely, as the L/d_p ratio increases, the change in strand stress at ultimate decreases. This relationship is common with that observed in NSC post-tensioned beams (Maguire et al. 2016). Because of the strong influence that d_p and L/d_p ratio had on the change in strand stress, it was decided to directly include both of these parameters on the formulation of Δf_{ps}.

Table 3.10. Effect of d_p on Δf_{ps}

Specimen ID	Specimen description[a]	Depth (mm)	Span length (mm)	Span config.	d_p (mm)	Δf_{ps} (MPa)
BH-1	152MPa267dp213RU1	305	8534	Single	267	232
BH-2	152MPa254dp213RU1	305	8534	Single	254	209
BH-3	152MPa241dp213RU1	305	8534	Single	241	194
BH-4	152MPa229dp213RU1	305	8534	Single	229	176
BH-5	152MPa216dp213RU1	305	8534	Single	216	164

[a]152MPa = f'c, 267dp = effective depth of tendon at mid-span in mm, 213 = 2-13 mm diameter strands, RU1 = Rectangular simple span beam

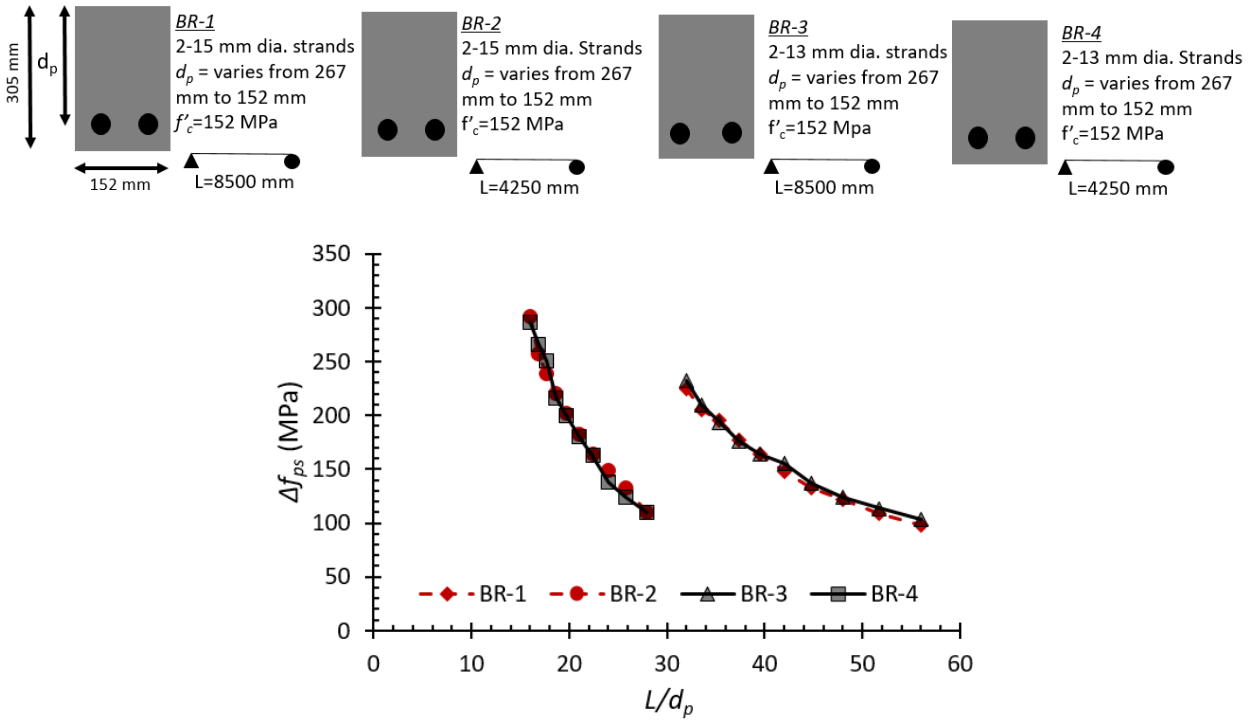

Fig. 3.10 Effect of d_p on the change in strand stress at the ultimate limit state

3.4.2.9 *Effect of Patterned Loading on Δf_{ps}*

The effect of patterned loading on the change in strand stress at ultimate was investigated by considering five different cases illustrated in Fig. 3.11. The default case is a simply supported beam, which represents the majority of the specimens. Case A represents a three span continuous beam in which all spans are loaded. Case B represents a three span continuous beam in which only the end span is loaded. Case C represents three span continuous beams in which only the middle

span is loaded, and Case D represents a three span continuous beam in which two out of three spans are loaded. The loading configurations featured a single concentrated load at mid-span as well as two point loading symmetrical about mid-span. The number of plastic hinges anticipated in the collapse mechanism is denoted for each case and varies from 1.0 to 5.0. The relationship between the number of hinges and the change in strand stress at ultimate is illustrated in Fig. 3.12 and summarized in Table 3.11. In the three span continuous beam specimens, the change in strand stress was lower when one span was loaded compared to cases when two or three spans were loaded. Similarly, in the three span continuous specimens, the change in strand stress was lower when two spans were loaded compared to when three spans were loaded. In general, the change in strand stress at ultimate was proportional to the ratio of the actual number of plastic hinges divided by the potential number of plastic hinges. This relationship is later in this paper included in the proposed formulation for determining Δf_{ps} to capture the influence of patterned loading. While there are a few exceptions to this rule, in general, this simple relationship was able to capture reasonably well the influence of patterned loading on the change in strand stress at the ultimate limit state, Δf_{ps}. For example, in the three span continuous beams the only exception is the case when 2.0 plastic hinges are formed, which results in a change in strand stress at ultimate that is either similar to or slightly smaller than the case when 1.5 plastic hinges are formed. In all other cases for the three span continuous beams, the described relationship properly characterizes the change in strand stress as a function of the number of plastic hinges. Another small deviation to the proposed relationship is the case between a single span beam and a three span continuous beam in which all spans are loaded. According to the proposed relationship, the change in strand stress for these two cases should be identical when in fact varies by 8% and 15% for one point and two-point loading, respectively. However, such differences were considered small for design purposes.

Table 3.11. Effect of number of hinges on Δf_{ps}

Specimen ID	Specimen description[a]	Loading type *(Figure 3.11)*	No. of hinges	Loading pattern	Span config.	Δf_{ps} (MPa)
BN-1	152MPa254dp213RU	Default Case	1.0	One point	1 span	156
BN-2	152MPa254dp213RU	Case A	5.0	One point	3 spans	145
BN-3	152MPa254dp213RU	Case B	1.5	One point	3 spans	69
BN-4	152MPa254dp213RU	Case C	2.0	One point	3 spans	55
BN-5	152MPa254dp213RU	Case D	3.5	One point	3 spans	117
BN-6	152MPa254dp213RU	Default Case	1.0	Two point	1 span	324
BN-7	152MPa254dp213RU	Case A	5.0	Two point	3 spans	372
BN-8	152MPa254dp213RU	Case B	1.5	Two point	3 spans	145
BN-9	152MPa254dp213RU	Case C	2.0	Two point	3 spans	138
BN-10	152MPa254dp213RU	Case D	3.5	Two point	3 spans	269

[a]152MPa = f'_c, 254dp = effective depth of tendon at mid-span in mm, 213 = 2-13 mm diameter strands, RU = Rectangular cross sectioned beam

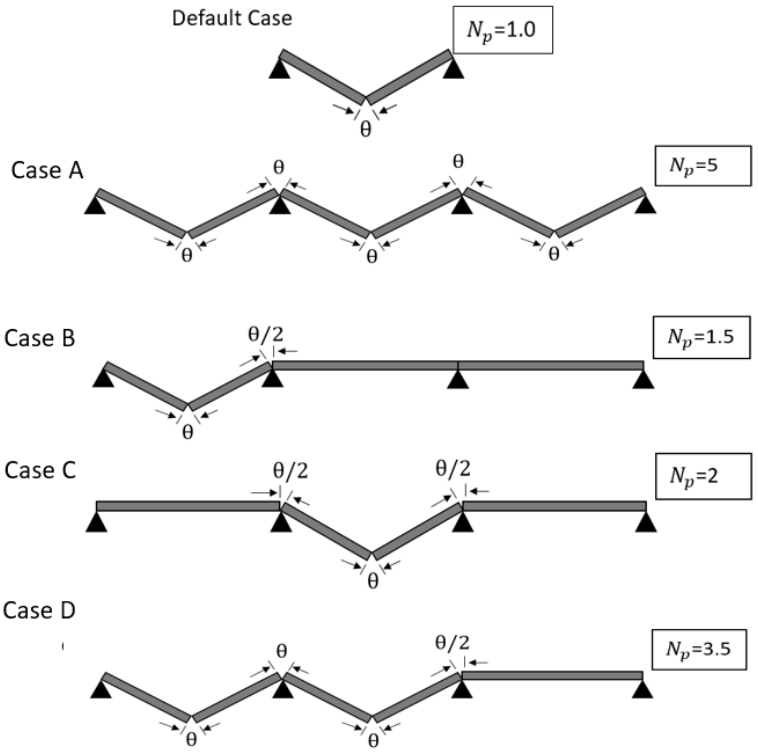

Fig. 3.11. Collapse mechanisms and total number of hinges for patterned loading (adapted after Harajli 2011)

The potential number of plastic hinges in a given beam can be calculated assuming that plastic hinges can form in each span and over the interior supports. For example, in a simply supported beam the total number of potential plastic hinges is 1.0 and in a three span continuous beam it is 5.0. The actual number of plastic hinges is equal to the minimum number of hinges required to create a collapse mechanism and is denoted for each case in Fig. 3.11.

Case A and Case D require simultaneous formation of all hinges. These mechanisms may occur if the amount of nonprestressed reinforcement at midspan, and interior supports is determined such that it allows for such a simultaneous formation of hinges (assuming that effective depth and the amount of prestressed reinforcement is the same). Even if this is realized, the simultaneous formation of such hinges requires material homogeneity and load uniformity or symmetry. Therefore, in reality, the default case combined with Case B and Case C are more likely to occur.

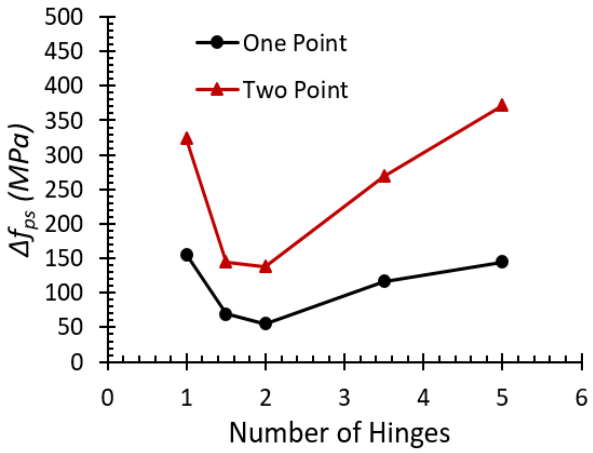

Fig. 3.12. Influence of the number of hinges on the change in strand stress at the ultimate limit state

3.4.2.10 *Effect of the friction coefficient on Δf_{ps}*

The influence of the friction coefficient, μ, on the change in strand stress at the ultimate limit state was investigated by varying the friction coefficient from 0.05 to 0.15 in increments of 0.025. This range represents the range for the friction coefficient reported in the PTI Manual (2006). As stated earlier, for the majority of cases the lower bound of this range (i.e. a friction coefficient of 0.05) was assumed to simulate maximum slip and consequently obtain minimum (conservative) estimates of tendon stress increase at the ultimate limit state. The results for the additional cases investigated featuring various friction coefficient are provided in Table 3.12.

Table 3.12. Effect of μ on Δf_{ps}

Specimen ID	Specimen description[a]	Depth (mm)	Span length (mm)	Span config.	μ	Δf_{ps} (MPa)
BFR-1	152MPa254dp213RU1	305	8534	Single	0.05	329
BFR-2	152MPa254dp213RU1	305	8534	Single	0.075	331
BFR-3	152MPa254dp213RU1	305	8534	Single	0.1	334
BFR-4	152MPa254dp213RU1	305	8534	Single	0.125	335
BFR-5	152MPa254dp213RU1	305	8534	Single	0.15	339

[a]152MPa = f'$_c$, 254dp = effective depth of tendon at mid-span in mm, 213 = 2-13 mm diameter strands, RU1 = Rectangular simple span beam

The change in strand stress at the ultimate limit state varies from 329 MPa to 339 MPa when the friction coefficient is varied from 0.05 to 0.15. This is a very small and negligible change. As a result, it was concluded that the friction coefficient does not play a significant role in the determination of the strand stress at ultimate and consequently on the nominal moment capacity of the beam

3.4.3 Flexural Design Methodology

A flexural design methodology as well as a set of equations for predicting strand stress at ultimate is presented for UHPC beams post-tensioned with unbonded tendons. The proposed methodology is presented in terms of the failure modes exhibited by such members. The kinematic mechanism at failure for both cases is shown in Fig. 3.13 and considers a cracked section at mid-span for a simply supported beam.

This kinematic mechanism is similar to the one used by Roberts-Wollmann et al. (2005) for normal strength concrete members. The crack is modeled by an isosceles triangle with a height of *h*-*c*. The area near the crack is perturbed with respect to the elastic behavior and corresponds to a curvature equal to φ. In this zone the beam is modeled as if it were made of two regions; at the top, an uncracked beam following Navier's hypothesis (linearity of strain), and at the bottom two rigid blocks connected by a hinge (perturbed region). The determination of the plastic hinge length

is required to conduct a kinematic analysis to relate the critical crack width, δ, plastic hinge length L_p, and the change in strand strain, $\Delta\varepsilon_{ps}$. Such kinematic analyses as well as the methodology to calculate the nominal moment capacity of UHPC members post-tensioned with unbonded tendons is presented in the next sections for concrete compression-controlled failures and fiber tension-controlled failures.

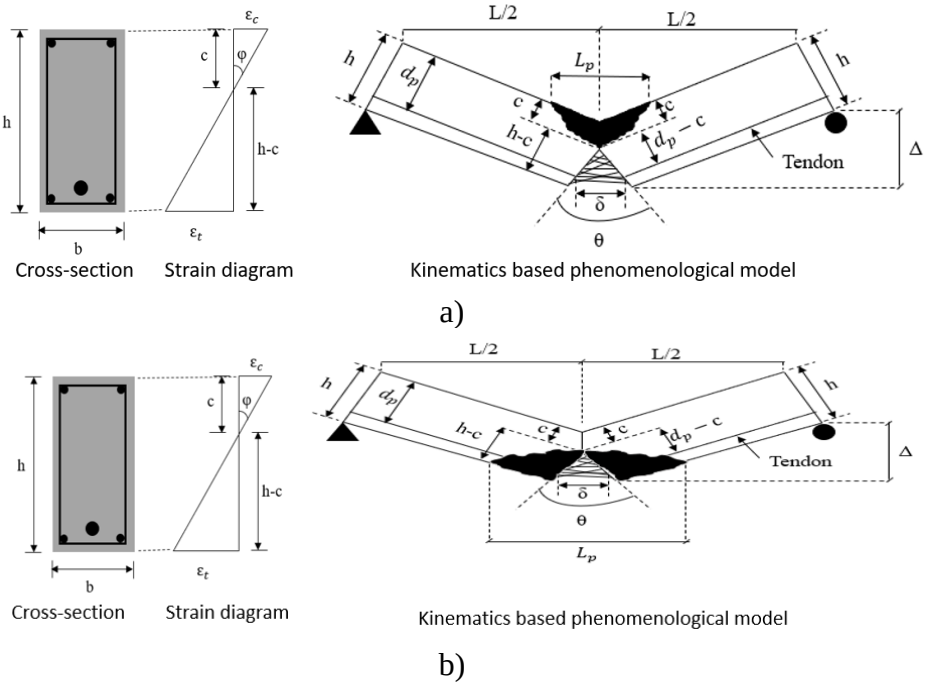

Fig. 3.13 Failure mechanism in UHPC beams post-tensioned with unbonded tendons: a) concrete compression-controlled members, and b) fiber tension-controlled members

3.4.3.1 *Plastic Hinge Length and Patterned Loading*

One of the most important parameters when determining strand stress at the ultimate limit state, f_{ps}, using a mechanics based approach is the length of the plastic hinge. Consider for example the kinematics based phenomenological model shown in Fig. 3.13a. The change in strand strain at failure in a simply supported beam, $\Delta\varepsilon_{ps}^{o}$, is calculated using Eq. 3.7 by dividing the change in tendon length, δ, by the original length of the tendon, L. The change in tendon length is calculated by multiplying the distance from the neutral axis to the centroid of tendons (d_p-c) by the total plastic rotation, θ_p, of the two beam portions at the considered crack. This total plastic rotation can

be calculated by integrating the curvature over the plastic hinge length, L_{pr} (Eq. 3.8). Because the integration of curvature over the plastic hinge length is cumbersome, the concept of an equivalent plastic hinge length has been introduced. The concept of equivalency is based on the condition that the product of the equivalent plastic hinge length and ultimate curvature will yield the same total plastic rotation as that obtained from the integration of the actual curvature diagram over the real plastic hinge length. Therefore, the equivalent plastic hinge length is the length over which a given plastic curvature is assumed to be constant to facilitate the member's flexural deflection and rotation capacity. The ultimate curvature, φ_u, can be calculated by dividing the ultimate compressive strain, ε_{cu}, by the depth to the neutral axis, c, assuming that plane sections before bending remain plane after bending. When Eq. 3.8 is substituted into Eq. 3.7, Eq. 3.9 is obtained. The only unknowns in Eq. 3.9 are the equivalent plastic hinge length, L_p, and the depth to the neutral axis c. While the depth to the neutral axis can be determined using equations of equilibrium, some guidance is required to determine the length of the equivalent plastic hinge.

$$\Delta\varepsilon_{ps}^{o} = \frac{\delta}{L} = \frac{(d_p - c)\theta}{L} \qquad \text{Eq. 3.7}$$

$$\theta_p = \int_0^{L_{pr}} \varphi(x)dx = L_p\,\varphi_u = L_p\,\frac{\varepsilon_{cu}}{c} \quad ,0.0038 \le \varepsilon_{cu} \le 0.0044 \qquad \text{Eq. 3.8}$$

$$\Delta\varepsilon_{ps}^{o} = \frac{(d_p - c)}{L}\,\frac{L_p\varepsilon_{cu}}{c} \qquad \text{Eq. 3.9}$$

The definition of the plastic hinge length is related to the definition of plasticity and what constitutes the beginning and extent of it. In normal strength reinforced concrete beams plasticity is typically defined by the yielding of the reinforcement, although in heavily loaded columns and compression-controlled beams, concrete may reach the inelastic range before tension steel yields.

One approach is to monitor the strains in both concrete and steel and designate the beginning of plasticity as the time step at which either concrete enters the inelastic range or tension steel commences to yield, whichever occurs first (Park and Pauley 1975). In general, the high nonlinearity of materials, interactions and relative movements between constituent materials in the plastic hinge zone greatly complicate the task of accurately calculating the length of the plastic hinge (Hines et al. 2004, Zhao et al 2011, Park and Pauley 1975). As a result, the equivalent plastic hinge length has been typically defined using closed form empirical equations with the ultimate validation of any proposed formulation being that the product of the equivalent plastic hinge length and ultimate curvature matches with the total plastic rotation obtained from experiments or validated numerical models.

The problem becomes even more challenging in post-tensioned UHPC members, in which the strands are unbonded, mild steel could be present in addition to unbonded tendons, the tensile strength of concrete cannot be neglected and introduces another source of plasticity due to the tensile ductility of UHPC, and the stress-strain curve for UHPC in compression is different from that assumed for NSC, featuring high compressive strengths and resulting in failure modes that are different from NSC members. The spread of plasticity in post-tensioned UHPC beams with unbonded tendons could be based on the region over which concrete has cracked, or on the region over which the unbonded tendons or mild steel have yielded. In either case, to account for the variation and fluctuations in curvature in the inelastic region, empirical equations for the equivalent plastic hinge length and corresponding curvature would have to be developed to facilitate the integration of curvature to determine the rotational capacity of the member at the ultimate limit state.

As a result, while it is possible to develop various formulations for the equivalent plastic hinge length based on a given definition for the determining the spread of plasticity, by dividing the actual area under the curvature diagram by a given plastic curvature, the strength and utility of these formulations would be assessed by their ability to correctly capture the plastic rotation of the member and consequently the change in strand stress, which is the focus of this study. Therefore, in this study the results from numerical simulations were used to obtain the change in the strands stress, $\Delta\varepsilon_{ps}^{o}$, which in turn was used to back calculate the equivalent plastic hinge length, L_p. Then, an empirical equation based on the formulation developed by Lee et al. (1999) and Harajli et al. (2002) is presented to calculate the equivalent plastic hinge length as a function of the loading configuration, f, L/d_p ratio, and length of the tendon, L. These parameters are believed to be key parameters in determining the length of the plastic hinge and in capturing the system effect on the strand stress at the ultimate limit state. It is clear from Eq. 3.7 through 3.9 that the change in strand stress at ultimate is a function of effective depth, d_p, neutral axis depth, c, plastic hinge length, L_p, span length, L, and maximum usable compressive, ε_{cu}, or tensile strain, ε_{tu}, for UHPC depending on whether the member is concrete compression controlled or fiber tension controlled. Eq. 3.9 supports the direct proportionality of d_p to $\Delta\varepsilon_{ps}^{o}$ and consequently to Δf_{ps}. Eq. 3.9 and 3.10 support the indirect proportionality of the L/d_p ratio on the change in strand stress at ultimate observed during the sensitivity analysis.

$$\mathrm{L_p} = \left(\frac{1}{\mathrm{f}} + \frac{1}{\mathrm{L/d_p}}\right) L \quad , f = 10 \; for \; one \; point \; load$$
$$f \geq 3 \; for \; two \; point \; load \; (use \; Fig. 3.9b)$$
$$f = 3 \; for \; uniform \; distributed \; loading \qquad \text{Eq. 3.10}$$

The proposed empirical equation for L_p was used to develop an idealized function, f, for capturing the effect of loading configuration on the strand stress at ultimate. The results from

numerical simulations were used to obtain $\Delta\varepsilon_{ps}^{o}$, which in turn was used to back calculate L_p and to develop a relationship between the function f and the distance between the applied point loads (Fig. 3.9b). This idealized function features a relationship in which f decreases as the distance between the point loads increases until it becomes equal to $L/3$, at which point f remains constant. For simplicity, three values are included in the proposed flexural design methodology; $f=10$ for point load, $f \geq 3$ for two point loads and $f=3$ for uniform distributed loading. Since the function f is in the denominator of Eq. 3.10, which is used to determine L_p, and since L_p is in the numerator of Eq. 3.9, which is used to determine $\Delta\varepsilon_{ps}^{o}$, this formulation is consistent with the results obtained from the sensitivity analysis, which showed that Δf_{ps} increased as the loading configuration changed from one point loading to two point loading and to distributed loading.

The change in strand stress for a simply supported beam, $\Delta\varepsilon_{ps}^{o}$, which can be calculated using Eq. 3.9, was adjusted to account for the effect of patterned loading in multi-span continuous beams discussed previously in this paper. As previously noted, the change in strand stress was generally proportional to the ratio of the actual number of plastic hinges over the potential number of plastic hinges as defined earlier. This simple adjustment is expressed in Eq. 3.11 and 3.12 and is deemed adequate for design purposes as demonstrated later in the section titled comparison of predicted and computed results. The previously noted observations regarding the fact that the change in strand stress in three span continuous specimens was lower for cases that featured partial loading compared to the cases in which all spans were loaded is consistent with Eq. 3.7 and with the derivation of the proposed design methodology. In Eq. 3.7, the change in strand strain in a simply supported beam is calculated as the change in strand length calculated at the location of the plastic hinge divided by the total length of the strand. For cases that feature multi-span continuous beams and partial loading, the ratio between the change in strand length and the total length of

strand is lower compared to cases that feature full loading, because the total length of the strand is the same whereas the change in strand length is assumed to take place at the location of the plastic hinges (i.e. it is a function of the number of plastic hinges).

Once the plastic hinge length is calculated and adjustments for patterned loading are made, Eq. 3.9-3.12 can be used to calculate the change in strand strain and Eq. 3.13 and 3.14 can be used to calculate the effective prestrain, ε_{pe}, and strain in strand at ultimate, ε_{ps}. Effective prestrain, ε_{pe}, is calculated using Hooke's Law given that the effective prestress, f_{pe}, is kept within the linear elastic branch of the stress-strain curve for the strand. (Tadros and Devalapura 1992) equation is then used to relate ultimate strand strain, ε_{ps}, to ultimate strand stress, f_{ps} (Eq. 3.6). Calculating f_{ps} in such a manner eliminates errors introduced by the commonly used assumption in normal strength concrete members that the relationship between tendons stress and strain is linear elastic at all strain levels, including strains close to yield. N_{actual} is actual number of hinges depending on spans loaded. N_{total} is total possible number of hinges when all spans are loaded.

$$\Delta\varepsilon_{ps} = \Delta\varepsilon_{ps}^{o}\lambda \qquad \text{Eq. 3.11}$$

$$\lambda = \frac{N_{actual}}{N_{total}} \qquad \text{Eq. 3.12}$$

$$\varepsilon_{pe} = \frac{f_{pe}}{E_{ps}} \; where \; E_{ps} = 196500 \; MPa \qquad \text{Eq. 3.13}$$

$$\varepsilon_{ps} = \varepsilon_{pe} + \Delta\varepsilon_{ps} \qquad \text{Eq. 3.14}$$

3.4.3.2 *Concrete Compression-Controlled Failure*

The nominal moment capacity of a UHPC compression-controlled beam post-tensioned with unbonded tendons can be determined using the strain, stress, and force diagrams as well as the equations of equilibrium and assumed stress-strain curves shown in Fig. 3.14a. In this figure, the transition from the strain diagram to the stress diagram is based on the assumption that the

stress-strain diagram for UHPC in compression is linear elastic, which is a reasonable assumption because the stress-strain relationship for UHPC in compression is typically linear with some softening taking place as the specified compressive strength is achieved (Fig. 3.4a). As a result, the stress-strain curve for UHPC in compression that is recommended for design is a linear curve in which the maximum compressive stress is equal to the specified compressive strength, f'_c, and the ultimate compressive strain, ε_{cu}, may be obtained by dividing f'_c, with the modulus of elasticity, E_c, which can be calculated using Eq. 3.4. In tension, the stress-strain relationship is assumed bilinear (elastic perfectly plastic) with the cracking stress, f_{cr}, determined based on Eq. 3.5 and the ultimate tensile strain, ε_{tu}, set equal to 0.01 or some other value depending on the amount of fibers used (Haber et al. 2018). However, the linear elastic portion on the tension side can be ignored and the entire block can be idealized as rectangle without an appreciable loss in accuracy.

Two approaches can be taken for the determining the depth to the neutral axis, c, and consequently the nominal moment capacity, M_n. The first is iterative in nature and the second is non-iterative. In the iterative approach an estimate for the depth to the neutral axis, c, is made and the change in strand strain at ultimate is calculated using Eq. 3.9-3.11. These equations are based on the assumption that the flexural failure is a concrete compression controlled failure because curvature is calculated as the ratio of the maximum usable concrete strain, ε_{cu}, to the depth of the neutral axis, c. Eq. 3.14 and 3.6 are then used to determine the strand stress at ultimate, f_{ps}. After strand stress at ultimate is determined, Eq. 3.15 and 3.16 can be used to check for internal equilibrium. If internal equilibrium exists, then the nominal moment capacity of the member can be calculated using Eq. 3.18. If it does not, then a different value for c is assumed and the procedure is repeated until internal equilibrium is reached. Alternatively, since the depth to the neutral axis,

c, is the only unknown in Eq. 3.16, a computer aided solver can be used to determine *c* without iteration.

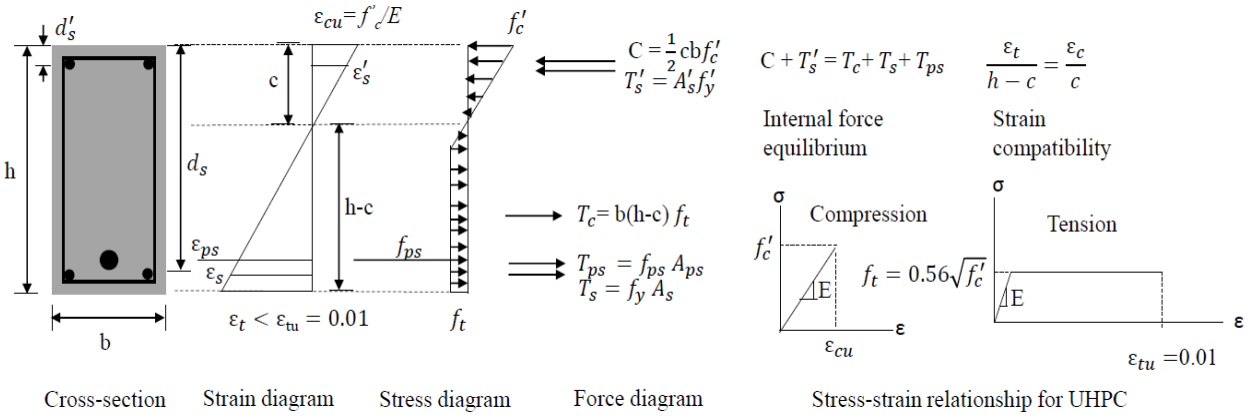

a)

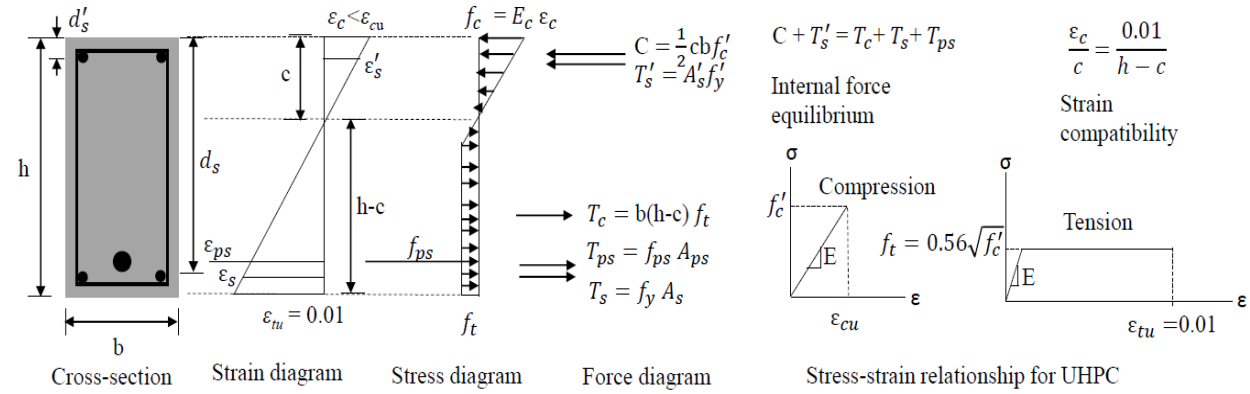

b)

Fig. 3.14 Proposed methodology for the flexural design of UHPC beams post-tensioned with unbonded tendons: a) Concrete compression-controlled failure, b) Fiber tension-controlled failure

The assumption that the considered member is indeed a concrete compression-controlled member is verified by using Eq. 3.17, which uses the ultimate compressive strain, ε_{cu}, as the anchor point in the strain diagram and provides the opportunity to check whether the tensile strain, ε_t, is smaller than the ultimate tensile strain ε_{tu}, which could be assumed to be equal to 0.01 based on the study conducted by Haber et al. (2018), but can also take other values depending on the amount of fibers used.

$$C + T_S' = T_C + T_{PS} + T_S \quad \text{Eq. 3.15}$$

$$\frac{1}{2}cbf_c' + A_S'f_y' = b(h-c)f_t + f_{ps}A_{ps} + f_yA_s \quad \text{Eq. 3.16}$$

$$\frac{\varepsilon_{cu}}{c} = \frac{\varepsilon_t}{h-c} \quad , \varepsilon_t \leq 0.01 \quad \text{Eq. 3.17}$$

$$M_n = \frac{1}{2}cbf_c'\left(h - \frac{c}{3}\right) + A_S'f_y'(h - d_s') - b(h-c)f_t\left(\frac{h-c}{2}\right) - f_{ps}A_{ps}(h - d_p) - f_yA_s(h - d_s) \quad \text{Eq. 3.18}$$

The procedure for determining the nominal moment capacity of a UHPC beam post-tensioned with unbonded tendons can be summarized below in its iterative form:

Step 1: Estimate *c*

Step 2: Use Eq. 3.10 to determine L_p

Step 3: Choose a value for ε_{cu} based on the class of UHPC material used

Step 4: Use Eq. 3.11 to determine $\Delta\varepsilon_{ps}$

Step 5: Use Eq. 3.14 to determine ε_{ps}

Step 6: Use Eq. 3.6 to determine f_{ps}

Step 7: Use strain compatibility and the assumed constitutive relationships for constructing strain and stress diagrams

Step 8: Use Eq. 3.15 and 3.16 to check for internal equilibrium

Step 9: If internal equilibrium is reached then proceed to Step 10. If not, return to Step 1.

Step 10: Calculate the nominal moment capacity of the beam using Eq. 3.18

3.4.3.3 *Fiber Tension-Controlled Failure*

The procedure for calculating the nominal moment capacity of UHPC beams post-tensioned with unbonded tendons whose failure mode is characterized as a fiber tension-controlled failure is similar to that of concrete compression controlled members except that the anchor point

in the strain diagram for calculating curvature is now the ultimate tensile strain for UHPC, ε_{tu}, and Eq. 3.8 and 3.9 are replaced with Eq. 3.19 and 3.20. Eq. 3.20 supports the direct proportionality of the ultimate tensile strain, ε_{tu}, on the change in strand stress at ultimate, Δf_{ps}, observed during the sensitivity analysis. The change in strand strain at ultimate, $\Delta\varepsilon_{ps}$, plastic hinge length, L_p, ultimate strand stress, f_{ps}, the depth to the neutral axis, c, and nominal moment capacity, M_n, are calculated using the same procedure described above for concrete compression-controlled members. The assumption that the member in question is a fiber tension controlled member is verified using Eq. 3.21, where the ultimate tensile strain is taken equal to 0.01 or any other assumed value, depending on the amount of fibers included in the concrete mix, and the computed concrete compressive strain is limited to the ratio f'_c / E_c. The strain, stress, and force diagrams as well as the equations of equilibrium and assumed stress-strain curves for a fiber tension controlled UHPC beam post-tensioned with unboned tendons are shown in Fig. 3.14b.Example can be seen in Appendix A.

$$\theta_p = \int_0^{L_{pr}} \varphi(x)dx = L_p\,\varphi_u = L_p\,\frac{\varepsilon_t}{h-c} \text{ where } \varepsilon_t = 0.01 \qquad \text{Eq. 3.19}$$

$$\Delta\varepsilon_{ps}^{o} = \frac{(d_p - c)}{L}\,L_p\,\frac{\varepsilon_t}{h-c} \qquad \text{Eq. 3.20}$$

$$\frac{\varepsilon_c}{c} = \frac{\varepsilon_t}{h-c} \quad where\ \varepsilon_t = 0.01, and\ \varepsilon_c < \varepsilon_{cu} \qquad \text{Eq. 3.21}$$

3.4.4 Comparison of Predicted and Computed Results

The results obtained from the validated numerical analyses were compared with those obtained using the proposed flexural design methodology for calculating the change in strand stress at ultimate, Δf_{ps}, the strand stress at ultimate, f_{ps}, and nominal moment capacity, M_n. As stated earlier, when evaluating prediction equations for f_{ps} for unbonded tendons, it would be prudent to assess the increment of stress beyond effective prestress, that is, $\Delta f_{ps}=f_{ps}-f_{pe}$, because the reference

stress for all equations is the same, that is, f_{pe}. Since Δf_{ps} is relatively small compared to f_{pe} one can be misled by the accuracy of a given equation simply by checking the accuracy of its predicted value of f_{ps} (Naaman 2012).

Numerical results were not compared with existing equations for predicting strand stress at ultimate in normal strength concrete beams with unbonded tendons because these equations were developed for normal strength concrete beams, whose behavior is significantly different than that of post-tensioned UHPC beams.

The numerical study described above resulted in a total of 221 nonlinear analyses. For each case Δf_{ps}, f_{ps}, and M_n obtained from the numerical models were compared with those obtained from the proposed flexural design methodology. The comparison was conducted using a variety of statistical indicators such as the minimum, maximum, and average ratio between computed and calculated values, standard deviation, coefficient of variation, and correlation coefficient. Table 3.13 and Fig. 3.15 summarize and illustrate the results of such a comparison.

The minimum and maximum ratio between predicted and computed Δf_{ps} is 0.75 and 1.66, respectively, average ratio is 1.03, the standard deviation is 0.13, the coefficient of variation is 12.6%, and the correlation coefficient is 0.93. These statistics indicate that despite the fact the change in strand stress at ultimate is small, the proposed methodology is able to capture with good accuracy this change.

When one examines the differences between predicted and computed f_{ps}, it becomes evident that these differences are very small. The minimum and maximum ratios between predicted and computed f_{ps} are 0.97 and 1.10, respectively, average ratio is 1.01, the standard deviation is 0.02, the coefficient of variation is 1.9%, and the correlation coefficient is 0.91.

Table 3.13. Comparison of predicted and computed Δf_{ps}, f_{ps}, M_n

Number of cases	Ratio	Statistical indicators					
		Min.	Max.	Avg.	Std. Dev.	COV %	r[a]
	Shape of stress-strain curve for UHPC (Fig. 3.4 – Default Curves for Compression and Tension)						
205	$\Delta f_{ps}^{predicted} / \Delta f_{ps}^{FEA}$	0.75	1.66	1.03	0.129	12.6	0.93
	$f_{ps}^{predicted} / f_{ps}^{FEA}$	0.97	1.10	1.01	0.019	1.9	0.91
	$M^{predicted} / M^{FEA}$	0.95	1.10	1.02	0.031	3.0	1.00
	Shape of stress-strain curve for UHPC (Fig. 3.4 – Other Curves for Compression)						
4	$\Delta f_{ps}^{predicted} / \Delta f_{ps}^{FEA}$	0.81	1.19	0.99	0.168	16.9	0.99
	$f_{ps}^{predicted} / f_{ps}^{FEA}$	0.97	1.01	1.0	0.029	2.9	0.99
	$M^{predicted} / M^{FEA}$	1.02	1.05	1.03	0.014	1.4	1.00
	Shape of stress-strain curve for UHPC (Fig. 3.4 – Other Curves for Tension)						
12	$\Delta f_{ps}^{predicted} / \Delta f_{ps}^{FEA}$	0.89	1.33	1.05	0.119	11.4	0.72
	$f_{ps}^{predicted} / f_{ps}^{FEA}$	0.99	1.02	1.01	0.017	1.7	0.72
	$M^{predicted} / M^{FEA}$	1.00	1.04	1.02	0.011	1.1	0.98

[a]r = correlation coefficient (f_{ps} in MPa, M in kN-m)

The differences between predicted and computed M_n are also very small. The minimum and maximum ratios between predicted and computed nominal moment capacity are 0.95 and 1.10, respectively, average ratio is 1.02, standard deviation is 0.03, the coefficient of variation is 3.0%, and the correlation coefficient is 1.0.

These results suggest that the proposed flexural design methodology for UHPC beams post-tensioned with unbonded strands is rather accurate, in terms of predicting the change in strand stress at ultimate, Δf_{ps}, the strand stress at ultimate, f_{ps}, and nominal moment capacity, M_n. In addition, the proposed methodology is general in the sense that it captures the influence of all relevant parameters on the change in strand stress at ultimate and consequently on the flexural capacity of post-tensioned UHPC beams. The proposed methodology accounts for various beam

cross-sectional shapes, various amounts and configurations of tendons, various amounts of mild steel, various loading configurations, patterned loading, simply supported and continuous configurations, and various classes of UHPC by directly capturing the influence of key parameters in the assumed stress-strain curve on the change in strand stress at ultimate. The influence of the most relevant parameters on the change in strand stress at ultimate such as loading configuration, patterned loading, effective tendon depth, d_p, span to effective depth ratio, L/d_p, and maximum usable UHPC tensile or compressive strain are included directly in the formulation of the proposed equations for determining Δf_{ps}. The influence of the rest of the parameters is captured by the equations of equilibrium through the calculation of the depth to the neutral axis, c.

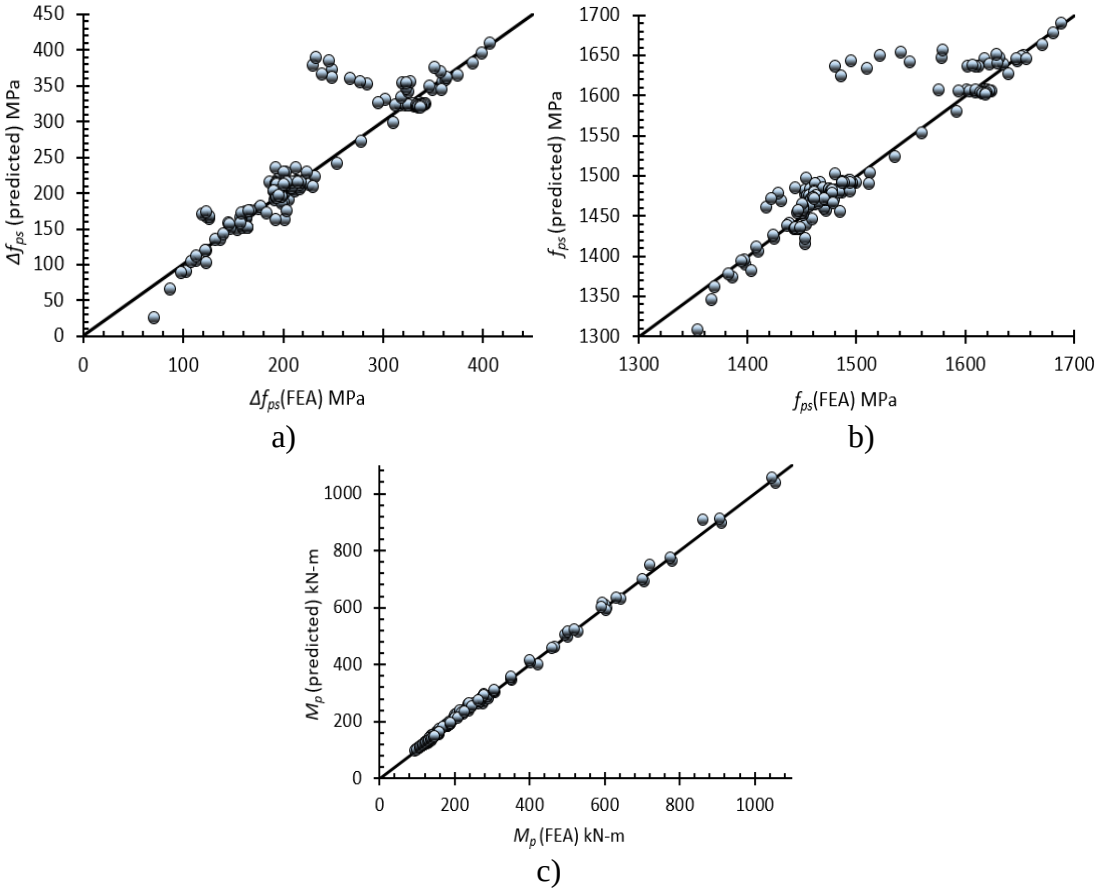

Fig. 3.15. Comparison of computed and predicted a) change in strand stress at ultimate limit state, b) strand stress at ultimate limit state, and c) nominal moment capacity of the member

3.4.5 Evaluation of the Proposed Methodology for Various Classes of UHPC Materials

The proposed methodology was evaluated for a variety of UHPC class materials that may feature stress-strain relationships in compression and in tension that are different from the default compression and tension stress-strain curves used in the majority of simulations (Fig. 3.4a). The additional stress-strain curves in compression and tension that were considered as part of this evaluation are illustrated in Fig. 3.4a. The stress-strain curves in compression feature various shapes and slopes for the descending branches and those in tension feature various strain hardening characteristics. A total of four additional stress-strain curves in compression and twelve additional stress-strain curves in tension were considered provided that in most cases the failure mode of the specimens was determined to be a tension-controlled failure. The four additional cases for the stress-strain curve in compression featured two unique descending branches each of which was used in the analyses of two beams each featuring a unique tendon area. The twelve additional cases for the stress-strain curve in tension featured twelve unique multilinear inelastic stress-strain relationships. The beams used for these additional investigations are 152 mm wide, 305 mm deep, and are subject to two point loads at a distance of *L/3* from the supports. The beams featured 2-13 mm diameter strands and a d_p of 254 mm. The span length of the beam is 8534 mm and the specified compressive strength of UHPC is 152 MPa.

For UHPC classes whose material behavior could be characterized by the default stress-strain curves in compression and tension the nominal moment capacity corresponds with the maximum usable tensile or compressive strain defined in Fig. 3.5a. As a result, for these cases the anchor point in the strain diagram is either the maximum usable tensile strain or maximum usable compressive strain depending on whether the failure mode is tension controlled or compression controlled.

However, for cases that feature other shapes of stress-strain curves such as those shown in Fig. 3.4a, the determination of the anchor point in the strain diagram requires an iterative procedure because the maximum moment capacity of a given beam section does not necessarily correspond with the maximum usable tensile or compressive strain in the most extreme fibers. This is due to the fact that as concrete fibers are strained into the inelastic region as the load increases the volume of the stress block increases, however, its centroid shifts towards the neutral axis thus reducing the moment arm. The strain that corresponds with the maximum moment capacity will be a value between the strain that corresponds with the peak compressive or tensile stress and the maximum usable tensile or compressive strain. It is therefore recommended that an iterative procedure is followed to determine the maximum moment capacity for UHPC classes that exhibit stress-strain relations that are different from the default curves in compression and tension.

Once the anchor point in the strain diagram was determined, cross-sectional stresses in concrete were calculated using the corresponding stress-strain curves for each class of UHPC. Then, the change in strand stress at ultimate, the total strand stress at ultimate, as well as the nominal moment capacity were determined using the proposed methodology and were compared with values obtained from numerical models. The results of this comparison are shown in Table 3.13.

The average ratios of predicted over computed changes in strand stress, total strand stress at ultimate, and nominal moment capacity for the four additional cases in compression are 0.99, 1.0, and 1.03, respectively. The corresponding COV are 16.9%, 2.9%, and 1.4%. Similarly, the average ratios of predicted over computed changes in strand stress, total strand stress at ultimate, and nominal moment capacity for the twelve additional cases in tension are 1.05, 1.01, and 1.02. The corresponding COV are 11.4%, 1.7%, and 1.1%. These results suggest that the proposed

prediction methodology can predict with good accuracy the change in strand stress, total strand stress at ultimate, and the nominal moment capacity for a variety of classes of UHPC.

3.5 SUMMARY AND CONCLUSIONS

A framework for predicting the flexural behavior of UHPC beams post-tensioned with unbonded tendons is proposed. A mechanics based phenomenological model is presented to predict flexural capacity, and a set of equations is proposed to predict the change in strand stress at the ultimate limit state, Δf_{ps}. The flexural design methodology is presented in terms of the failure mode observed when the considered specimens reach their ultimate load carrying capacity. The failure mode is characterized as either a fiber tension-controlled failure, or a concrete compression controlled failure. Nonlinear numerical simulations based on validated submodels are used to investigate the behavior of 221 post-tensioned UHPC beams from the onset of loading to failure. A sensitivity analysis is conducted to understand the influence of concrete compressive strength, area of tendons, effective depth of tendons, continuity, loading configuration, loading pattern, area of mild steel, maximum usable UHPC tensile strain and cracking stress, and friction coefficient on the strand stress at ultimate. The considered beams feature rectangular as well as T cross-sections in simply supported as well as continuous configurations.

The following conclusions are drawn:

1) The proposed flexural design methodology is general and provides numerous advantages: a) it accounts for simple span and continuous members featuring various loading configurations and loading patterns, b) it accounts for rectangular and T-section behavior, c) it captures the influence of key parameters such as beam cross-sectional dimensions, effective depth of tendons and span over effective depth ratio, area of tendons and mild steel, and different classes of UHPC exhibiting various compressive and tensile properties.

2) The proposed methodology results in rather accurate predictions of the change in strand stress at ultimate, Δf_{ps}, the strand stress at ultimate, f_{ps}, and nominal moment capacity, M_n, of post-tensioned UHPC beams featuring average predicted values that are within 5% of computed ones and coefficients of variation no greater than 17%.
3) The majority of investigated beams exhibited a fiber tension-controlled failure. The only exceptions were continuous T-beams and heavily post-tensioned beams, which exhibited UHPC compression-controlled failures.
4) Loading configuration, patterned loading, effective depth, span to effective depth ratio, and maximum usable UHPC compressive and tensile strains, had a strong influence on the magnitude of the change in strand stress at ultimate and therefore were directly included in the calculation of Δf_{ps}.
5) The influence of specified UHPC compressive strength, tendon area, mild steel area, UHPC cracking stress, and continuity on Δf_{ps} was considered small enough to allow the equations of equilibrium capture their effect through the calculation of the depth to the neutral axis.

3.6 RECOMMENDATIONS FOR FUTURE WORK

Although the modeling protocol used to generate the database of UHPC beams post-tensioned with unbonded strands was based on two validated submodels and is believed to simulate the behavior of such beams rather accurately, experimental testing of post-tensioned UHPC beams is recommended to increase fidelity in the proposed flexural design methodology and proposed equations for strand stress at ultimate. Future experimental work can be informed by the conclusions drawn from this study in terms of: 1) locating strain, displacement, and load sensors at key locations to validate the two types of failure modes discussed in this paper, 2) confirming the influence of the parameters identified as the ones with the greatest impact on $\Delta \varepsilon_{ps}$, and 3)

confirming the accuracy of the proposed equations for predicting the change in strand strain at the ultimate limit state.

4. Chapter 4 : Moment-Curvature-Deformation Response of UHPC Beams Post-tensioned with Internal Unbonded Tendons: Analysis and Algorithm

4.1 Introduction

Post-tensioned concrete flexural members have the ability to offer enhanced rentable space, architectural freedom, and adaptable structures by offering floor systems that feature very few columns. This characteristic has been well explored in the construction industry and post-tensioned concrete floors with unbonded tendons are the system of choice in many midrise and high-rise building structures. The ability to offer slender structures in general and slender floor systems in particular can be further enhanced if the post-tensioned (PT) flexural member is constructed with ultra-high performance concrete (UHPC), which in addition to its high compressive strength also offers considerable tensile strength. According to Annex 8.1 of Canadian Standards Association (2019) S6 Fibre Reinforced Concrete (FRC), ultra-high performance fiber reinforced concrete (UHPFRC), herein referred to as UHPC, is defined as a discrete fiber reinforced cementitious composite material with enhanced compressive strength and durability compared to high performance concretes with a minimum compressive strength of 120 MPa. According to the Federal Highway Administration (FHWA)(Russel and Graybeal 2013), “UHPC-class materials are cementitious based composite materials with discontinuous fiber reinforcement, compressive strengths above 150 Mpa, tensile strengths above 5 Mpa, and enhanced durability via their discontinuous pore structure”. In this study the FHWA (Russel and Graybeal 2013) definition for UHPC is adopted, although the variability of key parameters in the constitutive model are considered to evaluate their impact on post-tensioned member behavior.

Typical post-tensioned concrete floor systems feature flat plates in midrise and high-rise building structures, or post-tensioned beams and one-way slabs in parking garages. Flat plates, beams, and one-way slabs are structural members whose behavior and failure are in many cases

dominated by flexure. While the flexural behavior of post-tensioned concrete members constructed with normal and high strength concrete has been investigated extensively, to the author's knowledge the complete response of UHPC flexural members post-tensioned with internal unbonded tendons to gravity induced loading appears to be unexamined.

The determination of the complete flexural response of a PT member is related to the determination of unbonded strand stress at various stages of loading. Various approaches have been used to determine this stress and consequently the complete flexural response for normal strength concrete (NSC) members. Some (Balaguru 1981, Naaman and Alkhairi 1991, Harajli and Kanj 1992, Pannell 1969, Tam and Pannell 1976, Au and Du 2004, Harajli 2006, Harajli 1990, Lee et al. 1999, Harajli et al. 2002, van Weerdhuizen and Bartlett 2020, Au et al. 2005, Vega and Dotreppe 1988) include the determination of strand stress at discrete points and limited ranges such as ultimate limit state and service, respectively, whereas others (Alkhairi and Naaman 1993, Knight et al. 2014, Ariyawardena and Ghali 2002, Ozkul et al. 2008, Vu et al. 2010, Kim et al. 2012) provide guidance for how to obtain the complete flexural response.

Balaguru (1981) proposed a methodology to predict strand stress at service and ultimate level loads for NSC beams post-tensioned with unbonded tendons. Change in strand strain at service was empirically expressed as a function of span-eccentricity and eccentricity-maximum deflection ratio. To obtain the change in strand stress at the ultimate limit state, a maximum deflection at ultimate is assumed based on what would be acceptable for this stage, and the attainability of this deflection is checked using the rotation capacity of the beam. Naaman and Alkhairi (1991) proposed a simplified methodology to predict the stress in unbonded tendons in NSC beams under service and ultimate loading conditions by employing empirically obtained bond reduction coefficients, which facilitate the use of solutions based on strain compatibility

while accounting for the lack of bond. This approach is attractive from a design perspective, since it addresses critical loading stages for a member, such as behavior both at service and at ultimate limit state. The concept of using a coefficient to account for the relative slip between concrete and tendons was also used by Harajli and Khanj (1992). Other researchers (Naaman and Alkhairi 1991, Pannell 1969, Tam and Pannell 1976, Au and Du 2004, Harajli 2006, Harajli 1990, Lee et al. 1999, Harajli et al. 2002) developed empirical formulations for calculating an equivalent plastic hinge length, which is attractive not only for calculating strand strain at the ultimate limit state, ε_{ps}, and consequently nominal flexural capacity, M_n, but also for calculating deflection at incipient failure, Δ_u, which has recently emerged as a warning of the failure metric (van Weerdhuizen and Bartlett 2020). Au et al. (2005) extended Pannell (1969) approach to investigate cracked PT NSC beam behavior under service loads. Vega and Dotreppe (1988) investigated the moment-curvature response of NSC beams prestressed with unbonded tendons at service and ultimate level loads using linear elastic beam flexure theory and an assumption for the plastic hinge length, respectively.

These studies dealt primarily with understanding the behavior of NSC beams post-tensioned with unbonded tendons under service and ultimate level loads. While these two stages of loading are of great importance to practicing engineers from the perspective of being able to calculate deflections at service and flexural capacities at the ultimate limit state, they provide limited insight about cross-section and member level ductility, the calculation of which is better informed by the availability of the full moment-curvature-deformation response. Additionally, as performance based design transitions from being an exception to becoming a norm in structural design, approaches that provide the means to obtain the full response of the structural members under loading will be needed. Alkhairi and Naaman (1993) and Knight et al. (2014) used

mechanics based approaches to address analytically the complete range of behavior of NSC beams post-tensioned with unbonded tendons thus addressing this need for NSC members. Similarly, Ariyawardena and Ghali (2002) developed a computer model to predict the complete response of PT NSC members. In this method of analysis the PT element is modeled as an assemblage of plane frame members connected at nodes. Ozkul et al. (2008) proposed a methodology, which considers the beam and tendon as a trussed beam system that allows for the use of equilibrium and compatibility equations as well as the law of conservation of energy to predict behavior at various load levels. Vu et al. (2010) proposed a model that allows the calculation of the structural response of PT NSC beams including deflections under service loading, before and after cracking, as well as at the ultimate limit state. The model uses a non-linear beam macro finite element, which is characterized mainly by its homogenous average moment of inertia (Vu et al. 2010). Kim and Lee (2012) developed an algorithm for predicting the load deformation response of continuous PT NSC members including the ability to capture moment redistribution.

While the need to predict the complete flexural response of PT NSC members has been met, there is currently no efficient tool to predict the complete response of PT UHPC members whose behavior is significantly different from that of their NSC counterparts. For example, the studies mentioned above are based on the assumption that concrete is a material that resists primarily compression forces after cracking and flexural capacity is achieved when concrete ultimately crushes in compression. These assumptions do not reflect the behavior of UHPC as a material, which has unique compressive and tensile domains and do not represent the flexural failure mode of PT UHPC members, which has been reported to be controlled by the pulling of fibers before the crushing of concrete (Dogu and Menkulasi 2020). As a result, the tensile domain of UHPC plays an important role in dictating the failure mode of such members.

Dogu and Menkulasi (2020) recently presented a flexural design methodology for UHPC beams post-tensioned with internal unbonded tendons. However, the goal of the study was limited to offering an approach for predicting the ultimate flexural capacity of such members, which is of interest for collapse prevention but does not provide insight in terms of their complete flexural response from the onset of loading to failure. Nonlinear finite element analysis can be used to obtain the complete flexural response of PT UHPC beams, however, the creation and analysis of reliable models even for simple beams requires considerable computational time.

The goal of the research provided in this paper is to present an efficient analytical method for obtaining the complete moment-curvature-deformation response of UHPC beams post-tensioned with internal unbonded tendons by taking into consideration the nonlinear domain of UHPC in tension and how this nonlinear domain affects the behavior of these beams throughout the entire range of loading. The proposed methodology is presented in the form of an algorithm, which can be implemented in any mathematical software with programming capabilities such as Mathcad and Matlab. The proposed method offers the users an efficient tool to obtain the complete flexural response of such members including deflection at incipient failure and offers insight about their ductility at the cross-section and member level. The proposed method does not require the definition of empirically obtained elastic and inelastic design parameters such as bond reduction coefficients and plastic hinge length. However, it can facilitate the use of approaches that employ these parameters by helping formulate them without having to rely on extensive experimental testing or time-consuming finite element analysis. The scope is limited to simply supported PT UHPC beams with a rectangular cross-section that feature straight and draped tendons as well as various loading configurations, reinforcement ratios and material properties.

4.2 Definition of Cross-sectional and Member Level Ductility

A typical moment-curvature-deformation relationship for an UHPC beam post-tensioned with internal unbonded tendons obtained using the proposed approach is provided in Fig. 4.1 and is characterized by four distinct phenomena. The application of prestress, the cracking of concrete, the yielding of reinforcement, and the attainment of ultimate moment capacity.

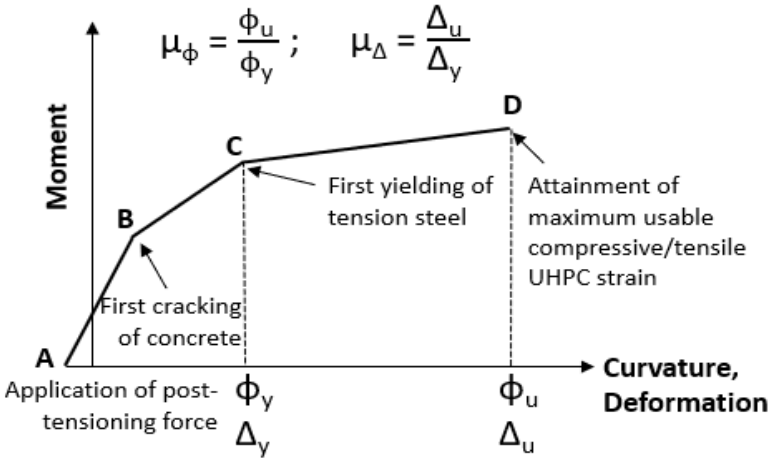

Fig. 4.1 Qualitative illustration of moment-curvature-deformation response for a typical UHPC beam post-tensioned with internal unbonded tendons

In this paper, curvature ductility, μ_φ, is defined as the ratio of the curvature at the maximum calculated flexural resistance, φ_u, over the curvature at the flexural resistance corresponding to yielding of the reinforcement in the tension zone, φ_y. This definition is consistent with that provided in Annex 8.1 of Canadian Standards Association (CSA) S6 Fibre Reinforced Concrete (2019), which requires a minimum curvature ductility ratio μ_{min} of 2.0 for members designed for the applied moments under an elastic analysis without any force redistribution. ACI 318-19 (2019) and AASHTO LRFD Bridge Design Specifications (2017) uses a strain based definition for cross-section level ductility of prestressed and nonprestressed concreted members constructed with NSC. A tension-controlled section is defined as a cross section in which the net tensile strain, ε_t, in the

extreme tension steel at nominal strength is greater than or equal to ε_{ty} + 0.003, where ε_{ty} is equal to 0.002 for all prestressed reinforcement and Grade 60 deformed reinforcement. This definition for ε_{ty} is used to determine the curvature corresponding to yielding of the reinforcement in the tension zone, φ_y. The net tensile strain, ε_t, is the tensile strain calculated in the extreme tension reinforcement at nominal strength exclusive of strains due to prestress, creep, shrinkage, and temperature (ACI 318-19 2019). If the limiting strain at the ultimate limit state for a tension-controlled member (0.005) is divided with the strain at first yield (0.002), a strain-based cross-section level ductility of 2.5 is obtained, which is slightly higher than the curvature based ductility of 2.0 specified in Canadian standard (2019) for fiber reinforced concrete (FRC). Both, the curvature-based definition provided in the Canadian standard (2019) for FRC and the strain-based definition provided in ACI 318-19 (2019) and AASHTO LRFD Specifications (2017) for NSC are used to quantify cross-section level ductility for UHPC beams post-tensioned with internal unbonded tendons.

In this paper, member level ductility is expressed using two metrics. The first is the ratio of displacement when the beam reaches its maximum load carrying capacity, Δ_u, over the displacement corresponding to yielding of the reinforcement in the tension zone, Δ_y. The second is the ratio of span length, L, over deflection at incipient failure, Δ_u (i.e. when the beam reaches its maximum load carrying capacity). It has been recently (van Weerdhuizen and Bartlett 2020) argued that deflection at incipient failure is a meaningful warning of the failure metric because such deflections provide visible indications that the condition of the member could soon become dangerous. There are currently no requirements for member level ductility for prestressed or nonprestressed members as it is typically assumed that ductility at the cross-sectional level will translate to ductility at the member level for flexural dominated failures provided that detailing

requirements in the applicable codes and standards are followed. The proposed algorithm for computing the moment-curvature-deformation response of PT UHPC beams is used to evaluate ductility at the cross-section and member level, and to provide insight about the complete flexural behavior of PT UHPC members.

4.3 Procedure for Computing Moment Curvature and Load Displacement Relationship

The rectangular UHPC beam shown in Fig. 4.2 was taken as a prototype to develop the proposed procedure for obtaining the complete moment-curvature-deformation response of a simply supported UHPC beam post-tensioned with internal unbonded tendons. This UHPC beam contains bonded compression and tension mild steel, A'_s and A_s, respectively, and unbonded post-tensioning tendons, A_{ps}.

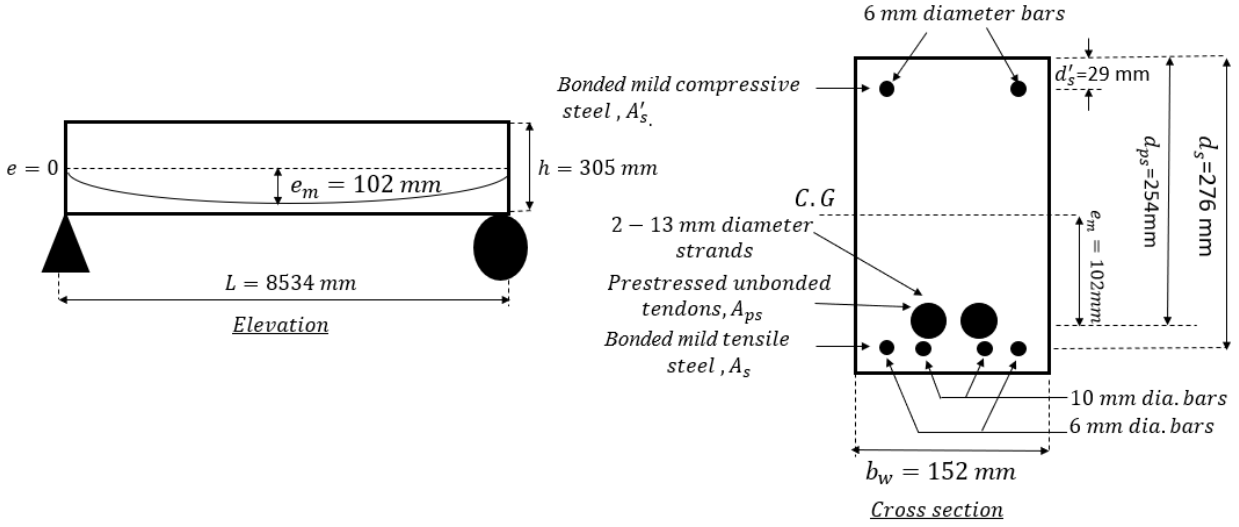

Fig. 4.2 Typical post-tensioned UHPC beam detail considered in moment-curvature and load-deformation response analysis

The proposed procedure includes analysis conducted at the member level as well as at the cross-section level. Member level analysis is required due to the lack of bond between the tendons and the surrounding concrete, which does not allow the application of a cross-section level analysis based on strain compatibility. Therefore, compatibility is enforced at the member level by equating

the total change in length in the concrete fiber at the centroid of the tendons to the total change in tendon length. This member level condition of compatibility is enforced before the beam cracks as well as after the beam cracks.

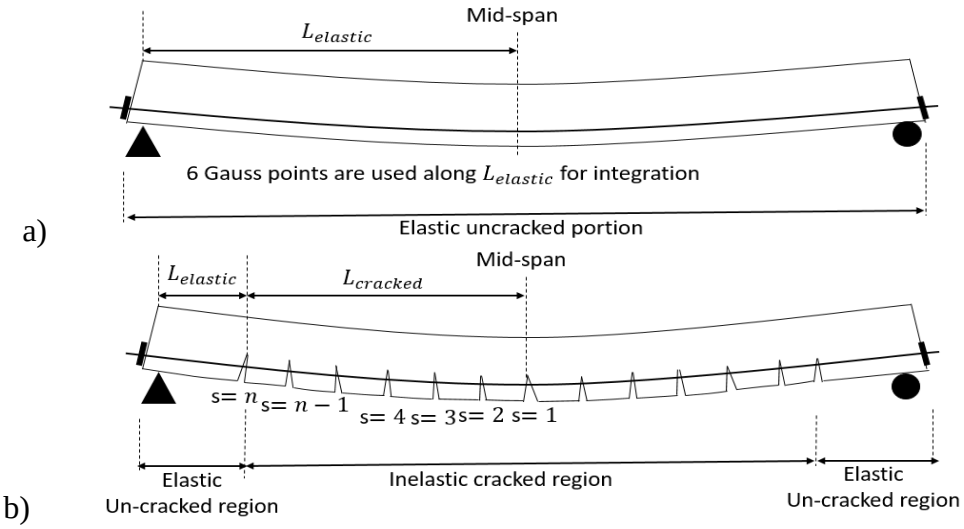

Fig. 4.3 Deformed a) uncracked and b) cracked configuration for a simply supported UHPC beam post-tensioned with internal unbonded tendons

The proposed procedure covers pre- and post-cracking behavior. Naturally, a cracked beam will have portions that have cracked as well as portions that have not cracked. The challenge in this case is to demarcate the cracked and uncracked regions so that the appropriate analysis approach can be followed in each case. This demarcation involves the determination of the point along the length of the member where the applied moment, $M_{applied}$, exceeds the cracking moment, $M_{cracking}$. This is a straightforward task when the tendon is straight, however, for draped configurations; it requires an iterative procedure because the location of the cracking moment depends on the effective depth as well as the applied loading configuration. Additionally, the demarcation between cracked and uncracked regions will shift as the applied moment intensity increases. After cracking, it is assumed that multiple cracks will form along the length of the member due to the presence of fibers and bonded mild reinforcement. The assumed deformed configurations for the uncracked and cracked beams are shown in Fig. 4.3a and 4.3b, respectively.

The assumed stress-strain relationships for all materials are shown in Fig. 4.4. These material constitutive models are important as they influence the flexural failure mode of the investigated beams. For example, Dogu and Menkulasi (2020) report that the failure mode of most UHPC beams post-tensioned with internal unbonded tendons is a tension-controlled failure in which the maximum usable tensile strain in UHPC, ε_{tu}, is attained before concrete crushes in compression or mild and prestressing steel fracture in tension. Therefore, a proper characterization of the tensile domain of UHPC is of outmost importance as it influences the failure mode of post-tensioned UHPC members.

This study considers UHPC formulations that exhibit an elasto-plastic (i.e. bilinear) tensile behavior as well as those that exhibit a trilinear (i.e. strain hardening followed by strain softening) behavior (Fig. 4.4a right). A total of three constitutive models are considered for the compression domain and a total of 13 for the tensile domain. The default compressive and tensile stress-strain curves are indicated in Fig. 4.4a. These curves are used in the majority of the parametric analysis, although the impact of other constitutive models on the complete flexural behavior of UHPC beams post-tensioned with internal unbonded tendons are considered. The validation of the constitutive model for the ascending branch of the compressive domain is provided by Graybeal (2017). Case 1 and 2 in the compressive domain differ from the default curve by exhibiting more gradual descending branches. In Case 1, the descending branch features a bilinear curve, which exhibits a stress of $0.5f'_c$ when the strain is equal to 0.006. In Case 2, the descending branch extends from the point when the peak stress is achieved to a point with strain and stress equal to $\varepsilon_{tu} = 0.01$ and $0.05f'_c$, respectively.

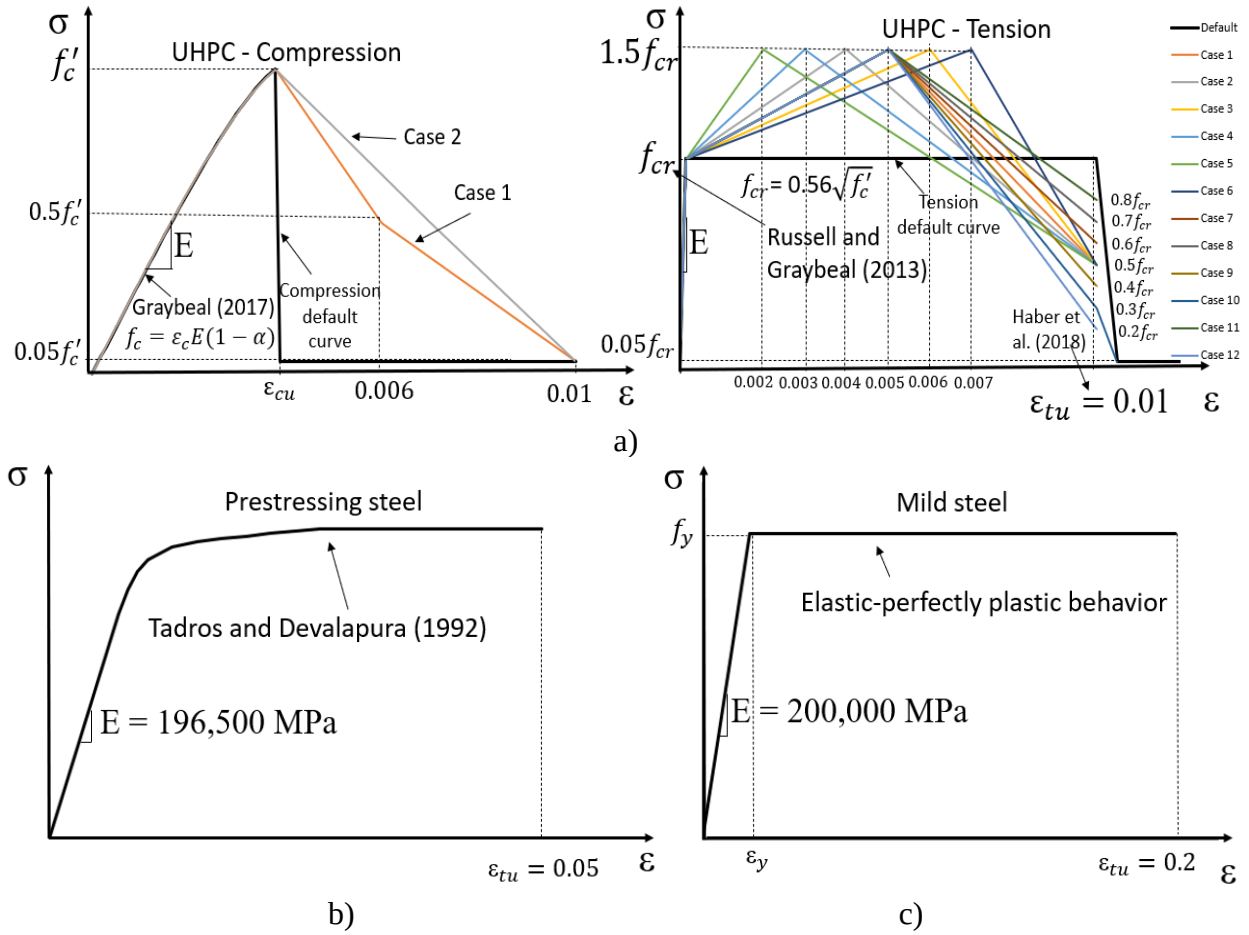

Fig. 4.4 Stress-strain relationship for: a) UHPC in compression (left) and tension (right), b) prestressing steel, and c) mild steel

The validation for the bilinear and trilinear models in the tensile domain is shown in Fig. 4.5a and 4.5b, respectively. The cracking stress is taken equal to $0.56\sqrt{f_c'}$ based on recommendations by Russell and Graybeal (2013). The maximum usable tensile strain ε_{tu} is limited to 0.01 based on test data provided by Haber et al. (2018). As can be seen, both the bilinear model and trilinear model provide rather accurate idealizations of the stress-strain behavior of UHPC in tension depending on which UHPC formulation is selected. Case 1-12 in the tensile domain differ from the default curve by exhibiting a strain hardening behavior after the first crack followed by a descending branch after the attainment of the peak tensile stress. To contain the scope of analysis, the peak tensile strength was taken equal to $1.5f_{cr}$ and the strain at which this

stress is achieved was varied to create a variety of constitutive models. The descending branches for Case 1-6 was determined such that the stress that corresponds to a strain of ε_{tu}= 0.01 is 0.5f_{cr}. For cases 7-12 the strain that corresponds with the peak stress was fixed at 0.005 and the stress that corresponds with ε_{tu}= 0.01 was varied from 0.2f_{cr} to 0.8f_{cr}.

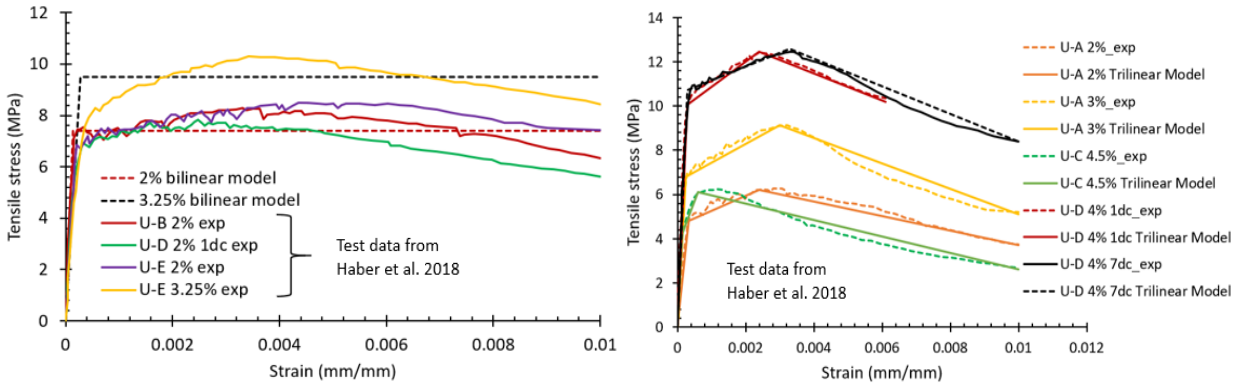

a) b)

Fig. 4.5 Validation of: a) bilinear model, and b) trilinear model for the tensile domain of UHPC

Several controls are introduced in the proposed procedure to distinguish beams that exhibit a fiber tension-controlled failure from those that exhibit a UHPC compression failure so that the appropriate procedure is used in each case. Long term losses are not considered because it is assumed that the designer has a methodology available to estimate short term and long-term losses. Guidance on how to estimate losses in pretensioned UHPC beams is provided by Graybeal (2006) and John et al. (2011). The goal of the proposed methodology is to provide guidance for how to calculate the change in strand strain $\Delta\varepsilon_{ps}$ so that this change in strand strain can be added to the effective prestrain ε_{pe} to calculate the total strand strain ε_{ps} and consequently the force in the tendons, F_{tendon}, internal moment, M_n, cross-sectional curvature, φ, total load, and mid-span displacements. In the proposed prediction methodology, the effective prestress, f_{pe}, is an input and can therefore take any value. The determination of long-term deformation, which is typically addressed using multiplier-based methods or more advanced incremental time step analysis (ACI 435R 2003), is outside the scope of work for this study.

The proposed methodology provides a tunable framework for accommodating UHPC formulations, prestressing strands, and bonded reinforcement whose behavior can be characterized using the relationships shown in Fig. 4.4. The following two sections provide a step-by-step explanation of the proposed procedure before and after cracking when the default compression and tension stress-strain curves for UHPC are used.

4.3.1 Before Cracking

The flowchart for obtaining the moment curvature and load deformation response of an uncracked UHPC beam post-tensioned with internal unbonded tendons is provided in Fig. 4.6. Half of the beam is taken as one section (Fig. 4.3a). No further discretization or meshing is required since numerical integration using the Gaussian quadrature rule is used to account for the variation of moment along the span when calculating tendon strain, ε_{ps}, and mid-span beam displacement. A total of six Gauss points are used to conduct the numerical integration based on Gauss-Legendre coefficients provided in Table 4.1.

Table 4.1 Gauss-Legendre Coefficients (Hornbeck 1975)

Gauss Coefficient No.	W_k	μ_k
1	0.467913	0.23861918
2	0.467913	-0.23861918
3	0.360762	0.66120938
4	0.360762	-0.66120938
5	0.171324	0.93246951
6	0.171324	-0.93246951

A change in strand stress, $\Delta f_{ps,assumed}$, is initially selected and this assumed change is added to the effective prestress, f_{pe}, to calculate the total strand stress, f_{ps}, and subsequently the total force in the tendon, F_{tendon}, before cracking. Using this tendon force, the cracking moment, $M_{cracking}$, at mid-span is calculated and the magnitude of the moment at the rest of the Gauss points is computed

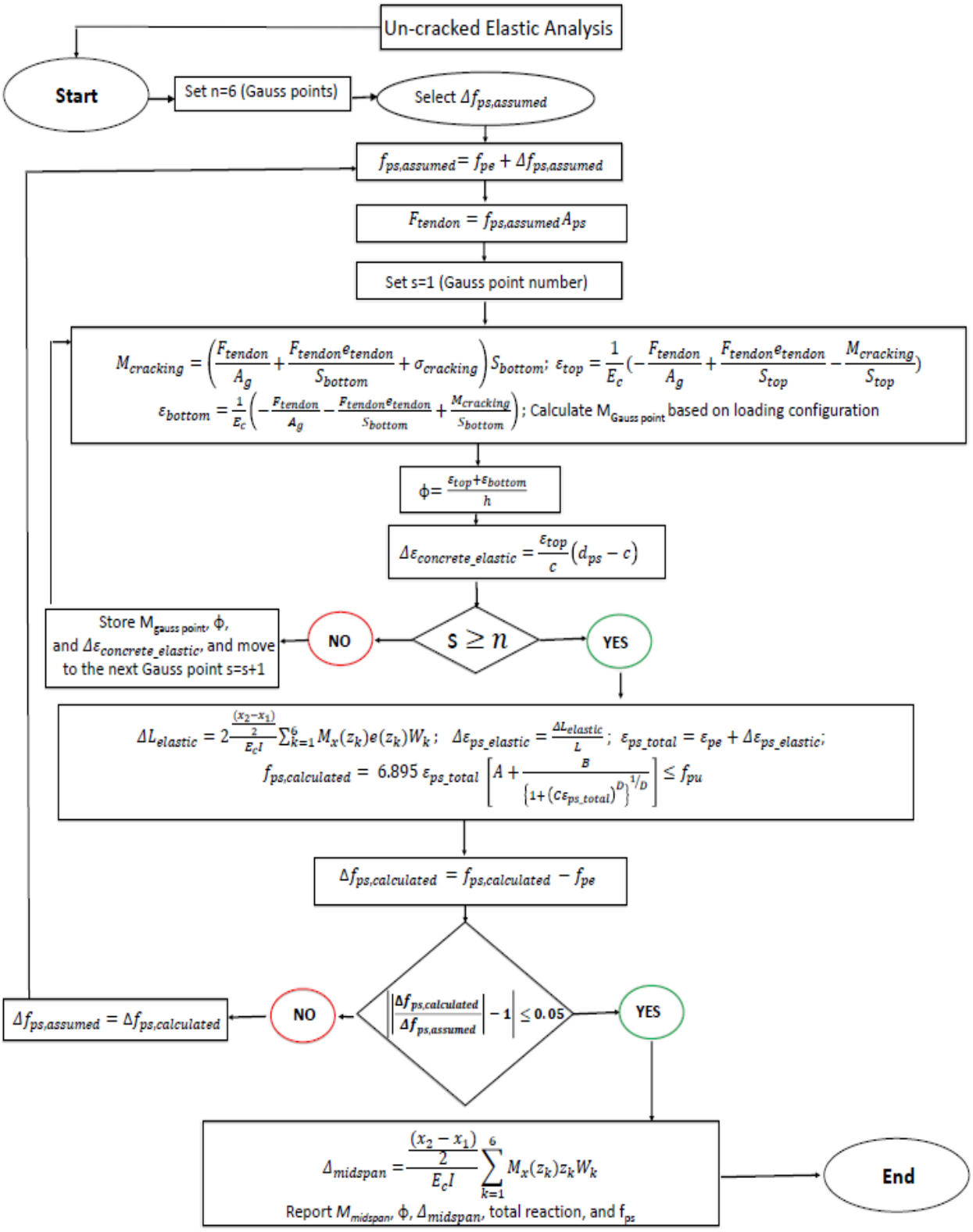

Fig. 4.6 Flowchart used to obtain moment-curvature-deformation response in an uncracked UHPC beam post-tensioned with internal unbonded tendons

by scaling the mid-span moment considering the loading configuration and its magnitude at mid-span.

For every Gauss point, starting at mid-span, the curvature, ϕ, and the strain in concrete at the centroid of tendons, $\Delta\varepsilon_{concrete\_elastic}$, is calculated for the given moment corresponding to that point. Once this procedure is conducted for all points, the strain in the concrete at the centroid of tendons is numerically integrated along the length of the beam to calculate the total change in fiber length at the centroid of tendons, $\Delta L_{elastic}$. The numerical integration is conducted using the Gauss Legendre coefficients provided in Table 4.1.

The total change in fiber length at the centroid of tendons, $\Delta L_{elastic}$, is set equal to the total change in tendon length to enforce member level deformation compatibility. This change in tendon length is then divided by the original tendon length, L, to calculate the change in tendon strain, $\Delta\varepsilon_{ps\_elastic}$. This change in tendon strain is added to the decompression strain, $\Delta\varepsilon_{decompression}$, and effective prestrain, ε_{pe}, to calculate the total strain in the strands, ε_{ps_total}. Using the stress-strain curve for prestressing strands the total strain is used to obtain the total strand stress, f_{ps}. The effective prestress, f_{pe}, is then subtracted from this total stress to determine the change in strand stress, $\Delta f_{ps,calculated}$, and to compare it to the value assumed at the beginning. If the two values match, then, moment, curvature, total load, and midspan deflection are reported, and the algorithm is terminated. Total load is calculated using the load configuration in question and the magnitude of the moment at mid-span; while mid-span deflection is calculated using the obtained curvature values at Gauss points and the second moment area theorem. If the assumed, $\Delta f_{ps,assumed}$, and calculated, $\Delta f_{ps,calculated}$, change in tendon stress do not match, the iteration continues with an assumed change in tendon stress set equal to that calculated in the previous iteration until the

assumed change in tendon stress matches with the calculated one. The step-by-step procedure including relevant equations is provided below.

Member Level Analysis

Step 1: Consider half of the beam as one section. Set $L_{elastic}=L/2$, where $L_{elastic}$ is the length of the elastic portion of the loaded member in half the span, and L is the span length.

Step 2: Assume a value for the change in strand stress, Δf_{ps}, and calculate the total strand stress $f_{ps} = f_{pe} + \Delta f_{ps}$ and total tendon force, F_{tendon}, (Eq. 4.1).

$$F_{tendon} = f_{ps}A_{ps} \quad \text{Eq. 4.1}$$

Cross-section Level Analysis (at all six Gauss points – start at mid-span)

Step 3.1: Determine the cracking moment, $M_{cracking}$, at mid-span using Eq. 4.2 where A_g is the gross area of the section, e_{tendon} is the eccentricity of the prestress tendon, S_{bottom} and S_{top} are the section moduli with respect to the bottom and top of the beam, respectively; and $\sigma_{cracking}$ (f_{cr} in Fig. 4.4a) is the cracking stress of UHPC. Eq 4.2 is considering signs. Determine the distribution of strain in the cross-section using Eq. 4.3-4.4 where ε_{top} and ε_{bottom} are the strains in the top most and bottom most fibers, respectively, and E_c is the modulus of elasticity of UHPC.

$$M_{cracking} = (\frac{F_{tendon}}{A_g} + \frac{F_{tendon}e_{tendon}}{S_{bottom}} + \sigma_{cracking})S_{bottom} \quad \text{Eq. 4.2}$$

$$\varepsilon_{top} = \frac{1}{E_c}(-\frac{F_{tendon}}{A_g} + \frac{F_{tendon}e_{tendon}}{S_{top}} - \frac{M_{cracking}}{S_{top}}) \quad \text{Eq. 4.3}$$

$$\varepsilon_{bottom} = \frac{1}{E_c}(-\frac{F_{tendon}}{A_g} - \frac{F_{tendon}e_{tendon}}{S_{bottom}} + \frac{M_{cracking}}{S_{bottom}}), \quad \text{Eq. 4.4}$$

Step 3.2: Calculate curvature at mid-span using Eq. 4.5 where h is the overall depth of the section. Store this curvature.

$$\varphi = \frac{\varepsilon_{top} + \varepsilon_{bottom}}{h} \quad \text{Eq. 4.5}$$

Step 3.3: Calculate the change in strain in concrete at the centroid of tendons, $\Delta\varepsilon_{concrete\_elastic}$, at mid-span for the applied moment using Eq. 4.6 where *c* is the neutral axis depth measured from the top most compression fiber, and d_{ps} is the distance from centroid of tendons to the top most compression fiber.

$$\Delta\varepsilon_{concrete\_elastic} = \frac{\varepsilon_{top}}{c}\left(d_{ps} - c\right) \quad \text{Eq. 4.6}$$

Step 3.4: Use the moment at mid-span and the considered loading configuration to determine the variation of moment, *M*, curvature, φ, and change in concrete strain at the centroid of tendons, $\Delta\varepsilon_{concrete\_elastic}$, at all six Gauss points.

Member Level Analysis

Step 4: Calculate the change in concrete fiber length at the centroid of tendons, $\Delta L_{elastic}$, by integrating the change in strain at this fiber along the member length (definite integral shown in Eq. 4.7a; numerical integration based on Gaussian-Legendre quadrature rule using six points employed in algorithm and shown in Eq. 4.7b)

$$\Delta L_{elastic} = \int_0^{L_{elastic}} \Delta\varepsilon_{concrete\_elastic} dx \quad \text{Eq. 4.7a}$$

$$\Delta L_{elastic} = 2\frac{\frac{(x_2 - x_1)}{2}}{E_c I}\sum_{k=1}^{6} M_x(z_k) e(z_k) W_k \quad \text{Eq. 4.7b}$$

where $z_k = \frac{x_2 + x_1}{2} + \frac{x_2 - x_1}{2}\mu_k$= Gauss-Legendre point; $e(z_k)$ = eccentricity of unbonded tendon evaluated at Gauss-Legendre point; $M_x(z_k)$ = external moment as a function of Gauss-Legendre point z_k; $x_1 = 0$; $x_2 = L_{elastic}$; W_k = Gauss-Legendre coefficient (Table 4.1); μ_k = Gauss-Legendre coefficient (Table 4.1)

Step 5: Calculate the change in strand strain, $\Delta\varepsilon_{ps\_elastic}$, (Eq. 4.8), the total strand strain, $\varepsilon_{ps\_elastic}$, (Eq. 4.9), and total strand stress, f_{ps} (Eq. 4.10).

$$\Delta\varepsilon_{ps\_elastic} = \frac{\Delta L_{elastic}}{L} \quad \text{Eq. 4.8}$$

$$\varepsilon_{ps\_elastic} = \varepsilon_{pe} + \Delta\varepsilon_{ps\_elastic} \quad \text{Eq. 4.9}$$

$$f_{ps} = 6.895\,\varepsilon_{ps\_elastic}\left[A + \frac{B}{\left\{1 + \left(C\varepsilon_{ps\_elastic}\right)^{D}\right\}^{1/D}}\right] \leq f_{pu} \quad \text{Eq. 4.10}$$

where A = 887; B = 27613; C= 112.4; and D = 7.36 for 1861.65 MPa tendon; $f_{py}/f_{pu} = 0.9$,

where f_{py} and f_{pu} are yield and ultimate stress of prestressing strands, respectively.

Step 6: Compare the assumed strand stress in Step 2 with that obtained in Step 5. If they match, proceed to Step 7, if not go back to Step 2 with calculated tendon stress obtained in Step 5.

Step 7: Using the curvature diagram along the length of the member and the second moment area theorem determine mid-span displacement, $\Delta_{midspan}$, using numerical integration based on Gauss-Legendre quadrature rule (Eq. 4.11). Also, determine total load considering the applied loading configuration and the magnitude of the cracking moment.

$$\Delta_{midspan} = \frac{\frac{(x_2 - x_1)}{2}}{E_c I}\sum_{k=1}^{6} M_x(z_k) z_k W_k \quad \text{Eq. 4.11}$$

Step 8: Report mid-span moment (cracking moment), mid-span curvature, mid-span displacement, and total load. Also, store concrete top fiber strain as this information will be useful for the procedure after cracking.

4.3.2 After Cracking

The flowchart for obtaining the moment curvature and load deformation response of a cracked UHPC beam post-tensioned with internal unbonded tendons is provided in Fig. 4.7. First, the section at mid-span is considered and is assigned a number (i.e. *S=1* at mid-span). Then the maximum usable strain in tension and compression for all materials considered are stored as this

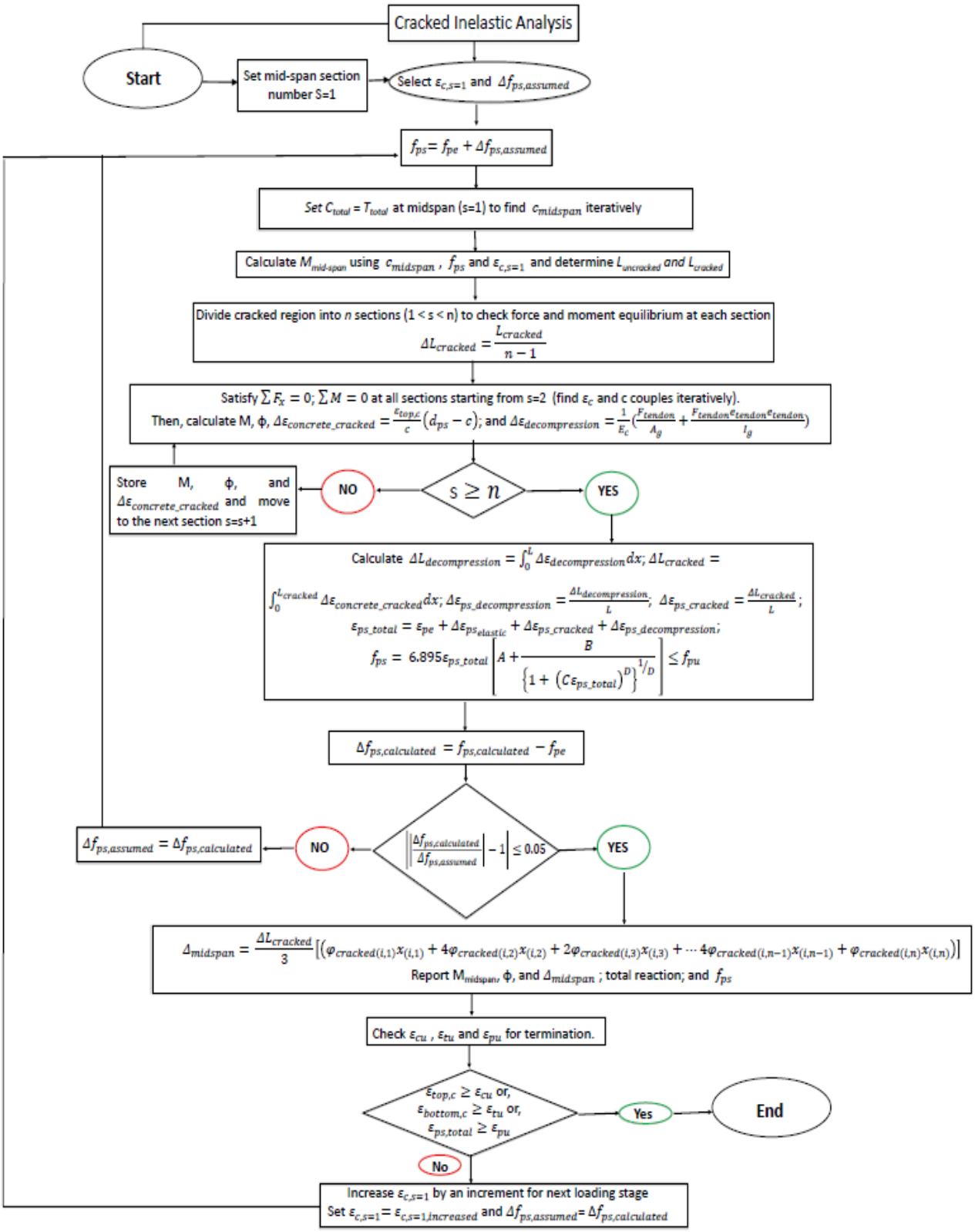

Fig. 4.7 Flowchart used to obtain moment-curvature-deformation response in a cracked UHPC beam post-tensioned with internal unbonded tendons

information will be used to validate the assumed failure mode. A maximum compressive strain for UHPC at mid-span is then assumed to determine the point up until which the algorithm is desired to be run. Then, an initial value for the top fiber compressive strain in UHPC at mid-span, $\varepsilon_{c,s=1}$, is assumed together with the change in strand stress, $\Delta f_{ps,assumed}$. The assumed change in tendon stress is then used to determine the total stress, f_{ps}, and the force in the tendon, F_{tendon}. Knowing the force in the tendon and an anchor point in the strain diagram, force equilibrium can be used to iteratively determine the depth to the neutral axis, *c*, at mid-span.

Once the depth to the neutral axis at midspan is determined, the internal moment at mid-span is computed. Then the location of the first crack in the beam is determined. This information is used to distinguish cracked regions, $L_{cracked}$, from uncracked regions, $L_{elastic}$. The cracked region in half of the beam is divided into an odd number of sections, *n*, to facilitate coefficient symmetry when implementing Simpson's rule for numerical integration (Fig. 4.3b). This creates an even number (*n-1*) of beam elements (segments) in the cracked region in half of the beam. For each section, the combination of concrete top fiber strain, $\varepsilon_{top,c}$, and neutral axis depth *c* that results in force and moment equilibrium is determined iteratively. Once the $\varepsilon_{top,c}$ and *c* couple is determined for every section, this information is used to calculate curvature, ϕ, at every section as well as the strain in concrete at the centroid of tendons, $\Delta\varepsilon_{concrete\_cracked}$. The uncracked region is considered as one section. Then, the total change in concrete fiber length at the centroid of tendons, $\Delta L_{cracked}$, is calculated by numerically integrating the strain in the concrete at the level of tendons along the length of the beam. While Gauss-Legendre quadrature is used to integrate strain in the uncracked region, Simpson's 1/3 rule is used to conduct the numerical integration in the cracked region because Gauss quadrature cannot be used since the method requires the integrated function to be

continuous rather than discrete to facilitate integration at the predetermined Gauss points. Simpson's 1/3 rule may be used with equally spaced beam sections and does not require the function to be continuous.

Once the total change in fiber length at the centroid of tendons is computed, this is equated to the change in tendon length to ensure member level deformation compatibility. Then the change in tendon length, $\Delta L_{cracked}$, is divided by the original tendon length, L, to determine the change in tendon strain, $\Delta\varepsilon_{ps\_cracked}$. The change in tendon strain is then added to the effective prestrain, ε_{pe}, and the decompression strain, $\Delta\varepsilon_{ps\_decompression}$, to compute the total strain in the tendon, ε_{ps_total}. The stress-strain curve for the strands is then used to obtain the total stress in the strand, f_{ps}. The change in strand stress, $\Delta f_{ps,calculated}$, is computed by subtracting the effective prestress, f_{pe}, from the total stress in the strands, f_{ps}. If this matches the assumed change in strand stress at the beginning of the algorithm then the mid-span moment, mid-span curvature, total reaction, and mid-span displacement are reported. Mid-span displacement is computed by using the second moment area theorem, the calculated curvature at various sections along the length of the beam, and Simpson's 1/3 rule for the cracked region and Gauss-Legendre quadrature rule for the uncracked region. This entire procedure is then repeated for different levels of strain at the top concrete fiber until the full moment-curvature-deformation response is obtained. Algorithm termination criteria is established to ensure that the analysis stops once flexural failure occurs. Flexural failure is defined as the attainment of maximum usable concrete strain in tension or compression, or strand rupture. If the calculated change in strand stress does not match with that assumed at the beginning of the algorithm, then the procedure is repeated until convergence is achieved by setting the assumed change in strand stress equal to the computed one for the next iteration. A detailed step-by-step procedure of the algorithm just described is provided below:

Cross-section Member Analysis

Step 1: Assume a top concrete fiber strain at mid-span, $\varepsilon_{c,s=1}$ and a change in strand stress Δf_{ps}.

Step 2: Determine the total stress in strands, f_{ps}, and the force in the strands, F_{tendon}, using Eq. 4.1.

Step 3: Determine the cracking moment, $M_{cracking}$, using the prestressing force obtained in Step 2 for a straight tendon configuration. For a draped tendon configuration, see Step 6.

Step 4: Using the assumed concrete top fiber strain and the calculated tendon force at mid-span determine the depth to the neutral axis, *c*, iteratively, using force equilibrium as indicated in Eq. 4.12-4.17; where C_{total} is the total compression force; $C_{concrete}$ and $C_{compression\ mild\ steel}$ are the compression forces provided by concrete and mild steel, respectively; b_w is the width of the section; d'_s and ds are the distances from compression and tension mild steel to the uppermost compression fiber, respectively; E'_s and Es are the moduli of elasticity of compression and tension mild steel, respectively; f'_c is the compressive strength of UHPC; f'_y and f_y are the yield stress of the compression and tension mild steel, respectively; ε_{cr} is the UHPC cracking strain; ε_t is the tensile strain in UHPC in the bottom most fiber; T_{total} is the total tension force; $T_{concrete}$ and $T_{tensionmildsteel}$ are the tension forces provided by concrete and mild steel, respectively; and T_{tendon} (F_{tendon}) is the tension force provided by tendon.

$$C_{total} = C_{concrete} + C_{compression\ mild\ steel} \quad \text{Eq. 4.12}$$

$$C_{total} = \frac{\varepsilon_{top,c} E_c b_w c}{2} + \frac{\varepsilon_{top,c}(c - d'_s) E'_s A'_s}{c} \quad \text{Eq. 4.13}$$

$$\text{where } \varepsilon_{top,c} E_c \le f'_c \text{ and } \frac{\varepsilon_{top,c}(c - d'_s) E'_s}{c} \le f'_y$$

$$\varepsilon_{cr} = \frac{f_{cr}}{E_c} \qquad \varepsilon_t = \frac{\varepsilon_{top,c}(h - c)}{c} \quad \text{Eq. 4.14}$$

$$T_{total} = T_{concrete} + T_{tension\ mild\ steel} + T_{tendon} \quad \text{Eq. 4.15}$$

$$T_{total} = \frac{(h-c)f_{cr}b_w}{2}\left(\frac{\varepsilon_{cr}}{\varepsilon_t}\right) + (h-c)f_{cr}b_w\left(\frac{\varepsilon_t-\varepsilon_{cr}}{\varepsilon_t}\right) + \frac{\varepsilon_{top,c}(d_s-c)E_sA_s}{c} + f_{ps}A_{ps} \quad \text{Eq. 4.16}$$

$$\text{where } \varepsilon_t \leq \varepsilon_{tu} \text{ and } \frac{\varepsilon_{top}(d_s-c)E_s}{c} \leq f_y$$

$$C_{total} = T_{total} \quad \text{Eq. 4.17}$$

Step 5: Once force equilibrium for the mid-span section is satisfied, determine the internal mid-span moment.

Member Level Analysis

Step 6: Determine the point that demarcates cracked and uncracked regions for the loading configuration in question (use Eq. 4.18-4.19 for a straight tendon configuration where $L_{uncracked}$ is the uncracked length of the member starting from each support (Fig. 4.3b), L is the length of the member, and $L_{cracked}$ is the cracked length of the member). If the tendon is draped, use the moment at mid-span, the external loading configuration, and the variation of tendon eccentricity to determine the point that demarcates cracked and uncracked regions.

$$L_{uncracked} = \frac{M_{cracking}L}{M_{midspan}2} \quad (one\ point\ loading\ in\ midspan) \quad \text{Eq. 4.18}$$

$$L_{uncracked} = \frac{M_{cracking}\alpha L}{M_{midspan}} \quad (two\ point\ loading) \quad \text{Eq. 4.19}$$

Step 7: For the uncracked region use steps 3 through 5 in the pre-cracking procedure to determine the change in strand strain in the uncracked region. For the cracked region, proceed with the next step.

Step 8: Determine the length of the cracked region, $L_{cracked}$, (Eq. 4.20), divide the cracked region into an odd number of sections, *n*, and determine the length of a typical cracked segment, $\Delta L_{cracked}$ (Eq. 4.21).

$$L_{cracked} = \frac{L}{2} - L_{uncracked} \quad \text{Eq. 4.20}$$

$$\Delta L_{cracked} = \frac{L_{cracked}}{n-1} \qquad \text{Eq. 4.21}$$

Step 9: Store the net moment due to prestress and externally applied loads at all sections. Also, store the total reaction.

Cross-section Member Analysis

Step 10.1: Satisfy moment and force equilibrium starting from *s=2* to *s=n* by assuming a concrete strain at the top fiber, $\varepsilon_{top,s\geq 2}$, and a neutral axis depth , *c* , to determine the strain distribution along the depth of the member. Using this strain distribution determine stresses using material constitutive relationships for concrete and bonded reinforcement and calculate corresponding forces. For prestress use the prestressing force assumed in Step 2. Force and moment equilibrium can be checked by establishing a tolerance for the acceptable error.

Step 10.2: If both, force and moment equilibrium are satisfied, proceed with the next step, otherwise go back to step 10.1 and assume another pair of $\varepsilon_{top,s\geq 2}$ and *c* for sections starting from *s=2* to *s=n*.

Step 10.3: Compute the change in concrete strain at the centroid of tendons in the cracked region, $\Delta\varepsilon_{concrete\_cracked}$, using Eq. 4.22.

$$\Delta\varepsilon_{concrete\_cracked} = \frac{\varepsilon_{top,c}}{c}\left(d_{ps} - c\right) \qquad \text{Eq. 4.22}$$

Step 10.4: Compute decompression strain in concrete at the centroid of tendons by considering the effect of prestressing only (Eq. 4.23). If the tendon is straight, this decompression strain will be constant along the beam length. If the tendon is draped, the decompression strain should be calculated at all sections under consideration.

$$\Delta\varepsilon_{decompression} = \frac{1}{E_c}\left(\frac{F_{tendon}}{A_g} + \frac{F_{tendon}e_{tendon}e_{tendon}}{I_g}\right) \qquad \text{Eq. 4.23}$$

Step 10.5: Repeat steps 10.1 to 10.4 for all sections under consideration (sections *i* through *n*)

Member Level Analysis

Step 11: Calculate the change in fiber length at the level of tendon due to decompression, $\Delta L_{decompression}$, and externally applied loads, $\Delta L_{cracked}$, by integrating the strain in concrete at the level of tendon along the cracked region (direct integration shown in Eq. 4.24 and 4.25). Use Gauss-Legendre quadrature rule as shown previously for calculating the change in fiber length due to decompression and Simpson's 1/3 rule for the cracked regions (Eq. 4.25b).

$$\Delta L_{decompression} = \int_0^L \Delta\varepsilon_{decompression}\,dx \quad \text{Eq. 4.24}$$

$$\Delta L_{cracked} = \int_0^{L_{cracked}} \Delta\varepsilon_{concrete\_cracked}\,dx \quad \text{Eq. 4.25a}$$

$$\Delta L_{cracked} = \frac{2\Delta L_{cracked}}{3}\Big[\Big(\Delta\varepsilon_{concrete\_cracked(i,1)} + 4\Delta\varepsilon_{concrete\_cracked(i,2)} + 2\Delta\varepsilon_{concrete\_cracked(i,3)} + \cdots 4\Delta\varepsilon_{concrete_{cracked(i,n-1)}} + \Delta\varepsilon_{concrete_{cracked(i,1)}}\Big)\Big] \quad \text{Eq. 4.25b}$$

Step 12: Calculate the change in strand strain ($\Delta\varepsilon_{ps\_decompression}$ and $\Delta\varepsilon_{ps\_cracked}$), the total strand strain (ε_{ps_total}), and total strand stress (f_{ps}) using Eq. 4.26-4.29.

$$\Delta\varepsilon_{ps\_decompression} = \frac{\Delta L_{decompression}}{L} \quad \text{Eq. 4.26}$$

$$\Delta\varepsilon_{ps\_cracked} = \frac{\Delta L_{cracked}}{L} \quad \text{Eq. 4.27}$$

$$\varepsilon_{ps\_total} = \varepsilon_{pe} + \Delta\varepsilon_{ps_{elastic}} + \Delta\varepsilon_{ps\_cracked} + \Delta\varepsilon_{ps\_decompression} \quad \text{Eq. 4.28}$$

$$f_{ps} = 6.895\varepsilon_{ps\_total}\left[A + \frac{B}{\left\{1 + \left(C\varepsilon_{ps\_total}\right)^D\right\}^{1/D}}\right] \le f_{pu} \quad \text{Eq. 4.29}$$

where A = 887, B = 27613 , C= 112.4 , D = 7.36 for 1861.65 MPa tendon $f_{py}/f_{pu} = 0.9$

Step 13: Compare the assumed change in strand stress in Step 1 with that obtained in Step 12. If they match, proceed to Step 14, if not go back to Step 1, use the same strain for the top concrete

fiber, $\varepsilon_{top,s=1}$, and set the assumed change in strand stress equal to the difference between, f_{ps}, obtained in Eq. 4.29 and, f_{pe}, (effective prestress) (i.e. set the total strand stress, f_{ps}, equal to that calculated in Step 12).

Step 14: Determine mid-span displacement using the curvature diagram along the length of the member, the second moment area theorem, and numerical integration using Simpson's 1/3 rule (Eq.4.30).

$$\Delta_{midspan} = \frac{\Delta L_{cracked}}{3}\left[\left(\varphi_{cracked(i,1)}x_{(i,1)} + 4\varphi_{cracked(i,2)}x_{(i,2)} + 2\varphi_{cracked(i,3)}x_{(i,3)} + \cdots 4\varphi_{cracked(i,n-1)}x_{(i,n-1)} + \varphi_{cracked(i,n)}x_{(i,n)}\right)\right] \quad \text{Eq. 4.30}$$

Step 15: Check the following subroutine termination criteria. First, ε_{ctop} at any section along the member should not exceed ε_{cu}, although this is unlikely to occur because the flexure failure of post-tensioned UHPC beams is typically a fiber tension controlled failure in which fibers pull out before concrete crushes (Dogu and Menkulasi 2020). Second, ε_t at any section along the member should not exceed ε_{tu}, which corresponds with the attainment of the peak load (Dogu and Menkulasi 2020). Therefore, the algorithm is written to characterize the moment-curvature-deformation response up until the point when the peak moment or load is achieved and not beyond. Lastly, f_{ps} should not exceed f_{pu}, which indicates the fracture of tendons. If none of the termination criteria is applicable, go to Step 1 and increase $\varepsilon_{top,s=1}$. The increment with which $\varepsilon_{top,s=1}$ is increased affects the run time of the algorithm. The change in strand stress, Δf_{ps}, can be taken equal to that computed in the previous iteration.

4.3.3 Discussion of the Proposed Procedure

It should be noted that the proposed procedure does not rely on any sort of empiricism other than the one included in the assumed material constitutive models. The proposed procedure relies on an extensive number of iterations to produce the moment-curvature-deformation response. The time required to run the proposed algorithm is orders of magnitude lower than that required to run high fidelity nonlinear finite element analysis (NFEA) such as those described in reference (Vu et al. 2010), which are capable of simulating the lack of bond and varying contact between unbonded tendons and the surrounding UHPC. The selection of the number of sections required to produce accurate results depends on the loading configuration and should be determined such that key changes in the moment diagram are captured. A total of 12 sections for half of the beam should be sufficient to produce reliable results. Fig. 4.8 shows a number of sections used for sensitivity analysis for the beam B-1 (see Table 4.2) when subject to a concentrated load at mid-span. As can be seen, even with three sections the results are rather accurate. The proposed algorithm can be used to obtain empirical coefficients, which can be used to determine plastic hinge length and strand stress at ultimate, or to obtain bond reduction factors for various stages of loading if an approach similar to that proposed by Naaman and Alkhairi (1991) is selected.

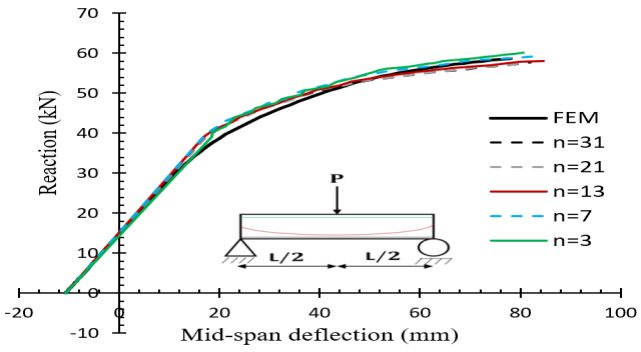

Fig. 4.8 Sensitivity analysis for the number of sections considered for half of the span in a typical UHPC beam post-tensioned with internal unbonded tendons

4.4 Validation of Proposed Procedure

Provided that there are currently no experimental tests on UHPC beams post-tensioned with unbonded tendons, the proposed procedure for computing the moment curvature and load deformation response of UHPC beams post-tensioned with internal unbonded tendons was compared with results obtained from validated nonlinear finite element analysis. The full validation as well as the details of the numerical modeling protocol used to create the finite element models is provided by Dogu and Menkulasi (2020) and was based on a submodel validation approach. In this approach, finite element models of normal strength concrete beams post-tensioned with unbonded tendons, and UHPC beams prestressed with bonded tendons were created and the results were compared with those obtained from physical tests. Good correlation between computed and measured results were obtained. It was therefore deduced that a modeling protocol that is able to correctly capture the behavior of UHPC beams prestressed with bonded tendons as well as the behavior of normal strength concrete beams with unbonded tendons should be able to correctly capture the behavior of UHPC beams post-tensioned with unbonded tendons.

Fig. 4.9 shows the comparison between results obtained using the proposed procedure and those obtained using validated nonlinear finite element analysis. The results agree well at various levels. Fig. 4.9a1 and 4.9b1 illustrate the behavior at the member level in terms of total load versus mid-span displacement. Fig. 4.9a2 and 4.9b2 illustrate cross-sectional level behavior in terms of moment versus curvature at mid-span, and Fig. 4.9a3, 4.9b3, 4.9a4, 4.9b4 illustrate the variation of tendon stress with respect to mid-span displacement. The variation in tendon stress with respect to mid-span displacement is illustrated in terms of the total tendon stress as well as the change in tendon stress. The close agreement between FEA results and those obtained using the proposed procedure in the latter case is noteworthy because the change in tendon stress is rather small. The

results shown in Fig. 4.9 demonstrate that the proposed procedure can be used to reliably simulate the behavior of UHPC beams at various levels.

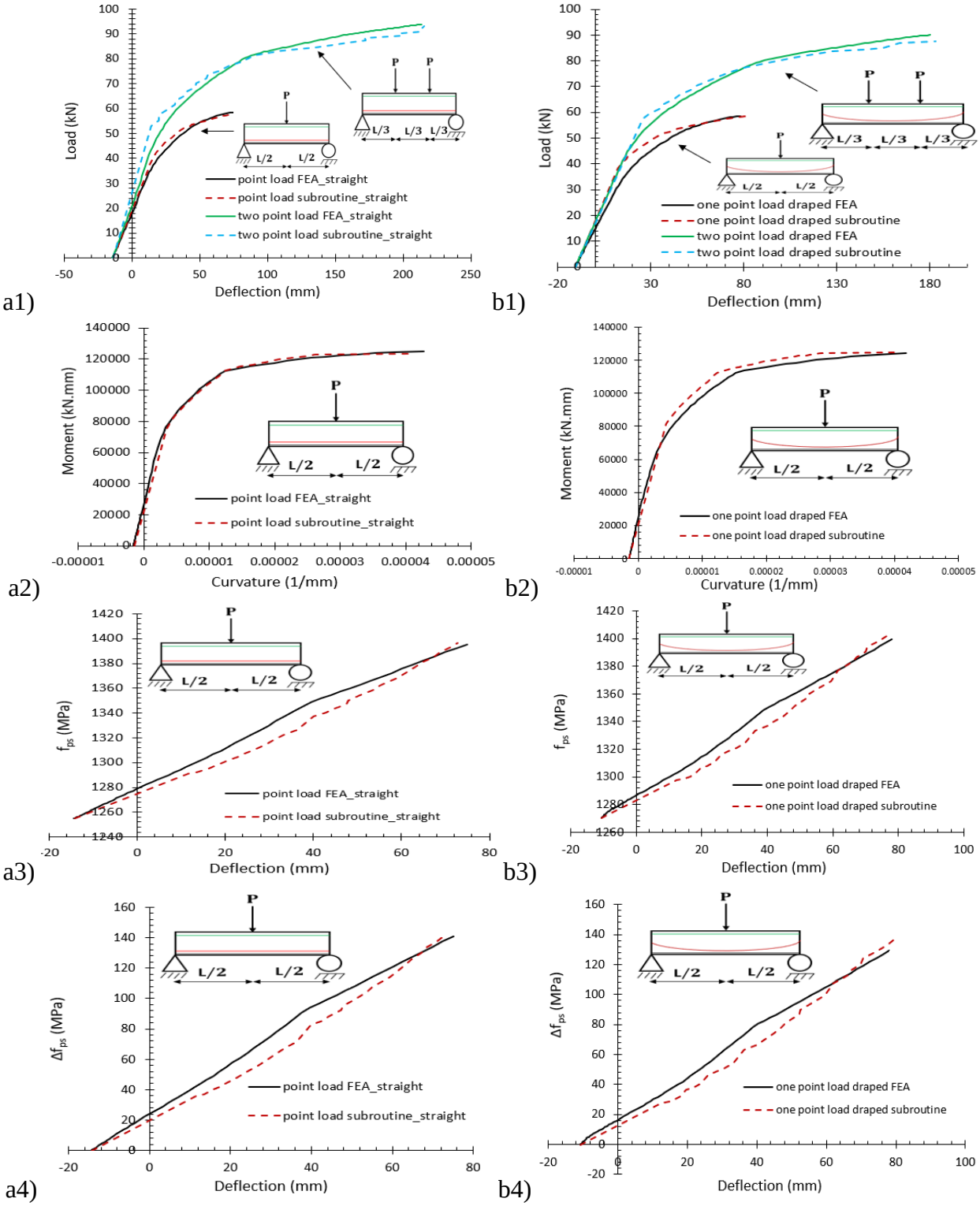

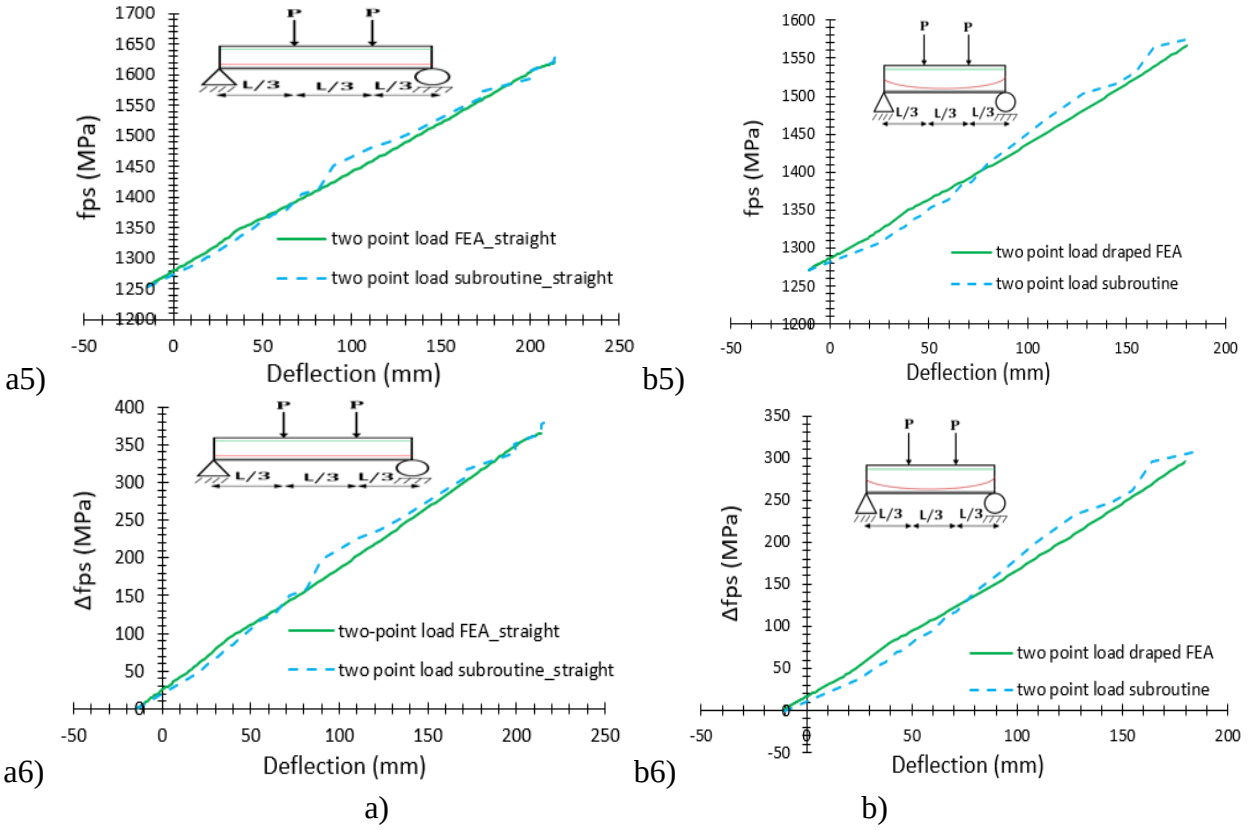

Fig. 4.9 Validation of proposed approach to compute moment-curvature-deformation response of UHPC beams post-tensioned with internal unbonded tendons: a) straight tendons, b) draped tendons

4.5 Parametric Analysis , Failure Mode and Ductility

Dogu and Menkulasi (2020) conducted an extensive parametric analysis on the influence of various parameters on the change in strand stress at the ultimate limit state. However, the influence of these parameters on flexural capacity and ductility of UHPC beams post-tensioned with unbonded tendons was not investigated. Therefore, a parametric analysis was conducted to understand the influence of various parameters on the complete moment curvature and load deformation response of UHPC beams post-tensioned with unbonded tendons. Table 4.2 shows the geometrical and material properties of the beam used for parametric analysis. This beam is considered to represent a baseline case. The beam is 152 mm wide (b_w) and 305 mm deep (h) with

a span length of 8.53 m (L), and it features 2-13 mm diameter draped tendons with zero eccentricity at ends (e) and 102 mm eccentricity at mid-span (e_m).

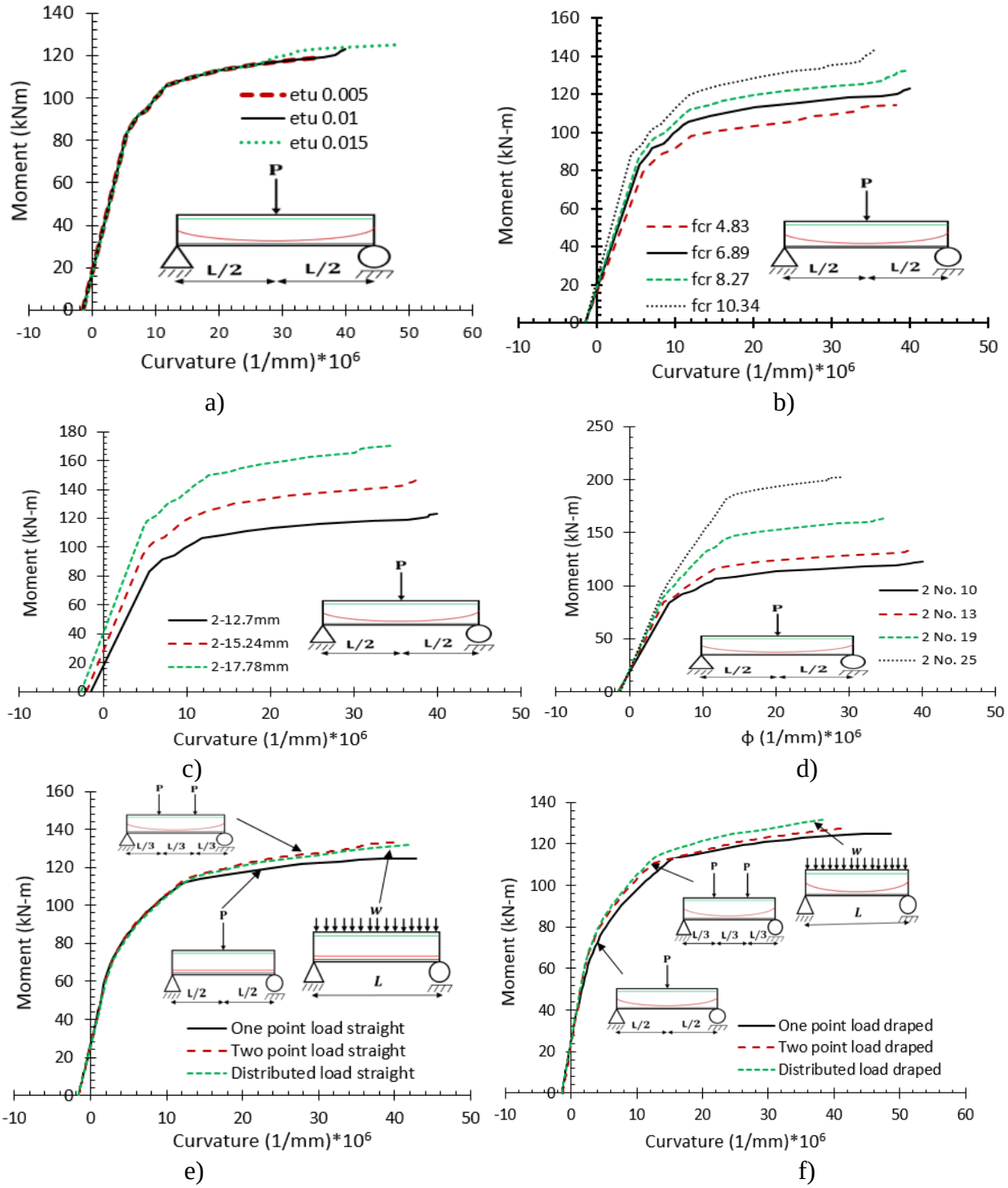

Fig. 4.10 Influence of various parameters on the moment-curvature relationship of UHPC beams post-tensioned with internal unbonded tendons: a) ε_{tu}, b) f_{cr}, c) A_{ps}, d) $A_{stension}$, e) loading configuration on straight tendon profile, f) loading configuration on draped tendon profile

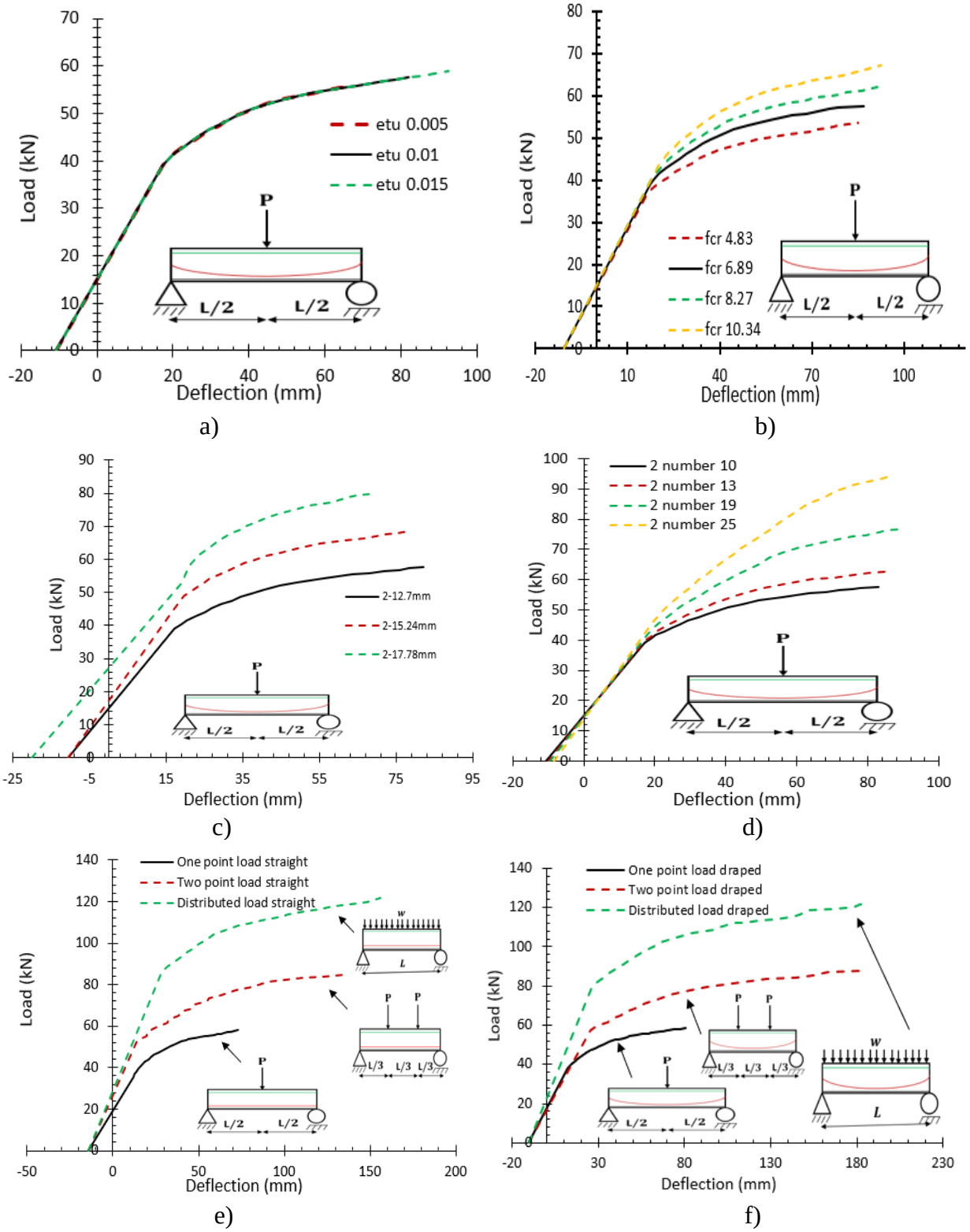

Fig. 4.11 Influence of various parameters on the load-deformation relationship of UHPC beams post-tensioned with internal unbonded tendons: a) ε_{tu}, b) f_{cr}, c) A_{ps}, d) $A_{stension}$, e) loading configuration on straight tendon profile, f) loading configuration on draped tendon profile

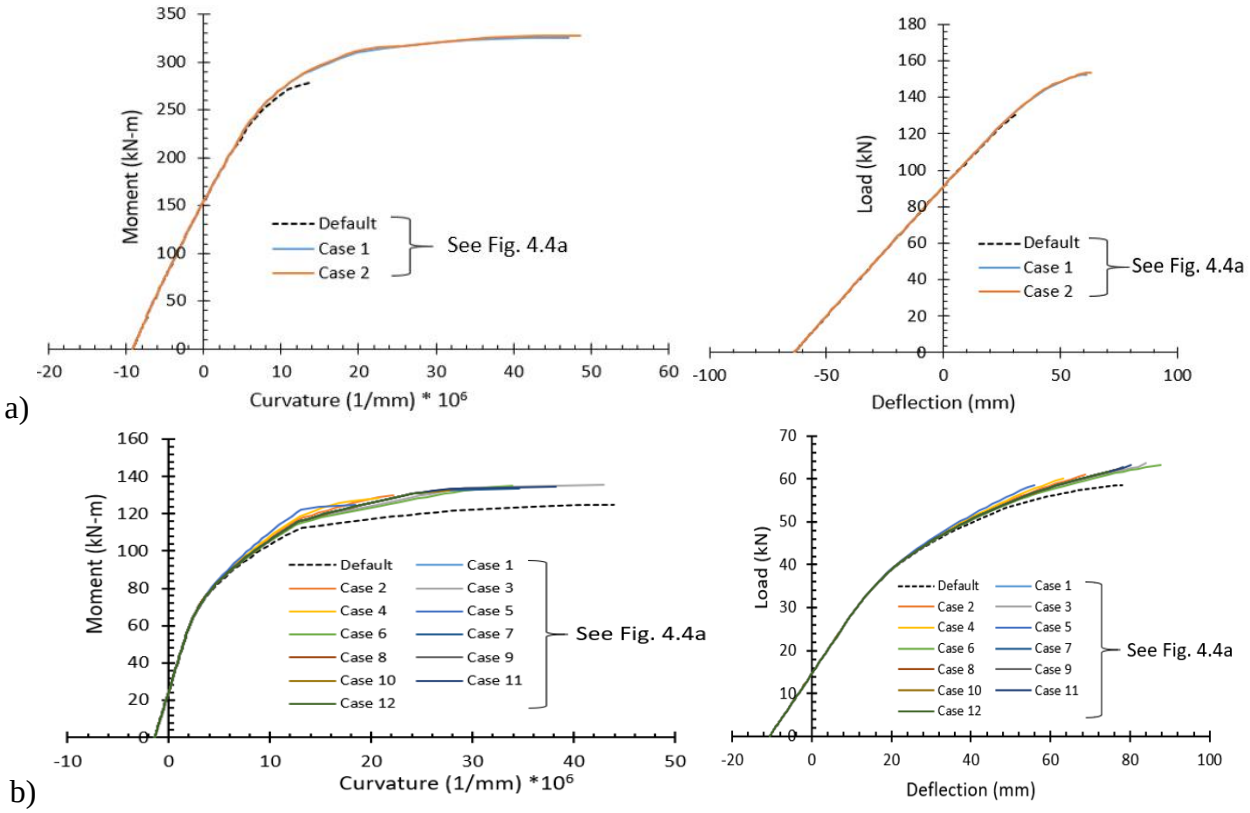

Fig. 4.12 Influence of various constitutive models for UHPC on the moment-curvature and load-deformation relationship: a) influence of the compressive domain, and b) tensile domain

Compressive strength of UHPC (f'_c) is 152 MPa and modulus of elasticity (E_c) and cracking stress (f_{cr}) are calculated using the equations shown in Fig. 4.4 and guidance provided in references (Russel and Graybeal 2013, Graybeal 2017). The prestressing strands are assumed to be low relaxation steel with 1862 MPa ultimate tensile strength (f_{pu}). The beam features 2-6 mm and 2-10 mm diameter mild steel bars in tension, and 2-6 mm diameter mild steel bars in compression. The yield stress of mild steel is assumed to be 414 MPa.

Table 4.2. Beam properties used in parametric analysis (See Fig. 4.2 for illustration)

Beam ID	Beam Properties												
	b_w (mm)	h (mm)	A_{ps}[1] (mm^2)	Tendon config.[2]	e_m (mm)	$A_{stension}$[3] (mm^2)	$A_{scomp.}$ (mm^2)	f'_c (MPa)	f_{cr}[4] (MPa)	f_y (MPa)	f_{pu} (MPa)	f_{pe} (MPa)	f_{py}/f_{pu}
B-1	152	305	198	Draped	102	205	63	152	6.89	414	1862	1262	0.9

[1]See Table 4.5 for range; [2]See Table 4.7 for range; [3]See Table 4.6 for range; [4]See Table 4.4 for range

4.5.1 Effect of ε_{tu} on complete flexural behavior

It has been previously (Dogu and Menkulasi 2020) demonstrated that PT UHPC members exhibit a tension controlled failure, which is characterized by fiber pull out in tension before concrete crushes in compression when the peak load is achieved. Fiber pullout in tension is characterized by a reduction in UHPC's ability to sustain tensile stresses accompanied by an increase in strain. The tensile strain at incipient fiber pullout is hereby called maximum usable tensile strain, ε_{tu}, and is considered to be a parameter worthy of investigation since its attainment represents the point when the beam reaches its maximum load carrying capacity. The influence of ε_{tu} on the complete flexural behavior of UHPC beams post-tensioned with unbonded tendons is shown in Table 4.3, Fig. 4.10a, and Fig. 4.11a. Table 4.3 shows a total of nine beams that feature three different loading configurations whereas Fig. 4.10a and 4.11a feature three beams that feature a one-point loading configuration. The magnitude of ε_{tu} was varied from 0.005 to 0.015 in increments of 0.005.

Table 4.3. Influence of ε_{tu} on flexural capacity and ductility

Beam ID	Loading configuration	ε_{tu}	c (mm)	M_n (m-kN)	% change (Moment)	Cross-section Level Ductility		Member Level Ductility	
						$\mu_\varepsilon = \frac{\varepsilon_u}{\varepsilon_y}$	$\mu_\phi = \frac{\phi_u}{\phi_y}$	$\mu_\Delta = \frac{\Delta_u}{\Delta_y}$	$\frac{L}{\Delta_u}$
B-1-ETU1-P	One Point	0.005	84	119	-4.57	2.19	1.80	1.26	143
B-1-ETU2-P	One Point	0.010	63	125	Baseline	4.48	3.30	1.65	109
B-1-ETU3-P	One Point	0.015	53	126	+0.47	6.38	4.45	1.73	104
B-1-ETU1-TP	Two Point	0.005	85	119	-7.21	2.23	1.81	1.41	74
B-1-ETU2-TP	Two Point	0.010	54	128	Baseline	4.29	3.27	2.20	47
B-1-ETU3-TP	Two Point	0.015	64	129	+0.98	6.74	5.15	2.37	44
B-1-ETU1-DP	Distributed	0.005	85	126	-4.68	2.23	1.80	1.73	60
B-1-ETU2-DP	Distributed	0.010	65	132	Baseline	3.91	3.03	2.24	46
B-1-ETU3-DP	Distributed	0.015	55	139	+5.65	6.31	4.77	3.74	28

The results shown in Table 4.3 and Fig. 4.13a suggest that +/-50% change in ε_{tu} causes only a marginal change in flexural capacity. There are several reasons for the disproportionate influence of ε_{tu} on flexural capacity. First, Fig. 4.14 shows that a significant increase in ε_{tu} causes

only a small decrease in the neutral axis depth (Table 4.3). The decrease in the neutral axis depth causes an increase in the height of the tension block provided by UHPC, however, this increase is much smaller than the increase in ε_{tu} as evinced in Fig. 4.15a, which shows a small increase in the tension force provided by UHPC compared to induced change in ε_{tu}.

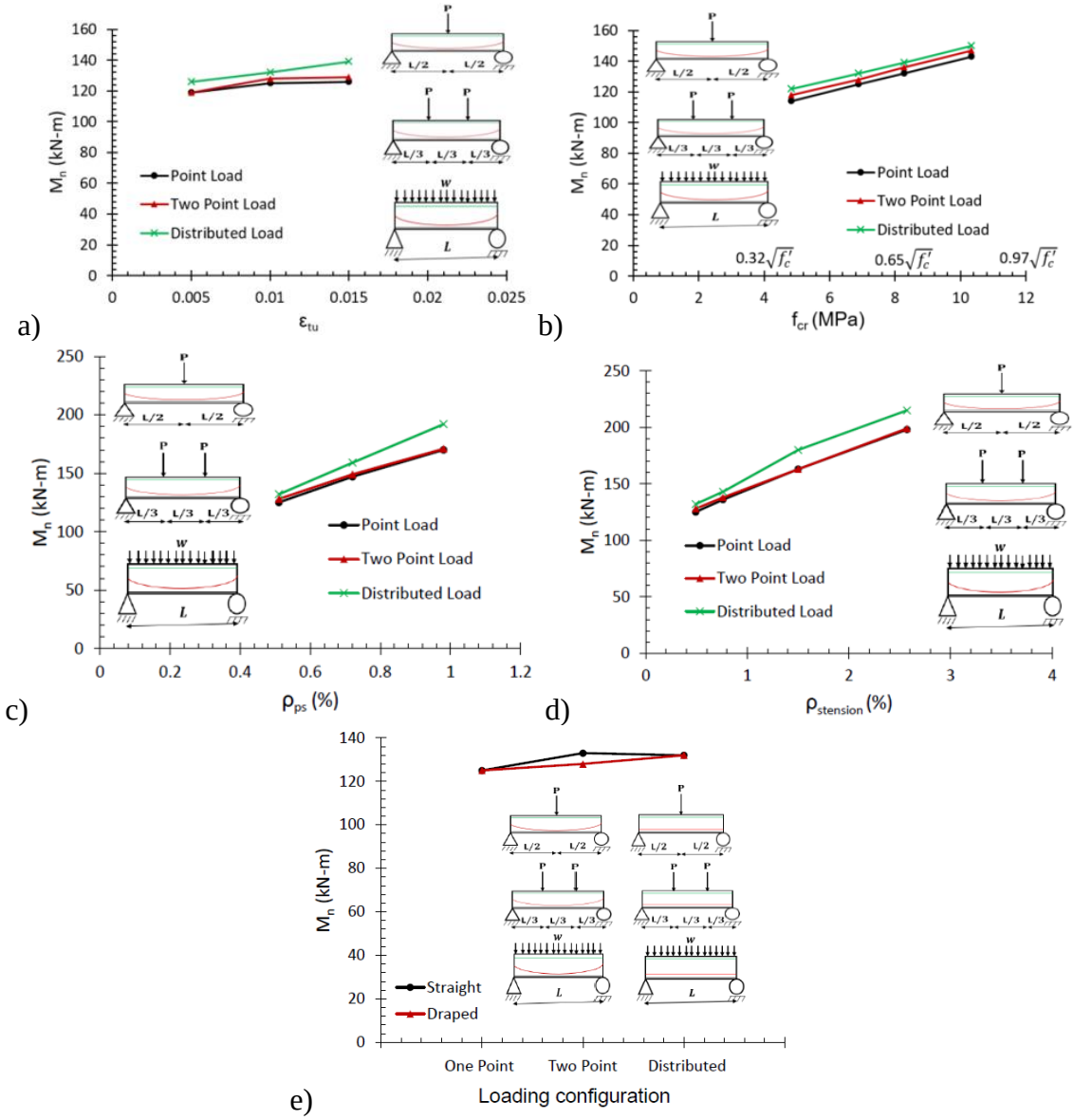

Fig. 4.13 Influence of various parameters on flexural capacity: a) ε_{tu}, b) f_{cr}, c) ρ_{ps}, d) $\rho_{stension}$, e) tendon profile

Second, since UHPC is not the only component providing tensile resistance to an applied external moment, a certain percentage increase in ε_{tu} cannot have a proportional increase in the moment capacity of the beam. This is illustrated in Fig. 4.15a, which shows the tensile force provided by UHPC, tendons, and mild steel as ε_{tu} increases. Third, an increase in ε_{tu} causes an expansion in the tension block height provided by UHPC, which results in a reduction in the moment arm for the tension force provided by UHPC due to an upward shift in the location of the neutral axis and the resultant tension force provided by UHPC. The upward shift in the neutral axis causes also a shift in the location of the resultant compression force provided by UHPC, however, this shift is smaller than that caused by the expansion of the tension block, because the compression block has a triangular shape whereas the tension block has a rectangular shape. Therefore, there is a net reduction in the moment arm between the resultant compressive and tensile forces provided by UHPC. While this reduction is small, it is one of the reasons why a change in ε_{tu} does not result in a proportional change in flexural capacity.

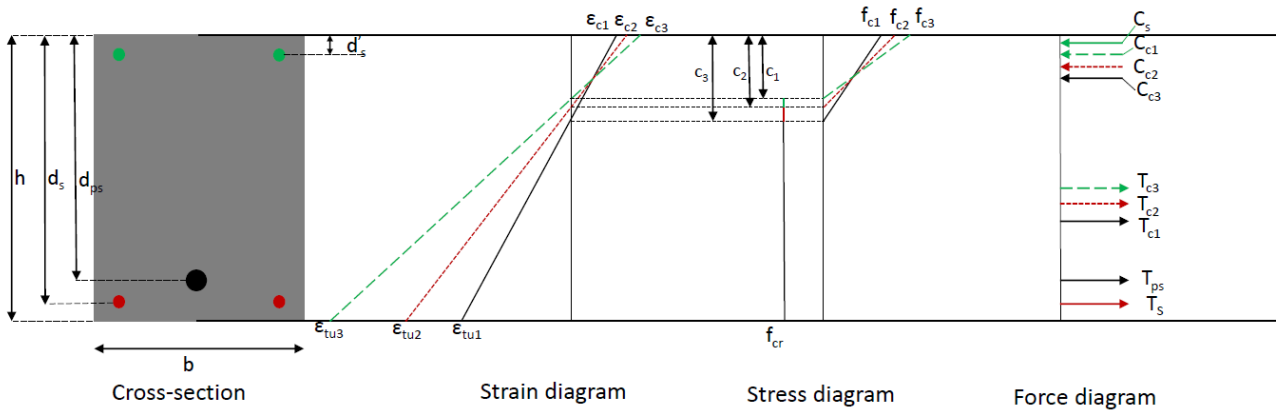

Fig. 4.14 Influence of the increase in ε_{tu} on strain, stress, and force diagrams for a typical UHPC beam post-tensioned with internal unbonded tendons

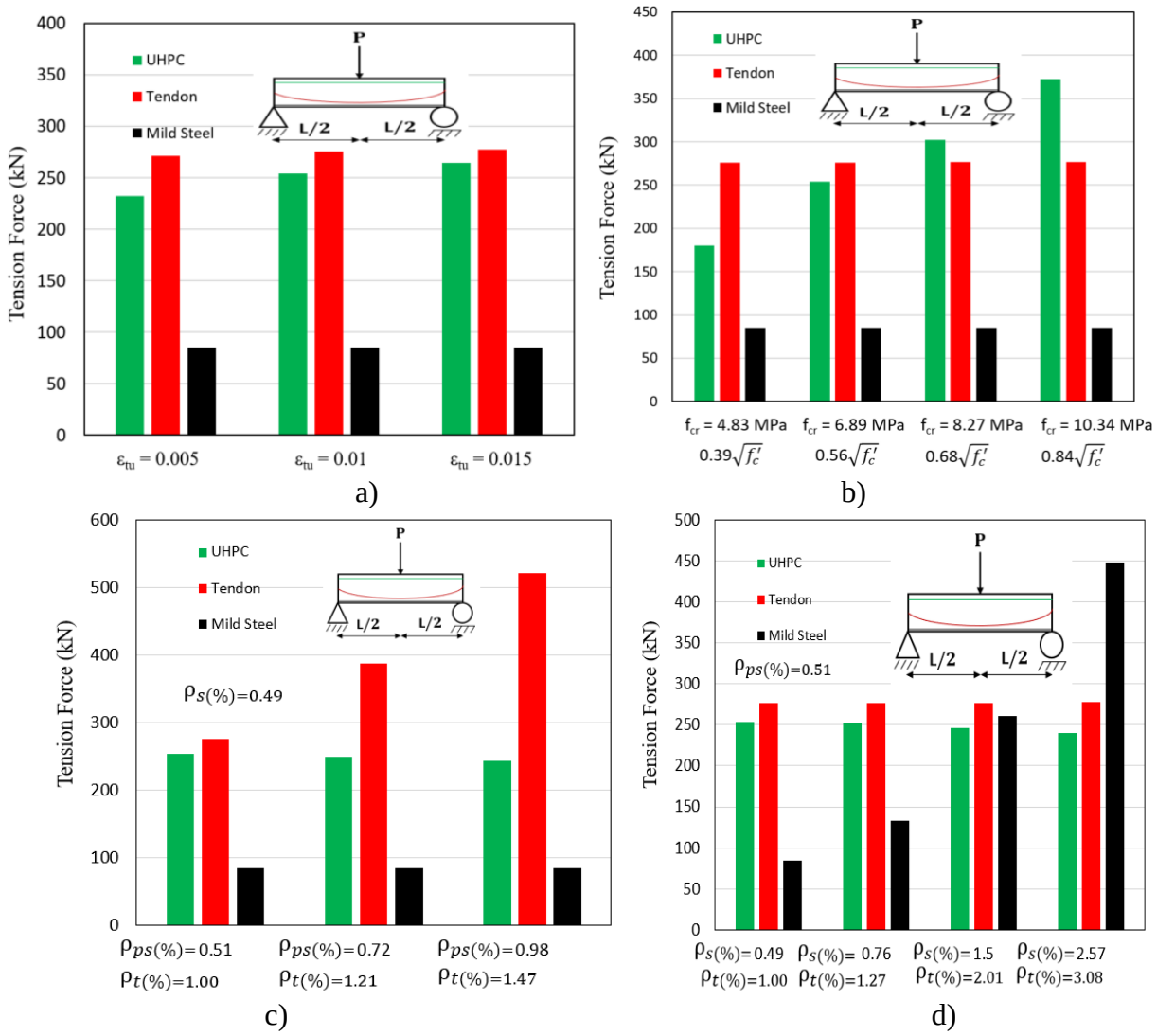

Fig. 4.15 Variation in the tension force provided by each component as a function of: a) ε_{tu}, b) f_{cr}, c) ρ_{ps}, and d) ρ_s.

Table 4.3 and Fig. 4.16a suggest that ε_{tu} has a direct influence on cross-sectional and member level ductility although the degree of this influence varies from cross-sectional to member level. Fig. 4.16 shows that ε_{tu} is the parameter with the strongest influence on cross-section level ductility. At the cross-sectional level, when ACI 318-19 (2019) and AASHTO (2017) strain-based definition for ductility is used, ε_{tu} has a proportional influence. A 100% increase in ε_{tu} typically results in a 100% increase in μ_{ε}. When the Canadian (2019) curvature-based definition is used, ε_{tu} has a slightly smaller influence on curvature ductility but still a very strong one. Out of the nine

beams considered in Table 4.3 only the ones that featured an ε_{tu} equal to 0.005 failed to meet minimum cross-section level ductility requirements provided in American (ACI 318-19 2019 and AASHTO 2017) and Canadian standards (2019) for NSC and FRC, respectively.

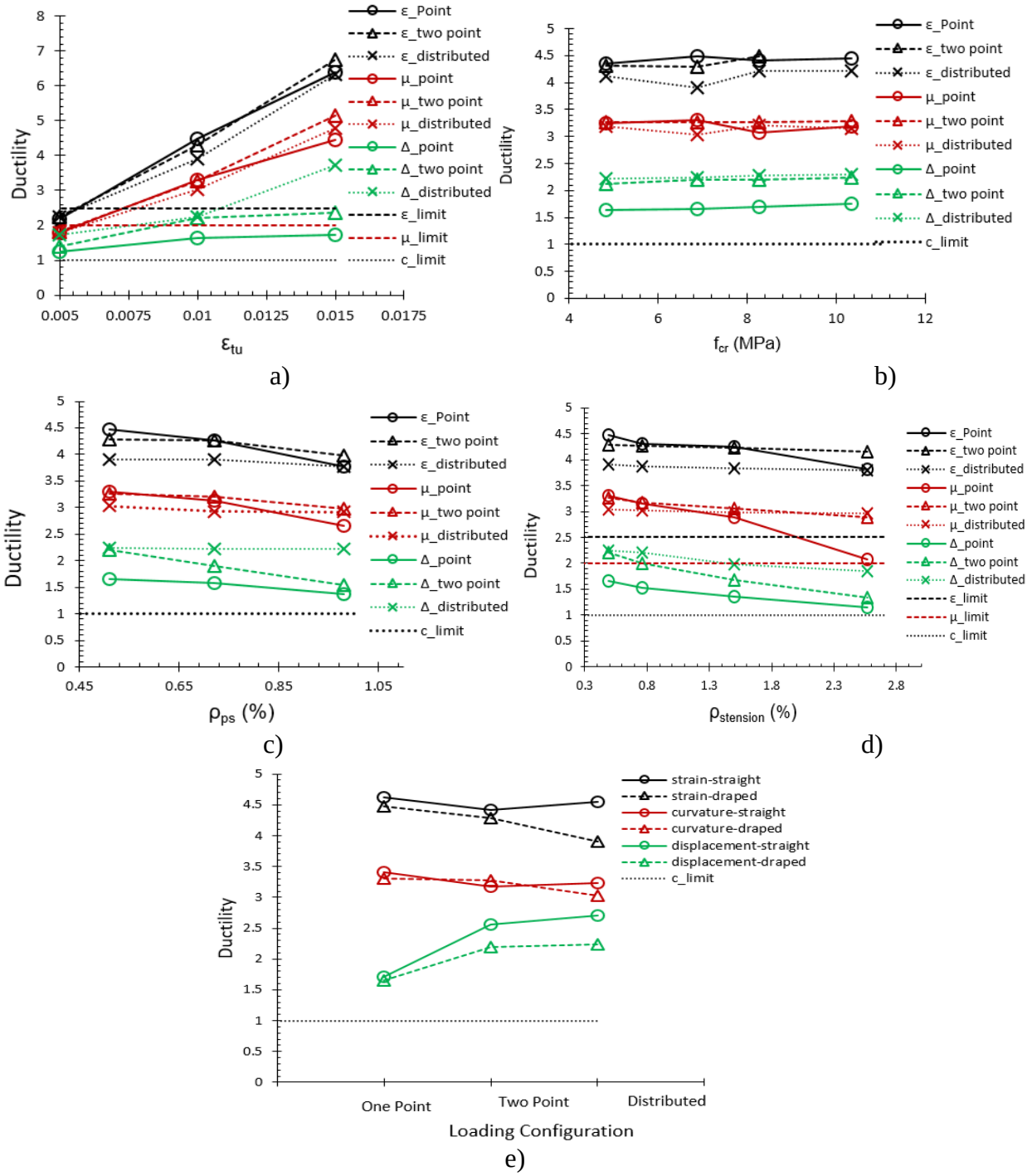

Fig. 4.16 Influence of various parameters on cross-section and member level ductility: a) ε_{tu}, b) f_{cr}, c) ρ_{ps}, d) $\rho_{stension}$, e) tendon profile

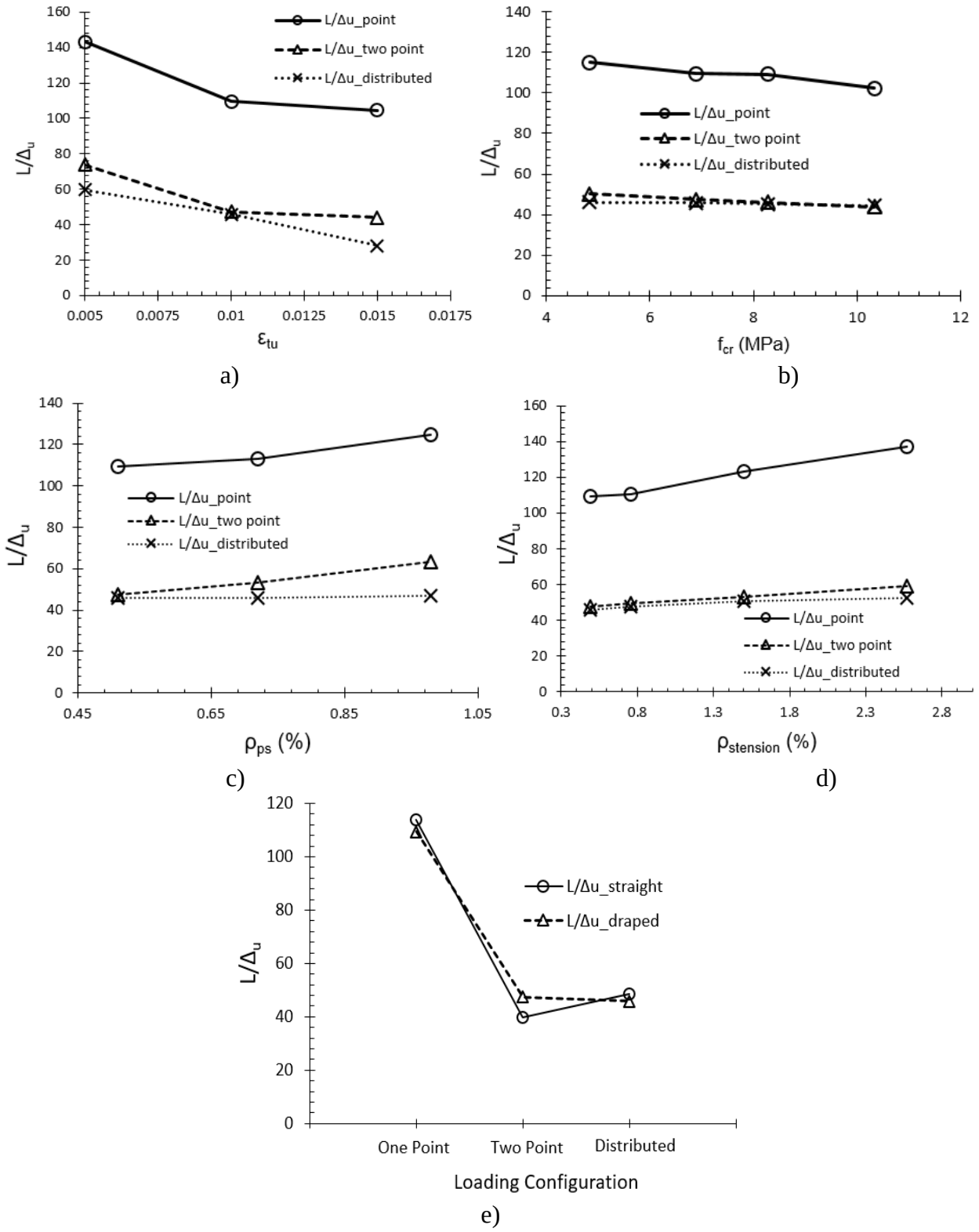

Fig. 4.17 Influence of various parameters on L/Δ_u: a) ε_{tu}, b) f_{cr}, c) ρ_{ps}, d) $\rho_{stension}$, e) tendon profile

This suggests that either the design of the UHPC formulation should be chosen such that there is a sufficient amount of fibers so that ε_{tu} is at least equal to 0.006, or the area of strands and tension mild steel should be adjusted accordingly. It is worth noting how the influence of ε_{tu} on member level ductility is not nearly as strong as that on cross-sectional level ductility especially for beams that feature one point and two point loading when the ratio of Δ_u/Δ_y is used to quantify ductility. For a distributed loading configuration the influence of ε_{tu} on member level ductility remains strong suggesting that ductility at the member level is highly dependent on the loading configuration. This observation is further corroborated when member level ductility is evaluated using the L/Δ_u ratio as shown in Fig. 4.17a. Beams with two point loading and distributed loading configurations exhibit much larger deflections at incipient failure than beams with a point load at mid-span.

4.5.2 Effect of f_{cr} on complete flexural behavior

Table 4.4, Fig. 4.13b, and Fig. 4.16b illustrate the influence of f_{cr} on flexural capacity and ductility. Fig. 4.15b illustrates the influence on f_{cr} on the magnitude of the tensile force provided by UHPC, and Fig. 4.10 and 4.11 illustrate the influence of f_{cr} on the full behavior of UHPC beams post-tensioned with unbonded tendons. The investigated beams featured a range of f_{cr} from $0.39\sqrt{f_c'}$ to $0.84\sqrt{f_c'}$ where f'_c is 152 MPa. A certain % change in the f_{cr} causes a proportional change in the magnitude of the tension force provided by UHPC. This is expected and is illustrated in Fig. 4.15b. The influence of f_{cr} on flexural capacity is more pronounced than that of ε_{tu}, because of the more significant impact that f_{cr} has on the tension force provided by UHPC (Fig. 4.13b).

Table 4.4, Fig. 4.16b, and Fig. 4.17b suggest that f_{cr} has almost no marked effect on cross section and member level ductility. All twelve investigated beams exhibited similar levels of

ductility and they all met minimum cross-section level ductility requirements provided in (ACI 318-19 2019 and AASHTO 2017) and Canadian standards (2019) for NSC and FRC, respectively. Fig. 4.17b suggests that when the ratio L/Δ_u was used to evaluate member level ductility, an increase in f_{cr} corresponded with a slight increase in ductility (i.e. a lower L/Δ_u). This observation applies in Fig. 4.16b as well, although the influence of f_{cr} on the Δ_u/Δ_y ratio is not as noticeable.

Table 4.4. Influence of cracking stress f_{cr} on flexural capacity and ductility

Beam ID	Loading configuration	f_{cr}		M_n (mm-kN x10^3)	% change (Moment)	Cross-section level ductility		Member level ductility	
		(MPa)	$\sqrt{f_c'}$			$\mu_\varepsilon = \frac{\varepsilon_u}{\varepsilon_y}$	$\mu_\phi = \frac{\phi_u}{\phi_y}$	$\mu_\Delta = \frac{\Delta_u}{\Delta_y}$	$\frac{L}{\Delta_u}$
B-1-fcr1	One Point	4.83	0.39	114	-8.74	4.36	3.24	1.63	115
B-1-fcr2	One Point	6.89	0.56	125	Baseline	4.48	3.30	1.65	109
B-1-fcr3	One Point	8.27	0.68	132	+5.66	4.41	3.08	1.69	109
B-1-fcr4	One Point	10.34	0.84	143	+14.67	4.44	3.19	1.75	102
B-1-fcr1	Two Point	4.83	0.39	118	-8.15	4.32	3.27	2.13	50
B-1-fcr2	Two Point	6.89	0.56	128	Baseline	4.29	3.27	2.20	47
B-1-fcr3	Two Point	8.27	0.68	136	+5.92	4.49	3.27	2.20	46
B-1-fcr4	Two Point	10.34	0.84	147	+14.57	4.48	3.28	2.24	44
B-1-fcr1	Distributed	4.83	0.39	122	-7.7	4.11	3.19	2.21	46
B-1-fcr2	Distributed	6.89	0.56	132	Baseline	3.91	3.03	2.24	46
B-1-fcr3	Distributed	8.27	0.68	139	+5.76	4.22	3.21	2.28	45
B-1-fcr4	Distributed	10.34	0.84	150	+13.85	4.22	3.15	2.30	44

4.5.3 Effect of ρ_{ps} on complete flexural behavior

Table 4.5, Fig. 4.13c, and Fig. 4.16c show the influence of longitudinal unbonded reinforcement ratio, ρ_{ps}, on flexural capacity and ductility. While an increase in ρ_{ps} causes a significant increase in flexural capacity, this increase is not directly proportional to that induced in the ρ_{ps} because tendons are not the only component providing tensile resistance as illustrated in Fig. 4.15c. Also, an increase in ρ_{ps} results in a decrease in the tendon stress at ultimate, f_{ps}, (Dogu and Menkulasi 2020) thus affecting the magnitude of the tension force provided by the tendons and their contribution to flexural capacity. Fig. 4.15c shows that an increase in ρ_{ps} causes a slight decrease in the tension force provided by UHPC due to a shift in the neutral axis, thus further dampening the increase in flexural capacity caused by an increase in ρ_{ps}. Table 4.5 shows that the

influence of ρ_{ps} on flexural capacity is stronger than the influence of f_{cr} for a given percentage change in these parameters from the baseline values.

Table 4.5. Influence of ρ_{ps} on flexural capacity and ductility

Beam ID	Loading configuration	ρ (%)		M_n (m-kN)	% change (Moment)	Cross-section level ductility		Member level ductility	
		ρ_{total}	ρ_{ps}			$\mu_\varepsilon = \frac{\varepsilon_u}{\varepsilon_y}$	$\mu_\phi = \frac{\phi_u}{\phi_y}$	$\mu_\Delta = \frac{\Delta_u}{\Delta_y}$	$\frac{L}{\Delta_u}$
B-1-Aps1	One Point	1.00	0.51	125	Baseline	4.48	3.30	1.65	109
B-1-Aps2	One Point	1.21	0.72	147	+17.28	4.27	3.13	1.57	113
B-1-Aps3	One Point	1.47	0.98	170	+35.82	3.77	2.65	1.37	125
B-1-Aps1	Two Point	1.00	0.51	128	Baseline	4.29	3.27	2.20	47
B-1-Aps2	Two Point	1.21	0.72	149	+16.34	4.26	3.20	1.90	54
B-1-Aps3	Two Point	1.47	0.98	171	+33.33	3.98	2.98	1.54	63
B-1-Aps1	Distributed	1.00	0.51	132	Baseline	3.91	3.03	2.24	46
B-1-Aps2	Distributed	1.21	0.72	159	+20.28	3.90	2.93	2.23	46
B-1-Aps3	Distributed	1.47	0.98	192	+45.69	3.77	2.92	2.22	47

$\rho_{total} = \rho_{stension} + \rho_{ps}$; $\rho_{stension} = A_{stension}/(b_w d_s)$; $\rho_{ps} = A_{ps}/(b_w d_{ps})$; $\rho_{min\_stension\_ACI} = 0.22\%$ ($A_{stension\_min\_ACI} = 0.004A_{ct}$)

Table 4.5, Fig. 4.16c, and Fig. 4.17c suggest that an increase in ρ_{ps} typically results in a decrease in cross-section and member level ductility although all nine investigated beams met minimum ductility requirements provided in American (ACI 318-19 2019 and AASHTO 2017) and Canadian (2019) standards for NSC and FRC, respectively. The investigated total longitudinal reinforcement ratio ρ_{total} (or ρ_t) varied from 1.00% to 1.47%, while the unbonded reinforcement ratio ρ_{ps} varied from 0.51% to 0.98%. The bonded reinforcement ratio, ρ_s (or $\rho_{stension}$) was kept constant at 0.49%, which is greater than the 0.22% required minimum ratio specified in ACI 318-19 (2019) for bonded reinforcement in NSC members post-tensioned with unbonded tendons. This required minimum bonded longitudinal reinforcement ratio, $\rho_{min\_stension\_ACI}$, was calculated as $A_{stension\_min\_ACI}/(b_w d_{stension})$ where $A_{stension\_min\_ACI} = 0.004A_{ct}$, and A_{ct} is the area of that part of cross section between the flexural tension face and centroid of gross section. Fig. 4.16c and 4.17c suggest that for beams with point and two point loading configurations ductility decreased as ρ_{ps}

increased, whereas the ductility of the beams with a distributed loading remained essentially unaffected by the increase in ρ_{ps}.

4.5.4 Effect of $\rho_{stension}$ on complete flexural behavior

Table 4.6, Fig. 4.13d, 4.16d, and 4.17d show the influence of the bonded longitudinal reinforcement ratio in tension, $\rho_{stension}$, on flexural capacity and ductility. Similar to the influence of ρ_{ps} on flexural capacity, while an increase in $\rho_{stension}$ causes a proportional increase in the tension force provided by mild steel, it does not cause a proportional increase in flexural capacity due to the contribution of tendons and UHPC. In general, Fig. 4.15 illustrates how the contribution of each component that provides tensile resistance varies for different scenarios. As $\rho_{stension}$ is changing, there is no significant difference in the tensile resistance provided by UHPC and prestressing tendons (Fig. 4.15d). The investigated total longitudinal reinforcement ratio ρ_{total} varied from 1.00% to 3.08%, while the reinforcement ratio for bonded tension steel, $\rho_{stension}$, varied from 0.49% to 2.57%. The unbonded reinforcement ratio, ρ_{ps}, was kept constant at 0.51%. Table 4.6 shows that while the influence of $\rho_{stension}$ on flexural capacity is not as strong as the influence of f_{cr} and ρ_{ps} for a given percentage change from the baseline values, $\rho_{stension}$ is still an influential factor on flexural capacity.

Table 4.6, Fig. 4.16d and 4.17d suggest that $\rho_{stension}$ has a similar effect with ρ_{ps} on cross-sectional and member level ductility with higher $\rho_{stension}$ values resulting in lower ductility although all twelve investigated beams met minimum cross-section level ductility requirements provided in American (ACI 318-19 2019 and AASHTO 2017) and Canadian standards (2019) for NSC and FRC, respectively. One of the beams exhibited a curvature-based cross-section level ductility of 2.08, which is close to the 2.0 Canadian limit (2019), however, this beam had a ρ_{total} of 3.08% and

a $\rho_{stension}$ of 2.57%, which suggest that the beam was heavily reinforced and the longitudinal reinforcement ratios were well beyond practical limits for NSC beams post-tensioned with unbonded tendons.

Table 4.6. Influence of $\rho_{stension}$ on flexural capacity and ductility

Beam ID	Loading configuration	ρ (%)		M_n (m-kN)	% change (Moment)	Cross-section level ductility		Member level ductility	
		ρ_{total}	$\rho_{stension}$			$\mu_\varepsilon = \frac{\varepsilon_u}{\varepsilon_y}$	$\mu_\phi = \frac{\phi_u}{\phi_y}$	$\mu_\Delta = \frac{\Delta_u}{\Delta_y}$	$\frac{L}{\Delta_u}$
B-1-As1	One Point	1.00	0.49	125	Baseline	4.48	3.30	1.65	109
B-1-As2	One Point	1.27	0.76	136	+8.46	4.30	3.15	1.52	110
B-1-As3	One Point	2.01	1.50	163	+30.56	4.24	2.88	1.35	123
B-1-As4	One Point	3.08	2.57	198	+58.58	3.82	2.08	1.15	137
B-1-As1	Two Point	1.00	0.49	128	Baseline	4.29	3.27	2.20	47
B-1-As2	Two Point	1.27	0.76	138	+7.55	4.27	3.17	2.00	49
B-1-As3	Two Point	2.01	1.50	163	+27.6	4.22	3.06	1.68	53
B-1-As4	Two Point	3.08	2.57	199	+55.16	4.15	2.89	1.34	59
B-1-As1	Distributed	1.00	0.49	132	Baseline	3.91	3.03	2.24	46
B-1-As2	Distributed	1.27	0.76	143	+8.46	3.87	3.02	2.20	48
B-1-As3	Distributed	2.01	1.50	180	+36.2	3.84	2.98	1.98	50
B-1-As4	Distributed	3.08	2.57	215	+62.94	3.79	2.97	1.85	53

$\rho_{total} = \rho_{stension} + \rho_{ps}$; $\rho_{stension} = A_{stension}/(b_w d_s)$; $\rho_{ps} = A_{ps}/(b_w d_{ps})$; $\rho_{min\_stension\_ACI} = 0.22\%$ ($A_{stension\_min\_ACI} = 0.004A_{ct}$)

4.5.5 Effect of loading configuration and tendon profile on complete flexural behavior

Table 4.7, Fig. 4.10e-f, 4.11e-f, and 4.13e illustrate the influence of loading configuration and tendon profile on the complete flexural behavior of UHPC beams post-tensioned with internal unbonded tendons. The beams with straight tendon profiles exhibit slightly higher ultimate tendon stress compared to beams with draped tendon profiles since the overall tendon deformation is larger when the tendon is closer to the most extreme tension fiber. This member level dependency results in slightly larger moment capacities at the ultimate limit state for beams with straight tendon profiles. However, these differences are marginal. This is the reason why many closed form formulations for f_{ps} do not include end eccentricity as part of the formulation. The greatest influence of tendon profile on moment capacity is exhibited in beams subject to a two point loading configuration (Table 4.7 and Fig. 4.13e) since in these beams there is a chance that the weakest

section is at the location of point loads rather than at mid-span due to the draping of the tendons and the reduced effective depth.

Table 4.7. Influence of tendon configuration on flexural capacity and ductility

Beam ID	Tendon config.	Loading config.	M_n (m-kN)	% change (Moment)	Cross-section level ductility		Member level ductility	
					$\mu_\varepsilon = \frac{\varepsilon_u}{\varepsilon_y}$	$\mu_\phi = \frac{\phi_u}{\phi_y}$	$\mu_\Delta = \frac{\Delta_u}{\Delta_y}$	$\frac{L}{\Delta_u}$
B-1S	straight	One Point	125	+0.04	4.62	3.40	1.71	114
B-1S	straight	Two Point	133	+6.77	4.42	3.17	2.56	40
B-1S	straight	Distributed	132	+5.57	4.55	3.23	2.70	48
B-1D	draped	One Point	125	Baseline	4.48	3.30	1.65	109
B-1D	draped	Two Point	128	+2.48	4.29	3.27	2.20	47
B-1D	draped	Distributed	132	+5.49	3.91	3.03	2.24	46

Table 4.7, Fig. 4.16e, and 4.17e suggest that the influence of loading configuration on ductility varies from mild to strong at the cross-section and member level, respectively. Tendon profile appears to have some effect on cross-section level ductility with beams featuring a straight tendon profile typically featuring higher ductility values compared to those with draped tendons. At the cross-section level, curvature ductility is barely influenced by loading configuration or tendon profile. Strain based cross-sectional ductility appears to be slightly influenced by loading configuration when draped tendon profiles are considered and barely influenced when beams with straight tendon configuration are considered. It is interesting how at the member level, loading configuration appears to have a marked difference with beams featuring a two point and distributed loading configurations possessing higher ductility than those with one point-loading configuration. This is especially evident in Fig. 4.17e.

In general, the most efficient approach to increase the flexural capacity of UHPC beams post-tensioned with unbonded tendons is to: 1) use a UHPC mix with high cracking strength and a minimum maximum usable tensile strain, 2) increase the area of the tendons, 3) or do both. While an increase in ε_{tu} increases the ductility of the beam at the cross-sectional and member level, it has a marginal effect on flexural capacity. An increase in mild steel area helps with flexural capacity,

but it is not as efficient as an increase in tendon area, which helps with the behavior of the member at all stages of loading including service by controlling deflections.

4.5.6 Effect of constitutive model for UHPC on complete flexural behavior

The influence of various constitutive models for UHPC on the complete flexural behavior of beams post-tensioned with internal unbonded tendons was investigated by considering three constitutive models for the compressive domain and 13 for the tensile domain (Fig. 4.4a). The impact of the various constitutive models is illustrated in Fig. 4.12 and Table 4.8. It is worth noting that the impact of the 12 additional constitutive models for the tensile domain of UHPC on flexural strength was contained to at most 8.6% change in nominal moment capacity (Table 4.8) compared to the default (bilinear) tensile curve.

Table 8. Influence of various constitutive models for UHPC on flexural strength and ductility

Beam ID	Tendon config.	Loading config.	M_n (m-kN)	% change (Moment)	Cross-section level ductility		Member level ductility	
					$\mu_\varepsilon = \frac{\varepsilon_u}{\varepsilon_y}$	$\mu_\phi = \frac{\phi_u}{\phi_y}$	$\mu_\Delta = \frac{\Delta_u}{\Delta_y}$	$\frac{L}{\Delta_u}$
Tension Domain								
B-1D-TD*	draped	One Point Loaded	125	Baseline	4.48	3.30	1.65	109
B-1D-T1	draped	One Point Loaded	133	5.97	2.43	1.95	1.51	112
B-1D-T2	draped	One Point Loaded	130	3.91	1.95	1.67	1.36	124
B-1D-T3	draped	One Point Loaded	136	8.57	4.38	3.33	1.72	102
B-1D-T4	draped	One Point Loaded	128	2.54	1.84	1.52	1.21	135
B-1D-T5	draped	One Point Loaded	125	-0.04	1.63	1.41	1.07	153
B-1D-T6	draped	One Point Loaded	135	7.88	3.16	2.60	1.79	97
B-1D-T7	draped	One Point Loaded	134	6.97	3.40	2.52	1.54	109
B-1D-T8	draped	One Point Loaded	133	6.61	2.65	2.09	1.54	109
B-1D-T9	draped	One Point Loaded	132	5.94	2.44	1.95	1.51	112
B-1D-T10	draped	One Point Loaded	132	5.93	2.55	2.02	1.51	112
B-1D-T11	draped	One Point Loaded	135	7.71	3.83	2.78	1.58	107
B-1D-T12	draped	One Point Loaded	132	5.27	2.30	1.86	1.47	115
Compression Domain								
B-1D-CD**	draped	One Point Loaded	279	Baseline	0.42	<1.0	<1.0	276
B-1D-C1	draped	One Point Loaded	325	16.64	2.62	2.01	1.27	140
B-1D-C2	draped	One Point Loaded	328	17.51	2.81	1.88	1.25	136

*TD = Default stress-strain curve in tension, T1 through T12= Tensile stress-strain curves 1-12; (Fig. 4.4a right)
** CD = Default stress-strain curve in compression, C1 and C2= Compression stress-strain curves 1 and 2, respectively (Fig. 4.4a left) ($\rho_{stension} = 0.49$ %; $\rho_{ps} = 3.06$ %; $\rho_{total} = 3.55$ %)

The use of UHPC formulations with strain hardening characteristics in the tensile domain (i.e. trilinear model) generally resulted in a decrease in ductility compared to the default bilinear model since in many of these cases the peak load was achieved prior to the attainment of the maximum usable tensile strain, ε_{tu}, for UHPC. However, there were a few trilinear constitutive models, which resulted in higher ductility compared to the baseline case. In general, the influence of the tensile domain on flexural strength and ductility is a function of the slope of the strain hardening branch and the slope of the descending branch after the peak tensile stress is achieved.

The consideration of the additional two stress-strain curves for UHPC in compression resulted in up to a 17.5% change in flexural capacity (Table 4.8). It should be noted that the failure mode for the beam specimen with the default stress-strain curve in compression was a compression-controlled failure and therefore the beam exhibits no ductility (i.e. ductility < 1). The inclusion of descending branches in compression switched the failure mode from compression controlled to steel tension-controlled, since the reinforcement yielded prior to the crushing of UHPC in compression. As a result, ductility increased in addition to the increase in flexural strength.

The proposed algorithm allows the modeling of various constitutive models for UHPC in tension and compression and uses that information to characterize cross-section and member level behavior.

4.5.7 Effect of no mild steel on subroutine

Unreinforced UHPC beams were modelled as draped and straight tendons. Validity of multiple crack formations were checked by comparing FEA and subroutine results. As seen in Fig. 4.18, total load versus deflection and tendon stress versus deflection from onset of loading to

ultimate load were captured by subroutine in case of post-tensioned UHPC beam without any mild steel reinforcement.

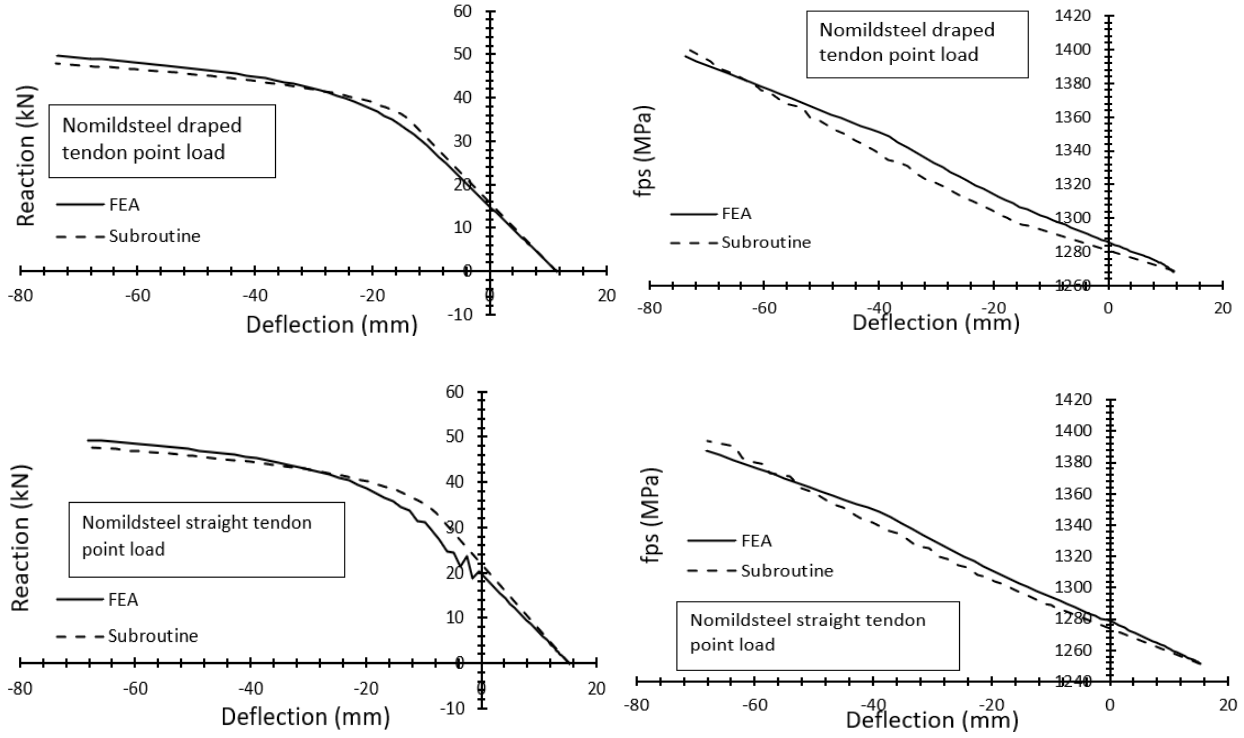

Fig. 4.18 Validation of unreinforced UHPC beam

4.6 Summary and Conclusions

A procedure for computing the moment curvature and load deformation response of UHPC beams post-tensioned with unbonded tendons was presented. The proposed procedure was validated using high fidelity nonlinear finite element analysis. A parametric study was conducted to understand the influence of various parameters on flexural capacity and ductility as well as on the full flexural behavior of UHPC beams post-tensioned with internal unbonded tendons. The following conclusions are drawn:

1) The proposed procedure is based on structural mechanics and is capable of reliably and efficiently computing the complete moment-curvature-deformation response of UHPC

beams post-tensioned with internal unbonded tendons and offers insight about their ductility at the cross-section and member level. This information is useful in cases when a performance-based design approach is selected and a characterization of member behavior under different load intensities is desired.

2) The proposed method does not require the definition of empirically obtained elastic and inelastic design parameters such as bond reduction coefficients and plastic hinge length. However, it can facilitate the use of approaches that employ these parameters by helping formulate them without having to rely on extensive experimental testing or time consuming finite element analysis.
3) Cross-section level ductility was generally higher than member level ductility. Additionally, strain-based computations resulted in higher levels of cross-section level ductility compared to curvature-based computations. Most beams met minimum cross-section level ductility requirements specified in American and Canadian standards for NSC and FRC, respectively.
4) The most influential parameter for cross-section level ductility is ε_{tu}. A minimum value of 0.006 is recommend for ε_{tu} to meet existing minimum ductility requirement set forth for NSC and FRC members. Additionally, while ε_{tu} is an important parameter related to the failure mode of UHPC beams post-tensioned with unbonded tendons, its variation does not cause a marked difference in flexural capacity.
5) The most influential parameter for member level ductility is the loading configuration especially when the ratio L/Δ_u was used as the metric for evaluating such ductility. The determination of deflection at incipient failure is indeed a useful metric for evaluating ductility at the member level and for serving as a warning of failure metric and the proposed

algorithm provides a tool for accurately estimating this deflection. The influence of loading configuration on cross-section level ductility was much smaller than that exhibited at the member level.

6) The most influential parameters in terms of increasing flexural capacity are the longitudinal unbonded reinforcement ratio, ρ_{ps}, followed by the UHPC cracking stress, f_{cr}, and the longitudinal bonded reinforcement ratio, $\rho_{stension}$, when the impact of these parameters for a given percentage change from the baseline case was considered. While a change in f_{cr} did not influence ductility at any level, and increase in ρ_{ps} and $\rho_{stension}$ resulted in a decrease in cross-section and member level ductility.

7) The influence of the constitutive models for the tensile and compressive domains was contained to a 8.6% and 17.5% change in flexural capacity when compared to the default stress-strain curves.

5. Punching Shear Strength of Post-tensioned UHPC Plates

5.1 INTRODUCTION

Punching shear is one of the controlling limit states in the design of post-tensioned flat plates and should be avoided due to its brittle nature and its potential to cause progressive collapse. The combination of ultra-high-performance concrete (UHPC) and unbonded post-tensioning provides an opportunity to create super thin and ultralight floor systems thus reducing the gravitational and seismic load demand on the entire structural system. The creation of such super slender elements warrants an investigation of their behavior under concentrated loads. The behavior of reinforced and post-tensioned concrete flat plates constructed with normal strength concrete (NSC) under concentrated loads has been investigated by Muttoni (2008) and Clement et al. (2012) and Clement et al. (2014) and that of fiber reinforced concrete (FRC) plates with nonprestressed reinforcement has been studied by Maya et al. (2012); Neto et al. (2014); and Gouveia et al. (2017). Similarly, the behavior of unreinforced UHPC plates under concentrated loads has been investigated by Joh et al. (2008), Harris (2004), and Harris and Roberts-Wollmann (2005). However, the behavior of punching critical post-tensioned UHPC flat plates under concentrated loads appears to be unexamined and provided the motivation for this study.

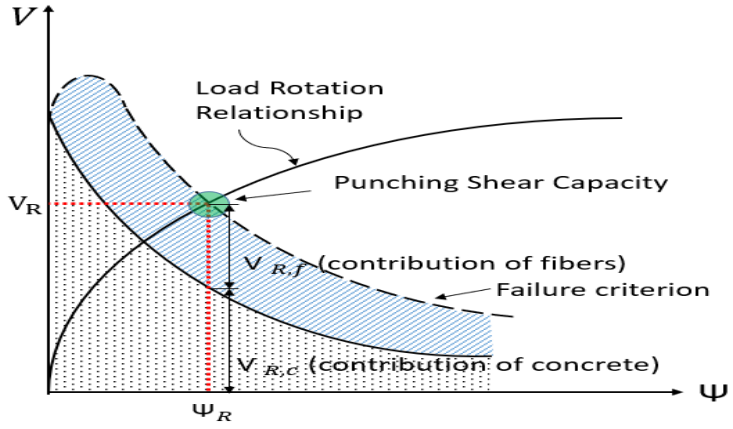

Fig. 5.1 Proposed framework for predicting punching shear capacity of PT UHPC plates

A methodology to predict the punching shear capacity of PT UHPC plates is presented and assumes that punching capacity is reached when a critical plate rotation is attained. The kinematics of a flat plate subject to concentrated loads are simplified with the purpose of creating a formulation to predict the load rotation relationship of the plate. This relationship is then superimposed with a rotation dependent failure criterion. The intersection of the two curves supplies the punching capacity of the plate as well as the critical plate rotation (Fig. 5.1). While the development of plate's load rotation relationship is based on principles of engineering mechanics, an empirical approach is used to develop the failure criterion by using a database of punching critical PT UHPC flat plate specimens. This approach was originally proposed by Kinnunen and Nylander (1960) for reinforced concrete flat plates and further developed by Hallgreen (1996), Broms (2006), and Muttoni (2008). Maya et al. (2012) and Neto et al. (2014) extended the method to FRC slabs with nonprestressed reinforcement, and Clement et al. (2012) and Clement et al. (2014) investigated the behavior of prestressed concrete slabs constructed with NSC. The purpose of this study is to extend this methodology to PT UHPC plates by providing a framework for how to obtain the PT UHPC plate load-rotation relationship and developing a rotation dependent failure criterion appropriate for such plates. An additional objective is the quantification of the impact of column size, plate thickness, prestressed and nonprestressed reinforcement ratio, tendon configuration, prestressing force, and fiber content and characteristics on plate punching capacity.

5.2 RESEARCH SIGNIFICANCE

There is currently no efficient method for obtaining the punching shear capacity of PT UHPC plates. The availability of such method is instrumental in facilitating PT UHPC flat plate designs and creating super slender and ultra-light floors that minimize building mass and offer large span

to depth ratios. A methodology to obtain the plate load rotation relationship is proposed and is informed by a simplified method to obtain the moment curvature relationship. The plate's load rotation relationship is superimposed with a rotation dependent failure criterion to supply the plate's punching and rotation capacity.

5.3 CREATION OF SPECIMEN DATABASE

Nonlinear finite element analyses were used to create a database of punching critical specimens because there are no punching shear tests available for PT UHPC plates. This database was used to validate a mechanics-based methodology for developing the plate load rotation relationship, as well as to inform the development of a nonlinear regression based failure criterion. The specimen database was created by first identifying the parameters that affect punching capacity and systematically changing them such that a large enough database of specimens was created to test the proposed prediction methodology as well as to gain an understanding of the impact of each parameter on the behavior of PT UHPC plates subject to concentrated loads. The UHPC plate and the hollow PT sheathings, which are embedded into the plate, are modeled using 8-node 3D continuum elements with reduced integration (C3D8R). The PT tendons are modeled using 2-node 3D truss elements (T3D2) and are inserted inside the PT sheathings. A friction coefficient is specified between the tendon and the sheathing in the direction of the axis of the tendon and a hard contact is defined in the perpendicular direction. PT anchorages are modeled using multi-point constraints (Dogu and Menkulasi 2020). The constitutive model for UHPC is selected based on the definition presented by the Federal Highway Administration (FHWA) (Haber et al. 2018), which states that: "*UHPC is a cementitious composite material composed of an optimized gradation of granular constituents, a water-to-cementitious materials ratio less than 0.25, and a high percentage of discontinuous internal fiber reinforcement. The mechanical*

properties of UHPC include compressive strength greater than 21.7 ksi (150 MPa) and sustained post-cracking tensile strength greater than 0.72 ksi (5 MPa)". The stress-strain curve for the compressive domain is based on recommendations by Graybeal (2007). Various stress-strain curves are considered for the tensile domain of UHPC including bilinear and trilinear (i.e. strain hardening) curves. The constitutive model for prestressing strands is based on recommendations by Devalapura and Tadros (1992) and non-prestressed reinforcement is modeled as elastic perfectly plastic with f_y = 414 MPa (60 ksi) and E=200 GPa (29000 ksi). Pinned and fixed edge plates are considered. The PT UHPC flat plat specimens are loaded monotonically to failure through the column using a displacement-controlled protocol. Table 5.1 shows the characteristics of the investigated specimens and Fig. 5.2 illustrates the modeling protocol, which is based on the approach used by Dogu and Menkulasi (2020) for PT UHPC beams.

Table 5.1 Characteristics of investigated PT UHPC plates

Range of variation								
h [mm] ([in.])	L [mm] ([in.])	s_c [mm] ([in.])	d_p [mm] ([in.])	ρ_{ps} (%)	ρ_s (%)	Tendon configuration	f_c' [MPa] ([ksi])	Boundaries
100-225 (3.9-9.8)	2000 (78.7)	100-300 (3.9-11.8)	70 – 200 (2.8-7.9)	0.07-1.32	0.04 – 5.8	Banded-Banded Banded-Distributed	91-153 (13.2-22.2)	Pin, fixed

h = plate thickness; L = plate width and length; s_c = column size; d_p = effective depth of prestressed reinforcement; ρ_{ps} = prestressed reinforcement ratio; ρ_s = nonprestressed reinforcement ratio; f'_c = UHPC compressive strength at 28 days

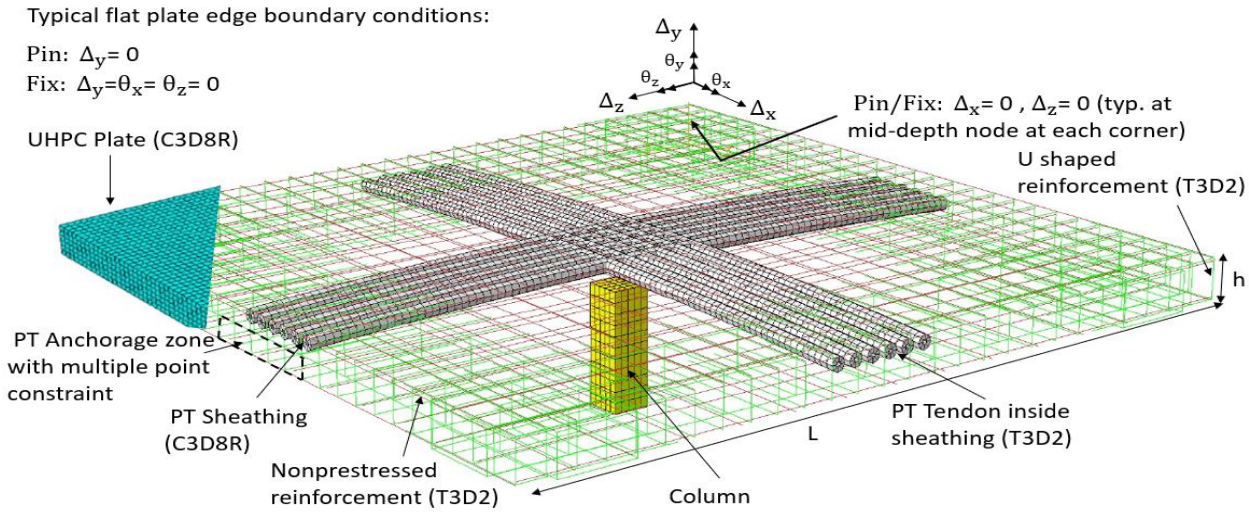

Fig. 5.2 Modelling approach for simulating the behavior of PT UHPC plates under concentrated loads

5.3.1 Distinction of Punching and Flexural Failures in the Numerical Model

Given that PT UHPC plates are likely to provide significant ductility, a criterion for distinguishing between punching and flexural failures was developed so that only flat plate specimens that failed in punching shear are used when developing and validating the proposed methodology. This criterion is based on the magnitude and location of principle tensile strains along the thickness of the plate and the maximum usable uniaxial tensile strain for UHPC. This approach is illustrated in Fig. 5.3, which shows a flat plate specimen controlled by a punching shear failure (Fig. 5.3a1-5.3c1) in which the peak load was attained when the maximum principal tensile strains in UHPC were created along the critical diagonal crack, and another specimen controlled by a flexural failure (Fig. 5.3a2 – 5.3c2), in which the maximum principle tensile strains when the peak load was achieved were created along the top fiber of the plate.

Fig. 5.3a shows the distribution of principal strains at failure in these two flat plate specimens. One features fixed edges (Fig. 5.3a1) and the other roller supported edges (Fig. 5.3a2). The evolution of the magnitude of the principal tensile strains in two finite elements is monitored and reported in Fig. 5.3b. Finite element, *a*, is located along the top fiber of the plate, where flexure induced principal tensile strains are expected to be maximum. Finite element, *b*, is located along the critical compression strut, where shear induced principal tensile strains are expected to be maximum. Fig. 5.3b1 suggests that the magnitude of the principal tensile strain in finite element *b* increases exponentially as the plate reaches its load carrying capacity. Conversely, the magnitude of the principal tensile strain in finite element *a* increases at a slower rate prior to the attainment of peak load and remains constant thereafter. Additionally, on average, the angle of inclination of the compressive struts, θ, in the specimen with fixed edges (θ_1) is higher than that in the specimens with free edges (θ_2). It should be noted that when the peak load is achieved, the principal tensile

strain in finite element *b* is 0.015, which is past the assumed fiber pullout limit of 0.01 based on the bilinear model shown in Fig. 5.3b1.

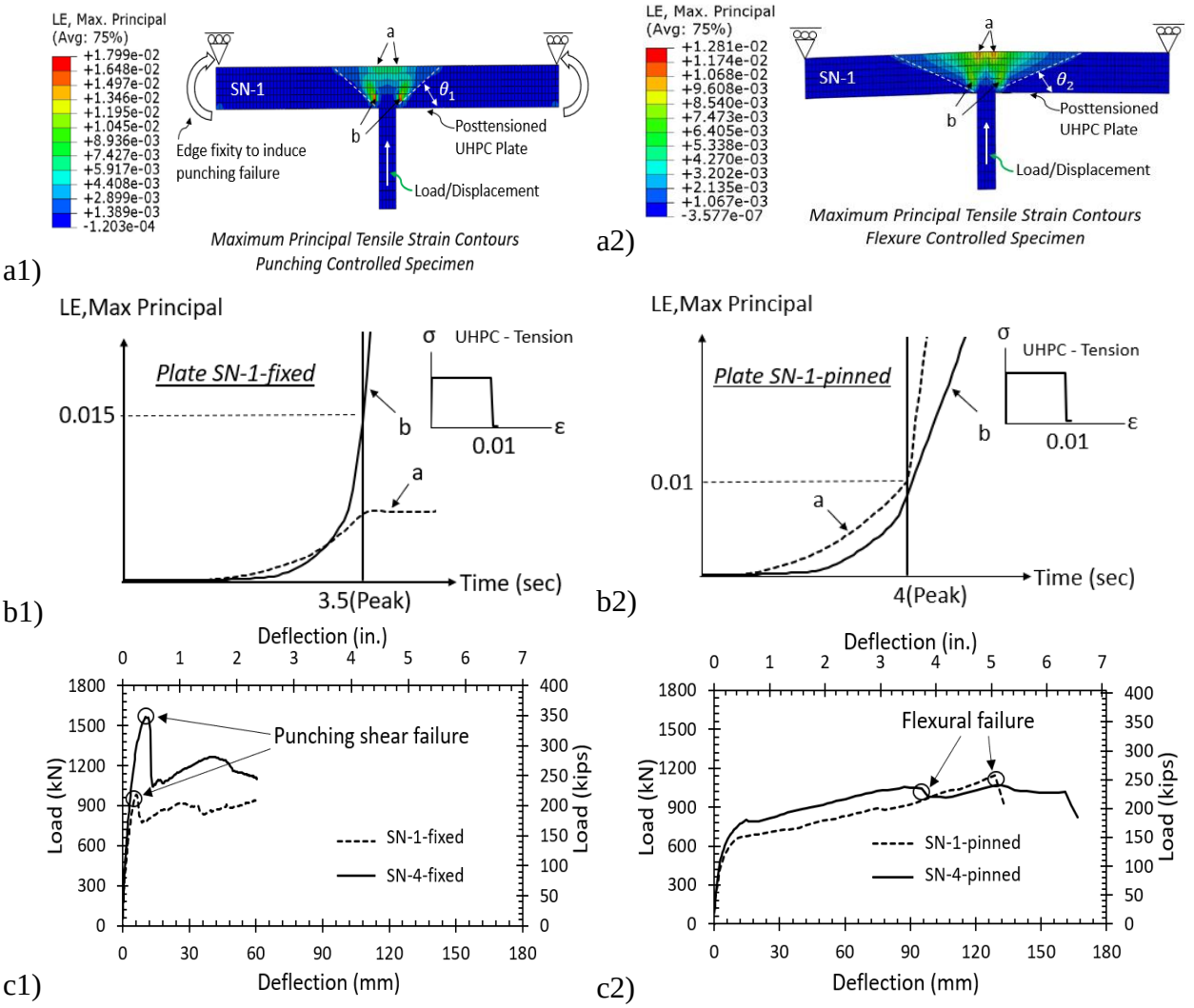

Fig. 5.3 a) PT UHPC plates subject to punching (a1) and flexural (a2) failures; b) variation of maximum principal tensile strain in punching (b1) and flexure (b2) critical plates; c) load-deflection relationship in punching (c1) and flexure (c2) critical plates.

This suggests that at this location, the fibers have pulled out, and the crack is progressing along the diagonal compressive strut. Also, Fig. 5.3c1 shows that the peak load for the plate with fixed edges is attained at small column displacements and that there is an abrupt reduction in capacity after the attainment of peak load, which is a characteristic of a punching shear failure.

The overall behavior of the plate with fixed edges suggests that its failure mode is controlled by punching shear.

Conversely, Fig. 5.3b2 suggests that in the specimen with roller supported edges, the magnitude of the principal tensile strain in finite element *a* increases more rapidly than that of finite element *b*, although the rate of increase in finite element *b* is also significant. Additionally, after failure, the rate of increase in finite element *a* continues to be more pronounced than that in finite element *b.* The peak load is achieved when the principal tensile strain in finite element *a* is 0.01, which is the fiber pullout limit in the assumed constitutive model. This suggest that a flexure failure has precipitated, characterized by crack formation and fiber pullout at the top of the plate. Also, as pointed out earlier, the average angle of inclination of the compressive struts in the specimen with roller supported edges is lower than that in the specimen with fixed edges further corroborating the presence of a flexure controlled failure. Based on these observations, the punching critical plate specimen database was created by selecting plates that were fixed at the edges, and monotonically loading them using small columns (Table 5.2) with the purpose of inducing a punching shear failure and documenting plate behavior

Table 5.2 Influence of several parameters on PT UHPC plate punching shear capacity

Plate ID	h [mm]	s_c [mm]	f_c' [MPa]	Prestressing				ρ_s (%)	Fibers				$P_{cr}{}^{FEA}$ [kN]	$P_{cr}{}^{P}$ [kN]	$\frac{P_{cr}{}^{FEA}}{P_{cr}{}^{P}}$
				Tendon[a]	ρ_{ps} (%)	f_{pe} (% f_{pu})	d_p [mm]		%	d_f [mm]	l_f [mm]	Type			
Effect of plate thickness (h)															
ST-1	100	100	150	Band.	0.38	70	80	0.84	2	0.3	16.5	straight	697	711	0.98
ST-2	125	100	150	Band.	0.33	70	90	0.65	2	0.3	16.5	straight	983	950	1.03
ST-3	150	100	150	Band.	0.24	70	125	0.53	2	0.3	16.5	straight	1319	1311	1.01
ST-4	175	100	150	Band.	0.30	70	150	0.45	2	0.3	16.5	straight	1679	1669	1.01
ST-5	200	100	150	Band.	0.17	70	175	0.39	2	0.3	16.5	straight	2086	2046	1.02
ST-6	225	100	150	Band.	0.15	70	200	0.34	2	0.3	16.5	straight	2564	2228	1.13
Effect of column size (s_c)															
SN-1	125	100	150	Band.	0.33	70	90	0.65	2	0.3	16.5	straight	983	950	1.03
SN-2	125	150	150	Band.	0.33	70	90	0.65	2	0.3	16.5	straight	1214	1075	1.13
SN-3	125	200	150	Band.	0.33	70	90	0.65	2	0.3	16.5	straight	1421	1185	1.20
SN-4	125	250	150	Band.	0.33	70	90	0.65	2	0.3	16.5	straight	1601	1304	1.23
SN-5	125	300	150	Band.	0.33	70	90	0.65	2	0.3	16.5	straight	1714	1442	1.19
Effect of d_p															
SH-1	125	100	150	Band.	0.33	70	70	0.65	2	0.3	16.5	straight	968	858	1.13

SH-2	125	100	150	Band.	0.33	70	80	0.65	2	0.3	16.5	straight	975	904	1.08
SH-3	125	100	150	Band.	0.33	70	85	0.65	2	0.3	16.5	straight	982	926	1.06
SH-4	125	100	150	Band.	0.33	70	90	0.65	2	0.3	16.5	straight	983	950	1.03
SH-5	125	100	150	Band.	0.33	70	95	0.65	2	0.3	16.5	straight	985	968	1.02
SH-6	125	100	150	Band.	0.33	70	100	0.65	2	0.3	16.5	straight	991	988	1.00
Effect of ρ_{ps}															
SP-1	125	100	150	Band.	0.07	70	90	0.65	2	0.3	16.5	straight	883	646	1.37
SP-2	125	100	150	Band.	0.13	70	90	0.65	2	0.3	16.5	straight	916	735	1.25
SP-3	125	100	150	Band.	0.19	70	90	0.65	2	0.3	16.5	straight	942	817	1.15
SP-4	125	100	150	Band.	0.26	70	90	0.65	2	0.3	16.5	straight	968	888	1.09
SP-5	125	100	150	Band.	0.33	70	90	0.65	2	0.3	16.5	straight	983	950	1.03
SP-6	125	100	150	Band.	0.41	70	90	0.65	2	0.3	16.5	straight	1001	1035	0.97
SP-7	125	100	150	Band.	0.49	70	90	0.65	2	0.3	16.5	straight	1021	1115	0.92
SP-8	125	100	150	Band.	0.58	70	90	0.65	2	0.3	16.5	straight	1038	1200	0.86
SP-9	125	100	150	Band.	0.66	70	90	0.65	2	0.3	16.5	straight	1045	1252	0.83
SP-10	125	100	150	Band.	0.83	70	90	0.65	2	0.3	16.5	straight	1082	1252	0.86
SP-11	125	100	150	Band.	0.99	70	90	0.65	2	0.3	16.5	straight	1105	1252	0.88
SP-12	125	100	150	Band.	1.16	70	90	0.65	2	0.3	16.5	straight	1137	1252	0.91
SP-13	125	100	150	Band	1.32	70	90	0.65	2	0.3	16.5	straight	1168	1252	0.93
Effect of f_{pe}															
SP-0	125	100	150	Band.	0.33	0	90	0.65	2	0.3	16.5	straight	857	603	1.42
SP-14	125	100	150	Band.	0.33	14	90	0.65	2	0.3	16.5	straight	888	682	1.30
SP-28	125	100	150	Band.	0.33	28	90	0.65	2	0.3	16.5	straight	918	764	1.20
SP-42	125	100	150	Band.	0.33	42	90	0.65	2	0.3	16.5	straight	943	833	1.13
SP-56	125	100	150	Band.	0.33	56	90	0.65	2	0.3	16.5	straight	967	897	1.08
SP-70	125	100	150	Band.	0.33	70	90	0.65	2	0.3	16.5	straight	983	950	1.03
Effect of tendon configuration															
SF-1	125	100	150	Band.	0.33	70	90	0.65	2	0.3	16.5	straight	983	950	1.03
SF-2	125	100	150	Dist.	0.33	70	90	0.65	2	0.3	16.5	straight	964	950	1.01
Effect of ρ_s															
SS-1	125	100	150	Band.	0.33	70	90	0.04	2	0.3	16.5	straight	920	827	1.11
SS-2	125	100	150	Band.	0.33	70	90	0.16	2	0.3	16.5	straight	932	856	1.09
SS-3	125	100	150	Band.	0.33	70	90	0.36	2	0.3	16.5	straight	957	899	1.06
SS-4	125	100	150	Band.	0.33	70	90	0.65	2	0.3	16.5	straight	983	950	1.03
SS-5	125	100	150	Band.	0.33	70	90	1.01	2	0.3	16.5	straight	1003	1003	1.00
SS-6	125	100	150	Band.	0.33	70	90	1.45	2	0.3	16.5	straight	1030	1053	0.98
SS-7	125	100	150	Band.	0.33	70	90	1.97	2	0.3	16.5	straight	1055	1099	0.96
SS-8	125	100	150	Band.	0.33	70	90	2.58	2	0.3	16.5	straight	1074	1126	0.95
SS-9	125	100	150	Band.	0.33	70	90	3.27	2	0.3	16.5	straight	1085	1150	0.94
SS-10	125	100	150	Band.	0.33	70	90	4.04	2	0.3	16.5	straight	1097	1175	0.93
SS-11	125	100	150	Band.	0.33	70	90	4.88	2	0.3	16.5	straight	1105	1231	0.90
SS-12	125	100	150	Band.	0.33	70	90	5.81	2	0.3	16.5	straight	1111	1243	0.89
Effect of fiber content and characteristics[d]															
UA2	125	100	112	Band.	0.33	70	90	0.65	2	0.55	30	end def	770	843	0.91
UA3	125	100	105	Band.	0.33	70	90	0.65	3	0.55	30	end def	897	888	1.01
UB2	125	100	150	Band.	0.33	70	90	0.65	2	0.3	16.5	straight	983	950	1.03
UB3.25	125	100	101	Band.	0.33	70	90	0.65	3.25	0.3	16.5	straight	949	921	1.03
UC2	125	100	94	Band.	0.33	70	90	0.65	2	0.3	13	straight	706	816	0.86
UC4.5	125	100	132	Band.	0.33	70	90	0.65	4.5	0.3	13	straight	845	905	0.93
UE2	125	100	119	Band.	0.33	70	90	0.65	2	0.2	13	straight	898	925	0.97
UE3.25	125	100	120	Band.	0.33	70	90	0.65	3.25	0.2	13	straight	1007	999	1.02
UD2C1	125	100	94	Band.	0.33	70	90	0.65	2	0.2	13	straight	822	883	0.93
UD2C7	125	100	128	Band.	0.33	70	90	0.65	2	0.2	13	straight	931	952	0.98
UD3C1	125	100	91	Band.	0.33	70	90	0.65	3	0.2	13	straight	840	929	0.90
UD3C7	125	100	126	Band.	0.33	70	90	0.65	3	0.2	13	straight	1016	1019	1.00

UD4C1	125	100	100	Band.	0.33	70	90	0.65	4	0.2	13	straight	1013	1049	0.97
UD4C7	125	100	124	Band.	0.33	70	90	0.65	4	0.2	13	straight	1160	1125	1.03

Note: 1 mm = 0.00394 in.; 1 MPa = 0.145 ksi; 1 kN = 0.225 kips; L = plate length = 2000 mm (78.7 in.); d_f = fiber diameter; l_f = fiber length; P_{cr}^{FEA} = computed punching shear capacity; P_{cr}^{P} = predicted punching shear capacity; [a]six tendons in each direction unless otherwise noted, Band = Banded-Banded, Dist. = Banded-Distributed; [b]mild steel top and bottom in each direction; [c] very high displacement is induced for pin cases, tendon ruptured at peak load before punching occurred; [d]details regarding fiber content, characteristics, and UHPC formulation are provided in reference (Haber et al. 2018)

5.3.2 Validation of Numerical Modeling Protocol

A total of 16 models of tested PT flat plates constructed with NSC and subject to concentrated loads were created with the purpose of demonstrating the capability of the modeling protocol to accurately simulate the behavior of such plates. Experimental data on the tested flat plates were obtained from Silva et al. (2007). Fig. 5.4a provides a comparison of measured and predicted plate load rotation relationship. It should be noted that the magnitude of measured mid-plate displacement at failure is extremely small (only a few millimeters) due to the brittle nature of the punching shear failure in NSC plates. Fig. 5.4a suggests that the numerical modeling protocol is able to capture with good accuracy the complete load versus mid-plate displacement relationship despite the small magnitude of plate deformation at failure.

Similarly, numerical models of tested unreinforced UHPC flat plates subject to concentrated loads were created to demonstrate the ability of the numerical modeling protocol to accurately simulate UHPC plate behavior. Experimental data on the tested UHPC flat plates were obtained from Joh et al. (2008). Fig. 5.4b shows a comparison of measured and computed plate load deflection relationship and suggests that there is good agreement between the two. Contrary to the behavior of PT NSC flat plates, UHPC flat plates exhibit a much more ductile behavior exhibiting mid-plate displacements at failure that are several times higher than those in NSC specimens.

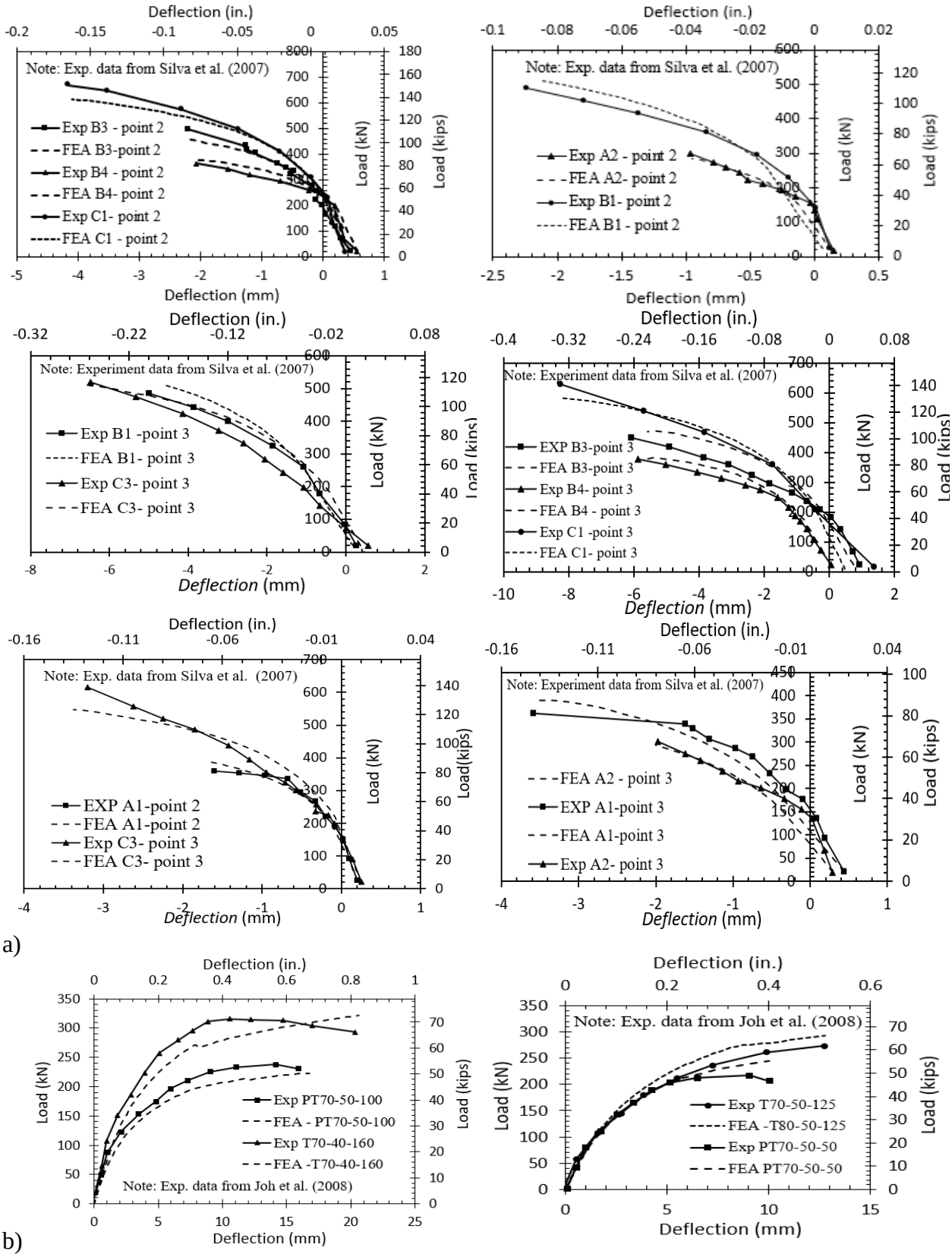

Fig. 5.4 Validation of numerical modeling protocol - comparison of computed and measured plate load-deflection relationship for: a) PT NSC plates; b) unreinforced UHPC plates

The similarity between experimental and numerical curves suggests that the adopted modeling protocol can predict with good accuracy not only the punching capacity of these plates, but also the full range of behavior from the onset of loading to failure. Using deductive reasoning in the absence of experimental data on PT UHPC flat plates, it is concluded that since the modeling protocol is able to capture with good accuracy the behavior of unreinforced UHPC plates and PT plates constructed with NSC subject to concentrated loads, it should be able to capture with good accuracy the behavior of PT UHPC plates subject to similar loading conditions.

5.4 PROPOSED PREDICTION METHODOLOGY

In the proposed prediction methodology, the plate's load rotation-relationship is superimposed with a rotation dependent failure criterion. The intersection of the two curves supplies punching capacity and the rotation of the plate when punching occurs. Plate's load-rotation relationship is obtained by simplifying the kinematics of a column supported plate and utilizing a quadrilinear moment curvature relationship. The failure criterion is obtained using nonlinear regression based on the specimen database discussed in the previous section. An adjustment for plate rotation proposed by Clement et al. (2014) for PT NSC plates is evaluated in terms of its appropriateness for PT UHPC plates. A criterion is proposed to distinguish between flexure and punching induced failures. The vertical contribution of prestressing force (V_p) is neglected due to the small thickness of the plate and the fact that the tendon angle between centerline of column and critical punching shear section is negligible.

5.4.1 Load-Rotation Relationship

The approach for calculating the punching capacity of a column supported plate is to define a plate region, which together with the column can be isolated from the rest of the slab for further

analysis. The geometry of this plate region is defined by the distance from the column centerline to the inflection point in each plate direction, r_s. For a plate with fixed boundary conditions, this inflection point may be taken as *0.25L* where *L* is the overall length of the plate with the distance from column to plate edge support being 0.5*L*. If the plate is roller supported at the edge, then the inflection point may be taken as *0.5L* (i.e. equal to the distance from column to plate edge support). For a plate supported my multiple columns, an elastic analysis can be conducted to determine the location of the inflection point. The isolated rectangular plate supported by a rectangular column is then converted into an equivalent circular plate supported by an equivalent circular column. This conversion is conducted by keeping the perimeter of the elements the same. For example, a square column with a width of s_c can be converted into an equivalent circular column with a radius of $r_c=2s_c/\pi$. The plate is then assumed to be loaded through the column while being roller supported at the perimeter.

The plate's load rotation relationship shown in the general form in Eq. 5.1 and mathematically simplified in Eq. 5.2 can be obtained by isolating a typical plate pie strip with an angle $\triangle\theta$, drawing the free body diagram, and summing moments about the critical shear crack (Fig 5.5). The punching capacity of the plate can be obtained by summing the load capacities of all pie strips. In Eq. 5.1, V_L is the total concentrated load applied to the plate; r_c and r_q are distances from the centerline of column to face of column and to plate edge support, respectively (Fig. 5.5); m_r, m_p, and m_t are radial, prestressing, and tangential moments, respectively; and r_o and r_m are distances from the centerline of column to the top of critical shear crack, and to the location of moment caused by prestressing, respectively.

The critical shear crack is assumed to occur at a distance r_o from the centerline of the column (Fig. 5.5a), which can be calculated as $r_o=r_c+d$, where *d* is the average effective depth of

nonprestressed reinforcement. The radii that define the regions that have cracked, r_{cr}, and the region where the nonprestressed reinforcement has yielded, r_y, can be calculated as $r_{cr} = \frac{\Psi}{\varphi_{cr}}$ and $r_y = \frac{\Psi}{\varphi_y}$ (Eq. 5.3) if both radii are greater than radius of critical shear crack, r_o. In Eq. 5.3, φ_{cr} and φ_y are plate curvatures at first crack and first yield of nonprestressed reinforcement, respectively, and Ψ is plate rotation. As the rotation of the plate changes, the radii that define cracking and yielding regions change. The radii for the cracking and yielding zones are limited to the radius of the equivalent circular plate, r_s, (Eq. 5.3).

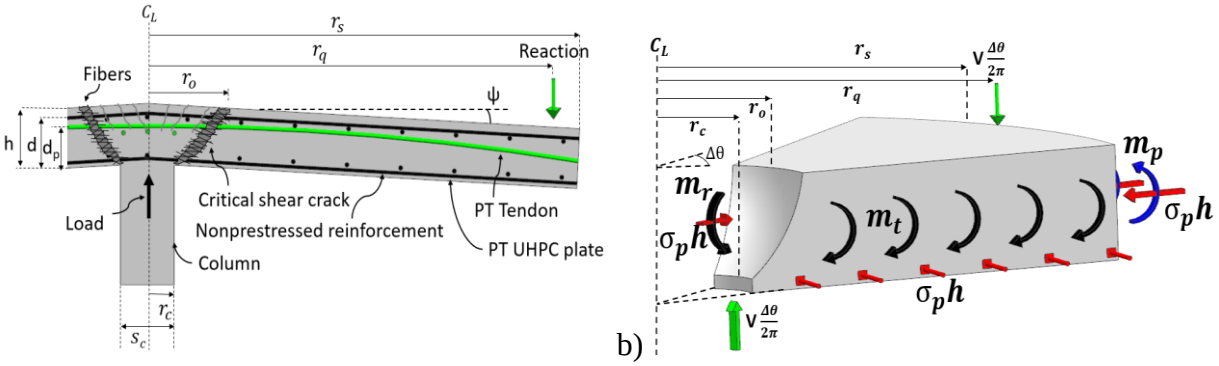

Fig. 5.5 a) Simplified plate kinematics at punching shear failure, b) internal and external forces acting on a typical plate pie strip.

Since the establishment of equilibrium in a typical plate pie strip requires the consideration of radial, m_r, tangential, m_t, and prestressing, m_p, moments, integration is required provided that tangential moments vary along the sides of the strip for a given load. The variation of tangential moments is a function of curvature, which in turn is a function of plate rotation. Curvature can be calculated as a function of plate rotation assuming that the deflected shape of the plate is conical outside the critical shear crack. Therefore, plate rotation in regions where $r > r_o$ can be calculated using Eq. 5.4, which assumes that radial curvature in this region is negligible. For the region where $r \leq r_o$ plate rotation can be calculated using Eq. 5.5, which assumes that curvatures in the radial, φ_r, and tangential, φ_t, direction are constant.

Once the variation of tangential curvature is determined, the variation of tangential moments can be obtained using the quadrilinear moment-curvature relationship shown in Fig. 5.6. The obtention of this relationship is discussed in subsequent section. Using this relationship, the load rotation relationship shown in Eq. 5.1 can be simplified as shown in Eq. 5.2. It should be noted that in Eq. 5.1 the unit radial moment m_r is present at the critical shear crack and can be different from the ultimate moment capacity of the plate; the unit tangential moment m_t is present along the sides of the strip; and the unit prestressing moment m_p created due to the eccentricity of the prestressing force is present at the critical shear crack, around the perimeter of the equivalent circular plate, as well as along the sides of the typical pie strip. These unit moments are multiplied with the distances in which they apply to obtain total internal moments. The total internal moment is then equated to the external moment to establish equilibrium (Eq. 5.1-5.2).

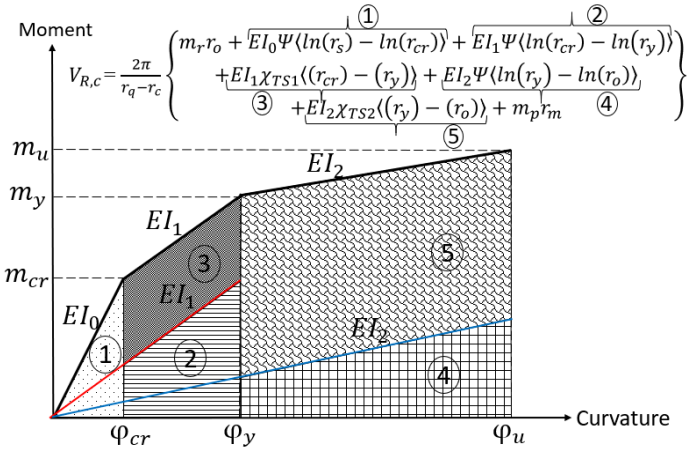

Fig. 5.6 Proposed moment-curvature relationship for PT UHPC elements used in the derivation of plate load-rotation relationship

The terms EI_o, EI_1, EI_2, in Eq. 5.2 represent flexural stiffnesses for a typical PT UHPC plate strip of unit width before cracking, EI_o, after cracking and before yielding of nonprestressed reinforcement, EI_1, and after yielding of nonprestressed reinforcement and before the attainment of ultimate moment capacity, EI_2, as shown in Fig. 5.6. These flexural stiffnesses are used to

determine the variation of the internal moment as a function of the variation of curvature and plate rotation. The operator $\langle x \rangle$ is x for x$>$ 0 and 0 for x$\leq$ 0.

The integration of the trapezoidal area between cracking and nonprestressed reinforcement yielding zones in the moment curvature relationship in Fig. 5.6 is represented using the two EI_1 terms in Eq. 5.2. The second EI_1 term includes the parameter χ_{TS1} , which represents the curvature difference in the EI_1 region and it can be found using Eq. 5.6 where m_y is the yield moment. Similarly, the integration of the trapezoidal shape between the regions of nonprestressed reinforcement yielding and attainment of ultimate moment capacity is represented using the two EI_2 terms. The second EI_2 term includes the parameter χ_{TS2}, which represents the curvature difference in the EI_2 region and can be found using Eq. 5.7, where φ_r is the curvature in the tangential direction. The prestressing moment, m_p, that is part of the last term in Eq. 5.2, can be calculated using Eq. 5.8, and is expressed as a function of the unit normal force, n, due to prestressing, average tendon eccentricity, e, plate thickness, h, and average effective depth of nonprestressed reinforcement, d. Unit normal force is calculated as $n = \frac{P_{ps}}{L}$ where P_{ps} is the total prestressing force, and L is the length of the plate.

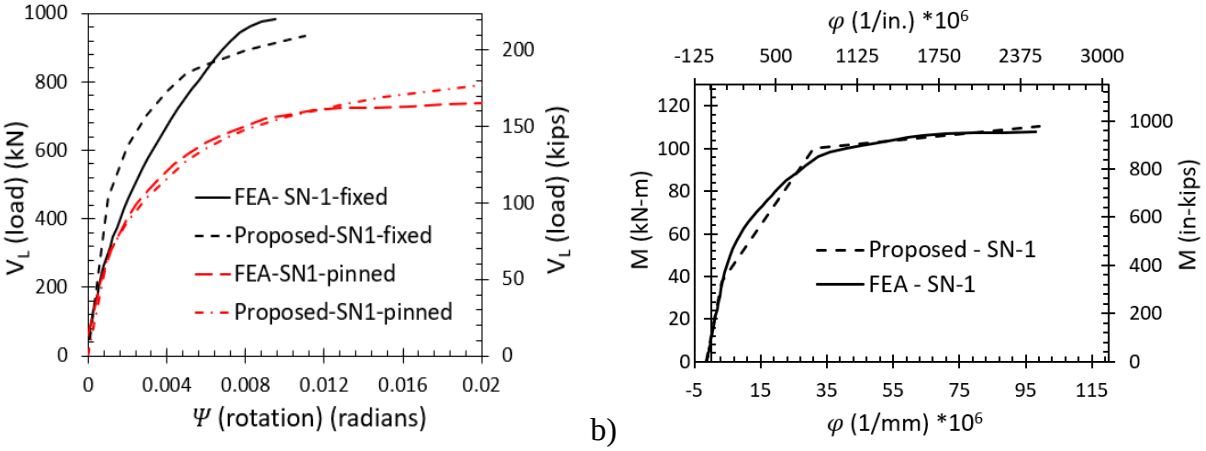

Fig. 5.7 Comparison of computed and predicted: a) plate load-rotation relationship; b) mid-plate moment-curvature relationship (per unit width of plate)

The PT UHPC plate load rotation relationship obtained using the proposed method was compared with that obtained using the validated numerical modeling protocol for roller-supported and fixed-supported plates with the characteristics shown in Fig. 5.7a. Fig. 5.7a suggest that the proposed method is able to capture accurately the load rotation relationship of PT UHPC plates.

$$V_L \frac{\Delta\theta}{2\pi}(\mathrm{r_q} - \mathrm{r_c}) = \mathrm{m_r}\Delta\theta\mathrm{r_o} + \mathrm{m_p}\Delta\theta\mathrm{r_m} + \Delta\theta \int_{\mathrm{r_o}}^{\mathrm{r_s}} \mathrm{m_t dr} \quad \text{Eq. 5.1}$$

$$V_L = \frac{2\pi}{r_q - r_c}\begin{Bmatrix} m_r r_o + EI_0\Psi\langle ln(r_s) - ln(r_{cr})\rangle + EI_1\Psi\langle ln(r_{cr}) - ln(r_y)\rangle \\ +EI_1\chi_{TS1}\langle (r_{cr}) - (r_y)\rangle + EI_2\Psi\langle ln(r_y) - ln(r_o)\rangle \\ +EI_2\chi_{TS2}\langle (r_y) - (r_o)\rangle + m_p r_m \end{Bmatrix} \quad \text{Eq. 5.2}$$

$$\mathrm{r_o} \le \frac{\Psi}{\varphi_{\mathrm{cr}}} \le \mathrm{r_s} \qquad \mathrm{r_o} \le \frac{\Psi}{\varphi_{\mathrm{y}}} \le \mathrm{r_s} \quad \text{Eq. 5.3}$$

$$\Psi = \varphi_{\mathrm{t}}\mathrm{r} \qquad \text{for } \mathrm{r} > \mathrm{r_o} \quad \text{Eq. 5.4}$$

$$\Psi = \varphi_t r_o = \varphi_r r_o \quad \text{for r} \le r_o \quad \text{Eq. 5.5}$$

$$\chi_{TS1} = \frac{m_y}{EI_1} - \varphi_y \quad \text{Eq. 5.6}$$

$$\chi_{TS2} = \frac{m_r}{EI_2} - \varphi_r \quad \text{Eq. 5.7}$$

$$\mathrm{m_p} = \mathrm{n}\left(\frac{\mathrm{h}^2}{12\left(\mathrm{d} - \frac{\mathrm{h}}{2}\right)} + \mathrm{e}\right) \quad \text{Eq. 5.8}$$

5.5 Moment Curvature

The moment curvature relationship of a typical PT UHPC plate strip of unit width can be characterized by four distinct phenomena (i.e. the application of prestress, the cracking of concrete, the yielding of nonprestressed reinforcement, and the attainment of ultimate moment capacity) (Fig. 5.6). The initial moment and curvature due to prestress and self-weight can be calculated using linear elastic engineering mechanics based on transformed section properties and the effective prestress. Similarly, moment and curvature at first cracking can be calculated assuming

material linearity, selecting a cracking stress for UHPC, and assuming that the stress in the strands is equal to the effective prestress. In reality, the stress in the strands at first cracking is slightly larger than the effective prestress, however, this difference was found to be negligible. The calculation of the ultimate moment and curvature can be obtained using the methodology proposed by Dogu and Menkulasi (2020), which is based on a collapse mechanism approach and requires the calculation of a plastic hinge length to determine the stress in the strands at the ultimate limit state, f_{ps}. The calculation of moment and curvature when the non-prestressed reinforcement yields, is calculated by reducing, f_{ps}, using a coefficient, κ. The values for κ were determined by using a database of specimens for which strand stress values at the ultimate limit state as well as at first yield were available from nonlinear finite element analysis (NLFEA). The average ratio and COV between strand stress at first yield and that at ultimate were 0.98 and 1%, respectively, suggesting notable consistency and justifying the use a single numerical value to slightly reduce ultimate strand stress. Moment curvature diagrams obtained using the proposed methodology were compared with those obtained from NLFEA and are shown in Fig. 5.7b. Fig. 5.7b suggests that the proposed approach provides a reasonable approximation of the plate's moment curvature relationship.

5.6 Failure Criteria

The proposed punching shear failure criterion represents the punching capacity of the plate, V_R, as the summation of the contribution provided by concrete, $V_{R,c}$, and fibers, $V_{R,f}$, (Eq. 5.9) both of which are rotation dependent. The contribution of the concrete strength to the plate's punching capacity, $V_{R,c}$, can be obtained using Eq. 5.10, where b_0 is control perimeter calculated at a distance $0.5d$ away from face of column, which can be obtained as $b_0 = 4b_c + \pi d$ (where b_c is column

width); f_c' is the UHPC compressive strength; $d_{g,0}$ is the reference aggregate size, which can be taken as 16 mm (0.63 in.); d_g is the aggregate size, which for UHPC can be taken as zero due to the lack of course aggregates; and $\Psi'$is the adjusted plate rotation, which can be calculated using Eq. 5.11 (Clement et al. 2014). The plate rotation, Ψ', is expressed as a function of the rotation of a non-prestressed plate, Ψ', minus $45\frac{\sigma_n}{E_c}$, which represents the increase in plate flexural stiffness due to the presence of post-tensioning. This term is expressed as a function of the ratio of the average compressive stress in UHPC due to prestressing, σ_n, and the modulus of elasticity of the concrete, E_c. Average UHPC compressive stress is calculated as $\sigma_n = \frac{P_{ps}}{Lh}$ where P_{ps} is the prestressing force, *L* is the length of the plate, and *h* is the thickness of the plate.

The coefficient 1.25 (15) was derived using nonlinear regression using the specimen database described earlier such that the intersection of proposed failure criterion and proposed plate rotation relationship resulted in punching capacities that matched those from NLFEA.

$$V_R = V_{R,c} + V_{R,f} \quad \text{Eq. 5.9}$$

$$\frac{V_{R,c}}{b_0 d\sqrt{f_c'}} = \frac{1.25}{1+15\frac{\Psi' d}{d_{g,0}+d_g}} \quad \text{(SI units: N, mm)}$$

$$\frac{V_{R,c}}{b_0 d\sqrt{f_c'}} = \frac{15}{1+15\frac{\Psi' d}{d_{g,0}+d_g}} \quad \text{(U.S. customary units: psi, in.)} \quad \text{Eq. 5.10}$$

$$\Psi' = \Psi - 45\frac{\sigma_n}{E_c} \geq 0 \quad \text{Eq. 5.11}$$

The contribution of fibers to the punching capacity of the plate, $V_{R,f}$, can be obtained using Eq. 5.12 based on the variable engagement model (Voo et al. 2010) except that the plate rotation is replaced with the adjusted plate rotation, Ψ', formulation proposed by Clement et al. (2014) for PT NSC plates. This contribution can be quantified by integrating the fiber bridging stress, σ_{tf}, over the projected cracked area, A_p. Fiber bridging stress is a function of crack width, *w*, which in

turn is a function of the adjusted plate rotation and the distance from the bottom of the plate, ξ. To simplify calculations, the varying fiber bridging stress can be replaced with the average fiber bridging stress, which may be obtained at a distance *d/3* from the bottom of the plate, and for which the corresponding crack width becomes $\frac{\Psi' d}{6}$. This average fiber bridging stress, σ_{tf}, may be obtained using Eq. 5.13 where K_f is the global orientation factor, α_f is the aspect ratio of fibers (ratio of fiber length, l_f, to fiber diameter, d_f, (Eq. 5.17)), ρ_f is the fiber reinforcement ratio by volume, and τ_b is the bond stress between the concrete matrix and fibers. The global orientation factor, K_f, can be obtained using Eq. 5.14, where the crack width, *w*, can be taken as, $\frac{\Psi' d}{6}$, α_I is the engagement parameter, and l_f is the length of fibers. The engagement parameter α_I can be calculated using Eq. 5.16 for straight and hooked fibers as a function of fiber aspect ratio (Eq. 5.17). Eq. 5.13 was derived assuming that the failure mode for the tensile domain of UHPC is fiber pullout rather than fiber fracture as expressed in Eq. 5.18, where σ_{fu} is the fiber tensile strength, and τ_b is the fiber bond stress. The fiber bond stress, τ_b, which can be calculated using Eq. 5.15, is a function of the bond factor k_b, which can be taken as 1.0 for end hooked fibers and 0.6 for straight fibers (Voo et al. 2010). When Eq. 5.13-5.18 are substituted into Eq. 5.12, Eq. 5.19 is obtained. The rotation dependent failure criteria for concrete and fibers may be substituted in Eq. 5.9 to express the punching capacity of the plate as a function of plate rotation. This expression together with the load rotation relationship can be solved simultaneously either graphically or mathematically to obtain plate rotation and punching capacity. Detailed example can be found in Appendix B.

$$V_{R,f} = \int \sigma_{tf}\big(w(\xi)\big)\,dA_p = \int \sigma_{tf}\left(w = \frac{\Psi' d}{6}, \xi\right) dA_p \qquad \text{Eq. 5.12}$$

$$\sigma_{tf} = K_f . \alpha_f . \rho_f . \tau_b \qquad \text{Eq. 5.13}$$

$$K_f = \frac{1}{\pi}\arctan\left(\frac{w}{\alpha_I l_f}\right)\left(1-\frac{2.w}{l_f}\right)^2 \quad \text{Eq. 5.14}$$

$$\tau_b = k_b\sqrt{f'_c} \quad \text{(SI units: N/ mm}^2\text{)}$$

$$\tau_b = 12.5k_b\sqrt{f'_c} \quad \text{(U.S. customary units: lb/ in.}^2\text{)} \quad \text{Eq. 5.15}$$

$$\alpha_I = \frac{1}{3.5\alpha_f} \quad \text{Eq. 5.16}$$

$$\alpha_f = \frac{l_f}{d_f} \quad \text{Eq. 5.17}$$

$$l_f < l_{crit} = \frac{d_f\sigma_{fu}}{2\tau_b} \quad \text{Eq. 5.18}$$

$$\frac{V_{R,f}}{b_0 d\sqrt{f'_c}} = \frac{1}{\pi}\arctan\left(3.5\frac{\Psi' d}{6d_f}\right)\left(1-\frac{\Psi' d}{3l_f}\right)^2 \alpha_f.\rho_f.k_b \quad \text{(SI units: MPa, mm)} \quad \text{Eq. 5.19}$$

$$\frac{V_{R,f}}{b_0 d\sqrt{f'_c}} = 12.5^2\frac{1}{\pi}\arctan\left(3.5\frac{\Psi' d}{6d_f}\right)\left(1-\frac{2\Psi' d}{6l_f}\right)^2 \alpha_f.\rho_f.k_b \quad \text{(U.S. customary units: psi, in.)}$$

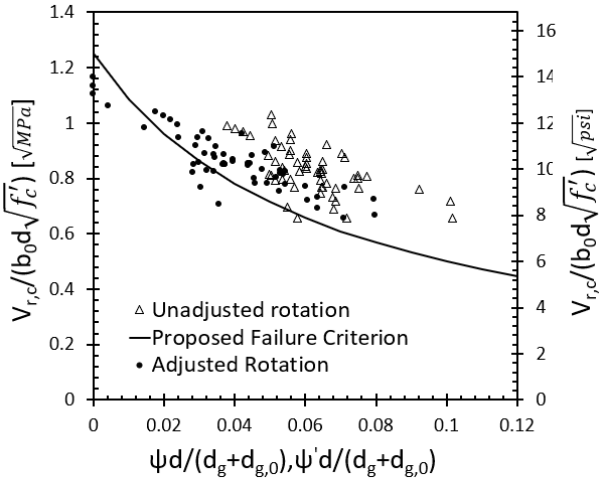

Fig. 5.8 Validation of proposed failure criterion and impact of adjusting plate rotation to account for prestressing force

The proposed failure criteria for the contribution of concrete to plate punching capacity was validated by subtracting the contribution of fibers obtained using Eq. 5.19 from computed plate punching capacities. The contribution of fibers was calculated once using the unadjusted plate rotation, Ψ', and another time using the adjusted plate rotation, Ψ', to demonstrate the

necessity of this adjustment for PT UHPC plates. The normalized computed plate rotation and $V_{r,c}$ terms were compared with those obtained from the proposed failure criterion for $V_{r,c}$ by varying plate rotation and obtaining corresponding $V_{r,c}$ values. Fig. 5.8 suggests that the use of the proposed coefficient of 1.25 (15) in the numerator of $V_{r,c}$ and the adjustment of plate rotation when calculating the contribution of fibers results in good agreement between predicted and computed punching and plate rotation capacities. If the unadjusted plate rotation is used, the discrepancy between computed and predicted results is larger.

5.7 Distinction of Punching Shear and Flexural Failures in the Proposed Method

Flexure and punching shear failure in PT UHPC plates can be distinguished by plotting the plate load rotation relationship and the rotation dependent failure criteria. The intersection of the two curves implies a punching shear failure. If the curves do not intersect, then the controlling failure mode is plate flexure. The flexural capacity of the plate in such cases can be obtained by noting the maximum load in the plate load rotation curve. Alternatively, Eq. 5.2 can be simplified by making the following substitutions: $m_r = m_u$ and $r_s = r_{cr} = r_y$, which reduce Eq. 5.2 to Eq. 5.20, where m_u is the ultimate moment capacity of the plate per unit length. Since the term EI_2 is rather small, tangential moments along the sides of the plate can be taken equal to the ultimate moment, which further simplifies Eq. 5.20 to Eq. 5.21.

$$V_{flex} = \frac{2\pi}{r_q - r_c}\left\{m_u r_o + EI_2 \Psi \langle ln(r_s) - ln(r_o)\rangle + EI_2 \chi_{TS2} \langle (r_s) - (r_o)\rangle + m_p r_m \right\} \quad \text{Eq. 5.20}$$

$$V_{flex} = \frac{2\pi}{r_q - r_c}\left\{m_u r_s + m_p r_m \right\} \quad \text{Eq. 5.21}$$

5.8 COMPARISON OF COMPUTED AND PREDICTED CAPACITIES

5.8.1 Parametric Analyses

A parametric analysis was conducted to: 1) understand the influence of several parameters on the behavior of PT UHPC plates subject to concentrated loads, and 2) demonstrate the ability of the proposed prediction methodology to accurately capture the influence of each considered parameter on plate punching shear capacity.

5.8.1.1 *Effect of plate thickness*

Six PT UHPC plates (Table 5.2) were considered to quantify the influence of plate thickness on punching shear capacity and on shear stress at failure. Table 5.2 and Fig. 5.9a suggest that increasing plate thickness is the most impactful technique to increase plate punching capacity.

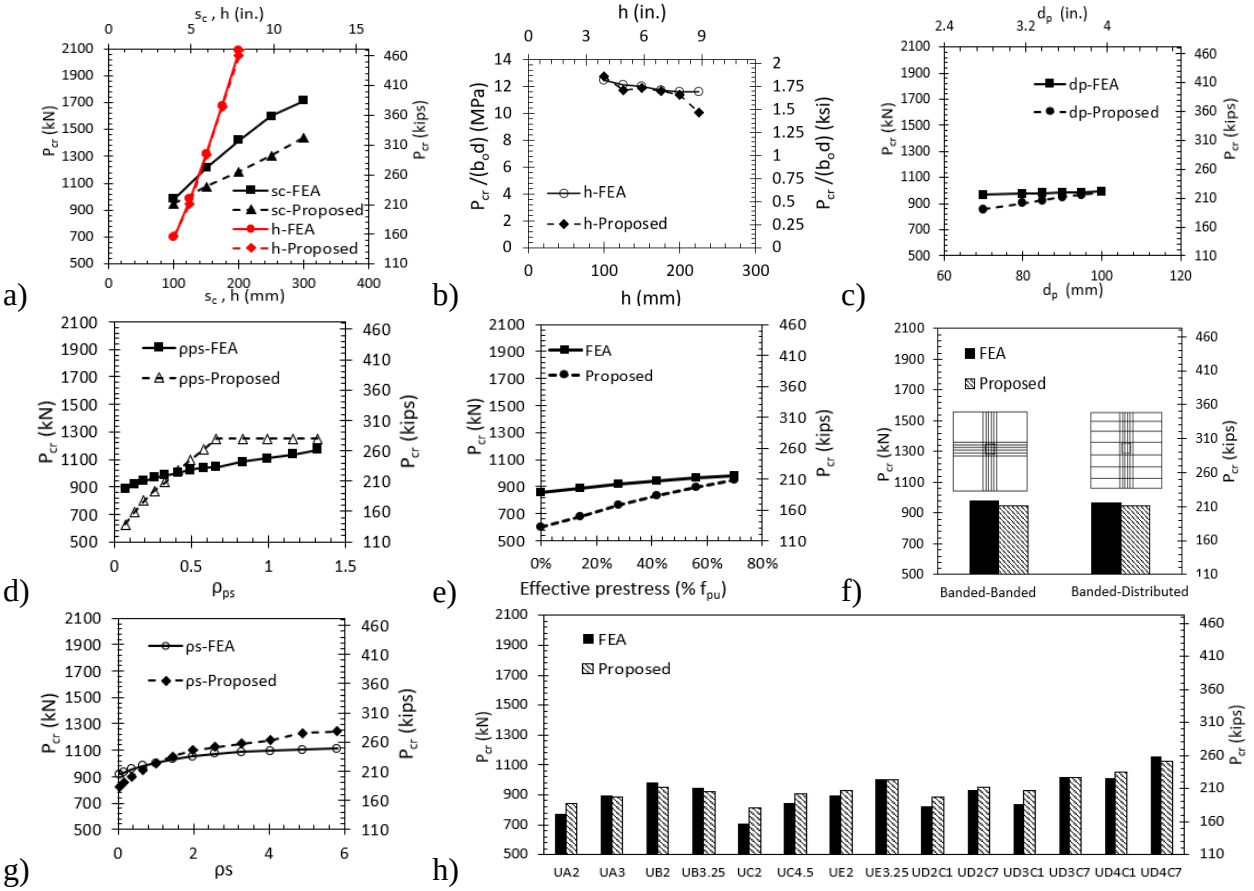

Fig. 5.9 Influence of various parameters on PT UHPC plate punching shear strength

This is expected as the influence of plate thickness, captured through the effective depth, *d*, elevates the failure criterion and increases plate stiffness, thus resulting in higher plate punching capacities. Conversely, an increase in plate thickness results in a decrease in the punching shear stress at failure as is evident in the proposed failure criterion for $V_{r,c}$. The computed and predicted punching capacities and punching shear stresses at failure are rather consistent for the considered range of plate thickness suggesting that the proposed methodology can accurately capture the influence of this parameter.

5.8.1.2 *Effect of column size*

While an increase in plate thickness may be the most impactful technique to increase plate punching shear capacity, it is not the most efficient, since a punching shear failure precipitates from the overstress of an isolated region around the column. Therefore, increasing plate thickness, increases floor dead load and consequently gravitational and seismic load demand on the entire structural system including foundations. A more efficient technique to address punching in flat plates is to increase the column size. Table 5.2 and Fig. 5.9a show that an increase in column size is also an impactful technique to increase punching capacity although not as impactful as increasing plate thickness as evidenced by the slope of the curves. The influence of column size in the prediction methodology is captured primarily through the failure criterion, through the critical punching shear perimeter, b_o, the outline of which is assumed to be at a distance *d/2* from the face of the column. The column size also influences the plate load rotation relationship as shown in Eq. 5.2 although this influence is marginal compared to that captured through the failure criterion. A comparison of computed and predicted results suggest that the proposed prediction method is able to accurately capture the influence of this parameter on plate punching capacity in terms of the

increase in punching capacity for a given change in column size, although, predicted capacities are generally lower (i.e. more conservative) than computed capacities.

5.8.1.3 *Effect of d_p*

The influence of the effective depth of prestressed reinforcement, d_p, on PT UHPC plate punching capacity was investigated by considering the range of d_p values shown in Table 5.2 and Fig. 5.9b. Larger d_p values correspond to larger plate punching capacities, however, this increase is marginal. A larger d_p results in a larger tendon stress as the plate approaches its punching capacity. This larger tendon stress results in a larger plate moment capacity captured through radial, m_r, prestressing, m_p, and tangential, m_t, moments in Eq. 5.2 thus resulting in a slightly stiffer load rotation response. However, this increase is rather small as the stiffness and flexural capacity of the plate is affected by the tensile domain of UHPC as well as non-prestressed reinforcement. Therefore, the variation of d_p alone does not amount to an appreciable increase in punching capacity. Computed and predicted capacities are generally consistent, which further demonstrates the ability of the proposed method to accurately capture the influence of this parameter on plate punching capacity.

5.8.1.4 *Effect of ρ_{ps}*

The effect of the prestressed reinforcement ratio, ρ_{ps}, on plate punching shear capacity was investigated by varying it from 0.07-1.32% as shown in Table 5.2 and Fig. 5.9d. An increase in ρ_{ps} generally results in an increase in plate punching shear capacity because ρ_{ps} affects the magnitude of prestressing force, which in turn affects the stiffness of the plate through the reduction of the critical shear crack width captured by the product of adjusted plate rotation and effective depth $\Psi' \mathrm{d}$ (Eq. 5.10). The contribution of fibers to the punching capacity of the plate is influenced similarly by the width of the critical shear crack through the $\frac{\Psi' \mathrm{d}}{6}$ term in Eq. 5.19. The

adjusted plate rotation Ψ' (Eq. 5.11) is a function of average normal stress due to prestressing, σ_n, and modulus of elasticity, E. As σ_n increases, Ψ' decreases resulting in an increase in punching capacity. However, Ψ' cannot be smaller than zero as indicated in Eq. 5.11. In cases when there is a high amount of prestressing force, the adjusted rotation assumes a value of zero and the contribution of concrete to plate punching capacity is reduced to a rotation independent formulation as shown in Eq. 5.22. Similarly, the contribution of fibers, $V_{r,f}$, becomes zero and the predicted plate punching capacity remains constant regardless of further increases in prestressed reinforcement ratio, ρ_{ps}. The increase in plate punching capacity is on average captured consistently in the numerical as well as in the proposed prediction model with average ratio and COV of computed over predicted capacity being 1.00 and 17%. Maximum and minimum ratios are contained to 1.37 and 0.83, respectively.

$$V_{R,c\Psi'} = 1.25 b_0 d \sqrt{f_c'} \quad \text{(SI units: N, mm)}$$

$$V_{R,c\Psi'} = 15 b_0 d \sqrt{f_c'} \quad \text{(U.S. customary units: psi, in.)} \qquad \text{Eq. 5.22}$$

5.8.1.5 ***Effect of Prestress Losses***

The impact of prestress losses on plate punching capacity was quantified by evaluating plates with various magnitudes of effective prestress. The considered plates are shown in Table 5.2 and feature effective prestress that varies from $0.7f_{pu}$ (i.e. full jacking stress – no losses) to 0 prestress. The magnitude of effective prestress, f_{pe}, affects the calculation of cracking moment, m_{cr}, yield moment, m_y, and ultimate moment, m_u, which define the proposed quadrilinear moment curvature relationship (Fig. 5.6). Effective prestress further influences the plate rotation relationship (Eq. 5.2) through the prestressing moment, m_p (Eq. 5.8), which is a function of the unit normal force, n, which in turn is a function of prestressing force when plate punching occurs. This prestressing force, P_{ps}, varies along the perimeter of the typical pie strip considered in the

derivation of plate's load rotation relationship, and can be obtained as function of curvature and the corresponding strand stress (which is a function of effective prestress). Strand stress also affects the critical shear crack width through the calculation of the adjusted rotation (Eq. 5.11). Table 5.2 and Fig. 5.9e suggest that for expected magnitudes of prestress losses (15-25% of jacking stress) the predicted plate punching capacities match well with computed values and for lower than expected effective prestress, the proposed method provides conservative estimates of plate punching shear capacity.

5.8.1.6 *Effect of tendon configuration*

The influence of tendon configuration on PT UHPC plate punching capacity was investigated by considering banded-banded and banded-distributed tendon configurations. Table 5.2 and Fig. 5.9f suggest that tendon configuration has very little influence on plate punching capacity and computed capacities were rather similar for both cases. Predicted capacities were identical since the proposed method does not distinguish between various tendon configurations and Fig. 5.9f suggest that such distinction is not warranted.

5.8.1.7 *Effect of ρ_s*

The effect of non-prestressed reinforcement ratio, $\boldsymbol{\rho_s}$, on the tensile zone was investigated by varying, $\boldsymbol{\rho_s}$, from 0.04% to 5.81% as illustrated in Table 5.2 and Fig. 5.9g. Higher ρ_s resulted in higher computed and predicted plate punching capacities with computed and predicted capacities being rather consistent. The influence of ρ_s on plate punching capacity is captured through the moment curvature and plate load rotation relationship with higher ρ_s values resulting in a stiffer load rotation response and consequently higher plate punching capacities.

5.8.1.8 *Effect of Fiber Content and Characteristics*

The effect of fiber content and characteristics on PT UHPC plate punching shear capacity was investigated by considering the UHPC formulations shown in Table 5.2. These formulations vary in terms of fiber content (2-4.5% by volume), fiber diameter (0.2-0.55 mm [0.0079-0.0217 in.]), fiber length (13-30 mm [0.51-1.18 in.]), fiber type (straight or with deformed ends), and UHPC compressive strength (f'_c = 91-153 MPa [13.2-22.2 ksi]). It should be noted that some of these formulations feature compressive strengths that are lower than the FHWA definition presented earlier but are classified as UHPC class materials (Haber et al. 2018). Details about these various UHPC formulations are provided in reference Haber et al. (2018). The influence on these various formulations on PT UHPC plate punching shear capacity is illustrated in Fig. 5.9h and Table 5.2. Computed and predicted capacities are rather consistent for all considered formulations demonstrating the flexibility and generality of the proposed method. The effect of fiber content, fiber length, fiber diameter, and fiber type are captured directly through the $V_{r,f}$ term in the failure criterion, and indirectly through the plate load-rotation relationship. Any differences in fiber amount and characteristics, and UHPC compressive strength will lead to differences in the UHPC constitutive relationship, which is a required input when computing the moment-curvature relationship and subsequently the plate load-rotation relationship. Measured constitutive models for the compressive and tensile domain of UHPC were available for the formulations shown in Table 5.2 and this information was used when obtaining computed and predicted plate punching shear capacities.

5.8.2 Comparison of Computed and Predicted Plate Punching Shear Capacities

The punching capacity of 58 punching critical PT UHPC plate specimens described earlier was compared with that obtained from validated NLFEA. The results are shown in Fig. 5.10. The

average of ratio of computed and predicted punching shear capacities is 0.99 and the COV is 11.3%. The minimum and maximum ratios of computed over predicted capacities are 0.73 and 1.20, respectively. These statistics suggest that the proposed prediction methodology can predict accurately the punching capacity of PT UHPC plates with various characteristics.

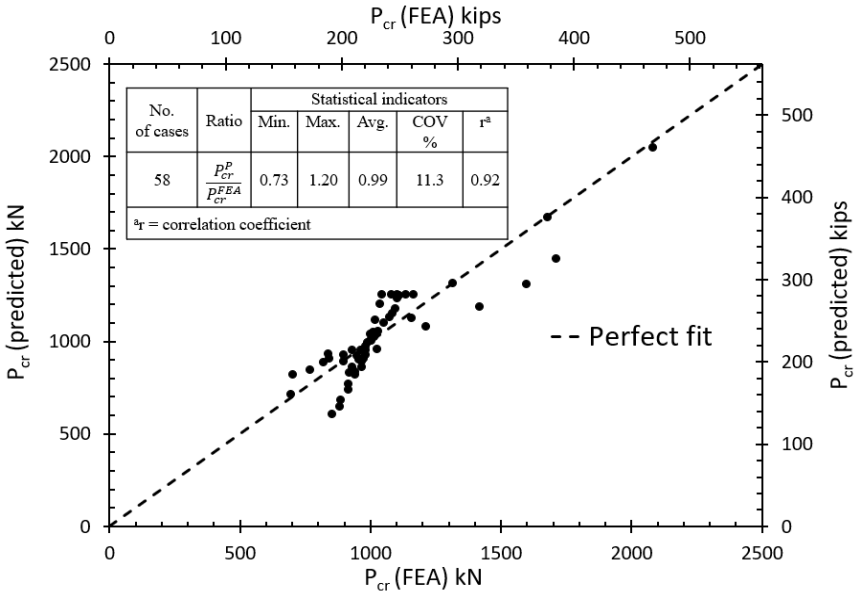

Fig. 5.10 Comparison of computed and predicted PT UHPC plate punching shear strength

5.9 SUMMARY AND CONCLUSIONS

1) A methodology to predict the punching shear capacity of PT plates was presented. The method supplies simultaneously plate's punching and rotation capacity by superimposing plate's load rotation relationship and a rotation dependent failure criterion. Punching shear capacities of 58 PT UHPC plates obtained from the proposed methodology were compared with results obtained from validated numerical models. The average ratio and COV of computed over predicted punching shear capacity are 0.99 and 11.3%, respectively, suggesting that the proposed methodology can accurately predict the punching shear capacity of PT UHPC plates.
2) A simplified procedure was proposed to predict the moment-curvature relationship for a PT UHPC plate strip of unit width and this procedure was used to generate the plate load rotation

relationship. Predicted and computed moment curvature and plate load rotation relationships were consistent.

3) A PT UHPC plate punching shear failure criterion was developed. The coefficient 1.25 (15) in Eq. 5.10 was derived using nonlinear regression using a database of punching shear in critical plates. An adjustment for plate rotation proposed by Clement et al. (2012) for PT NSC plates was evaluated and was found to be appropriate for PT UHPC plates. The inclusion of this adjustment was necessary when computing the contribution of fibers using the formulation proposed by Voo et al. (2010) for nonprestressed beams.
4) A criterion was proposed to distinguish between punching and flexure induced plate failures in the numerical models. This criterion was used to create a database of punching critical PT UHPC plate specimens, which were used to validate and inform the development of the proposed methodology. Similarly, the proposed method provides a graphical as well as a mathematical approach for how to distinguish between punching and flexure induced plate failures.
5) The proposed method captures accurately the influence of plate thickness, column size, prestressed and non-prestressed reinforcement ratio, tendon configuration, prestressing force, and fiber content and characteristics on PT UHPC plate punching capacity.

6. Chapter 6: Summary, Conclusions, and Recommendations

6.1 Summary

Procedures for predicting the flexural strength, moment-curvature-deformation response, and punching shear capacity of PT UHPC elements are presented. The prediction method for flexural strength is based on a mechanics based phenomenological model. A set of equations is provided to predict strand stress at the ultimate limit state as a function of plastic hinge length. The procedure for obtaining the moment-curvature-deformation response does not rely on empiricism other than what is included in the assumed material constitutive models, and provides the means to determine the variation of curvature and deflection as the beam is loaded to failure thus providing an avenue to quantify ductility at the cross-section and member level. The method presented for predicting the punching shear capacity of PT UHPC plates supplies simultaneously plate's punching and rotation capacity by superimposing plate's load rotation relationship and a rotation dependent failure criterion. The derivation of plates load-rotation relationship is based on engineering mechanics and is informed by the moment curvature relationship of a typical plate strip developed. Criteria are presented for distinguishing between punching and flexural failures in numerical and prediction models. All prediction methods are validated using nonlinear finite element analysis.

6.2 Conclusions

The following conclusions can be drawn for each topic:

6.2.1 Flexural Strength of PT UHPC Beams

(1) The proposed flexural design methodology is general and provides numerous advantages: (a) it accounts for simple span and continuous members featuring various loading configurations and loading patterns, (b) it accounts for rectangular and T-section behavior,(c) it captures the influence of key parameters such as beam cross-sectional dimensions, effective depth of tendons and span over effective depth ratio, area of tendons and mild steel, and different classes of UHPC exhibiting various compressive and tensile properties.

(2) The proposed methodology results in rather accurate predictions of the change in strand stress at ultimate, Δf_{ps}, the strand stress at ultimate, f_{ps}, and nominal moment capacity, M_n, of post-tensioned UHPC beams featuring average predicted values that are within 5% of computed ones and coefficients of variation no greater than 17%.

(3) The majority of investigated beams exhibited a fiber tension-controlled failure. The only exceptions were continuous T-beams and heavily post-tensioned beams, which exhibited UHPC compression controlled failures.

(4) Loading configuration, patterned loading, effective depth, span to effective depth ratio, and maximum usable UHPC compressive and tensile strains, had a strong influence on the magnitude of the change in strand stress at ultimate and therefore were directly included in the calculation of Δf_{ps}.

(5) The influence of specified UHPC compressive strength, tendon area, mild steel area, UHPC cracking stress, and continuity on Δf_{ps} was considered small enough to allow the equations of equilibrium capture their effect through the calculation of the depth to the neutral axis.

6.2.2 Moment Curvature Deformation Response of PT UHPC Beams

1) The proposed procedure is based on structural mechanics and is capable of reliably and efficiently computing the complete moment-curvature-deformation response of UHPC beams post-tensioned with internal unbonded tendons and offers insight about their ductility at the cross-section and member level. This information is useful in cases when a performance-based design approach is selected and a characterization of member behavior under different load intensities is desired.
2) The proposed method does not require the definition of empirically obtained elastic and inelastic design parameters such as bond reduction coefficients and plastic hinge length. However, it can facilitate the use of approaches that employ these parameters by helping formulate them without having to rely on extensive experimental testing or time-consuming finite element analysis.
3) Cross-section level ductility was generally higher than member level ductility. Additionally, strain-based computations resulted in higher levels of cross-section level ductility compared to curvature-based computations. Most beams met minimum cross-section level ductility requirements specified in American and Canadian standards for NSC and FRC, respectively.
4) The influence of the considered constitutive models for the tensile and compressive domains was contained to an 8.6% and 17.5% change in flexural capacity when compared to the benchmark stress-strain curves. Most members exhibited a fiber tension-controlled failure.
5) The most influential parameter for cross-section level ductility is ε_{t1}. A minimum value of 0.006 is recommend for ε_{t1} to meet existing minimum ductility requirement set forth for

NSC and FRC members. Additionally, while ε_{t1} is an important parameter related to the failure mode of UHPC beams post-tensioned with unbonded tendons, its variation does not cause a marked difference in flexural capacity.

6) The most influential parameter for member level ductility is the loading configuration especially when the ratio L/Δ_u was used as the metric for evaluating such ductility. The proposed methodology provides a framework for accurately determining the deflection at incipient failure, Δ_u. The influence of loading configuration on cross-section level ductility was much smaller than that exhibited at the member level.
7) The most influential parameters in terms of increasing flexural capacity are the longitudinal unbonded reinforcement ratio, ρ_{ps}, followed by the UHPC cracking stress, f_{cr}, and the longitudinal bonded reinforcement ratio, $\rho_{stension}$, when the impact of these parameters for a given percentage change from the baseline case was considered. While a change in f_{cr} did not influence ductility at any level, and increase in ρ_{ps} and $\rho_{stension}$ resulted in a decrease in cross-section and member level ductility.

6.2.3 Punching Shear Strength of PT UHPC Plates

1) A methodology to predict the punching shear capacity of PT plates was presented. The method supplies simultaneously plate's punching and rotation capacity by superimposing plate's load rotation relationship and a rotation dependent failure criterion. Punching shear capacities of 58 PT UHPC plates obtained from the proposed methodology were compared with results obtained from validated numerical models. The average ratio and COV of computed over predicted punching shear capacity are 0.99 and 11.3%, respectively,

suggesting that the proposed methodology can accurately predict the punching shear capacity of PT UHPC plates.

2) A simplified procedure was proposed to predict the moment-curvature relationship for a PT UHPC plate strip of unit width and this procedure was used to generate the plate load rotation relationship. Predicted and computed moment curvature and plate load rotation relationships were consistent.

3) A PT UHPC plate punching shear failure criterion was developed. The coefficient 1.25 (15) in Eq. 5.10 was derived using nonlinear regression using a database of punching critical plates. An adjustment for plate rotation proposed by Clement et al. (2014) for PT NSC plates was evaluated and was found to be appropriate for PT UHPC plates. The inclusion of this adjustment was necessary when computing the contribution of fibers using the formulation proposed by Voo et al. (2010) for nonprestressed beams.

4) A criterion was proposed to distinguish between punching and flexure induced plate failures in the numerical models. This criterion was used to create a database of punching critical PT UHPC plate specimens, which were used to validate and inform the development of the proposed methodology. Similarly, the proposed method provides a graphical as well as a mathematical approach for how to distinguish between punching and flexure induced plate failures.

5) The proposed method captures accurately the influence of plate thickness, column size, prestressed and non-prestressed reinforcement ratio, tendon configuration, prestressing force, and fiber content and characteristics on PT UHPC plate punching capacity.

6.3 Recommendation for Future Work

- Experimental testing of post-tensioned UHPC beams is recommended to increase fidelity in the numerical modelling protocol, proposed flexural design methodology, and proposed procedure for obtaining the moment-curvature-deformation response. The specimens should be designed such that they feature different failure modes to validate anticipated behavior. Work on this topic is currently underway.
- Experimental testing to evaluate PT UHPC plate punching shear capacity is recommended to validate the numerical modeling protocol and to evaluate the accuracy of the proposed prediction methodology. The angle of inclination of the compressive struts at failure (i.e. angle of diagonal tension cracks) should be measured to validate assumptions. The influence of casting method on punching shear strength should be evaluated.
- Experimental testing of beams and plates with various amounts of fibers and no nonprestressed reinforcement is recommended. These cases are important to determine whether minimum nonprestressed reinforcement requirement for PT NSC plates can be waived if plates are constructed with PT UHPC. Elimination of this requirement, if proved possible, would simplify the construction process of PT UHPC plates.
- Beams or plates with high span to depth ratios (L/d_p) should also be investigated to ensure that proposed methodology for the ultimate tendon stress (f_{ps}) is valid for such cases.
- Since the combination of PT and UHPC can lead to super slender floors, these floors should be evaluated for vibrations to ensure satisfactory performance during service.
- Long term deflections of super thin post-tensioned UHPC plates should be investigated to ensure that deflection values are within acceptable limits.

- The behavior of plate column connections under natural hazard induced loading should be investigated.

APPENDIX A

***Example:* Flexural Design Methodology for PT UHPC Beams (English Units)**

Fiber-tension controlled failure

Problem Statement

Consider a single span simply supported beam with a draped tendon configuration. The beam features 2 No. 2 bars (0.049 in^2) as nonprestressed compression reinforcement, 2 No. 2 bars (0.049 in^2) and 2 No. 3 bars (0.11 in^2) as nonprestressed tension reinforcement. Assume that that tensile domain of UHPC may be idealized using a bilinear stress-strain curve and that the compression domain may be represented as linear elastic to failure. Assume that the beam is subject to uniformly distributed loading. Using the following additional information determine the nominal moment capacity of the beam.

$f_c' = 22\ ksi$ (compressive strength of UHPC)

f = 3, distributed loading coefficient (loading configuration coefficient)

L = 336 in. (total length of beam);

h = 12 in. (total beam height)

b = 6 in. (width of beam);

A_{ps} = 0.306 in^2 (total area of prestressing strands)

d_p = 10 $in.$ (distance from centroid of strands to uppermost compression fiber)

f_{pe} = 185 ksi (effective tendon stress);

f_y = 60 ksi (yield stress of non-prestressed reinforcement);

E_c = 6853 ksi (modulus of elasticity of UHPC obtained from E_c = 46200 $\sqrt{f_c'}$ (f_c' in psi)

d_s = 10.875 in. (distance from centroid of nonprestressed tension reinforcement to uppermost compression fiber)

d_s' = 1.125 in. (distance from nonprestressed compression reinforcement to uppermost compression fiber)

E_s = 29000 ksi (modulus of elasticity of nonprestressed reinforcement);

ε_{tu} = 0.01 (ultimate tensile strain of UHPC)

E_{ps} = 28500 ksi (modulus of elasticity of prestressing strands);

c = neutral axis depth

$\varepsilon_{pe} = \frac{f_{pe}}{E_{ps}} = 6.491 * 10^{-3}$ (initial effective strain in prestressing strands)

f_{cr} = 0.994 ksi (cracking stress of UHPC) = 6.7 $\sqrt{f_c'}$ (f_c' in psi)

Solution

Use force equilibrium at mid span (total tensile forces = total compressive forces) to determine the neutral axis depth. ($\sum H = 0$) Assume that compression steel has not yielded, and tension steel has yielded. Assume that the governing strain distribution at failure is represented by a tensile strain of 0.01 in UHPC in the most extreme tension fiber. Use the proposed equation for f_{ps}.

$2*0.0049*\left[\frac{\varepsilon_{tu}*(c-d_s')*E_s}{(h-c)}\right]$ + c*$\frac{b}{2}$*$\left[\frac{\varepsilon_{tu}*c*E_c}{(h-c)}\right]$ = (h-c)*$b*f_{cr}$ + 2*0.0049*f_y + 2*0.11*f_y +

$$A_{ps}*\left[\varepsilon_{pe}+\left[\left(\frac{1}{\frac{L}{d_p}}+\frac{1}{f}\right)*L\right]*\left(\frac{\varepsilon_{tu}}{L}\right)*\left(\frac{d_p-c}{h-c}\right)\right]\left[A+\frac{B}{\left[1+\left[C*\left[\varepsilon_{pe}+\left[\left(\frac{1}{\frac{L}{d_p}}+\frac{1}{f}\right)*L\right]*\left(\frac{\varepsilon_{tu}}{L}\right)*\left(\frac{d_p-c}{h-c}\right)\right]\right]^D\right]^{1/D}}\right]$$

where A = 887, B = 27613, C = 112.4, D = 7.36

c = 2.566 in. Check assumptions:

$\left[\frac{\varepsilon_{tu}*(c-d_s')*E_s}{(h-c)}\right] = 44.31\ ksi\ < 60\ ksi$ (compression steel has not yielded)

$\left[\frac{\varepsilon_{tu}*(c)*E_c}{(h-c)}\right] = 18.64\ ksi\ < 22\ ksi$ (UHPC has not crushed in compression region)

$\left[\frac{\varepsilon_{tu}*(d_s-c)}{(h-c)}\right] = 8.807 * 10^{-3} > 2.069 * 10^{-3} = \frac{f_y}{E_s}$ (tension steel has yielded)

Using the calculated depth to the neutral axis, determine f_{ps} using the proposed equation:

$$f_{ps} = \left[\varepsilon_{pe}+\left[\left(\frac{1}{\frac{L}{d_p}}+\frac{1}{f}\right)*L\right]*\left(\frac{\varepsilon_{tu}}{L}\right)*\left(\frac{d_p-c}{h-c}\right)\right]\left[A+\frac{B}{\left[1+\left[C*\left[\varepsilon_{pe}+\left[\left(\frac{1}{\frac{L}{d_p}}+\frac{1}{f}\right)*L\right]*\left(\frac{\varepsilon_{tu}}{L}\right)*\left(\frac{d_p-c}{h-c}\right)\right]\right]^D\right]^{1/D}}\right] =$$

237 ksi

Determine the nominal moment capacity of the beam:

M_p = 2*0.0049*$\left[\frac{\varepsilon_{tu}*(c-d_s')*E_s}{(h-c)}\right](h-d_s')$ + c*$\frac{b}{2}$*$\left[\frac{\varepsilon_{tu}*c*E_c}{(h-c)}\right]\left[h-\frac{c}{3}\right]$ - (h-c)*$b*f_{cr}$ $\left[\frac{h-c}{2}\right]$ -

2*0.0049*f_y*(h - d_s) - 2*0.11*f_y * (h − d_s) - A_{ps}*f_{ps}*(h - d_p) = ***<u>1524 in – kips</u> (Answer)***

Concrete-compression controlled failure:

Problem Statement:

Consider a single span simply supported beam with a draped tendon configuration. The beam features 2 No. 2 bars (0.049 in^2) as non-prestressed compression reinforcement, and 2 No. 2 bars (0.049 in^2) and 2 No. 3 bars (0.11 in^2) as nonprestressed tension reinforcement. Assume that the tensile domain of UHPC may be idealized using a bilinear stress-strain curve and the compressive domain may be idealized using a linear elastic stress-strain relationship. Assume that the beam is subject to uniformly distributed loading. Using the following additional information determine the nominal moment capacity of the beam.

$f_c' = 22\ ksi$ (compressive strength of UHPC)

ε_{cu} = 0.0038 (ultimate compressive strain of UHPC)

f = 3 , distributed loading coefficient (loading configuration coefficient)

L = 336 in. (total length of beam) ;

h = 12 in. (total beam height)

b = 6 in. (width of beam) ;

A_{ps} = 0.918 in^2 (prestressing tendon area)

d_p = 10 $in.$ (distance from tendon location to uppermost compression fiber)

f_{pe} = 185 ksi (effective tendon stress) ;

f_y = 60 ksi (yield strength of mild steel);

E_c = 6853 ksi (modulus of elasticity of UHPC) = 46200 $\sqrt{f_c'}$ (f_c' in psi)

d_s = 10.875 in. (distance between tension mild steel to uppermost compression fiber)

d_s' = 1.125 in. (distance between compression mild steel to uppermost compression fiber)

E_s = 29000 ksi (modulus of mild steel) ;

ε_{tu} = 0.01 (ultimate tensile strain of UHPC);

E_{ps} = 28500 ksi (modulus of prestressing tendon) ;

c = neutral axis depth;

$\varepsilon_{pe} = \frac{f_{pe}}{E_{ps}} = 6.491 * 10^{-3}$ (initial effective strain in prestressing tendon);

f_{cr} = 0.994 ksi (cracking stress of UHPC) = 6.7 $\sqrt{f_c'}$ (f_c' in psi);

Solution:

Use force equilibrium at mid span (total tensile forces = total compressive forces) to determine depth to neutral axis ($\sum H = 0$). Assume that compression steel and tension steel has yielded. Assume that the governing strain distribution at failure is represented by a compressive strain of 0.0038 in UHPC in the most extreme compression fiber. Use the proposed equation for f_{ps}.

2*0.0049*f_y + c*$\frac{b}{2}$*f_c' = (h-c)*b*f_{cr} + 2*0.0049*f_y + 2*0.11*f_y

$$+ A_{ps}*\left[\varepsilon_{pe} + \left[\left(\frac{1}{\frac{L}{d_p}} + \frac{1}{f}\right) * L\right] * \left(\frac{\varepsilon_{cu}}{L}\right) * \left(\frac{d_p - c}{c}\right)\right]\left[A + \frac{B}{\left[1 + \left[C * \left[\varepsilon_{pe} + \left[\left(\frac{1}{\frac{L}{d_p}} + \frac{1}{f}\right) * L\right] * \left(\frac{\varepsilon_{cu}}{L}\right) * \left(\frac{d_p - c}{c}\right)\right]\right]^D\right]^{1/D}}\right]$$

where A = 887, B = 27613, C = 112.4, D = 7.36

c = 4.059 in. Check assumptions:

$\left[\frac{\varepsilon_{cu}*(c-d_s')*E_s}{(c)}\right] = 79.65\ ksi\ >\ 60\ ksi$ (compression steel has yielded)

$\left[\frac{\varepsilon_{cu}*(h-c)}{(c)}\right] = 7.435 *\ 10^{-3}\ < 0.01$ (maximum tensile strain is smaller than maximum usable tensile strain 0.01)

$\left[\frac{\varepsilon_{cu}*(d_s-c)}{(c)}\right] = 6.382 *\ 10^{-3}\ > 2.069 *\ 10^{-3} = \frac{f_y}{E_s}$ (tension steel has yielded)

Using the calculated depth to the neutral axis, determine f_{ps}:

$$f_{ps} = \left[\varepsilon_{pe} + \left[\left(\frac{1}{\frac{L}{d_p}} + \frac{1}{f}\right) * L\right] * \left(\frac{\varepsilon_{cu}}{L}\right) * \left(\frac{d_p - c}{c}\right)\right]\left[A + \frac{B}{\left[1 + \left[C * \left[\varepsilon_{pe} + \left[\left(\frac{1}{\frac{L}{d_p}} + \frac{1}{f}\right) * L\right] * \left(\frac{\varepsilon_{cu}}{L}\right) * \left(\frac{dp - c}{c}\right)\right]\right]^D\right]^{1/D}}\right] =$$

226 ksi

Determine nominal moment capacity:

M_p = 2*0.0049*$\left[f_y\right](h - d_s')$ + c*$\frac{b}{2}$*$[f_c']\left[h - \frac{c}{3}\right]$ - (h-c)*b*f_{cr} $\left[\frac{h-c}{2}\right]$ - 2*0.0049*f_y*(h - d_s) - 2*0.11*f_y * (h $-$ d_s) - A_{ps}*f_{ps}*(h - d_p) = **2292 in – kips** ***Answer***

APPENDIX B

***Example:* Punching shear capacity of a PT UHPC Plate (SI Units)**

Problem Statement

Consider a two-way square flat plate with a draped tendon configuration in both direction. Assume that there are 15 No. 8 bars (50.27 mm^2) as nonprestressed compression reinforcement, and 28 No. 8 bars (50.27 mm^2) as nonprestressed tension reinforcement. Assume that the tensile domain of UHPC may be idealized using a bilinear stress-strain curve and that the compression domain may be represented by a linear elastic relationship. Assume that there are 6 tendons with a 14.7 mm diameter placed in each direction. Determine the punching shear capacity of the plate using the additional information provided below:

$f_c' = 151.1\ MPa$ (compressive strength of UHPC)

L = 2000 mm (plate length);

h = 125 mm (total plate height)

b = 2000 mm (plate width);

A_{ps} = 592.2 mm^2 (prestressing tendon area in one direction);

d_p = 90.8 mm (distance from tendon location to uppermost compression fiber);

d_{pavg} = 76.65 mm (average tendon depth from uppermost compression fiber);

f_{pe} = 1292 MPa (effective tendon stress);

f_y = 420 MPa (yield strength of mild steel);

E_c = 47200 MPa (modulus of elasticity of UHPC) = 3840 $\sqrt{f_c'}$ (f_c' in MPa);

d_s = 109 mm (distance between tension mild steel to uppermost compression fiber);

d_s' = 16 mm (distance between compression mild steel to uppermost compression fiber);

E_s = 200 GPa (modulus of mild steel) ;

ε_{tu} = 0.01 (ultimate tensile strain of UHPC);

E_{ps} = 196.5 GPa (modulus of prestressing tendon) ;

c = neutral axis depth;

$\varepsilon_{pe} = \frac{f_{pe}}{E_{ps}} = 6.576 * 10^{-3}$ (initial effective strain in prestressing tendon);

f_{cr} = 6.884 MPa (cracking stress of UHPC) = 0.56 $\sqrt{f_c'}$ (f_c' in MPa);

d_g = 0 mm (maximum aggregate size in diameter);

d_f = 0.3 mm (diameter of fiber in matrix);

d_{go} = 16 mm (reference aggregate size in diameter);

l_f = 16.5 mm (length of fiber in matrix);

k_b = 0.6 mm (bond factor for straight fiber) ;

ρ_f = 2% (fiber reinforcement ratio in volume);

b_c = 100 mm (side length of square column) ;

$r_c = \frac{2*b_c}{\pi} = 63.66$ mm (radius of circular column);

$r_o = r_c + d_s = 172.66$ mm (radius of critical shear crack, d away from face of support);

$r_q = 500$ mm (radius of isolated slab element);

$r_m = 500$ mm (radius of isolated slab element);

$r_s = \frac{L}{2} = 500$ mm (radius of load introduction at perimeter);

$b_o = (4 * b_c + \pi * d_s) = 742.4$ mm (control perimeter d/2 away from face of support);

Solution:

Using the proposed procedure to obtain the moment curvature relationship determine the following points:

$\phi_{initial} = 1.5 * 10^{-6}$ 1/mm (initial curvature after prestressing)

$M_{cr} = 1.16 * 10^{8}$ N.mm (cracking moment of slab)

$\phi_{cr} = 1.04 * 10^{-5}$ 1/mm (curvature at cracking moment)

$M_y = 1.8 * 10^{8}$ N.mm (moment at mild steel yielding)

$\phi_y = 3.15 * 10^{-5}$ 1/mm (curvature at mild steel yielding)

$M_u = 1.99 * 10^{8}$ N.mm (ultimate moment, fiber-tension controlled)

$\phi_u = 9.58 * 10^{-5}$ 1/mm (curvature at ultimate moment)

$f_{ps} = 1345$ MPa (tendon stress at ultimate)

Determine unit moments and forces as follows:

$m_{cr} = \frac{M_{cr}}{b} = 5.8 * 10^{4}$ N-mm/mm (cracking moment of slab per unit length)

$m_y = \frac{M_y}{b} = 9 * 10^4$ N-mm/mm (moment at mild steel yielding per unit length)

$m_u = \frac{M_u}{b} = 9.95 * 10^4$ N-mm/mm (moment at ultimate per unit length)

$n = \frac{f_{ps} * A_{ps}}{b} = 398.2$ N /mm (unit force due to prestressing tendon)

$m_p = n\left[\frac{h^2}{12(d_s - \frac{h}{2})} + e\right] = 1.96 * 10^4$ N.mm/mm (decompression moment per unit length)

r_m = location of prestressing effect;

e = tendon eccentricity

$\sigma_n = \frac{n}{h} = 3.186$ MPa (unit normal stress due to prestressing tendon)

ψ = rotation of slab outside of column region;

m_r = radial moment at critical shear crack region;

Determine the terms required to obtain the load rotation relationship:

$EI_0 = \frac{m_{cr}}{\phi_{cr} - \phi_{initial}} = 5.577 * 10^9$ MPa.mm^4/mm (slope between cracking and onset of loading)

$EI_1 = \frac{m_y - m_{cr}}{\phi_y - \phi_{cr}} = 1.517 * 10^9$ MPa.mm^4/mm (slope between cracking and yielding moment)

$EI_2 = \frac{m_u - m_y}{\phi_u - \phi_y} = 1.477 * 10^8$ MPa.mm^4/mm (slope between yielding moment and ultimate)

$X_{TS1} = \frac{m_y}{EI_1} - \phi_y = 2.784 * 10^{-5}$ 1/mm (curvature difference between cracking and yielding)

$X_{TS2} = \frac{m_u}{EI_2} - \phi_u = 5.777 * 10^{-4}$ 1/mm (curvature difference between yielding and ultimate)

General the load-rotation relationship as follow:

$$V_R = \frac{2*\pi}{r_q - r_c}\left\{\begin{array}{c} m_r * r_o + EI_0 * \psi * \left[\ln(r_s) - \ln\left(\frac{\psi}{\phi_{cr}}\right)\right] + EI_1 * \psi * \left[\ln\left(\frac{\psi}{\phi_{cr}}\right) - \ln\left(\frac{\psi}{\phi_y}\right)\right] \\ +EI_1 * X_{TS1} * \left[\left(\frac{\psi}{\phi_{cr}}\right) - \left(\frac{\psi}{\phi_y}\right)\right] + EI_2 * \psi * \left[\ln\left(\frac{\psi}{\phi_y}\right) - \ln(r_o)\right] \\ +EI_2 * X_{TS2} * \left[\left(\frac{\psi}{\phi_y}\right) - (r_o)\right] + m_p * r_m \end{array}\right\}$$

Equate the total load (V_R) to the punching shear capacity of the plate (V_R) and solve for the critical plate rotation at punching failure.

$V_R = V_{R,c} + V_{R,f}$; $\psi' = \psi - 45 * \frac{\sigma_n}{E_c}$;

$\frac{V_{R,c}}{b_0 * d * \sqrt{f_c'}} = \frac{1.25}{1+15*\frac{\psi' * d_s}{d_{go}+d_g}}$; $\frac{V_{R,f}}{b_0 * d_s * \sqrt{f_c'}} = \frac{1}{\pi} * \arctan\left(3.5 * \frac{\psi' * d_s}{6 * l_f}\right) * \left(1 - \frac{\psi' * d_s}{3 * l_f}\right)^2 * \frac{l_f}{d_f} * \rho_f * k_b$

$$\frac{2*\pi}{r_q - r_c}\left\{\begin{array}{c} m_r * r_o + EI_0 * \psi * [\ln(r_s) - \ln(r_s)] + EI_1 * \psi * \left[\ln(r_s) - \ln\left(\frac{\psi}{\phi_y}\right)\right] \\ +EI_1 * X_{TS1} * \left[(r_s) - \left(\frac{\psi}{\phi_y}\right)\right] + EI_2 * \psi * \left[\ln\left(\frac{\psi}{\phi_y}\right) - \ln(r_o)\right] \\ +EI_2 * X_{TS2} * \left[\left(\frac{\psi}{\phi_y}\right) - (r_o)\right] + m_p * r_m \end{array}\right\}$$

$$= \frac{1.25}{1 + 15 * \frac{\psi' * d_s}{d_{go} + d_g}} + \frac{1}{\pi} * \arctan\left(3.5 * \frac{\psi' * d_s}{6 * l_f}\right) * \left(1 - \frac{\psi' * d_s}{3 * l_f}\right)^2 * \frac{l_f}{d_f} * \rho_f * k_b$$

$\psi = 0.009914$; $\psi - 45 * \frac{\sigma_n}{E_c} = 6.896 * 10^{-3} > 0$

Using this critical plate rotation determine the punching shear capacity of the plate.

$\frac{\psi}{\phi_{cr}} = 953.25 > r_s$, so, take it as r_s ; $\frac{\psi}{r_o} = 5.742 * 10^{-5}$ 1/mm (curvature at critical shear crack)

$\frac{\psi}{\phi_y} = 314.723 < r_s$, so, take it as r_y ; $m_r = 9.5 * 10^4$ N.mm/mm (unit radial moment at $\frac{\psi}{r_o}$)

$\boldsymbol{V_R = 932.3}$ ***kN (Answer)*** (punching shear capacity of post-tensioned UHPC slab)

REFERENCES

American Association of State Highway and Transportation Officials (AASHTO). 2017. AASHTO LRFD Bridge Design Specifications, 8th ed. Washington, DC: AASHTO.

Abaqus [Computer Software]. Dassault Systemes Americas Corp., Waltham, MA.

ACI (American Concrete Institute). (2014). Building code requirements for structural concrete and commentary. ACI 318-14, Farmington Hills, MI.

ACI (2019). "Building Code Requirements for Structural Concrete and Commentary", ACI 318-19, Farmington Hills, MI.

ACI Committee 435. (2003). Control of Deflection in Concrete Structures (ACI 435R),Farmington Hills, MI: American Concrete Institute.

AFGC. (2013). *Ultra High Performance Fibre-Reinforced Concrete Recommendations* . Paris, France : Association Francaise de Genie Civil .

Alkhairi F.M., Naaman A.E. (1993) Analysis of Beams Prestressed with Unbonded Internal or External Tendons. J. Struct. Eng. 119(9):2680-2700.

Al-Quraishi, H. (2014). *Punching Shear Behavior of UHPC Flat Slabs* . Faculty of Civil and Environmental Engineering of University of Kassel PhD Defense .

Ariyawardena, N., Ghali, A. (2002). Prestressing with unbonded internal or external tendons: Analysis and computer model. Journal of structural engineering, 128(12), 1493-1501.

ASCE (2020). Future World Vision: What's Next? The Megacity . ASCE 2020 Convention

Au, F. T. K., Du, J. S. (2004). Prediction of ultimate stress in unbonded prestressed tendons. Magazine of Concrete Research, 56(1), 1-11.

Au, F. T. K., Du, J. S., & Cheung, Y. K. (2005). Service load analysis of unbonded partially prestressed concrete members. Magazine of Concrete Research, 57(4), 199-209.

Baghi, H., Menkulasi, F.,Parker, J., Barros, J.A.O. (2017). Development of a High-Performance Concrete Deck for Louisiana's Movable Bridges: Numerical Study .J. Bridge Eng., 22(7)

Balaguru P. Increase of stress in unbonded tendons in prestressed concrete beams and slabs. Canadian Journal of Civil Engineering 1981;8(2):262-268.

Broms, C. E. (2006), Concrete flat slabs and footings Design method for punching and detailing for ductility, *Royal Institute of Technology*, Stockholm, Sweden, pp. 104

BSI (British Standards Instituition). (2001). Structural use of concrete. BS8110, London

Canadian Standards Association (CSA) S6. (2019). “Canadian Highway Bridge Design Codes” Annex 8.1 on Fibre Reinforced Concrete, Rexdale, Canada.

Chen, L.C., Graybeal, B.A. (2012). Modeling Structural Performance of Second-Generation Ultrahigh-Performance Concrete Pi-Girders. J. Bridge Eng, 17(4): 634-643

Chen, L.C., Graybeal, B.A. (2012). Modeling Structural Performance of Ultrahigh Performance Concrete I-Girders. J. Bridge Eng, 17(5): 754-764

Clément, T.; Ramos, A.P.; Ruiz, M.F.; and Muttoni, A. (2012), Design for punching of prestressed concrete slabs, *Structural Concrete*, pp. 157-167.

Clement, T.; Ramos, A.P.; Ruiz, M.F.; and Muttoni, A. (2014), Influence of prestressing on the punching strength of post-tensioned slabs, *Engineering Structures*, pp. 56-69.

Devalapura R.K., Tadros M.K. (1992) Stress-strain modeling of 270 ksi low-relaxation prestressing strands. PCI J.100-106

DIN (Deutches Institut fur Normung). (1980). Spannbeton, dautile mit vorspannung ohne verbund. DIN 4227, Teil 6, Berlin

Dogu M, Menkulasi F. (2020) A flexural design methodology for UHPC beams posttensioned with unbonded tendons. Engineering Structures .207.

Du, G., Tao, X. (1985). Ultimate stress of unbonded tendons in partially prestressed concrete beams. PCI J., 30(6), 72-91.

Esmaeeli, Esmaeel (2015). Development of Hybrid Composite Plate (HCP) for the Strengthening and Repair of RC Structures., http://repositorium.sdum.uminho.pt/handle/1822/40465, DoctoralThesis, University of Minho, Guimaraes.

fib. (2013). *FIP Model Code for Concrete Structures 2010.* Lausanne, Switzerland: Federation Internationale de la Precontrainte.

Ji-Hyun, P. (2015). *Estimation of Punching Shear on UHPC Slab.* Seoul: Seoul National University, PhD Thesis.

Joh, C., Hwang, H., & Kim, B.-S. (2008). Punching shear and flexural strengths of ultra high performance concrete slabs. *High Performance Structures and Materials IV*, 97-106.

Joh, C., Kim, B., Hwang, H., Choi, K., & Choi, S. (2011). Punching Shear Strength of Deck Slabs Made of Ultra High Performance Concrete. *Journal of Korea Institute*, 221-231.

John, E. E., Ruiz, E. D., Floyd, R. W., Hale, W. M. (2011). Transfer and development lengths and prestress losses in ultra-high-performance concrete beams. Transportation research record, 2251(1), 76-81.

JSCE. (2008). *JSCE82: Recommendations for design and constructuin of high performance fibre reinforced cement composites with multiple fine cracks (HPFRCC).* Tokyo, Japan: Japan Society of Civil Engineers .

Gouveia, N.D.; Lapi, M.; Orlando, M.; and Faria, D.M.V. (2017), Experimental and theoretical evaluation of punching strength of steel fiber reinforced concrete slabs, *Structural Concrete*, pp. 217-229.

Graddy, J., Kim, J., Whitt, J., Burns, N., & Klingner, R. (2002). Punching-Shear Behavior of

Bridge Decks under Fatigue Loading. *ACI Structural Journal*, 257-266.

Graybeal B.A. (2017) Compressive behavior of ultra-high-performance fiber-reinforced concrete. ACI Material J. 104(2):146-152.

Graybeal, B. A. (2006). Structural behavior of ultra-high performance concrete prestressed I-girders (No. FHWA-HRT-06-115). United States. Federal Highway Administration. Office of Infrastructure Research and Development.

Haber, Z. B., De la Varga, I., Graybeal, B. A., Nakashoji, B., & El-Helou, R. (2018). Properties and behavior of UHPC-class materials (No. FHWA-HRT-18-036). United States. Federal Highway Administration. Office of Infrastructure Research and Development.

Hallgreen, M. (1996), Punching Shear Capacity of Reinforced High Strength Concrete Slabs, *Royal institute of Technology*, Stockholm, Sweden, 206 pp.

Harajli, M. H. (1990). Effect of span-depth ratio on the ultimate steel stress in unbonded prestressed concrete members. Structural Journal, 87(3), 305-312.

Harajli, M. H. (2006). On the stress in unbonded tendons at ultimate: Critical assessment and proposed changes. ACI Structural Journal, 103(6), 803.

Harajli, M.H. (2011). Proposed Modification of AASHTO-LRFD for Computing Stress in Unbonded Tendons at Ultimate. J. Bridge Eng., 828-838

Harajli, M. H.,Kanj, M.Y. (1992). Service Load Behavior of Concrete Members Prestressed with Unbonded Tendons . J.Struct. Eng. , 2569-2589

Harajli, M., Maalouf, D., & Khatib, H. (1995). Effect of fibers on punching shear strength of slab-column connections. *Cement and Concrete Composties*, 161-170.

Harajli, M.H., Mabsout, M.E., Al-Hajj, J.A (2002). Response of externally post-tensioned continuous members. ACI Struct. J. 99(5), 671-680

Harris, D.K. (2004). Characterization of punching shear capacity of thin UHPC plates. Virginia Polytechnic Institute and State University, Blacksburg, Virginia

Harris, D., & Roberts-Wollmann, C. (2005). *Characterization of Punching Shear Capacity of Thin Ultra-High Performance Concrete Slabs.* Virginia: Virginia Polytechnic Institute and State University.

He, Z.-Q., Liu, Z. (2010). Stresses in External and Internal Unbonded Tendons Unified Methodology and Design Equations . J. Struc. Eng, 1055-1065.

Higashiyama, H., Ota, A., & Mizukoshi, M. (2011). Design equation for punching shear capacity of SFRC slabs . *International Journal of Concrete Structures and Materials*, 35-42.

Hines, E.M., Restrepo, J.I., Seible, F. (2004). Force-displacement characterization of well-confined bridge piers. ACI Structural Journal. V. 1O1, No 4, 537-548

Hognestad, E. (1951). A study on combined bending and axial load in reinforced concrete members. Univ of Illinois at Urbana-Champaign, IL,42-46 : Univ. of Illinois Engineering Experiment Station

Hornbeck R.W. (1975), Numerical Methods, Prentice-Hall, Inc., Englewood Cliffs, N.J., 293-294

Huang, Y.,Kang, T.H-K., Ramseyer, C., Rha, C. (2010). Background to multi-scale modelling of unbonded Post-Tensioned concrete structures. Int. J. Theoretical and Applied Multiscale Mechanics, 219-235.

Kim, K., Kang, T. H. (2019). Experiments on Continuous Unbonded Post-Tensioned Beams with 2400 MPa (350 ksi) Strands. ACI Structural Journal, 116(5), 125-136.

Kim, K. S., & Lee, D. H. (2012). Nonlinear analysis method for continuous post-tensioned concrete members with unbonded tendons. Engineering Structures, 40, 487-500.

Kinnunen, S.; and Nylander, H., (1960) Punching of Concrete Slabs Without Shear Reinforcement,

Royal Institute of Technology, Stockholm, Sweden

Knight D., Visintin P., Oehlers D.J., Ali M. (2014) Simulating RC beams with unbonded FRP and steel prestressing tendons. Composites: Part B ;60:392-399.

K-UHPC. (2012). *Design Guidelines for Ultra High Performance Concrete K-UHPC Structure.* Korea Concrete Institute.

Lampropoulos, A., Duncan, J., & Tsioulou, O. (2019). Punching shear resistance of UHPFRC. *IABSE Congress.* New York: Metropolis.

Lee, J., Fenves, G.L. (1998). Plastic-Damage Model for Cyclic Loading of Concrete Structures. J Eng Mech, 124(8), 892-900.

Lee, L.H., Moon, J.H., Lim, J.H. (1999). Proposed methodology for computing of unbonded tendon stress at flexural failure. ACI Struct. J., 96(6), 1040-1050

Lubliner, J., Oliver, J., Oller, S., Onate, E. (1989). A plastic-damage model for concrete. Int J.Solids Struct; 25(3), 229-326

MacGregor, R.J.G., Kreger, M.E., Breen, J.E. (1989). Strength and Ductility of a Three-Span Externally Post-Tensioned Segmental Box Girder Bridge Model. Research report no. 365-3F, Center for Transportation Research, University of Texas at Austin

Mahmud, G., Yang, Z., Hassan, A. (2013). Experimental and numerical studies of size effects of Ultra High Performance Steel Fibre Reinforced Concrete(UHPFRC) beams. Construction and Building Materials, 48: 1027-1034

Maguire, M.; Collins, W. M.; Halbe, K. R.; and Roberts-Wollmann, C. L., (2016), Multi-Span Members with Unbonded Tendons: Ultimate Strength Behavior, ACI Structural Journal, V. 113, No. 2, Mar.-Apr., pp. 195-204.

Maguire, M.; Chang, M.; Collins, W.; and Sun, Y., 2017, Stress Increase of Unbonded Tendons in

Continuous Posttensioned Members. Journal of Bridge Engineering, ASCE, V. 22, No. 2, Feb., p. 04016115 doi: 10.1061/(ASCE)BE.1943-5592.0000991

Mattock, A.H., Yamazaki, J.,Kattula, B.T. (1971). Comparative Study of Prestressed Concrete Beams, With and Without Bond . ACI Journal, 116-125.

Maya, L.F.; Ruiz, M.F.; Muttoni, A.; and Foster, S.J. (2012) Punching shear strength of steel fibre reinforced concrete slabs. *Engineering Structures*, pp. 83-94.

Meng, W., Khayat, K.H. (2016). Flexural Performance of Ultra-High Performance Concrete Ballastless Track Slabs. Joint Rail Conference Paper

Moreillon, L. (2013). *Shear strength of structural elements in high performance fibre reinforced concrete (HPFRC).* Paris: Universite Paris-Est, PhD Thesis.

Moreillon, L., Suter, R., & Roy, R. (2013). Punching shear resistance of UHPFRC slabs: Experimental works and design model. *AFGC Int. Symposium on Ultra-High Performance Fibre-Reinforced Concrete, UHPFRC 2013* (pp. 577-586). Marseille, France: RILEM-fib.

Muttoni, A. (2008) Punching Shear Strength of Reinforced Concrete Slabs without Transverse Reinforcement, *ACI Structural Journal* , pp. 441-450.

Naaman, A.E. (2012). "Prestressed Concrete Analysis and Design - Fundamentals", Techno Press 3000, Ann Arbor, MI.

Naaman, A.E, Alkhairi,F.M (1991). Stress at Ultimate in Unbonded Post-tensioning Tendons Part 1 - Evaluation of State-of-the-Art. ACI Structural Journal, 641-651.

Naaman, A.E, Alkhairi,F.M. (1991). Stress at Ultimate in Unbonded Post-tensioned Tendons: Part 2 -Proposed Metholodgy . ACI Structural Journal, 683-692.

Narayanan, R., & Darwish, I. (1987). Punching Shear Tests on Steel Fibre Reinforced Micro-concrete Slabs. *Magazine of Concrete Research* , 42-50.

Neto, B., Barros, J., & Melo, G. (2014). Model to simulate the contributon of fibre reinforcement for the punching resistance of RC slabs . *Journal of Materials in Civil Engineering* , 1-10.

Nyugen-Minh, L., Rovnak, M., & Tran-Quoc, T. (2012). Punching shear capacity of interior SFRC slab-column connections. *Journal of Structural Engineering* , 613-624.

Ozkul, O., Nassif, H., Tanchan, P., & Harajli, M. (2008). Rational approach for predicting stress in beams with unbonded tendons. ACI Structural Journal, 105(3), 338.

Pannell, F. N. (1969). The ultimate moment of resistance of unbonded prestressed concrete beams. Magazine of concrete research, 21(66), 43-54.

Park, R., Pauley,.T. (1975). Reinforced Concrete Structures. New York: Wiley.

Peng, F., Xue, W. (2019). Calculating Method for Ultimate Tendon Stress in Internally Unbonded Prestressed Concrete Members. ACI Structural Journal, 116(5).

PTI (Post-Tensioning Institute). (2006). Post-Tensioning Manual, 6th Edition. Phoenix, AZ.

Roberts-Wollmann, C.L.,Kreger, M. E.,Rogowsky, D.M.,Breen, J.E. (2005). Stresses in External Tendons at Ultimate. ACI Structural Journal, 206-213

Russel, H.G., Graybeal, B.A.(2013). Ultra-High Performance Concrete: State-of-the-Art Report for the Bridge Community, Federal Highway Administration

Shaaban, A., & Gesund, H. (1994). Punching Shear Strength of Steel Fiber Reinforced Concrete Flat Plates. *ACI Structural Journal*, 406-414.

Shoukry, M., Tarabia, A., & Yassin, A. (2020). Punching shear strength of ultra-high-performance fibre concrete slab-column connections. *Structures and Buildings* , 1-13.

SIA (Swiss Society of Engineers and Architects). (1979). Ultimate load behavior of slabs. SIA 162, Zurich, Switzerland

Silva, R.J.C.; Regan, P.E.; and Melo, G.S.S.A., (2007) Punching of Post-Tensioned Slabs—Tests

and Codes. *ACI Structural Journal* ,pp. 123-132.

Six, P., Tawadrous, R., Syndergaard, P., & Maguire, M. (2019). Flexural behavior of three span continuous unbonded post-tensioned members with variable bonded reinforcement. Engineering Structures, 200, 109704.

Solhmirzaei, R., Kodur, V.K.R. (2017). Modeling response of ultra high performance fiber-reinforced concrete beams. Procedia Engineering, 211-219

Tam, A., Pannel, F.N. (1976). The ultimate moment of resistance of unbonded partially prestressed reinforced concrete beams. Mag. Concr. Res., 28(97), 203-208

Toutlemonde, F., Renaud, J., Lauvin, L., Brisard, S., & Resplendino, J. (2007). *Local bending tests and punching failure of ribbed UHPFRC bridge deck.* Catania, Italy : IA-FraMCoS.

van Weerdhuizen, M., & Bartlett, F. M. (2020). Deflection at Incipient Failure as Warning-of-Failure Metric. ACI Structural Journal, 117(4), 233-241.

Vecchio, F. J.,Collins, M.P. (1986). The Modified Compression-Field Theory for Reinforced Concrete Elements Subjected to Shear . ACI Journal, 219-231.

Vega M., Dotreppe J.C. (1988). Numerical procedure for the analysis of the ultimate limit state behavior of prestressed concrete structures. Federation International de la Precontrainte

Voo, Y.L.; Poon, W.K.; and Foster, S.J., (2010) Shear Strength of Steel Fiber-Reinforced Ultrahigh-Performance Concrete Beams without Stirrups, *Journal of Structural Engineering*, pp. 1393-1400.

Vu, N. A., Castel, A., & François, R. (2010). Response of post-tensioned concrete beams with unbonded tendons including serviceability and ultimate state. Engineering Structures, 32(2), 556-569.

Xu, X., & Hou, Z. (2020). Experimental Study on One-Way BFRP Bar-Reinforced UHPC Slabs

under Concentrated Load. *Materials*.

Zhao, X., Wu, Y.F., Leung, A.Y., Lam, H.F. (2011). Plastic Hinge Length in Reinforced Concrete Flexural Members. Procedia Engineering , 1266-1274.

Zheng, W., Zhou, W. (2014). Unbonded Tendon Stresses in Continuous Post-Tensioned Beams. ACI Structural Journal, 525-536.

Zhou, W., Hu, Y. (2018). Ultimate Stress of Large-Diameter Strands in Simple Unbonded Post-Tensioned Beams. ACI Structural Journal, 115(5).

ABSTRACT

FLEXURE AND PUNCHING SHEAR BEHAVIOR OF UHPC ELEMENTS POST-TENSIONED WITH UNBONDED TENDONS

by

Mehmet Dogu

August 2021

Advisor: Dr. Fatmir Menkulasi

Major: Civil and Environmental Engineering (Structural Engineering)

Degree: Doctor of Philosophy

Procedures for predicting the flexural strength, moment-curvature-deformation response, and punching shear capacity of PT UHPC elements are presented. The prediction method for flexural strength is based on a mechanics based phenomenological model. A set of equations is provided to predict strand stress at the ultimate limit state as a function of plastic hinge length.

The procedure for obtaining the moment-curvature-deformation response does not rely on empiricism other than what is included in the assumed material constitutive models, and provides the means to determine the variation of curvature and deflection as the beam is loaded to failure thus providing an avenue to quantify ductility at the cross-section and member level.

The method presented for predicting the punching shear capacity of PT UHPC plates supplies simultaneously plate's punching and rotation capacity by superimposing plate's load rotation relationship and a rotation dependent failure criterion. The derivation of plates load-rotation relationship is based on engineering mechanics and is informed by the moment curvature relationship of a typical plate strip developed. Criteria are presented for distinguishing between punching and flexural failures in numerical and prediction models. All prediction methods are validated using nonlinear finite element analysis.

AUTOBIOGRAPHICAL STATEMENT

I have completed my primary education in small village in Turkey. For high school, I have moved to metropolitan city. Buildings, towers and especially bridges started to impress me while in city. I have found my career path, which was structural engineering. Even if my family was insisting on me becoming medical doctor, I was thinking I was not going to be happy if I became doctor. I have selected civil engineering in university and pursued my own dream. That was not enough for me since I was thinking I have not taken enough courses and knowledge regarding structural engineering. I have picked post-tensioning topic as my topline in education career. I have found a university where I can work on post-tensioning and do master and PhD degree in structural engineering. That university was Wayne State University. After I have gained more knowledge on structural engineering, I would like to work on big international company where I can work in design team especially on bridge designs. I would like emphasis on dreams. Pursuing your own dreams is far more important than pursuing for dreams that does not belong to you or money. Pursuing money may make you sad for your entire life if you are not happy with your work and discipline. Go for your dreams even if there will be time where you will pay high price for those dreams…